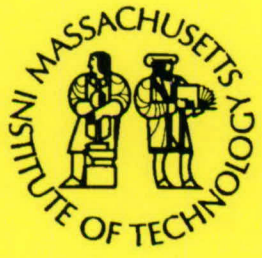
MIT/WHOI 2005-02

Massachusetts Institute of Technology
Woods Hole Oceanographic Institution



Joint Program in Oceanography/ Applied Ocean Science and Engineering



DOCTORAL DISSERTATION

Blooms of the Toxic Dinoflagellate *Alexandrium fundyense* in the Gulf of Maine: Investigations Using a Physical-Biological Model

by

Charles A. Stock

February 2005

DISTRIBUTION STATEMENT A
Approved for Public Release
Distribution Unlimited

MIT/WHOI

2005-02

Blooms of the Toxic Dinoflagellate
Alexandrium fundyense in the Gulf of Maine:
Investigations Using a Physical-Biological Model

by

Charles A. Stock

Massachusetts Institute of Technology
Cambridge, Massachusetts 02139

and

Woods Hole Oceanographic Institution
Woods Hole, Massachusetts 02543

February 2005

DOCTORAL DISSERTATION

Funding was provided by EPA STAR fellowship 91574901, National Science Foundation Grant OCE-9808173, and the WHOI Academic Programs Office.

Reproduction in whole or in part is permitted for any purpose of the United States Government. This thesis should be cited as: Charles A. Stock, 2004. Blooms of the Toxic Dinoflagellate Alexandrium fundyense in the Gulf of Maine: Investigations Using a Physical-Biological Model. Ph.D. Thesis. MIT/WHOI, 2005-02.

Approved for publication; distribution unlimited.

Approved for Distribution:

W. Rockwell Geyer, Chair
Department of Applied Ocean Physics and Engineering

Paola Malanotte-Rizzoli
MIT Director of Joint Program

John W. Farrington
WHOI Dean of Graduate Studies

Blooms of the Toxic Dinoflagellate *Alexandrium fundyense* in the Gulf of Maine: Investigations Using a Physical-Biological Model

By

Charles A. Stock

B.S.E., Princeton University, 1997
M.S., Stanford University, 1998

Submitted in partial fulfillment of the requirements for the degree of

DOCTOR OF PHILOSOPHY

at the

MASSACHUSETTS INSTITUTE OF TECHNOLOGY

and the

WOODS HOLE OCEANOGRAPHIC INSTITUTION

February 2005

© 2005, Charles A. Stock
All rights Reserved

The author hereby grants to MIT and WHOI permission to reproduce paper and electronic copies of this thesis in whole or in part and to distribute them publicly.

Signature of Author 

Joint Program in Oceanography/Applied Ocean Science and Engineering
Massachusetts Institute of Technology
and Woods Hole Oceanographic Institution
February, 2005

Certified by 

Dennis J. McGillicuddy
Thesis Supervisor

Accepted by 

Mark A. Grosenbaugh
Chair, Joint Committee for Applied Ocean Science and Engineering
Massachusetts Institute of Technology/
Woods Hole Oceanographic Institution

Blooms of the Toxic Dinoflagellate *Alexandrium fundyense* in the Gulf of Maine: Investigations using a Physical-Biological Model

by
Charles A. Stock
MIT/WHOI Joint Program in Oceanography and Oceanographic Engineering

Submitted to the Massachusetts Institute of Technology/Woods Hole Oceanographic Institution Joint Program in Oceanography and Oceanographic Engineering on December 21, 2004 in partial fulfillment of the requirements for the Degree of Doctor of Philosophy

ABSTRACT

Blooms of the toxic dinoflagellate *Alexandrium fundyense* are annually recurrent in the western Gulf of Maine (WGOM) and pose a serious economic and public health threat. Transitions between and vital rates within the life stages of *A. fundyense* are influenced by diverse environmental factors, and these biological dynamics combine with energetic physical motions to yield complex bloom patterns. In this thesis, a biological model of the *A. fundyense* life cycle developed from laboratory and field data is combined with a circulation model to test hypotheses concerning the factors governing *A. fundyense* blooms in the springs of 1993 and 1994.

There is considerable uncertainty with the biological dynamics, and several biological model structures are tested against the 1993 observations. Maximum likelihood theory is used to evaluate the statistical significance of changes in model/data fit between structures. Biological formulations that do not include either nitrogen limitation or mortality overestimate observed cell abundances and are rejected. However, formulations using a wide range of mortality and nitrogen dependence, including the exclusion of one or the other, were able to match observed bloom timing and magnitude and could not be statistically differentiated. These simulations suggest that cysts germinating offshore of Casco Bay provide a plausible source of cells for the blooms, although cell inputs from the eastern Gulf of Maine gain importance late in the spring and in the northeast portion of the study area. Low net growth rates exert a notable yet non-dominant influence on the modeled bloom magnitude.

When simulations tuned to 1993 were applied to 1994 the degree of model/data fit is maintained only for those simulations including nitrogen dependence. The model suggests that differences in toxicity between the two years result from variability in the wind and its influence on the along and cross-shore transport of cells. Extended simulations generally predict a proliferation of *A. fundyense* abundance in mid-June within areas of retentive circulation such as Cape Cod Bay. This proliferation is not observed, and better resolution of the losses and limitations acting on *A. fundyense* is needed at this stage of the bloom.

Thesis Supervisor: Dennis J. McGillicuddy
Title: Associate Scientist, Woods Hole Oceanographic Institution

Acknowledgements

This work would not have been possible were it not for the efforts of many. I would like to start by thanking my advisor, Dennis McGillicuddy for his guidance, patience, and clarity of thought. I would also like to thank my committee members: Don Anderson, Dan Lynch, and Penny Chisholm for all of their advice and efforts on my behalf. The time and insight of the investigators on the ECOHAB-Gulf of Maine and RMRP programs is also greatly appreciated. Particular gratitude in this regard is due to Andy Solow, Bruce Keafer, John Cullen, Rich Signell, Ted Loder, Paty Matrai and Dave Townsend. Penny and Ole Madsen contributed greatly to the success and enjoyment of my studies while at MIT, and I thank them for this. I would also like to that Peter Franks for his encouragement. The diverse interests of the scientists of the Department of Applied Ocean Physics and Engineering, especially those within the Coastal Ocean and Fluid Dynamics Laboratory were a constant source of inspiration, and I thank them for their generosity and open doors. I would like to particularly recognize Ruoying He for his modeling insights during the final year of my studies. I would also like to thank Olga Kosnyreva, my officemate during my time at Woods Hole, for her warmth, kindness, and tolerance of my filing system (or lack thereof). Gratitude is also due to the Woods Hole Academic Programs Office for their support, guidance, and never-ending patience. Finally, I would like to end by earnestly thanking my family and friends for all of their support, warmth, generosity, and humor over the past years. Particular gratitude is due to my parents, my brother, and Nancy - thank you.

This research was funded by EPA STAR fellowship 91574901, National Science Foundation Grant OCE-9808173, and the WHOI Academic Programs Office. This generous support is gratefully acknowledged.

Table of Contents:

1. Introduction **9**

2. The Application of Maximum Likelihood Estimation Theory to a Physical-Biological Modeling Study of Harmful Algal Blooms in the Gulf of Maine **19**

3. Evaluating hypotheses for the initiation and development of *Alexandrium fundyense* blooms in the western Gulf of Maine using a coupled physical-biological model **85**

4. A Comparative Modeling Study of Blooms of the Toxic Dinoflagellate *Alexandrium fundyense* in the western Gulf of Maine in 1993 and 1994 **143**

5. Summary **211**

6. Appendix A: The Germination Model **223**

7. Appendix B: The Growth Model **259**

Chapter 1

Introduction

Blooms of the toxic dinoflagellate *Alexandrium fundyense* are annually recurrent phenomena in the Gulf of Maine during the spring and summer months. Toxins produced by *A. fundyense* lead to paralytic shellfish poisoning (PSP), a potentially fatal illness caused by consumption of shellfish from exposed regions. This public health risk necessitates rigorous monitoring of potentially affected areas and has lead to repeated closures of shellfish beds along the coast and in the offshore waters of the Gulf of Maine (Shumway, et al., 1988). Within the marine food web, PSP has been linked to mortality of larval and juvenile stages of fish (White, et al., 1989), and even the death of marine mammals such as humpback whales (Geraci, et al., 1989). An understanding of the factors that determine the distribution and abundance of *A. fundyense* within the Gulf of Maine is therefore of considerable scientific, economic, and public health interest.

Alexandrium species are characterized by a life cycle that includes both a resting benthic cyst and a vegetative cell (Anderson, 1998). Transitions between these stages have long been thought critical to understanding bloom dynamics in coastal waters (Anderson and Wall, 1978, Anderson, et al., 1983). The transition between resting and vegetative stages occurs through the process of germination. Rates of germination are controlled by diverse factors including light, temperature, oxygen in the sediments, and an internal endogenous clock (Anderson, 1980, Anderson and Keafer, 1987, Anderson, et al., 1987, Anderson, et al., submitted, Matrai, et al., submitted). Upon germination, vegetative *A. fundyense* cells swim upward to the euphotic zone, where they undergo a stage of vegetative growth. Some strains enlist coordinated vertical migrations in response to nutrients and light during this stage (MacIntyre, et al., 1997, Cullen, et al., 2004). The vegetative growth stage terminates with the formation of gametes that fuse to

form a new cyst. The onset of encystment has been difficult to observe in the field, but it is thought to be a reaction to environmental stress and has been induced by nutrient depletion in the laboratory (Anderson, et al., 1984, Anderson and Lindquist, 1985).

Blooms of *A. fundyense* in the Gulf of Maine do not develop in static water columns, but within a dynamical physical context characterized by energetic motions covering a broad range of scales. At the largest scales, a persistent Gulf-wide circulation is driven by density gradients between high salinity slope water in the Gulf's deep basins and fresher coastal waters derived from the Scotian shelf and local river inputs (Bigelow, 1927, Brooks, 1985, Fig. 1). This current is subdivided into a series of segments and branch points (Lynch, et al., 1997). The direction of flow at the branch points is modulated by a diverse set of factors including wind, river input, bathymetric effects, and the strength of the geopotential low that generally forms over Jordan Basin in response to dense slope water in its interior (Brooks and Townsend, 1989, Brooks, 1994, Lynch, et al., 1997, Pettigrew, et al., 1998). Within each branch, interactions between local river inputs, bathymetry and wind forcing can create energetic motions over daily time scales and tens of kilometers (e.g. Fong, et al., 1997, Geyer, et al., 2004). *A. fundyense* blooms have been demonstrated to strongly interact with the physical dynamics over the full range of scales described above (Franks and Anderson, 1992a, Townsend, et al., 2001, McGillicuddy, et al., 2003, Anderson, et al., 2004a, McGillicuddy, et al., submitted-b). This interweaving of the complex life history of *A. fundyense* and the dynamic physical environment of the WGOM suggests the use of a coupled physical-biological model to diagnose bloom dynamics.

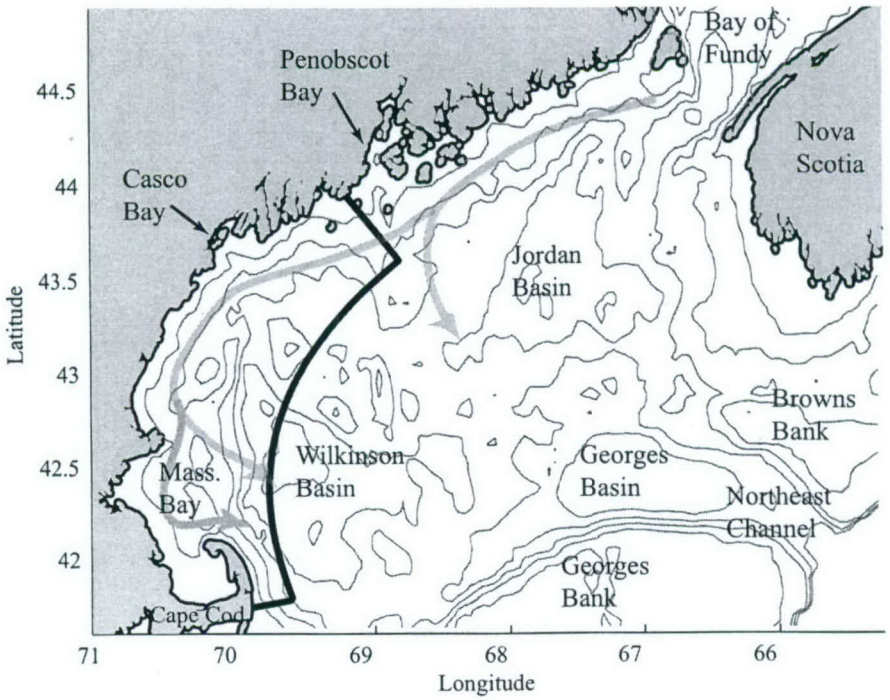


Figure 1: The Gulf of Maine and study region. The study domain is outlined in black. Depth contours are at 50, 100, 150 and 200 meters. The direction of flow of the Maine Coastal Current (adapted from Lynch et al., 1997) is shown as a thick gray line. Branch points offshore of Penobscot Bay and Cape Ann are notable. The region of interest for the studies herein is the western Gulf of Maine (WGOM), and is outlined by the thick, dark line.

This thesis focuses on bloom patterns in the western Gulf of Maine, which is the region south and west of Penobscot Bay in Fig. 1. Shellfish toxicity has been observed continuously in the region since a large events toxicity events in 1972 and 1974 (Shumway, et al., 1988). While there was initial conjecture that blooms in the region were linked to coastal upwelling (Mulligan, 1973, Hartwell, 1975, Mulligan, 1975), a series of papers by Franks and Anderson (1992a, 1992b) demonstrated that patterns of WGOM shellfish toxicity were more consistent with the along-shore advection of cells in association with the buoyant plume of the Kennebec and Androscoggin rivers. This finding led to the formulation of the "plume advection hypothesis", which consisted of several components paraphrased below:

- A source of *Alexandrium fundyense* in the north of the region possibly associated with the Kennebec/Androscoggin estuaries.
- A pulse of freshwater in May carries cells out of the estuaries, entrains nearshore populations, and is critical to the along-coast propagation of cells and associated shellfish toxicity.
- Upwelling winds force the river plume and cells offshore and away from shellfish beds, and downwelling winds hold the plume to the coast and increase southward transport.

This conceptual model was found to be consistent with a observations along a series of transects near Cape Ann (Franks and Anderson, 1992a), and with long terms toxicity records (Franks and Anderson, 1992b).

A second study was undertaken in 1993 and 1994 in an effort to test the dynamics of the plume advection hypothesis, and to refine and resolve its elements (Anderson, et al., 2004a, Geyer, et al., 2004). This study included broad survey coverage, as well as mooring and drifter deployments. Shellfish toxicity was prevalent along the entire coast in 1993, but was less severe in 1994 and restricted to areas north of Cape Ann. Differences in toxicity were primarily attributed to variations in the wind forcing between the two years, with winds being more upwelling favorable in the spring of 1994 (Anderson, et al., 2004a). Potential mechanisms for the delivery of cells to inshore regions related to circulation induced around the edges of river plumes were also discussed. Finally, a "two source" model for *A. fundyense* cells was proposed, with one source in inshore waters near Casco Bay, and a second derived from germination within offshore cyst beds and inflows of vegetative cells from the EGOM.

In this thesis, a coupled physical-biological model is constructed to synthesize present knowledge of the physical and biological dynamics that govern *A. fundyense* blooms in the western Gulf of Maine. This model is compared with observations to test hypotheses concerning bloom dynamics. The primary goals are to rigorously test the plausibility of the plume advection hypothesis, to further resolve the factors controlling bloom transport and net growth, to provide quantitative estimates of various sources and sinks of cells, and to identify major remaining uncertainties.

Chapter 2 provides a detailed description of the application of maximum likelihood theory to test hypotheses concerning the parameters governing bloom dynamics. While determined laboratory and field efforts have constrained key aspects of the biological dynamics, the potential complexity of the modeled processes and the measurement challenges inevitably produce uncertain model parameters. This problem is ubiquitous within coupled physical-biological modeling, and parameter values are often tuned within their uncertainty to best match observations. However, observations can be sparse and noisy, and approaching this procedure in a statistically rigorous fashion is essential if false conclusions regarding the parameter values are to be avoided. Chapter 2 begins by demonstrating key properties of maximum likelihood estimates and the use of the maximum likelihood ratio test to constrain parameter values using the example of a linear regression. This is followed by a detailed methodological discussion of the application of these tools for testing hypotheses concerning *A. fundyense* blooms in the Gulf of Maine. Particular attention is paid to pragmatic steps that must be taken in translating theory into practice. Limitations of and potential improvements to the approach are also discussed.

Chapter 3 tests the ability of four potential biological model structures to match the timing and magnitude of the observed *A. fundyense* bloom in the spring of 1993. The methodology applied is that described in detail within Chapter 2. The model structures are nested, in that each adds an additional degree of freedom to the prior structure. As each new parameter is added, maximum likelihood estimation is used to determine if the skill added supports the rejection of the previous model structure for the more complex alternative. The focus of the model diagnosis is the estimation of the contributions of the various sources of *A. fundyense* to the western Gulf of Maine, identification of the factors controlling net growth, and assessment of the impact of net growth on bloom magnitude and the cell distribution.

Chapter 4 tests a range of parameter values found optimal in 1993 against the 1994 data set to evaluate the inter-annual robustness of the model. Diagnosis focuses on the underlying physical and biological causes for the differences in *A. fundyense* abundance, distribution, and associated shellfish toxicity between the two years. Central to the analysis is a series of exchanges in model forcing for the two years. Estimates of the sources and sinks of cells are provided both in a domain-averaged sense, and within specific regions (Casco Bay and within Massachusetts and Cape Cod Bays) in order to further resolve elements of the bloom dynamics.

The thesis concludes by summarizing contributions of this thesis to the understanding of *A. fundyense* bloom dynamics in the western Gulf of Maine. Key aspects of the hypothesis testing procedure and potential improvements are also discussed. Lastly, prospects for future model improvement are addressed.

Anderson, D. M., 1980. Effects of temperature conditioning on development and germination of *Gonyaulax tamarensis* (Dinophyceae) hypnozygotes. Journal of Phycology 16, 166-172.

Anderson, D. M., 1998. Physiology and bloom dynamics of toxic *Alexandrium* species, with emphasis on life cycle transitions. In: Anderson, D. M., Cembella, A. D. ,Hallegraeff, G. M. (Eds.), Physiological Ecology of Harmful Algal Blooms. Springer-Verlag, Berlin, pp. 29-48.

Anderson, D. M., Chisholm, S. W., Watras, C. J., 1983. The importance of life cycle events in the population dynamics of *Gonyaulax tamarensis*. Marine Biology 76, 179-190.

Anderson, D. M., Keafer, B. A., 1987. The endogenous annual clock in the toxic dinoflagellate *Alexandrium tamarensis*. Nature 325, 616-617.

Anderson, D. M., Keafer, B. A., Geyer, W. R., Signell, R. P., Loder, T. C., 2004. Toxic *Alexandrium* blooms in the Gulf of Maine: the "plume advection hypothesis" revisited. Limnology and Oceanography (submitted).

Anderson, D. M., Kulis, D. M., Binder, B. J., 1984. Sexuality and cyst formation in the dinoflagellate *Alexandrium tamarensis*: Cyst yield in batch cultures. Journal of Phycology 20, 418-425.

Anderson, D. M., Lindquist, N. L., 1985. Time-course measurements of phosphorous depletion and cyst formation in the dinoflagellate *Gonyaulax tamarensis* Lebour. Journal of Experimental Marine Biology and Ecology 86, 1-13.

Anderson, D. M., Stock, C. A., Keafer, B. A., Bronzino, A. C., Matrai, P., Thompson, B., Keller, M., McGillicuddy, D. J., Hyatt, J., submitted. Experimental and modeling observations of *Alexandrium fundyense* cyst dynamics in the Gulf of Maine. Deep-Sea Research, Part II

Anderson, D. M., Taylor, C. D., Armbrust, V. E., 1987. The effects of darkness and anaerobiosis on dinoflagellate cyst germination. Limnology and Oceanography 32, 340-351.

Anderson, D. M., Wall, D., 1978. Potential importance of benthic cysts of *Gonyaulax tamarensis* and *G. excavata* in initiating toxic dinoflagellate blooms. Journal of Phycology 14, 224-234.

Bigelow, H. B., 1927. Physical oceanography of the Gulf of Maine. Fisheries Bulletin 40, 511-1027.

Brooks, D. A., 1985. Vernal circulation in the Gulf of Maine. Journal of Geophysical Research 90, 4687-4705.

Brooks, D. A., 1994. A model study of the buoyancy-driven circulation in the Gulf of Maine. Journal of Physical Oceanography 24, 2387-2412.

Brooks, D. A., Townsend, D. W., 1989. Variability of the coastal current and nutrient pathways in the eastern Gulf of Maine. Journal of Marine Research 47, 303-321.

Cullen, J. J., Wood, Barnett, Normandeau, Ryan, 2004. Behavioral and physiological variability among strains of the toxic dinoflagellate *Alexandrium fundyense* from the Gulf of Maine. Deep-Sea Research, Part II (submitted).

Fong, D. A., Geyer, W. R., Signell, R. P., 1997. The wind-forced response of a buoyant coastal current: Observations of the western Gulf of Maine plume. Journal of Marine Systems 12, 69-81.

Franks, P. J. S., Anderson, D. M., 1992a. Alongshore transport of a toxic phytoplankton bloom in a buoyancy current: *Alexandrium tamarense* in the Gulf of Maine. Marine Biology 112, 153-164.

Franks, P. J. S., Anderson, D. M., 1992b. Toxic phytoplankton blooms in the Gulf of Maine: testing hypotheses of physical control using historical data. Marine Biology 112, 165-174.

Geraci, J. R., Anderson, D. M., Timperi, R. J., Staubin, D. J., Early, G. J., Prescott, J. H., Mayo, C. A., 1989. Humpback Whales (*Megaptera novaeangliae*) fatally poisoned by dinoflagellate toxin. Canadian Journal of Fisheries and Aquatic Science 46, 1895-1898.

Geyer, W. R., Signell, R. P., Fong, D. A., Wang, J., Anderson, D. M., Keafer, B. A., 2004. The freshwater transport and dynamics of the western Maine Coastal Current. Continental Shelf Research 24, 1339-1357.

Hartwell, A. D., 1975. Hydrographic factors affecting the distribution and movement of toxic dinoflagellates in the western Gulf of Maine. In: LoCicero, V. R., (Ed.), Proceedings of the first international conference on toxic dinoflagellate blooms, Boston. Massachusetts Science and Technology Foundation, pp. 47-68.

Lynch, D. R., Holboke, M. J., Naimie, C. E., 1997. The Maine coastal current: spring climatological circulation. Continental Shelf Research 17, 605-634.

Matrai, P., Thompson, B., Keller, M. D., submitted. *Alexandrium* spp. from eastern Gulf of Maine: Circannual excystment of resting cysts. Deep Sea Research II

McGillicuddy, D. J., Anderson, D. M., Lynch, D. R., Townsend, D. W., 2004. Mechanisms regulating the large-scale seasonal development of *Alexandrium fundyense* blooms in the Gulf of Maine. Deep-Sea Research, Part II

McGillicuddy, D. J., Signell, R. P., Stock, C. A., Keafer, B. A., Keller, M. D., Hetland, R. D., Anderson, D. M., 2003. A mechanism for offshore initiation of harmful algal blooms in the coastal Gulf of Maine. Journal of Plankton Research 25, 1131-1139.

Mulligan, H. F., 1973. Probable causes of the 1972 red tide in the Cape Ann region of the Gulf of Maine. Canadian Journal of Fisheries and Aquatic Science 30, 1363-1366.

Mulligan, H. F., 1975. Oceanographic factors associated with New England red tide blooms. In: LoCicero, V. R., (Ed.), Proceedings of the first international conference on toxic dinoflagellate blooms, Boston, MA. Massachusetts Science and Technology Foundation, pp. 23-40.

Pettigrew, N., Townsend, D., Xue, H., Wallinga, J., Brickley, P., Hetland, R., 1998. Observations of the eastern Maine Coastal Current and its offshore extensions in 1994. Journal of Geophysical Research Vol. 103, 30,623-30,639.

Shumway, S. E., Sherman-Caswell, S., Hurst, J. W., 1988. Paralytic shellfish poisoning in Maine: Monitoring a monster. Journal of Shellfish Research 7, 643-652.

Townsend, D. W., Pettigrew, N. R., Thomas, A. C., 2001. Offshore blooms of the red tide dinoflagellate *Alexandrium* sp., in the Gulf of Maine. Continental Shelf Research 21, 347-369.

White, A. W., Fukuhara, O., Anraku, M., 1989. Mortality of fish larvae from eating toxic dinoflagellates or zooplankton containing dinoflagellate toxins. In: Okaichi, T., Anderson, D. M. ,Nemoto, T. (Eds.), Red Tides: Biology, Environmental Science, and Toxicology. Elsevier, New York, pp. 395-398.

Chapter 2

The Application of Maximum Likelihood Estimation Theory to a Physical-Biological Modeling Study of Harmful Algal Blooms in the Gulf of Maine

Abstract

Models formulated to represent the dynamics of ocean ecosystems often contain parameters and processes that are subject to a high degree of uncertainty. Observations provide a means to test these models and constrain parameters. However, the challenges of oceanographic observation often lead to sparse and noisy data. In addition, the model/data misfit in such comparisons likely contains contributions of physical, biological, and chemical origin that make the properties of the error difficult to interpret and predict. These aspects suggest the desirability of a quantitative, statistical approach to model/data comparison if erroneous conclusions are to be avoided. Maximum likelihood estimation and the maximum likelihood ratio test (m.l.r.t.) provide the means for one such approach. This paper details an application of these tools to test hypotheses concerning the initiation and development of Harmful Algal Blooms in the Gulf of Maine using a physical-biological model. The key aspects of the theory are first presented using the example of a linear regression. Convergence to several familiar results is demonstrated, and relationships between the quality and quantity of data and the ability to constrain model parameters are explored. Application to the study of harmful algal blooms in the Gulf of Maine is then detailed. Emphasis is placed on the pragmatic decisions required to translate the theory to application as well as the consequences of these decisions. The steps most critical to successful application were: 1) The use of an appropriately defined sensitivity metric to limit the number of parameters considered to those reflected in the observations and most critical to the question of interest, and 2) The application of basic *a-priori* knowledge of parameter ranges to focus the model optimization. While these tools are not the solution for all the challenges facing the evaluation and diagnosis of ocean ecosystem models, they can offer inroads in several areas. These include aiding in the extraction of reliable information from sparse and noisy data sets, providing guidance concerning the choice of misfit weights, and providing information for model assessment, diagnosis, and further model improvement. Future coupling of these tools with more advanced optimization techniques such as the adjoint method may greatly increase their utility. However, interpretation of results is often impeded by the potentially diverse origins of model/data misfit. Additional investigation character of the various components of the misfit is therefore also needed.

1. Introduction

Models formulated to represent the dynamics of ocean ecosystems are often subject to a high degree of uncertainty due to the potential complexity of the physical, chemical, and biological processes involved (e.g. Hofmann and Lascara, 1998). This uncertainty must be carefully considered when evaluating models against observational data if false rejection of hypothesized dynamics is to be avoided. This often entails varying the values of model parameters within their envelopes of uncertainty until a fit that is in some sense optimal is achieved. The best-fit parameter values provide estimations of rates, thresholds, and other controls on ocean ecosystems that may be difficult to observe directly. The model/data fit achieved by a hypothesized set of dynamics provides an assessment of the explanatory power of the hypothesis and analysis of the remaining misfit along with model sensitivity can guide further improvement. Competing hypotheses can be tested against one another by comparing the relative fit achieved under each. Evaluation of the achieved fit relative to that expected if the hypothesized model correctly represents the dynamics of the natural system provides the basis for model validation. Lastly, model results can be diagnosed to gain dynamical insight beyond that which can be gleaned from the observations alone.

While the steps outlined above are simple in concept, extracting reliable information from them can be challenging. Observations are often sparse and noisy, and model/data misfits can derive from a combination of physical, biological, and chemical origins. These limitations greatly influence the degree to which model parameters can be constrained, and care must be taken not to draw conclusions based on differences in parameter values having a negligible influence on the model/data fit. The diverse origins of the misfit raise the possibility of inventing biological explanations for chemical and/or

physical deficiencies and vice-versa. They may also confound precise definition of the achievable fit, and thus hinder formal model validation. The definition of the optimal fit can also be complicated by uncertainty surrounding the best choice of misfit weights and/or how to blend misfits with different units (Evans, 2003).

This paper describes the application of maximum likelihood estimation theory to address some of the issues just described within the context of a coupled physical-biological model of harmful algal blooms in the Gulf of Maine. Maximum likelihood estimation provides a robust tool for obtaining model parameter estimates, confidence intervals, and for testing hypotheses concerning model dynamics. The methodology also provides information for assessing the scales of variability in the observations captured by the model, and offers guidance in the choice of misfit weights. The approach is generally applicable to cases with an abundance of uncertain parameters, of which only a few may be of primary interest. The largest limitation of the methodology is its reliance on large sample approximations to test for statistical significance.

The first section of this paper is dedicated to reviewing the likelihood concept, the asymptotic theory of maximum likelihood estimates, and the asymptotic likelihood ratio test (where asymptotic in this context refers to properties achieved as the number of observations (n) becomes large). This review is done using a simple example: that of a linear regression. Convergence to several familiar results is demonstrated, and several relationships between the results and the quantity and quality of the data are highlighted. Next, the application of the methodology to a model of the initiation and development of harmful algal blooms in the Gulf of Maine is described. Particular attention is paid to the pragmatic decisions that must be made in translating theory to practice and the impact of

these decisions on the conclusions drawn from the analysis. The paper concludes by suggesting critical steps for the successful application of this methodology to coupled physical/biological models, as well as potential improvements to the application described here.

2. Maximum Likelihood Estimation Theory

The likelihood concept is extensively used for statistical inference, and the related literature is vast. This section does not attempt a detailed review, but focuses on illuminating key concepts using a simple example: the linear regression. It begins by defining the likelihood function and the maximum likelihood estimate (m.l.e.), and then reviews the properties of such estimates for large samples. It then proceeds to discuss the use of the maximum likelihood ratio test to calculate confidence intervals around model parameters and to test hypotheses. Lastly, it discusses some guidelines for choosing a misfit model. The relationship between the misfit model and the misfit weights is highlighted and objective means of determining the suitability of the misfit model are discussed. For a more complete treatment, dozens of texts are available. The texts of Hogg and Craig (1995) and Cox and Hinkley (1974) are particularly useful, with the former being the more introductory of the two. Cox and Hinkley also provide a brief review of some of the seminal papers pertaining to maximum likelihood estimation.

2.1 The Likelihood Function and Maximum Likelihood Estimates

Consider the set of generic observations shown in Fig. 1. A linear model is proposed to explain the variation in the $n \times 1$ vector of observations $\boldsymbol{y}$ with $\boldsymbol{x}$, but there is some random noise ($\boldsymbol{\varepsilon}$) associated with each data point. The model is thus written:

$$y = \beta_0 + \beta_1 x + \varepsilon = \hat{y} + \varepsilon \quad (1)$$

Where β_0 is the intercept and β_1 the slope. In this example, the true values of the parameters are $\beta_0 = 0.0$, $\beta_1 = 1.0$, and the stochastic noise is normally distributed with $\sigma^2 = 100$. In real applications these true values are unknown and the goal is to use the observations to obtain estimates $(\hat{\beta}_0, \hat{\beta}_1, \hat{\sigma}^2)$ of the true values and confidence intervals. This section will therefore proceed as if ignorant of the true parameter values.

Assume that considerations of the observational noise and the processes that are expected to be resolved deterministically by the linear model chosen suggest that the misfits between the model and the data should be normally distributed with 0 mean, have uncertain variance σ^2, and independent. No *a-priori* estimate of the misfit variance has been asserted in this example, as the fitting process will determine the amount of noise remaining after the linear model is applied. However, the methodology described herein is applicable to cases where the noise is asserted *a-priori* (this will be discussed in greater detail in Section 2.3). The stochastic description of the misfit will be referred to herein as the misfit model[1], and is differentiated from the dynamics model: $\hat{y} = \beta_0 + \beta_1 x$. The combination of the dynamics model and the misfit model is referred to simply as "the model". The initial misfit model can be derived from a variety of sources including theoretical considerations, previous study of the observational apparatus being used, exploratory analysis of the data set, or simply be a good first guess based on experience.

[1] This stochastic description is often referred to as the "error model", with the error being formally defined as the difference between the observations and the true value of the quantity being measured. If the model is correct, the difference between model and data (i.e. the misfit) approaches the difference between truth and data (i.e. the error). The "misfit model" designation is used herein in recognition that even the most skillfull of physical/biological models are likely to have unresolved and non-deterministically resolved processes that contribute to the noise between the model and data. The best that can be hoped for is thus a model that matches the data to this expected extent, and not one that attains absolute truth.

In either case, it is only a description under consideration and must be critically examined against the eventual model/data misfits before the model is diagnosed and conclusions are made (section 2.3). The likelihood (L) of a set of n model/data misfits is defined as the product of the probabilities of each individual misfit (i.e. the joint probability) calculated according to the misfit model. For misfit model above:

$$L(\boldsymbol{\theta};\mathbf{y}) = L(\beta_0,\beta_1,\sigma^2;y_i\ldots y_n) = \prod_{i=1}^{n}\frac{1}{\sqrt{2\pi\sigma^2}}\exp\left\{-\frac{(y_i-\hat{y}_i)^2}{2\sigma^2}\right\} \qquad (2)$$

The notation $L(\boldsymbol{\theta};\mathbf{y})$ is used to emphasize the fact that the likelihood associated with each choice of the uncertain parameters from the $p\times 1$ parameter vector $\boldsymbol{\theta} = [\beta_0,\beta_1,\sigma^2]$ is dependent upon the degree to which they explain the $n\times 1$ vector of observations $\mathbf{y}$. It is common to deal with the log of the likelihood function, as this changes product in (2) to a sum and does not influence the position of the maximum:

$$\ln L(\boldsymbol{\theta};\mathbf{y}) = -\frac{n}{2}\ln(2\pi\sigma^2) - \frac{1}{2\sigma^2}\sum_{i=1}^{n}(y_i-\hat{y})^2 \qquad (3)$$

It seems sensible that good estimates of β_0, β_1 and σ^2 are those that maximize (3). Estimates of parameters obtained in this way are referred to as maximum likelihood estimates (m.l.e.'s), and written as $\hat{\beta}_0$, $\hat{\beta}_1$, and $\hat{\sigma}^2$. For the example above,

$\hat{\beta}_0 = -1.38$, $\hat{\beta}_1 = 1.02$, and $\hat{\sigma}^2 = 101.58$ (Fig. 2a).

To see the close relationship between maximum likelihood for normally distributed misfits and least squares, note that the partial derivatives with respect to the three uncertain parameters $(\beta_0,\beta_1,\sigma^2)$ are necessarily 0 at the likelihood maximum. Taking the partial derivative of (3) with respect to σ^2 yields the condition:

$$\frac{\partial \ln L(\boldsymbol{\theta};\mathbf{y})}{\partial \sigma^2} = -\frac{n}{2\sigma^2} + \frac{1}{2(\sigma^2)^2}\sum_{i=1}^{n}(y_i - \hat{y})^2 = 0 \tag{4}$$

That requires:

$$\hat{\sigma}^2 = \frac{\sum_{i=1}^{n}(y_i - \hat{y})^2}{n} \tag{5}$$

The maximum likelihood estimate of σ^2 is thus the variance of the sample of misfits associated with any choice of β_0 and β_1. Inspection of (3) in light of this result reveals that the second term of the left side necessarily approaches n after substitution of $\hat{\sigma}^2$ regardless of the degree of fit. Thus, to maximize the likelihood, one must choose β_0 and β_1 to minimize $\hat{\sigma}^2$ in the first term of (3). Which, by (5), is accomplished through minimizing $\sum_{i=1}^{n}(y_i - \hat{y})^2$ (Fig. 2b). Thus, even when the misfit variance is left to the estimation, the criterion that the variability not explained by the model is minimized leads to least squares when the misfit is normally distributed.

Maximum likelihood estimates often have desirable properties regardless of the sample size, but such estimates are particularly good for large samples and if certain mild regularity conditions on the probability density are met (Table 1, LeCam, 1970, Cox and Hinckley, 1974, pp. 279-311). Perhaps most notable is that, when the misfit model is an accurate stochastic description of the misfit, the difference between the m.l.e.'s and the true parameter value[2] ($\hat{\boldsymbol{\theta}} - \boldsymbol{\theta}^*$) has a limiting normal distribution as $n \to \infty$ with

[2] Herein, the notation $\boldsymbol{\theta}^*$ has been used to differentiate the true values of a parameters from the generic argument $\boldsymbol{\theta}$, the value set by a null hypothesis $\boldsymbol{\theta}_0$, and the estimate of the true parameter values $\hat{\boldsymbol{\theta}}$. Notation varies depending on the source. Most notably, $\boldsymbol{\theta}$ is often used for both the true parameter value and the generic argument.

variance-covariance $\boldsymbol{I}^{-1}(\boldsymbol{\theta})$. $\boldsymbol{I}(\boldsymbol{\theta})$ is referred to as the Fisher Information Matrix, which can be written in terms of the likelihood using two alternate but equivalent expressions. In the present case:

$$\boldsymbol{I}(\boldsymbol{\theta}) = \begin{bmatrix} E\left\{\left(\frac{\partial \ln L}{\partial \beta_0}\right)^2\right\} & E\left\{\frac{\partial \ln L}{\partial \beta_0}\frac{\partial \ln L}{\partial \beta_1}\right\} & E\left\{\frac{\partial \ln L}{\partial \beta_0}\frac{\partial \ln L}{\partial \sigma^2}\right\} \\ E\left\{\frac{\partial \ln L}{\partial \beta_1}\frac{\partial \ln L}{\partial \beta_0}\right\} & E\left\{\left(\frac{\partial \ln L}{\partial \beta_1}\right)^2\right\} & E\left\{\frac{\partial \ln L}{\partial \beta_1}\frac{\partial \ln L}{\partial \sigma^2}\right\} \\ E\left\{\frac{\partial \ln L}{\partial \sigma^2}\frac{\partial \ln L}{\partial \beta_0}\right\} & E\left\{\frac{\partial \ln L}{\partial \sigma^2}\frac{\partial \ln L}{\partial \beta_1}\right\} & E\left\{\left(\frac{\partial \ln L}{\partial \sigma^2}\right)^2\right\} \end{bmatrix} = \tag{6a}$$

$$-\begin{bmatrix} E\left\{\frac{\partial^2 \ln L}{\partial \beta_0{}^2}\right\} & E\left\{\frac{\partial^2 \ln L}{\partial \beta_0 \partial \beta_1}\right\} & E\left\{\frac{\partial^2 \ln L}{\partial \beta_0 \partial \sigma^2}\right\} \\ E\left\{\frac{\partial^2 \ln L}{\partial \beta_1 \partial \beta_0}\right\} & E\left\{\frac{\partial^2 \ln L}{\partial \beta_1{}^2}\right\} & E\left\{\frac{\partial^2 \ln L}{\partial \beta_1 \partial \sigma^2}\right\} \\ E\left\{\frac{\partial^2 \ln L}{\partial \sigma^2 \partial \beta_0}\right\} & E\left\{\frac{\partial^2 \ln L}{\partial \sigma^2 \partial \beta_1}\right\} & E\left\{\frac{\partial^2 \ln L}{(\partial \sigma^2)^2}\right\} \end{bmatrix} \tag{6b}$$

Where E is the expected value operator, and $L = L(\boldsymbol{\theta}; \boldsymbol{y})$. The presence of the second derivative in representation (6b) suggests that the difference between parameter estimates and true parameter values is strongly linked to the curvature of the likelihood surface in the neighborhood of the true parameter value. The properties of this matrix are reflected in the log-likelihood surface (Fig. 2a). If the peak is sharp, the likelihood quickly decreases as parameter values are perturbed, the diagonal elements of $\boldsymbol{I}(\boldsymbol{\theta})$ are large, and the corresponding variance between m.l.e. and true parameter value is small (i.e. the parameter is well constrained by the data). The relationship between this result and the quantity and quality of the data will be explored further in section 2.2.

A further consequence of the asymptotic normality of m.l.e.'s is that the sum of the squared difference between the m.l.e. and the true value of the parameter, scaled by the variance-covariance matrix $\boldsymbol{I}^{-1}(\boldsymbol{\theta})$:

$$\left[\hat{\boldsymbol{\theta}} - \boldsymbol{\theta}^*\right]^T \boldsymbol{I}(\boldsymbol{\theta})\left[\hat{\boldsymbol{\theta}} - \boldsymbol{\theta}^*\right] \tag{7}$$

has a limiting χ^2 distribution with p degrees of freedom, where p is the number of uncertain parameters in $\boldsymbol{\theta}$ (Cox and Hinckley, 1974). This is also true of normally distributed sets of model/data residuals scaled by their covariance, a fact that is commonly used to test hypotheses concerning the degree of model/data fit attained relative to prior expectation (Muccino, et al., 2004). The difference herein is that the relationship is used to estimate the variance of estimates of uncertain parameters about their true values. Not surprisingly, the relationship between (7) and the χ^2 distribution is the basis for hypothesis tests concerning parameter values (section 2.2).

It must be stressed that although the results above were presented using the specific example of linear regression with normal errors, they are general to any probability density function that satisfies the mild regularity conditions. These conditions primarily require the smooth variation of the likelihood function with changes in the parameter values and the finite dimension of the parameter space. Most notably, the first three derivatives of the likelihood must exist in the neighborhood of the true parameter value, as Taylor expansions are necessary to demonstrate several of the properties described in Table 1. The mildness of these conditions makes it possible to deal with many non-gaussian misfits. The persistence of the properties in Table 1 for non-gaussian statistics is primarily due to the action of the central limit theorem on large samples. Refer to Cox and Hinkley (1974) or LeCam (1970).

2.2 The Maximum Likelihood Ratio Test

The maximum likelihood ratio test (m.l.r.t.) provides a means to test hypotheses regarding model parameters and to construct confidence intervals based on changes in the likelihood. The ratio (λ) is constructed by comparing the likelihood maximized over a parameter space (Ω) to that obtained over a nested subspace (Ω_0) restricted by setting precise values for 1 or more of the parameters in Ω. For example, the following ratio is formed when testing the hypothesis that $\beta_0 = 5.0$, $\beta_1 = 0.9$:

$$\lambda = \frac{L(\beta_0 = 5.0, \beta_1 = 0.9, \hat{\sigma}_0^2; \boldsymbol{y})}{L(\hat{\beta}_0, \hat{\beta}_1, \hat{\sigma}^2; \boldsymbol{y})} = \frac{L(\hat{\Omega}_0)}{L(\hat{\Omega})} = \frac{L(\hat{\boldsymbol{\theta}}_0)}{L(\hat{\boldsymbol{\theta}})} \tag{8}$$

The restricted maximized likelihood in the numerator serves as the null hypothesis, while the denominator forms the alternative. In the above example, maximization under the null hypothesis requires only that the 1D space Ω_0 (containing different values of σ^2) be searched. This yields an estimate of the parameter set under the null hypothesis $\hat{\boldsymbol{\theta}}_0$. In the alternative, the 3D space Ω must be searched, yielding the parameter set $\hat{\boldsymbol{\theta}}$. Note that in (8), two estimates of σ^2 are produced: $\hat{\sigma}^2$ and $\hat{\sigma}_0^2$. The "0" designation is used to specify that the second estimate was determined under the restrictions of the null hypothesis. Such "nuisance parameters" occur whenever the precise value of a parameter is not specified within the null hypothesis. While such parameters can ruin the properties of some hypothesis testing procedures, the m.l.r.t. is robust to their presence (Cox and Hinckley, 1974, p. 323). This is a notable advantage when dealing with the large parameter spaces common in ecosystem models.

Clearly, the likelihood of the alternative hypothesis will be greater than that of the null due to the increased search space. How much greater the likelihood of the alternative must be before rejection of the null is supported can be approximated using the asymptotic properties of the m.l.e. (Table 1). It can be shown that the quantity:

$$-2\ln(\lambda) = -2\left(\ln(L(\hat{\Omega}_0)) - \ln(L(\hat{\Omega}))\right) = -2\left(\ln(L(\hat{\boldsymbol{\theta}}_0) - \ln L(\hat{\boldsymbol{\theta}})\right) \tag{9}$$

Will have an approximate χ^2 distribution with the number of degrees of freedom equal to the difference in the number of free parameters between the null and the alternative hypotheses ($\dim(\Omega)$-$\dim(\Omega_0)$) *if the null hypothesis is true* (i.e. $\boldsymbol{\theta}_0 = \boldsymbol{\theta}^*$). Derivations of this result can be found in Cox and Hinkley (1974, pp. 311-331). However, the plausibility of this result can be seen in the 1D case by performing a Taylor expansion of $\ln(\lambda)$ about $\hat{\theta}$ to solve for the ratio at θ^*:

$$\begin{aligned}\ln L(\theta^*) - \ln L(\hat{\theta}) = \ln L(\hat{\theta}) - \ln L(\hat{\theta}) + \left(\theta^* - \hat{\theta}\right)\frac{d}{d\theta}\left(\ln L(\theta) - \ln L(\hat{\theta})\right)\Big|_{\theta=\hat{\theta}} - \\ \frac{1}{2}\left(\theta^* - \hat{\theta}\right)^2 \frac{d^2}{d\theta^2}\left(\ln L(\theta) - \ln L(\hat{\theta})\right)\Big|_{\theta=\theta^-}\end{aligned} \tag{10}$$

Where θ^- is a point satisfying $\left|\theta^- - \theta^*\right| \le \left|\hat{\theta} - \theta^*\right|$. After cancellation and noting that the derivative with respect θ evaluated at the likelihood maximum is 0 by definition, (10) simplifies to:

$$\ln L(\theta^*) - \ln L(\hat{\theta}) = -\frac{1}{2}\left(\theta^* - \hat{\theta}\right)^2 \frac{d^2 L(\theta^-)}{d\theta^2} \tag{11}$$

Noting that $\theta^{\sim} \rightarrow \theta^{*}$ as the sample size becomes large due to the consistency property of m.l.e.'s (table 1) and that $-d^2L(\theta^{*})/d\theta^2 = I(\theta)$ allows one to write:

$$-2\ln(\lambda) = \left(\hat{\theta} - \theta^{*}\right) I(\theta) \left(\hat{\theta} - \theta^{*}\right) \tag{12}$$

Which, by (7) is known to have a χ^2 distribution with 1 degree of freedom. The extension to a $p \times 1$ vector of parameters is simply a straightforward expansion of this result.

Applying this result to the hypothesis (8), the maximum log-likelihood under the null hypothesis is -378.50, while that under the alternative is -372.94. The quantity $-2\ln(\lambda)$ is 11.03, which is larger than ~99.6% of the points one would expect from a χ^2 distribution with 2 degrees of freedom. The null hypothesis can thus be firmly rejected. Confidence intervals can also be constructed. For example, 90% of the values from a χ^2 distribution with 2 degrees of freedom are less than 4.6. Substitution of this value into the R.H.S. of (7) and solving for $\ln(\hat{\Omega}_0)$ defines the value of the 90% confidence contour (Fig. 2a, thick dark contour). That is, null hypotheses stating values outside of this contour can be rejected with 90% confidence. It is notable that this contour is nearly identical to that derived by the commonly used F-test (e.g. Draper and Smith, 1981), which is much more restricted in its use (thick gray contour in Fig. 2a). The size and shape of confidence intervals reflect the properties of $\boldsymbol{I}(\boldsymbol{\theta})$: the diagonal terms set the scale of the interval in parameter space, while the off-diagonal covariances control the tilt of the confidence region (i.e. shallow slopes are more likely coupled with "+" y-

intercepts in Figs. 2, 3, and 4). The point $\beta_0 = 5.0, \beta_1 = 0.9$ (filled square) clearly falls outside of this contour, and would thus be rejected with greater than 90% confidence.

While the change in likelihood required to reject a hypothesis is set by the characteristics of the χ^2 distribution, the size of the shift away from the true parameter necessary to produce that change depends on 1) the number and quality of the observations, and 2) the sensitivity of the parameters to the information within them. Decreases in either the number of the observations (Fig. 3) or their quality (Fig. 4) decrease the sharpness of the peak in the likelihood surface near the m.l.e.. This reflects a decrease in the information about the parameter values within the sample (i.e. the terms of the information matrix $\boldsymbol{I}(\boldsymbol{\theta})$ decrease) and leads to an expansion in the confidence interval. In one case (panel C in Fig. 4) it is no longer possible to reject the null hypothesis $\beta_0 = 5.0, \beta_1 = 0.9$ at the 90% significance level.

The m.l.r.t. is also useful when testing for the necessity of another variable. Such an approach is useful for identifying the simplest model that can explain the data as well as any more complex options. For example, if the alternative model:

$$y = \beta_0 + \beta_1 x + \beta_2 x^2 \tag{13}$$

Is proposed, the necessity of the additional term can be tested by forming the ratio:

$$\lambda = \frac{L(\hat{\beta}_{00}, \hat{\beta}_{10}, \hat{\sigma}_0^2, \beta_2 = 0)}{L(\hat{\beta}_0, \hat{\beta}_1, \hat{\beta}_2, \hat{\sigma}^2)} \tag{14}$$

The maximization of the likelihood with this additional parameter for this realization is -372.49, only slightly greater than the likelihood associated with the linear model (-372.94). This difference ($-2\ln(\lambda) = 0.90$) is only significant at ~ 66% level based on a

χ^2 distribution with 1 degree of freedom. The null hypothesis is thus not rejected, which is comforting given that the true model is known to be (1).

Lastly, the fact that the null hypothesis in (14) is known to be true provides an opportunity to demonstrate that $-2\ln(\lambda)$ does in fact have a χ^2 distribution with dim(Ω) - dim(Ω_0) degrees of freedom. Repetition of test (14) 1000 times with different realizations of the generic linear data set in Fig. 1 produces the histogram of values of $-2\ln(\lambda)$ shown in Fig. 5. The χ^2 distribution (dark line) with 1 degree of freedom closely follows the histogram. As expected, 896 of the 1000 realizations fall below the 90% cumulative threshold, confirming the theoretical result. This figure also reiterates the rationale behind the m.l.r.t.: Since the behavior of λ when the null hypothesis is true can be well approximated, the ability to reject a null hypothesis can be quantified based on departures from this expected behavior.

2.3 The Choice of a Misfit Probability Model and Implications for Misfit Weights

A probability distribution that adequately describes the statistical properties of the model/data misfit is critical to the validity of the analysis. This choice determines the misfit weights: if a misfit is improbable relative to the expectations of the error model, then it is weighted heavily. This choice can rarely be made on purely theoretical grounds, and exploratory analysis, experience, and prior study often are required to refine the description. Although there are no steadfast rules to reference, Cox and Hinkley (1974, pp. 4-5) offer the following guidelines that have been paraphrased:

1. The family of distributions should if possible establish a link with any theoretical knowledge about the system and with previous experimental work.

2. There should be consistency with known limiting behavior.
3. So far as possible, the parameters in the distribution should have clear-cut interpretations.
4. A family of distributions containing few parameters is preferable.
5. It is desirable for the statistical theory associated with the model to be as simple as possible.

The normal distribution is often justified on the grounds that, if the model misfit results from the sum of random noise from many different sources, the sum of these will be approximately normal by the central limit theorem. However, if the dominant misfit source is strongly non-normal, this logic can fail. Fortunately, various diagnostics are available to help determine if a particular choice of an misfit model is appropriate (e.g. Draper and Smith, 1981, Cook and Weisberg, 1982, D'Agostino and Stevens, 1986, Cuthbert and Wood, 1987). Such diagnostics are critical to resolving ambiguities in the best choice of weights (e.g. Evans, 2003).

Figure 6 (A-C) shows 3 simple diagnostic plots for the misfit of the example above. The histogram (panel A) shows that the misfits are largely symmetric about 0 and have tails consistent with the normal distribution, although there does seem to be a slightly higher than the expected number of large positive values. Panel B plots the residuals as a function of x, suggesting that the residual properties do not change as a function of the independent variable. In the case of this simple example, invariance in x also implies invariance as a function of $\hat{y}$ since the two are linearly related. Panel C shows a probability plot, which compares the ordered misfits (normalized by the variance) to those expected based on the standard cumulative distribution function of the error model. If the misfits are consistent with the error model, the plot will form a

straight line. Curvature is indicative of discrepancies in the tails of the distribution or skewness. The plot in panel C is largely straight, despite a short increase in the slope associated with the slight prevalence of large positive values apparent in the histogram.

In the simple linear regression example, the diagnostic plots largely support the assumed misfit distribution. There is no strong asymmetry, no extreme outliers, and the width of the tails of the distribution is consistent. In deciding if the misfit model may require additional refinement, the appropriate question that must be asked is: are any refinements in the properties of the expected misfit distribution likely to materially change the conclusions of the study? If conclusions depended on very fine scale delineations of the parameters in question, more exhaustive tests of the distribution may be required (see above references). However, in many cases a simple set of diagnostic plots such as those in Fig. 6, along with any additional plots with particular relevance to the problem at hand, should be sufficient to ensure the validity of the most prominent aspects of an analysis.

Lastly, it is notable that for many inverse modeling applications, setting the misfit variance before inversion is advocated (e.g. Bennett, 2002). The *a-priori* estimate of the misfit is included in the inversion and the model is optimized subject to physically realistic constraints on the initial conditions, boundary conditions, forcing, and model parameters. This fitting is most often carried out in a generalized least squares sense, which produces maximum likelihood estimates for normally distributed noise. The primary hypothesis considered is if the model can match the observations within the expected achievable fit after adjusting controls within reasonable bounds (e.g. Muccino, et al., 2004). The same general machinery described herein is being applied in this case.

Setting the variance simply places more parameter restrictions for the null hypothesis in (8), and relationship (9) can still be used to identify parameter constraints based on the relative performance of the model with different parameter values. Likewise, the *a-posteriori* estimates of the misfit produced in the example herein can be compared to any available *a-priori* estimates of the achievable fit for comparisons similar to that described by Muccino et al. (2004). The choice of fixing the misfit variance *a-priori* or leaving it to estimation is a function of the scientific question being considered and the information available. If it is of primary interest to analyze the degree of fit after all known processes have been incorporated into the model, leaving the misfit to be estimated seems sensible. For either case, the parameter estimates will result from minimization of the unexplained variance between the model and the data.

3. Application of Maximum Likelihood Theory to Study HABs in the Gulf of Maine

The application of the methodology described above to test hypotheses regarding the initiation and development of blooms of the toxic dinoflagellate *Alexandrium fundyense* in the western Gulf of Maine is now presented. Transition of the theory above to application in a physical-biological model is challenging, and particular attention is paid to pragmatic decisions required to make this transition and the influence that these decisions have on the analysis. The section begins with a brief description of the observations and the formulation of the dynamics model. Steps taken to reduce the parameter space to a manageable dimension are then described, before proceeding to the misfit model formulation, hypothesis testing, and misfit model verification. The section concludes with a discussion of model assessment and diagnosis based on analysis results.

3.1 Observations and the Dynamics Model Formulation

Blooms of *A. fundyense* in the western Gulf of Maine (WGOM, Fig. 7) evolve within a dynamic physical and biological environment (Franks and Anderson, 1992a, Franks and Anderson, 1992b, Anderson, et al., 2004a). It is therefore hoped that a coupled physical biological model can lend insight into the factors controlling the timing and magnitude of the bloom beyond those that can be gleaned from the observations alone. A field program including 5 ship surveys (Fig. 8) and mooring deployments carried out in 1993 provides the observations for the study (Anderson, et al., 2004a, Geyer, et al., 2004). The duration of each survey was 2-3 days and they were spaced approximately 2 weeks apart (April 12-14, April 28-30, May 10-13, May 24-27, June 4-6). *A. fundyense* cell counts were taken at the surface (Fig. 8, top panel) and, for ~75% of the stations, at 10 meters. Hydrographic and nutrient data, including phosphate, silicate, nitrate, nitrite, and ammonium (Martorano and Loder, 1997) was also collected (Fig. 8, bottom panel).

The physical component of the dynamics model is provided by the Estuarine, Coastal and Ocean Model (ECOM) (Blumberg and Mellor, 1987). The study domain (Fig. 7) is covered by a grid of 130 cells in the along-shore direction and 70 in the cross-shore. Grid cells dimensions range from 1.5-3 km. 12 sigma layers (i.e. each layer is a constant fraction of the water depth) are specified in vertical with increased resolution near the surface to better resolve river plume dynamics. Vertical mixing is calculated using the Mellor-Yamada level 2.5 turbulence closure (Mellor and Yamada, 1982, Galperin, et al., 1988). Model Forcing is summarized in Table 2, and was chosen to capture the principle aspects of the large-scale circulation and hydrography in the

WGOM (Chapters 3 and 4 of this thesis provide comparisons of the modeled circulation and data).

Alexandrium species are characterized by a life cycle that includes both a resting cyst and a vegetative cell (Anderson, 1998). The transition between resting and vegetative stages occurs through the process of germination. The biological model is therefore a single component model constructed from laboratory-based parameterizations of *A. fundyense* germination, swimming behavior, and growth as functions of the environmental conditions. The baseline model functions are summarized in Fig. 9, and the parameters are cataloged in Table 3. Detailed descriptions of the model construction can be found in Anderson et al. (submitted) and within the Appendix.

The baseline model structure provides the first null hypothesis. Additional structures are then considered in an effort to find the combination of parameters most capable of explaining the data (Table 4). The second structure adds the possibility of a spatially uniform averaged mortality (m), the third adds the possibility of a dependence of growth on dissolved inorganic nitrogen (DIN), while the fourth considers both mortality and nutrient dependence in combination. Mortality is loosely defined as a vegetative cell being removed from the water column (e.g. by grazing, formation of a new cyst, and/or cell mortality). It is given a range to allow the possibility of negligible rates, to rates that would overwhelm all but the swiftest growth. The nutrient dependence is modeled using a Monod formulation with half-saturation constant K_N.

$$\mu(DIN,T,S) = \mu(T,S) \times \frac{[DIN]}{K_N + [DIN]} \tag{15}$$

Where μ is the growth rate and T and S are temperature and salinity respectively. The range of K_N considered was chosen to encompass the range of half saturation constants

for nitrogen dependent growth and uptake commonly encountered in the literature (Table 3). These formulations are admittedly limited in their ability to recreate detailed ecosystem dynamics. However, they do provide a means to test the necessity of a first-order mortality term and/or nutrient dependence in order to match the observed timing and magnitude of *A. fundyense* blooms.

3.2 Parameter Space Reduction

The coupled physical/biological model described above replaces the simple linear and quadratic dynamics models discussed in Section 2. This dynamics model can be viewed as an operator, A, that houses many parameter dependent relationships which eventually yield estimates of the cell abundance ($\hat{\boldsymbol{y}}$):

$$\boldsymbol{y} = A(\boldsymbol{\theta}) + \boldsymbol{\varepsilon} = \hat{\boldsymbol{y}} + \boldsymbol{\varepsilon} \tag{16}$$

The parameter vector $\boldsymbol{\theta}$ now contains all of the biological model parameters in Table 3, and all of the uncertain parameters in the physical model formulation (including the forcing). The misfit ($\boldsymbol{\varepsilon}$) is expected to arise from uncertainty in the observations, and from dynamics that cannot be resolved deterministically by the physical and/or biological model.

Maximizing the likelihood over all $\boldsymbol{\theta}$, even for the relatively simple dynamics model described above, could quickly become computationally untenable without the employment of advanced techniques such as adjoint models (Lawson, et al., 1996, Spitz, et al., 1998). In addition, testing hypotheses concerning parameters with little influence or those with strong covariance with more dominant parameters will likely be a fruitless exercise, as the amount of independent information about the parameter within the observations is small. That is, the Fisher Information Matrix contains low values on the

diagonal associated with these parameters and/or high off-diagonal values associated with a second dominant parameter. The parameter space is therefore pared down by limiting it to those parameters most critical to the question of primary interest: what factors control the timing and magnitude of the observed bloom. In lieu of attempting an ad-hoc numerical approximation of $\boldsymbol{I}(\theta)$, a bulk sensitivity metric reflecting the degree that the uncertainties in Table 3 influence bloom magnitude is enlisted:

$$SM(\theta_i,t) = \frac{\left(\iiint_{domain} C(x,y,z,t)dxdydz\right)_{\theta_i=\theta_{i,high}}}{\left(\iiint_{domain} C(x,y,z,t)dxdydz\right)_{\theta_i=\theta_{i,low}}} \quad (17)$$

Where C is the concentration of *A. fundyense*, $\theta_{i,high}$ is the value of the parameter under consideration that is most favorable to cell abundance, and $\theta_{i,low}$ is the value least favorable. Multiplied by 100, this metric yields the percentage change in the total number of cells in the domain as a function of time (t) induced by varying each parameter over its approximate range of uncertainty. Two parameters clearly dominate this uncertainty metric (Fig. 10). The germination depth (d_g) dominates for the first 1.5 months of the simulation. This is the depth of sediment over which resting *A. fundyense* cells can germinate and gain the water column through the sediment grain matrix. Late in the simulation, the magnitude is most sensitive to the maximum growth rate, which can drive 10 fold changes by mid-may and nearly 100 fold changes by simulation's end.

Based on the strong dominance of d_g and μ_{max} demonstrated above, the free parameters within the baseline biological model are limited to these two, with model structures 2, 3, and 4 adding combinations of the uncertain parameters K_N and m. The remaining baseline biological model parameters are given central values within their

uncertainty ranges. This transfers any unique observed patterns that these parameters could account for within their uncertainty into the misfit term (i.e. they are now in the null space of the dynamical model), and leaves the portions that covary with the dominant parameters to be compensated for by those parameters. While the former consequence simply increases the expected noise between model and data, the latter action risks the introduction of a bias to the estimates of d_g, μ_{max}, K_N and m. For example, if the true value of the growth efficiency α_g is actually higher than the central value it is given, then the m.l.e. $\hat{\mu}_{max}$ may compensate and tend to be higher than its true value. Reduction of the parameter space must be approached with caution for this reason. In the present case, the dominance of the remaining parameters is such that both the additional noise and any potential bias introduced by the reduction are expected to be small.

The second assumption aiding in the reduction of the parameter space is that uncertainty of physical origin is small relative to uncertainty of biological origin. Comparisons of the physical model with current meter data, surface salinity data, and surface temperature data all suggest that the primary features of the springtime evolution of WGOM river plumes, vernal warming, and the strength and direction of the coastal current are being captured (see Chapters 3 and 4). However, this step is as much justified by the large uncertainty in the biology (e.g. Fig. 10) as it is by the performance of the physical model. It is unlikely that even the most egregious physical errors could cause > 10 fold changes in bloom magnitude. If the misfits of physical origin persist over relatively small space/time scales and occur in a random manner (e.g. those stemming from the inability to deterministically simulate the exact placement and timing of

mesoscale phenomena), this physical noise will be manifest in an increase in the noise that will simply make hypotheses more difficult to reject (e.g. Fig. 4). However, conclusions will be tempered by recognition that any persistent bias in the physical dynamics, particularly in sensitive regions within the domain, could lead to bias in the estimates of biological model parameters.

3.3 Misfit Model Formulation

The reductions of the model parameter space described above allows the following simplification of (16):

$$y = A(\mu_{max}, d_g, K_N, m) + \varepsilon = \hat{y} + \varepsilon \tag{18}$$

Although the same symbol has been used for the misfit as in (16), ε now contains contributions from the observational noise, unresolved physical and biological processes, any contributions from the imperfect physical model parameterization and forcing, as well as any misfit produced by setting the remaining biological model parameters to central values within their uncertainty. This diversity of misfit sources complicates the construction of a misfit model. Since the total misfit is the sum of many components that are at least partly independent, it could be argued that it would be approximately normal. However, the observations themselves vary over several orders of magnitude and the underlying dynamics (i.e. growth and mortality) are exponential in nature. This suggests that the log-transformed misfits may be normally distributed, which would grant consistency in the weighting of misfits over orders of magnitude. The latter description will serve as the first misfit model guess.

An additional aspect of the dynamical model is that it was constructed in the hope of capturing the general timing and magnitude of bloom events, not their detailed

structure. It is thus expected that some covariance may exist between the misfits in both space and time. Inspection of the patch decorrelation scales (Fig. 11) in the along-shore and cross-shore directions suggests the possibility of an anisotropic spatial misfit decorrelation. A misfit covariance matrix, $C_{\varepsilon\varepsilon}$, is therefore included, where covariance decay is modeled with a simple function:

$$C_{ij} = \rho_{\Delta t} \times \sigma^2 \times \exp\left(- r_y \times \sqrt{\Delta y^2 + \left(\frac{r_x}{r_y} \Delta x \right)^2} \right) \tag{19}$$

Where r_x and r_y are exponential decay coefficients (km^{-1}) in the cross-shore and alongshore directions respectively, Δx and Δy are the along-shore and cross-shore distances between any two points i, j, and σ^2 is the misfit variance. The possibility of temporal correlation is introduced with the factor $\rho_{\Delta t}$. The roughly equal bi-weekly spacing of the cruises makes it possible to use the number of cruises separating any two observations as a proxy for temporal lag. Thus, $\rho_{\Delta t=1}$ corresponds to the correlation between points at the same spatial location, but separated by 1 cruise. For points taken during the same cruise, this factor ($\rho_{\Delta t=0}$) has a value of 1. Only correlations between points separated by 1 or 2 cruises are considered herein. This simple representation of the covariance would likely be inadequate if, for example, the detailed dynamics across hydrodynamic fronts were being explored, but it should suffice for the goals of this analysis.

With this preliminary choice of misfit model, the likelihood can be written:

$$L(\boldsymbol{\theta}; \boldsymbol{\varepsilon}) = \frac{\exp(-\frac{1}{2} \times \boldsymbol{\varepsilon}^T C_{\varepsilon\varepsilon}^{-1} \boldsymbol{\varepsilon})}{(2\pi)^{n/2} \sqrt{\det(C_{\varepsilon\varepsilon})}} \tag{20}$$

Which is the N-dimensional joint normal distribution for a set of n misfits (e.g. Wunsch, 1996). $\boldsymbol{\theta}$ is a vector consisting of the 4 free parameters in the biological model (μ_{max}, d_g, K_N, m) and 5 parameters in the misfit model $(\sigma^2, r_{cs}, r_{as}, \rho_{\Delta t=1}, \rho_{\Delta t=2})$, and ε is the $n \times 1$ vector of log-transformed model/data misfits:

$$\varepsilon_i = \ln(\hat{y}_i + 1) - \ln(y_i + 1) \tag{21}$$

One has been added to allow for the inclusion of 0 abundance observations in the analysis.

While an *a-priori* estimate of the misfit variance is not applied in the optimization directly, it is still useful to consider an expected level of fit. The goal of the analysis is to identify dynamics capable of recreating the timing and magnitude of the observed bloom. It is thus hoped that the model captures those portions of the data that are explained by the prominent, deterministically resolved aspects of the spring circulation combined with prominent seasonal patterns in the biological sources and sinks. Fig. 11 offers information regarding how this level of agreement might translate to misfit variance. Much of the variability in the observations occurs over relatively short spatial scales (10-30 km), suggesting that small spatial displacements (that are acceptable to the goals of the analysis) will likely lead to large misfit variances. Recent data assimilative modeling efforts within the Gulf of Maine comparing the paths of modeled and observed drifters in the region just north of this domain (He, et al., submitted) show separations of this scale are typical between 1 and 7 days after release despite considerable success at matching observed ADCP, mooring, and coastal sea level observations. It is not certain if the motions responsible for the separation in this particular set of drifters were random turbulent eddies or a persistent deterministic error in the flow field. However, if it is

assumed that displacements in *A. fundyense* patch transport between model and data herein have similar properties to the drifters of He et al. (submitted), it is likely that even those models capturing prominent aspects of the observed bloom will have a misfit variance and decorrelation scale of the same order as the data ($\mathrm{var}\{\ln(\boldsymbol{y}+1)\}=2.61$). This is before consideration of the influence of observational uncertainty and small (< grid scale) variability, which is also not resolved by the model.

3.4: Parameter Estimation and Hypothesis Testing

Now that a dynamical model has been constructed (section 3.1), the dominant parameters identified (section 3.2), and a misfit model formulated (section 3.3), various hypotheses concerning the model structures in Table 4 can be tested. First, the "mortality only" model structure is considered relative to the baseline model. Both a best estimate of m and confidence intervals are desired. These are constructed with the ratio:

$$\lambda = \frac{\ln L(\hat{\boldsymbol{\theta}}_{\varepsilon 0}, \hat{\mu}_{\max 0}, \hat{d}_{g0}, m = m_0, K_N = 0; \varepsilon)}{\ln L(\hat{\boldsymbol{\theta}}_{\varepsilon}, \hat{\mu}_{\max}, \hat{d}_g, \hat{m}, K_N = 0; \varepsilon)} \tag{22}$$

Where $\hat{\boldsymbol{\theta}}_{\varepsilon}$ is used to denote the vector of 5 parameters associated with the misfit model. $\hat{\boldsymbol{\theta}}_{\varepsilon}$, $\hat{\mu}_{\max}$, and $\hat{d}_g$ are all nuisance parameters, and the "0" subscript is used to differentiate the estimate of the parameter under the restrictions of the null hypothesis from the estimate derived from the broader alternative space. The search for the biological model parameters that maximize the likelihood is carried out manually using a large number of simulations to map out the prominent features of the likelihood associated with the parameters of interest. The parameters within the error model are chosen to maximize L for the set of misfits produced by each choice of biological parameters using a simplex

parameter space search (Press, et al., 1985). The parameter search space is limited to the approximate uncertainty ranges in Table 3. This application of prior knowledge to the fitting is a pragmatic decision rather than an attempt at a Bayesian approach and its consequences will be discussed shortly.

The m.l.e. for the denominator of (20) occurs at $m = 0.15$ day^{-1}, and confidence intervals around the m.l.e. are constructed using χ^2 distribution with 1 degree of freedom (Fig. 12, panel A). Null hypotheses stating values of $m < 0.9$ day^{-1} or > 0.225 day^{-1} can be rejected with ~90% confidence (threshold defined by the dashed line), while those stating values < 0.075 day^{-1} and > 0.26 day^{-1} can be rejected with ~99% confidence (threshold defined by solid line). Alternatively, the "true" value of m is inferred to be in the interval $0.9 \leq m \leq 0.225$ day^{-1} 90% of the time, and within the interval $0.075 \leq m \leq 0.26$ day^{-1} 99% of the time. The baseline model ($m_0 = 0$ day^{-1}) lies well outside both these intervals and is thus strongly rejected. The reason for this is apparent in Fig. 13, which compares the modeled cell distribution under each of the 4 model structures in table 4 (rows B-E) to that observed (row A). Comparison of rows B and A clearly shows that the baseline model strongly overestimates the observations at the end of the simulations. This misfit is greatly reduced when moderate mortality is introduced (row C).

A similar analysis carried out for the nutrients only case reveals that nutrient dependence also significantly improves the fit to data relative to the baseline (Fig. 12, panel B). Null hypotheses purporting values of $K_N \leq 1.5$ μM can be rejected with 90% confidence, and those purporting values ≤ 1.0 μM can be rejected with 99% confidence. The fact that the maximum occurs at the edge of the considered parameter space makes it

difficult to define the upper limit of confidence intervals, and this will be discussed in more detail shortly. However, it is clear that the baseline case lies well outside the lower limit of the confidence interval and it can thus again be rejected. Comparison of Fig. 13, rows A, B, and D suggests that the reason for the rejection is again the baseline model's tendency for overestimation late in the simulation.

Next, to assess the skill added using both K_N and m, confidence intervals are constructed using the ratio:

$$\lambda = \frac{\ln L(\hat{\theta}_{\varepsilon 0}, \hat{\mu}_{\max 0}, \hat{d}_{g0}, m = m_0, K_N = K_{N0}; \varepsilon)}{\ln L(\hat{\theta}_{\varepsilon}, \hat{\mu}_{\max}, \hat{d}_g, \hat{m}, \hat{K}_N; \varepsilon)} \tag{23}$$

The results of this analysis are in Fig. 12, panel C, and reveal a broad swath of parameter values that can produce statistically similar results. The m.l.e. is $\hat{m} = 0.1$ day^{-1} and $\hat{K}_N =$ 0.05 μM, but the observations can only restrict the "true" parameter value to the space within the thick dashed contour 90% of the time, and within the thick solid contour 99% of the time. Despite the broadness of this confidence region, it is still possible to firmly reject the baseline. Comparison of row E of Fig. 13 with rows A and B confirms once more that the baseline model has been rejected primarily on account of its tendency to overestimate cell abundance late. Comparison of rows C through E suggests no dramatic differences between the size and scale of the misfits in the three cases. The model/data comparison thus suggests the need for the addition of a loss or limitation to the baseline model, but that it is difficult to differentiate whether it is best imposed by nutrients or mortality.

Inspection of the misfit properties (Fig. 14, top 4 panels) offers insight into the relationship between the magnitude and scale of the misfits, and the likelihood. The

broad swath of high likelihood in Fig. 12, panel C is not surprisingly associated with low misfit variance and small misfit spatial scales. Although qualitative inspection of Fig. 13 suggests that broad-scale aspects of the observed bloom are captured by the best models, the estimated misfit variance for the best case is indeed of similar magnitude to the data variance (this will be further discussed in Section 3.6). It is also notable that the highest likelihood no longer precisely coincides with the lowest variance. This is due to the presence of spatial and temporal covariance within the misfit model. Increases in the spatial/temporal temporal scales of the misfits are accompanied by increases in the misfit variance. The increased variance is the dominant effect, and drives the likelihood down. However, greater covariance between misfits effectively decreases the number of independent observations that need to be explained. In some cases, depending on the detailed space/time organization of the misfits, the influence of covariance can be strong enough to make it probabilistically easier to explain a set of misfits as slightly larger with a higher covariance, then slightly smaller with more independence.

The temporal covariance of the misfits is uniformly low, even for the baseline case where it seems that the persistent overestimates by the model during the last two cruises might be explained as one temporally correlated misfit of large spatial scale. However, the likelihood suggests that it is probabilistically easier to explain this persistent overestimation as two independent misfits of large spatial scale, rather than imposing a high temporal correlation over all 5 cruises.

It was noted that the confidence regions in both panel B and C of Fig.12 intersect the edges of the parameter space defined by Table 3. Furthermore, plots of the nuisance parameters $\hat{\mu}_{\max 0}$ and $\hat{d}_{g0}$ (Fig. 14, bottom two panels) indicate that the limits placed on

these parameters are also playing a role in the analysis. The over-estimation in the baseline case, for instance, is largely the result of the fact that cell populations proliferate late in the season even when μ_{max} and d_g are pinned to the lower limits of their uncertainties. Likewise, the poor performance of many of the high m and high K_N simulations in Fig. 12 is primarily due to the fact that the model cannot create cell abundances high enough to match observations in these cases even if μ_{max} and d_g are pinned to the upper limits of their uncertainties. This demonstrates the sizeable dependence of the analysis results on the range of the values considered, and the results must be interpreted with these ranges and their reliability in mind. For example, it is ill-advised to base the final conclusions of a study on the assertion that $K_N \neq 4.0\,\mu\text{M}$ based on the results in Figs. 12b,c due to the informal manner in which the K_N range was chosen. However, it would be safe to conclude that, when parameters are allowed to vary over a range suggested in the literature, the addition of a moderate to high nutrient dependence produces a significant improvement relative to the baseline model.

Despite the fact that the ranges in Table 3 were given generous width, it could be suggested that the parameter search be expanded well beyond the range of values thought reasonable. Indeed, this would provide additional information by identifying how high or low a parameter would need to be before a specified result can be achieved. However, while potentially useful, this approach would quickly prove computationally infeasible in the present application. Furthermore, many of the estimates it yields would likely warrant ultimate rejection based on their extreme values relative to existing knowledge.

In some cases, the edges of the confidence intervals are set not by the limits in Table 3, which are admittedly subject to some uncertainty, but by the theoretical limits of

the parameter values under consideration. One such case occurs in Fig. 12c, where the confidence interval intercepts $m = 0$ day^{-1}. Such theoretical limits can be problematic primarily because they can interfere with the asymptotically normality of m.l.e.'s which implies a symmetry in the uncertainty that is not achievable when the m.l.e. lies on or near a hard limit in the parameter space. While such boundaries do not prevent usage of the methodology entirely, rejection of a hypothesis based on fine delineations in the likelihood near such boundaries should be avoided. Mapping the likelihood surface rather than only reporting p-values is useful for spotting and diagnosing potential trouble spots.

3.5: Misfit Model Verification

Before engaging in any further analysis, consistency between the misfits and the proposed misfit model must be verified. The raw misfits (Fig.15, left panel) suggest some asymmetry, with an increased prevalence of overestimation by the model. However, this histogram does not account for spatial or temporal covariance. Inspection of Fig. 13 reveals several regions of persistent over-estimation by the model, most notably in the Massachusetts Bay and Cape Cod Bay region during cruise 3. Misfits associated with the individual observations in these patches are not independent, but part of the same larger misfit. This can be accounted for by scaling the misfits according to $C_{\varepsilon\varepsilon}^{-1/2} \times \varepsilon$, where $C_{\varepsilon\varepsilon}^{-1/2}$ is the Cholesky decomposition of the covariance matrix (Houseman, et al., 2004). If the covariance description is appropriate, this multiplication will isolate the independent portions of the misfit and normalize them. The result is shown in Fig. 15 panel B, which clearly suggests that the misfits adjusted for covariance are both symmetric and normal.

Plots of the scaled misfit as a function of $\hat{y}$ and as a function of the order in which they were taken (Fig. 16, panels A and B) suggest no dramatic non-stationarity in the misfit. There is a predictable absence of large negative misfits at small values of $\hat{y}$, as observations are necessarily positive and bounded by a lower limit of 1 cell/L. However, the effect on the misfit variance is limited to values of $\hat{y} \leq 2$ (~5-10 cells/L), and is not pronounced even then. The linearity of the probability plot of the scaled misfits (Fig. 16, panel C) adds further support to the conclusions suggested by Fig. 15. The estimated decorrelation scales are largely consistent with that suggested by the autocorrelation of the misfits (Fig. 16, panels D and E), although the estimated cross-shore decay rate is slightly lower than suggested by the autocorrelation (panel E). Diagnosis (not shown) suggests that this primarily results from a limited number of more prominent misfits in the Massachusetts/Cape Cod Bay region, particularly during cruise 3. Aside from this suggestion of a mild outlier, the representation of the spatial correlation decay (19) appears suitable. The choice of the misfit model and the implicit assumptions about the misfit weights associated with it thus seem reasonable.

3.6 Model Assessment and Diagnosis

The methodology described above determines if the skill of a simple model can be improved with the addition of extra dependencies and it provides confidence intervals to constrain parameters based on the relative changes in the statistical properties of the misfit. The best model and those that cannot be strongly differentiated from it must still be assessed to understand what features of the observations have actually been captured, and diagnosed to gain insight into bloom dynamics. Treatment of the model diagnosis is limited here, apart from mentioning that it is critical to diagnose the model results over

the range of parameter uncertainty to ensure robust conclusions. Examples of this can be found in Chapters 3 and 4.

Assessment of what has been resolved by the model is critical before diagnosis, as this determines the nature of the questions that should be asked of the model. The graphical comparison of Fig. 13 suggests that the model has produced a smoothed version of the observations of similar magnitude to that observed. This serves as a first check of model plausibility, as it was unclear *a-priori* if the germination of cysts shown in Fig. 9C could produce a source of *A. fundyense* cells remotely near that required by observed cell concentrations. In addition to this basic agreement, some of the first order observed space-time variability is also apparent. For example, the progression of the bloom magnitude from April to June and the high *A. fundyense* concentrations in coastal regions, near Casco Bay, and near Boston Harbor are qualitatively similar in the model and the data. Considerable misfits exist at individual points, and some persist over larger scales. Most notable of these is the absence of cells within Cape Cod and Massachusetts Bay in the observations during cruise 3 relative to their presence in the model.

While graphical comparison provides a general assessment of the level of fit achieved and a sense for its spatial and temporal organization, more quantitative metrics are also useful. The raw misfit correlation coefficient (r) and the coefficient of determination (r^2) are a humbling 0.32 and 0.10 respectively based on a point-to-point comparison. If the misfit variance estimate from the m.l.e., which accounts for spatial correlation in the misfit, is used, these values drop to 0.19 and 0.035 respectively. Both these calculations suggest that the model is weakly correlated with the data and only accounts for a small fraction of the observed variance. However, it was noted in Section

3.3 that poor fit at the 10-30 km patch scale was expected even for models that captured many of the low frequency features of the observed bloom due to uncertainty in the precise patch positioning. The model output and the data are thus spatially averaged, starting with the largest (cruise) scale and decreasing to scales of 10 km in order to more accurately assess the models ability to represent different bloom features (Table 5). For the cruise comparison, the mean of all the modeled values at the sample points is compared with the mean of all the observations on a cruise-by-cruise basis. For the spatial comparisons, all observations within a radius of the specified scale were averaged to provide a mean observed value within the region near the observation. This was compared with the area-weighted mean of the model output (averaged over the M2 tidal cycle centered on the cruise) within the same region. All comparisons are done with the natural log transformed data.

The cruise-by-cruise comparison (Table 5) suggests that the model captures much of the variability in the mean cell level between cruises. Inspection of the values (Fig. 17) shows the model starting slowly, but then tracking the data in a fairly consistent manner. While the standard deviations around the means do not always overlap, a high correlation is apparent. Within cruises the model skill steadily decays as smaller spatial scales are considered. Correlation is moderate at 50-100 km length scales, which cover ~1/3 and ~1/6 of the along-shore extent of the domain respectively and have little cross-shore resolution. Correlation predictably weakens and the variance accounted for by the model is small as the averaging scale encounters the patch scale (25 km and 10 km).

There are significant drops in skill between the cruise comparison, the 100 km scale, and the 50 km scale. This suggests that there may be some prominent misfits

within this range. Inspection of Fig. 13 suggests that cruise 3, with its notable over-estimation of *A. fundyense* in Massachusetts and Cape Cod Bays and moderate under-estimation to the North of Cape Ann may be the cause. Indeed, removing this cruise from the analysis causes a notable increase in skill for comparisons on both these scales (Table 6). The skill at the 100 km length scale is now nearly equal to that demonstrated by the cruise averages, and a fairly strong correlation exists at the 50 km length scale. Comparisons at 10 and 25 km also improve with removal of cruise 3, but changes are less marked than those at larger scales.

The analysis above and the misfit properties derived from the m.l.e. suggest the following assessment: The best model has captured the progression of the average concentration on a cruise-by-cruise basis fairly well. It also demonstrates a fair amount of success capturing mean conditions over length scales of 50 km or greater, although potential for some considerable misfit at this scale exists (i.e. cruise 3). At the patch scale and below, skill is very limited and this dominates the point-to-point variance. Diagnosis should therefore avoid questions that critically depend on dynamics at this scale. The overall predominance of misfits at the patch scale further suggests potential difficulty detecting further model improvement as long as motions on these scales (e.g. meso-scale turbulent dynamics, detailed frontal dynamics) are largely incorporated into the error term in (16), as this yields a low signal to noise ratio.

While the dominance of misfit at the patch scale discussed above suggests a diminishing ability to differentiate between increasingly complex biological models, some larger-scale misfits are present which might suggest further model improvement. However, the origin of this misfit in Cape Cod Bay and Massachusetts Bay in cruise 3 is

ambiguous. There is branch point in the coastal current near Cape Ann that partitions the flow between an inshore route, leading into the Bays; and an offshore root, which directs flow around Cape Cod. Any persistent bias in the physics controlling the flow at this branch point could generate such a misfit. However, it could also be generated by errors in the biological processes that control the vertical distribution of cells, as this can have a profound effect on the wind driven transport into the region. Dynamics of the source term not included in the model can also not be ruled out, as this source and subsequent transport determines when *A. fundyense* cells reach the Cape Ann branch. Lastly, the misfit may result from unresolved spatial and temporal variability in the growth and mortality within Massachusetts and Cape Cod Bays.

4. Conclusions

While maximum likelihood estimation and the maximum likelihood ratio test are not solutions for all the challenges facing the evaluation of ocean ecosystem models, they are valuable tools that can offer inroads in several areas. These include aiding in the extraction of reliable information from sparse and noisy data sets, providing guidance concerning the choice of misfit weights, and providing information useful for model assessment, diagnosis, and further model improvement. Perhaps the most critical contribution of these tools is the ability to test hypotheses in a statistically rigorous way and produce parameter confidence intervals. The wide uncertainty apparent in Fig. 12 clearly highlights the danger of reporting only the best-fit parameter values.

Several steps highlighted herein were critical to the successful application of m.l.e. and the m.l.r.t. to a spatially and temporally resolved physical-biological model. First, the reduction of the parameter space to include only those parameters critical to the

question of primary interest and reflected in the observations was essential. During this reduction, caution is required to avoid removing potentially important parameters from the analysis, as this risks the introduction of bias to the remaining parameter estimates. This suggests that reasonably precise questions must be formulated and appropriate sensitivity metrics defined to avoid computational difficulty and potentially misleading results.

The implementation of more advanced optimization techniques such as the adjoint method (Lawson, et al., 1995, Lawson, et al., 1996, Spitz, et al., 1998) may reduce the need for extensive *a-priori* reduction of the parameter space. The likelihood function naturally enters the adjoint methodology as a cost function to be minimized subject to the constraints of the dynamical model equations. Indeed, the cost function often used in such methods is generalized least squares, which is the m.l.e. for normally distributed misfits. However, the risk of misinterpretation of results is greatly reduced through translation of the cost function to an explicit likelihood and subsequent application of the m.l.r.t.. It is also notable that the adjoint method provides estimates of the partial derivatives of the cost function (i.e. the likelihood) with respect to the uncertain parameters in the neighborhood of the optimum parameter values. Such estimates are extremely useful to understanding the sensitivity of the model/data fit to perturbations in the control parameters and can be used to estimate the entries in the Fisher Information Matrix (6a,b) directly.

A second aspect of the approach was that *a-priori* knowledge of the likely parameter values was used to focus the parameter space search. Search limits should be given generous width and the reliability of the uncertainty bounds and the influence they

have on the analysis results must temper conclusions. More advanced optimization techniques would facilitate expansion of the search space if parameters are not well constrained. Alternatively, if exceptional knowledge of the likely parameter values is available, a more formal Bayesian approach to the estimation process could be implemented.

An additional area where improvement could be made is through an increased understanding of the different components of the misfit. For example, knowledge of the typical misfits resulting from comparison of a "correct" biological model to observations in the presence of only physical uncertainty would be a useful benchmark. This information could also be used to construct a filter designed to identify misfits not explained by such physics. Alternatively, such a filter could be applied before comparison in the hope that filtering "noise" *a-priori* will tighten parameter constraints. Characterization of this physically generated noise could be approached using Monte-Carlo simulations that perturb various aspects of the physical model forcing and track the variability generated at observation points.

Anderson, D. M., 1998. Physiology and bloom dynamics of toxic *Alexandrium* species, with emphasis on life cycle transitions. In: Anderson, D. M., Cembella, A. D. ,Hallegraeff, G. M. (Eds.), Physiological Ecology of Harmful Algal Blooms. Springer-Verlag, Berlin, pp. 29-48.

Anderson, D. M., Keafer, B. A., Geyer, W. R., Signell, R. P., Loder, T. C., 2004a. Toxic *Alexandrium* blooms in the Gulf of Maine: the "plume advection hypothesis" revisited. Limnology and Oceanography (submitted).

Anderson, D. M., Stock, C. A., Keafer, B. A., Bronzino, A. C., Matrai, P., Thompson, B., Keller, M., McGillicuddy, D. J., Hyatt, J., 2004b. Experimental and modeling observations of *Alexandrium fundyense* cyst dynamics in the Gulf of Maine. Deep-Sea Research, Part II (submitted).

Anderson, D. M., Stock, C. A., Keafer, B. A., Bronzino, A. C., Matrai, P., Thompson, B., Keller, M., McGillicuddy, D. J., Hyatt, J., submitted. Experimental and modeling observations of *Alexandrium fundyense* cyst dynamics in the Gulf of Maine. Deep-Sea Research, Part II

Bauerfeind, E., Elbrachter, M., Steiner, R., Throndsen, J., 1986. Application of Laser Doppler Spectroscopy (LDS) in determining swimming velocities in motile phytoplankton. Marine Biology 93, 323-327.

Bennett, A. F., 2002. Inverse Modeling of the Ocean and Atmosphere. Cambridge University Press, Cambridge, 234 pages.

Blumberg, A. F., Mellor, G. L., 1987. A description of a three-dimensional coastal ocean circulation model. In: Heaps, N. (Ed.), Three-Dimensional Coastal Ocean Models. American Geophysical Union, pp. 1-16.

Carpenter, E. J., Guillard, R. R. L., 1971. Intraspecific differences in the nitrate half-saturation constants for three species of marine phytoplankton. Ecology 52, 183-185.

Cook, R. D., Weisberg, S., 1982. Residuals and influence in regression. Chapman and Hall, New York, 230 pages.

Cox, D. R., Hinckley, D. V., 1974. Theoretical Statistics. Chapman Hall, London, 511 pages.

Cuthbert, D., Wood, F. S., 1987. Fitting Equations To Data: Computer Analysis of Multifactor Data. John Wiley and Sons, New York, 458 pages.

D'Agostino, R. B., Stevens, M. A., 1986. Goodness-of-fit techniques. M. Dekker, New York, pages.

Draper, N. R., Smith, H., 1981. Applied Regression Analysis. John Wiley and Sons, New York, 709 pages.

Eppley, R. W., Rogers, J. N., McCarthy, J. J., 1969. Half-saturation constants for uptake of nitrate and ammonium by marine phytoplankton. Limnology and Oceanography 14, 912-920.

Eppley, R. W., Thomas, W. H., 1969. Comparison of half-saturation "constants" for growth and nitrate uptake of marine phytoplankton. Journal of Phycology 5, 365-369.

Etheridge, S. M., Roesler, C. S., Doucette, G. J., 2004. *Alexandrium fundyense* isolate-specific responses to temperature, irradiance, and salinity: Potential growth rate

and toxicity in the Gulf of Maine and Bay of Fundy. Deep-Sea Research, Part II (submitted).

Evans, G. T., 2003. defining misfit between biogeochemical models and data sets. Journal of Marine Systems 40-41, 59-54.

Franks, P. J. S., Anderson, D. M., 1992a. Alongshore transport of a toxic phytoplankton bloom in a buoyancy current: *Alexandrium tamarense* in the Gulf of Maine. Marine Biology 112, 153-164.

Franks, P. J. S., Anderson, D. M., 1992b. Toxic phytoplankton blooms in the Gulf of Maine: testing hypotheses of physical control using historical data. Marine Biology 112, 165-174.

Fung, I. Y., Harrison, D. E., Lacis, A. A., 1984. On the variability of the net longwave radiation at the ocean surface. Reviews of Geophysics and Space Physics 22, 177-193.

Galperin, B., Kantha, L. H., Hassid, S., Rosati, A., 1988. A quasi-equilibrium turbulent energy model for geophysical flows. Journal of Atmospheric Science 45, 55-62.

Geyer, W. R., Signell, R. P., Fong, D. A., Wang, J., Anderson, D. M., Keafer, B. A., 2004. The freshwater transport and dynamics of the western Maine Coastal Current. Continental Shelf Research 24, 1339-1357.

He, R., McGillicuddy, D. J., Lynch, D. R., Smith, K. W., Stock, C. A., Manning, J. P., submitted. Data Assimilative Hindcast of the Gulf of Maine Coastal Circulation. Journal of Geophysical Research, Oceans 47 pages.

Hofmann, E. E., Lascara, C. M., 1998. Overview of interdisciplinary modeling of marine ecosystems. In: Brink, K. L. ,Robinson, A. R. (Eds.), The Sea. John Wiley and Sons, New York, pp. 507-540.

Hogg, R. V., Craig, A. T., 1995. Introduction to Mathematical Statistics. Prentice Hall, Upper Saddle River, NJ, 564 pages.

Houseman, E. A., Ryan, L. M., Coull, B. A., 2004. Cholesky Residuals for Assessing Normal Errors in a Linear Model with Correlated Outcomes. Journal of the American Statistical Association 99, 383-394.

Kamykowski, D., Reed, R. E., Kirkpatrick, G. J., 1992. Comparison of the sinking velocity, swimming velocity, rotation and path characteristics among six marine dinoflagellate species. Marine Biology 113, 319-328.

Kuhl, M., Jorgensen, B. B., 1994. The light of microbenthic communities: Radiance distribution and microscale optics of sandy coastal sediments. Limnology and Oceanography 39, 1368-1398.

Langdon, C., 1987. On the causes of interspecific differences in the growth-irradiance relationships for phytoplankton. Part I. A comparitive study of the growth irradiance relationships of three marine phytoplankton species: *Skelotonema costatum, Olithodiscus luteus* and *Gonyaulax tamarensis*. Journal of Plankton Research 9, 459-482.

Large, W. G., Pond, S., 1981. Open ocean momentum flux measurements in moderate to strong winds. Journal of Physical Oceanography 11, 329-336.

Large, W. G., Pond, S., 1982. Sensible and latent heat flux measurements over the ocean. Journal of Physical Oceanography 12, 464-482.

Lawson, L. M., Hofmann, E. E., Spitz, Y. H., 1996. Time series sampling and data assimilation in a simple marine ecosystem model. Deep Sea Research, Part II 43, 625-651.

Lawson, L. M., Spitz, Y. H., Hofmann, E. E., Long, R. B., 1995. A data assimilation technique applied to a predator-prey model. Bulletin of Mathematical Biology 57, 593-617.

LeCam, L., 1970. On the assumptions used to prove the asymptotic normality of maximum likelihood estimates. Ann. Mathematical Statistics 41, 802-828.

Lomas, M. W., Glibert, P. M., 2000. Comparison of nitrate uptake, storage, and reduction in marine diatoms and flagellates. Journal of Phycology 36, 903-913.

Lynch, D. R., Naimie, C. E., 1993. The M2 tide and its residual on the outer banks of the Gulf of Maine. Journal of Physical Oceanography 23, 2222-2253.

MacIsaac, J. J., Grunseich, G. S., Glover, H. J., Yentsch, C. M., 1979. Light and nutrient limitation in *Gonyaulax excavata*: nitrogen and carbon trace results. In: Taylor, D. L. ,Seliger, H. H., (Eds.), Toxic Dinoflagellate Blooms: proceedings of the second conference on toxic dinoflagellate blooms, Key Biscayne, Florida. Elsevier/North-Holland, pp. 107-110.

Martorano, C. D., Loder, T. C., 1997. Nutrient dynamics during blooms of *Alexandrium* spp. in the southwestern Gulf of Maine. Masters Thesis, University of New Hampshire, Biogeochemical Systems Center, Durham, NH, USA, unpublished.

Mellor, G. L., Yamada, T., 1982. Development of a turbulence closure model for Geophysical Fluid Problems. Reviews of Geophysical and Space Physics 20, 851-875.

Muccino, J. C., Hubele, N. F., Bennett, A. F., 2004. Significance testing for variational assimilation. Quarterly Journal of the American Meteorological Society 130, 1815-1838.

Naimie, C. E., Loder, J. W., Lynch, D. R., 1994. Seasonal variation in the three-dimensional residual circulation on Georges Bank. Journal of Geophysical Research 99, 15,967-15,989.

Platt, T., Jassby, A. D., 1976. The relationship between photosynthesis and light for natural assemblages of coastal marine phytoplankton. Journal of Phycology 12, 421-430.

Prakash, A., 1967. Growth and toxcity of a marine dinoflagellate, *Gonyaulax tamarensis*. Journal of the Fisheries Research Board of Canada 24,

Press, W. H., Flannery, B. P., Teukolsky, S. A., Vetterling, W. T., 1985. Numerical Recipes, The Art of Scientific Computing. Cambridge University Press, Cambridge, 818 pages.

Sommer, U., 1991. A comparison of the Droop and Monod models of nutrient limited growth applied to natural populations of phytoplankton. Functional Ecology 5, 535-544.

Spitz, Y. H., Moisan, J. R., Abbot, M. R., Richman, J. G., 1998. Data assimilation and a pelagic ecosystem model: parameterization using time series observations. Journal of Marine Systems 16, 51-68.

Townsend, D. W., Pettigrew, N. R., Thomas, A. C., 2001. Offshore blooms of the red tide dinoflagellate *Alexandrium* sp., in the Gulf of Maine. Continental Shelf Research 21, 347-369.

Watras, C. J., Chisholm, S. W., Anderson, D. M., 1982. Regulation of growth in an estuarine clone of *Gonyaulax tamarensis* Lebour: salinity-dependent temperature responses. Journal of Experimental Marine Biology and Ecology 62, 25-37.

Wunsch, C., 1996. The Ocean Circulation Inverse Problem. Cambridge University Press, New York, 442 pages.

Table 1: Summary of the properties of the maximum likelihood estimates.

Property	**Description**
Consistency	The value of the m.l.e. approaches the value of the true parameter as $n \to \infty$
Asymptotically normal	The distance between the m.l.e.'s and the true parameter values $(\boldsymbol{\theta}^* - \hat{\boldsymbol{\theta}})$ when the model is true, is normally distributed with covariance matrix $I^{-1}(\boldsymbol{\theta})$.
Asymptotically unbiased	$E(\hat{\boldsymbol{\theta}}) = \boldsymbol{\theta}$. Some m.l.e.'s are unbiased regardless of the sample size, but this is not a general property.
Efficient	The variance of an m.l.e. about the true parameter value: approaches the Rao-Cramér lower variance bound.
Asymptotically Sufficient	The m.l.e. reflects all of the information contained within the sample about the parameters $\boldsymbol{\theta}$. That is, no other statistics exist that can provide additional constraints.

Table 2: Physical Model Forcing

Forcing	Source/Description
Sea Surface Elevation	M_2 tide from Gulf of Maine tidal model (Lynch and Naimie, 1993) Mean elevation from bi-monthly climatology (Naimie, et al., 1994)
Wind	Portland off-shore buoy (NDBC #44007), applied throughout domain and translated to shear via Large and Pond (1981)
River discharge	USGS stream gauges at 4 major rivers: Charles, Saco, Merrimack, and the Kennebec/Androscoggin
Boundary T,S	Interpolated and extrapolated from mooring and survey data
Initial T,S	spatially averaged climatology (Naimie, et al., 1994)
Heat Flux	Shortwave radiative heat flux from land-based sensor at Woods Hole Sensible and latent heat fluxes estimated using Portland off-shore buoy data and the bulk formulae of Large and Pond (1982). Longwave flux estimated using Portland off-shore buoy data and relationships of Berliand and Berliand as described in Fung et al. (1984)

Table 3: Biological Model Parameters

Symbol	Definition	Units	Range	Sources
K_N	Half-saturation constant for nutrient limited growth	μM	0-3	Eppley et al. (1969), Eppley and Thomas (1969), Lomas and Glibert (2000), Carpenter and Guillard (1971), MacIsaac et al. (1979), Sommer (1991)
m	Spatially and temporally averaged mortality	day^{-1}	0-0.3	see text
$\mu_{max}(T_{opt},S_{opt})$	The maximum growth rate under optimal temperature and salinity conditions.	day^{-1}	0.46-0.70	Cullen et al. (this volume), Langdon (1987), Etheridge et al. (this volume), Watras et al. (1982), Keafer and Kulis (unpub. data)[1]
μ_o^r	The maintenance respiration rate	day^{-1}	0.15-0.25	Cullen et al. (this volume)
α_g	The growth efficiency	$day^{-1} W^{-1} m^2$	0.017-0.056	Cullen et al. (this volume)
d_g	The mean depth of sediment over which cysts are able to germinate and contribute to the bloom	cm	0.5-1.5	Anderson et al. (2004b)
E_{lgt}	Light level for germination under "light" conditions.	$watts/m^2$	1.2-3.6	Anderson et al. (this volume)
E_{drk}	Light level for germination under dark conditions.	$watts/m^2$	0.1% of I_{lgt} to 10% of I_{lgt}.	Anderson et al. (this volume)
k_w	Mean diffuse attenuation in water column.	m^{-1}	0.15-0.25	Townsend et al. (2001)
k_s	Mean diffuse attenuation in the sediment	mm^{-1}	2-5	Kuhl and Jorgensen (1994)
w_a	Vertical swimming speed	m/day	5-15	Bauerfiend et al.(1986), Kamykowski et al. (1992)

[1] Sources used for formulation of the growth versus temperature dependence polynomial are: Etheridge et al. (2004), Langdon (1987), Watras et al. (1982), and Keafer and Kulis (unpublished data). Sources used for the salinity dependence polynomial are: Etheridge et al. (2004) and Prakash (1967).

Table 4: Summary of the growth rate dependence for the 4 biological model structures. T = temperature, S = salinity, E = irradiance, N = nutrients (i.e. dissolved inorganic nitrogen).

Structure	Growth Rate Dependence	Mortality
baseline	T, S, E	no
mortality	T, S, E	yes
nutrients	T, S, E, N	no
mortality and nutrients	T, S, E, N	yes

Table 5: Comparison of the sample correlation (r) and the sample coefficient of determination (r^2) for comparisons of the model and the data (after log transform) averaged over different spatial scales.

Averaging Scheme	**Data Variance**	**Misfit Variance**	**(r / r^2)**
Cruise by Cruise	0.39	0.13	0.82/0.68
100 km scales	0.44	0.22	0.71/0.51
50 km scales	0.79	0.54	0.57/0.32
25 km scales	1.36	1.05	0.48/0.23
10 km scales	1.98	1.65	0.41/0.17
Point-to-Point	2.60	2.33	0.32/0.10

Table 6: Comparison of the sample correlation (r) and the coefficient of determination (r^2) for comparisons of the model and the data (after log transform) excluding cruise 3.

Averaging Scheme	**Data Variance**	**Misfit Variance**	**(r / r^2)**
Cruise by Cruise	0.48	0.11	0.88/0.77
100 km scales	0.45	0.12	0.86/0.73
50 km scales	0.73	0.35	0.72/0.52
25 km scales	1.35	0.88	0.59/0.35
10 km scales	2.01	1.49	0.51/0.26
Point-to-Point	2.66	2.22	0.41/0.17

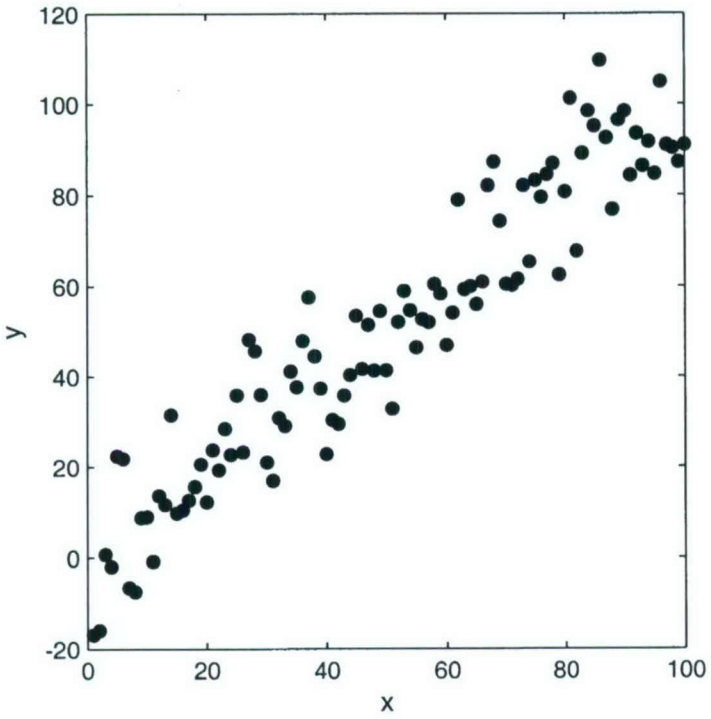


Figure 1: A sample data set. It is hypothesized that that a linear model plus normally distributed observational noise can explain this data.

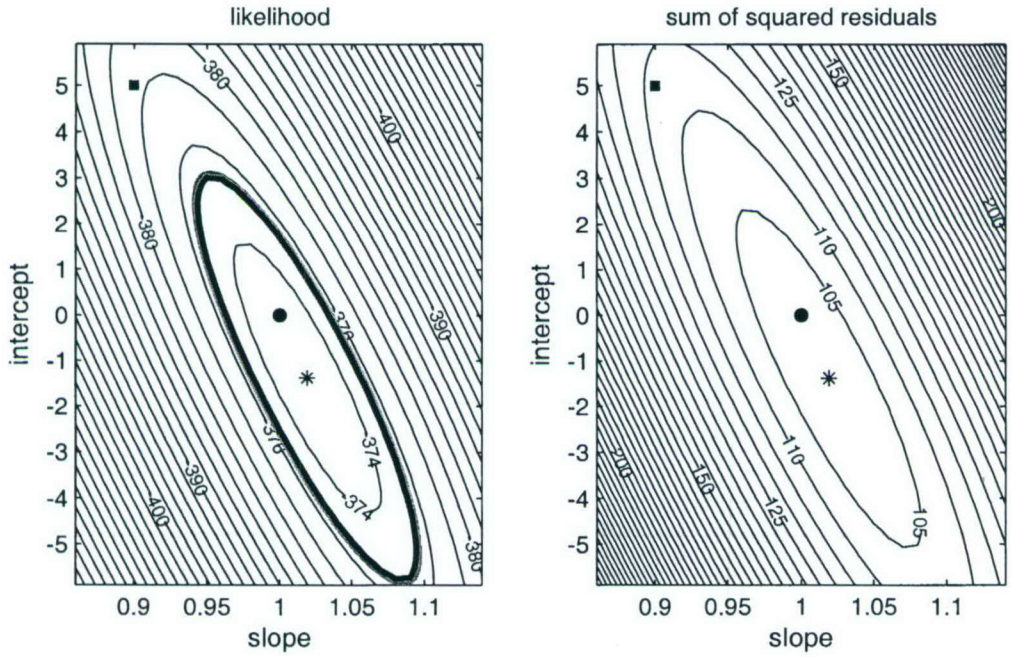


Figure 2: Left Panel: ln(L) as a function of β_0 (intercept) and β_1 (slope) for the data in Fig. 1 (contour interval = 2). The maximum likelihood estimates are $\hat{\beta}_0$ = -1.38, $\hat{\beta}_1$ = 1.02, and $\hat{\sigma}^2$ =101.58 (*). The true values of the parameters are β_0 = 1.00, β_1 = 0.0 and σ^2 = 100.0 (•). The filled square (■) corresponds to the parameter values for the null hypothesis (6). The thick dark contour corresponds to the 90% confidence interval calculated using the m.l.r.t, and the thick gray line represents that calculated using the F-test. **Right Panel:** The sum of the squared residuals as a function of β_0 (intercept) and β_1 (slope) for the data in Fig. 1 (contour interval = 5). The position of the minimum sum of squared residuals (*) and the maximum likelihood coincide for the case of independent, identically distributed normally distributed misfits. Other points are as the left panel.

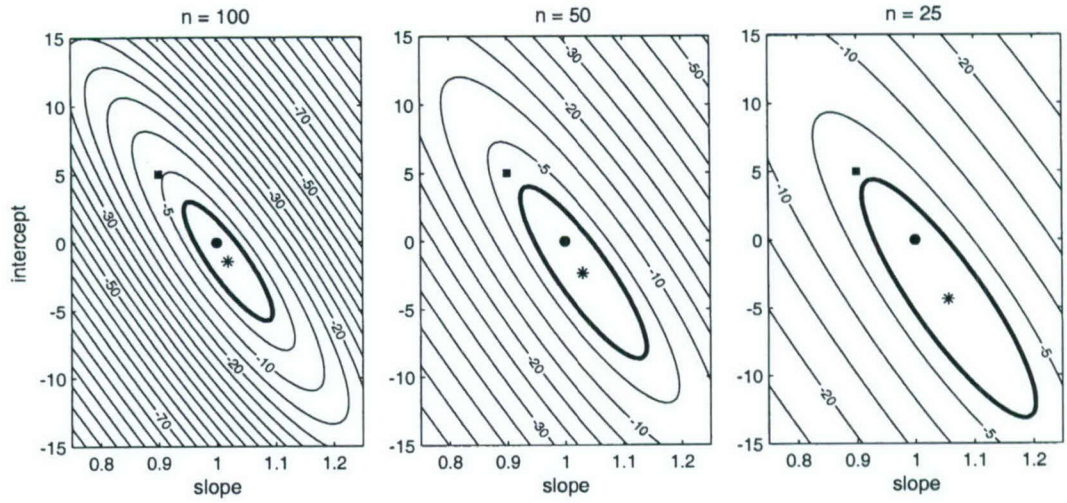


Figure 3: The influence of changing the number of observations on the parameter confidence intervals. **Left Panel:** Change in ln(L) relative to the maximum value as a function of β_0 (intercept) and β_1 (slope) for the complete data set of Fig. 1 (n=100 points). The contour interval is 5. Marks are the m.l.e. (*), the true value (•), and the null hypothesis from (6) (■). The thick dark contour marks the 90% confidence interval. **Center Panel:** Change in ln(L) relative to the maximum value if only every other data point in the Fig. 1 were available (n = 50). Markings are as in panel a. The m.l.e.'s in this case are: $\hat{\beta}_0$ = -2.32, $\hat{\beta}_1$ = 1.03 and $\hat{\sigma}^2$ = 101.65. **Right Panel:** ln(L) if only every fourth data point in Fig. 1 were available (n = 25). The m.l.e's in this case are: $\hat{\beta}_0$ = -4.36, $\hat{\beta}_1$ = 1.06 and $\hat{\sigma}^2$ = 89.81.

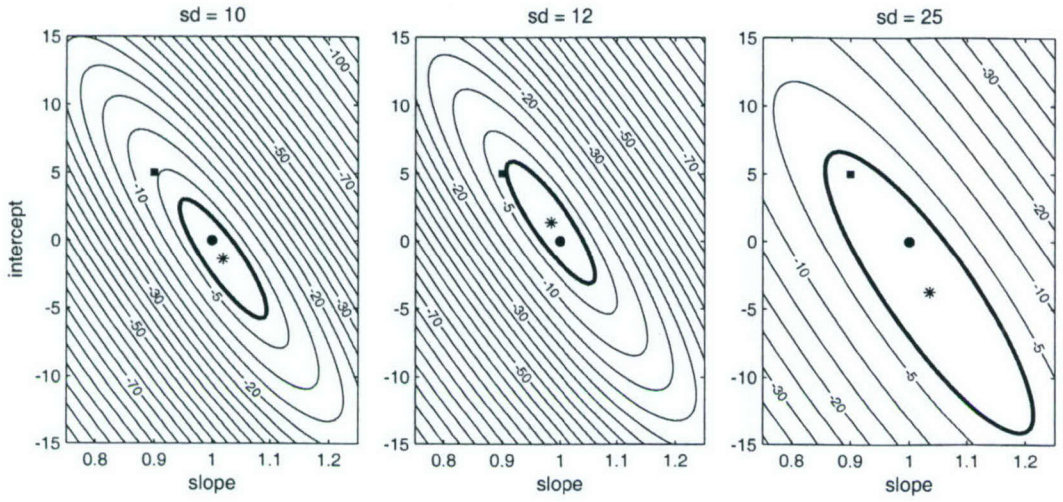


Figure 4: The influence of increasing the data noise on the parameter confidence intervals. **Left Panel:** Change in ln(L) relative to the maximum value as a function of β_0 (intercept) and β_1 (slope) for the complete data set of Fig. 1, where the standard deviation of the noise is 10. Markings are as in Fig. 3. **Center Panel:** Change in ln(L) relative to the maximum value if the n = 100, but with standard deviation of the data noise is 12. The m.l.e.'s in this case are: $\hat{\beta}_0 = 1.38$, $\hat{\beta}_1 = 0.98$ and $\hat{\sigma}^2 = 107.32$. **Right Panel:** Change in ln(L) relative to the maximum value if n = 100, but with standard deviation of the data noise = 25. The m.l.e's in this case are: $\hat{\beta}_0 = 1.04$, $\hat{\beta}_1 = -3.74$ and $\hat{\sigma}^2 = 565.52$.

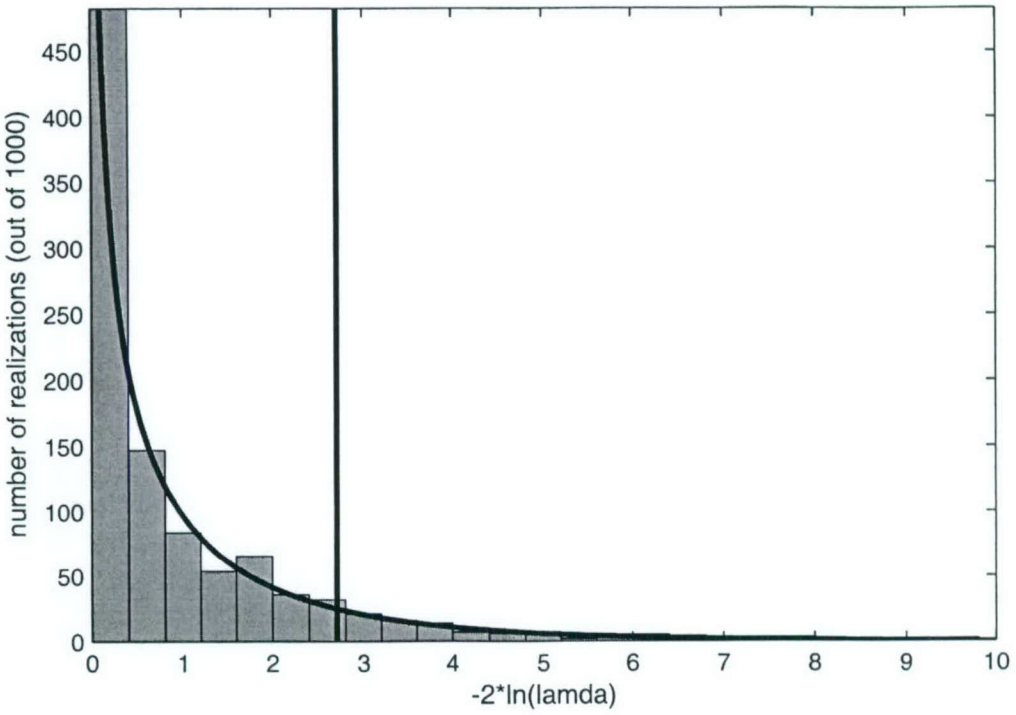


Figure 5: The histogram of values of $-2\ln(\lambda)$ in equation (11) for 1000 realizations of the linear data in Fig. 1. The dark curved line is the theoretical χ^2 distribution with 1 degree of freedom. The dark vertical line is the value of $-2\ln(\lambda)$ below which 90% of the realizations should fall when the null hypothesis is true. 896 of the 1000 realizations (89.6%) meet this requirement.

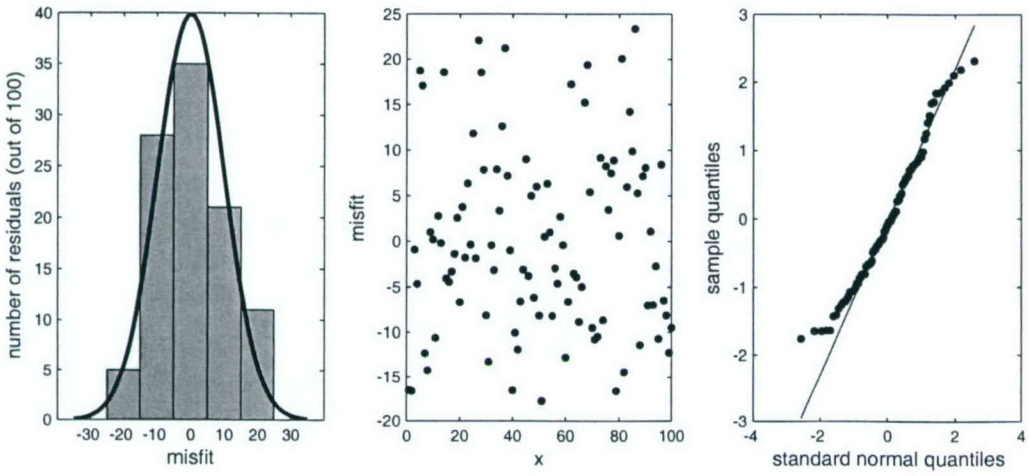


Figure 6: Verification of the misfit model. **Left panel:** The misfit histogram. The dark line is the pattern expected from normally distributed errors. **Middle Panel:** Plot of the residuals against the independent variable x suggesting a constant variance over x. **Right Panel:** Probability plot of the observed normalized misfits sorted increasing order versus the values predicted from a normal distribution with mean 0 and variance $\hat{\sigma}^2$. Quantiles are defined as: $F^{-1}\{(i-1/2)/n\}$, $i = 1,2....n$, where F is the cumulative distribution function of the distribution of interest.

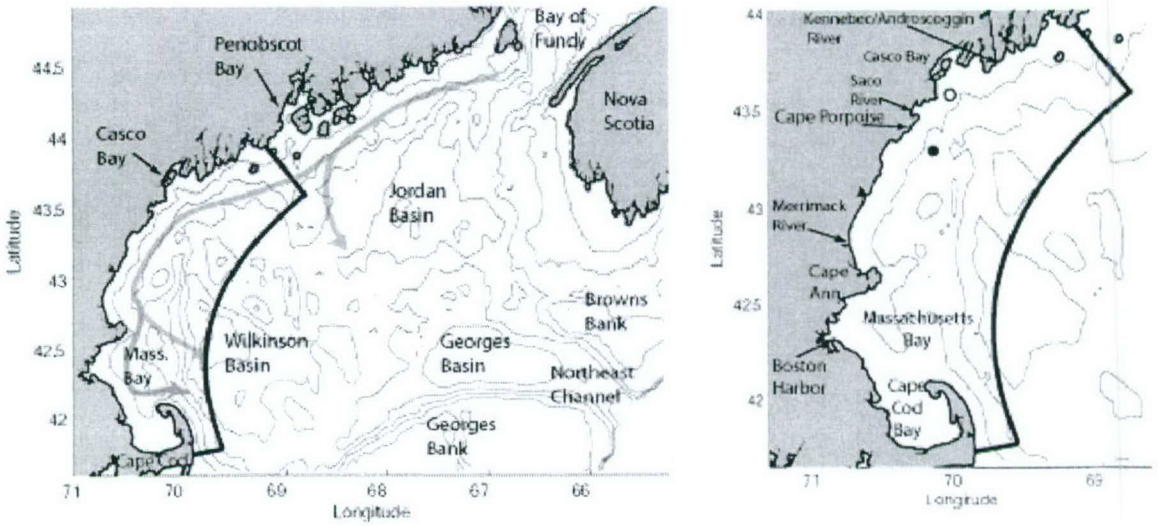


Figure 7: **Left Panel:** The Gulf of Maine and study region. The study domain is outlined in black. Depth contours are at 50, 100, 150 and 200 meters. The direction of the flow of the Maine Coastal Current (adapted from Lynch et al., 1997) is shown as a thick gray line. Branch points off-shore of Penobscot Bay and Cape Ann are notable. **Right Panel**: Close-up of the study region. River outflow locations are highlighted (the Charles River outflow is within Boston Harbor). The closed circle marks the location of the Cape Porpoise Mooring, while the open circle marks the location of the Portland Meteorological Buoy (NDBC station #44007).

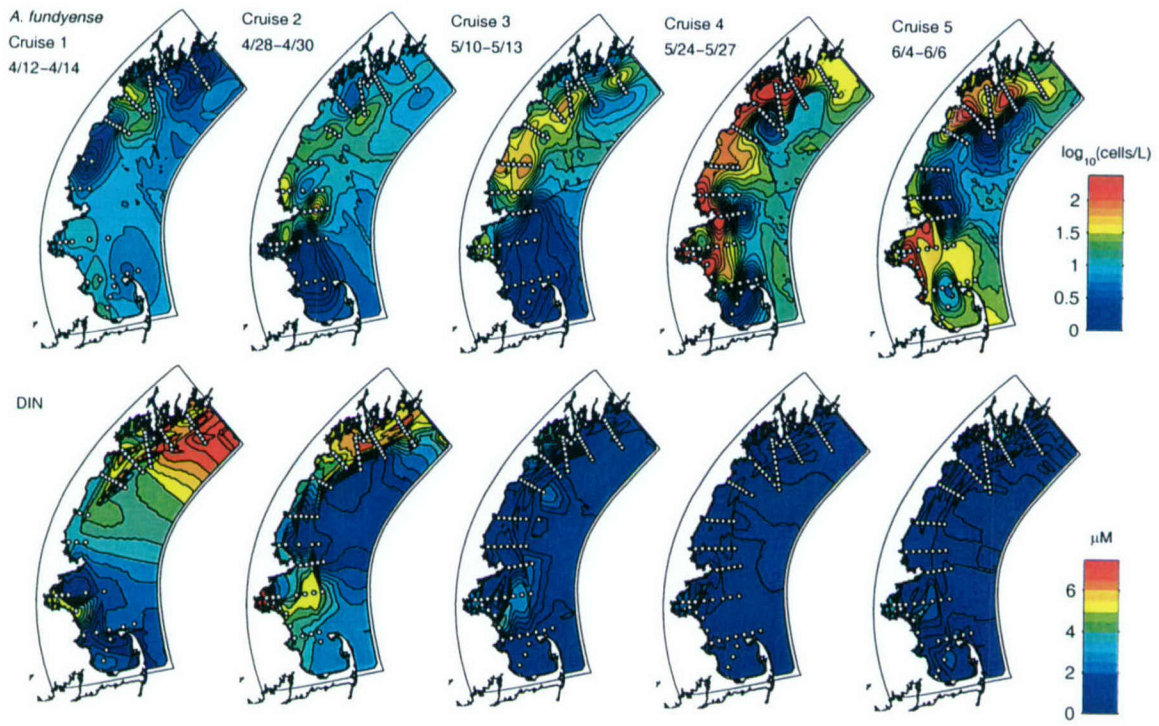


Figure 8: The RMRP field data. White circles are observation points. Columns correspond to cruises 1-5. **Top Panel:** The observed surface distribution of *A. fundyense* (cells/L on a $\log_{10}$ scale) during the spring 1993 RMRP surveys. The contour interval is 0.125. **Bottom Panel:** Surface dissolved inorganic nitrogen (DIN, µM) measured during the 1993 RMRP surveys. The contour interval is 0.5 µM. Nutrient ratios consistently suggest that nitrogen is limiting relative to phosphorous assuming Redfield Stoichiometry (Martorano and Loder, 1997)

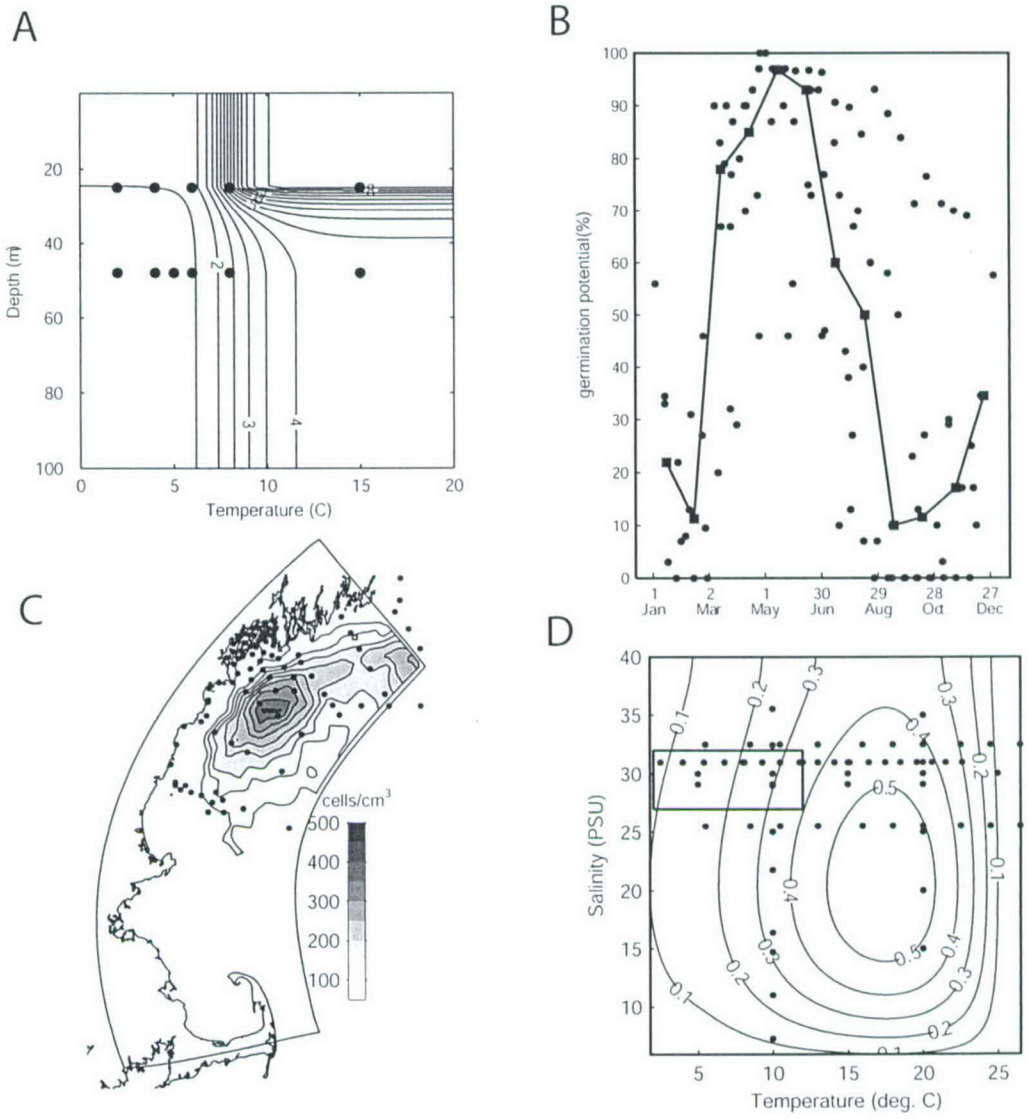


Figure 9 (A-D): The baseline biological model summary. In all plots, observations are shown as black dots. The germination rate is estimated as a function of temperature and light experienced by the resting cyst according to the laboratory derived relationship **A** (note that light has been translated to depth in the water column using a diffuse irradiance attenuation typical for Gulf of Maine waters). This rate is modified according to the germination potential **B**, which is controlled by an internal endogenous clock. The resulting rate is applied to a mapping of benthic cysts **C** to provide an estimate of the germination source. Once germinated, the cells swim up in the water column and grow according to the rates in panel **D** and a hyperbolic light/growth curve of the form suggested by Platt and Jassby (1976) for photosynthesis (not shown).

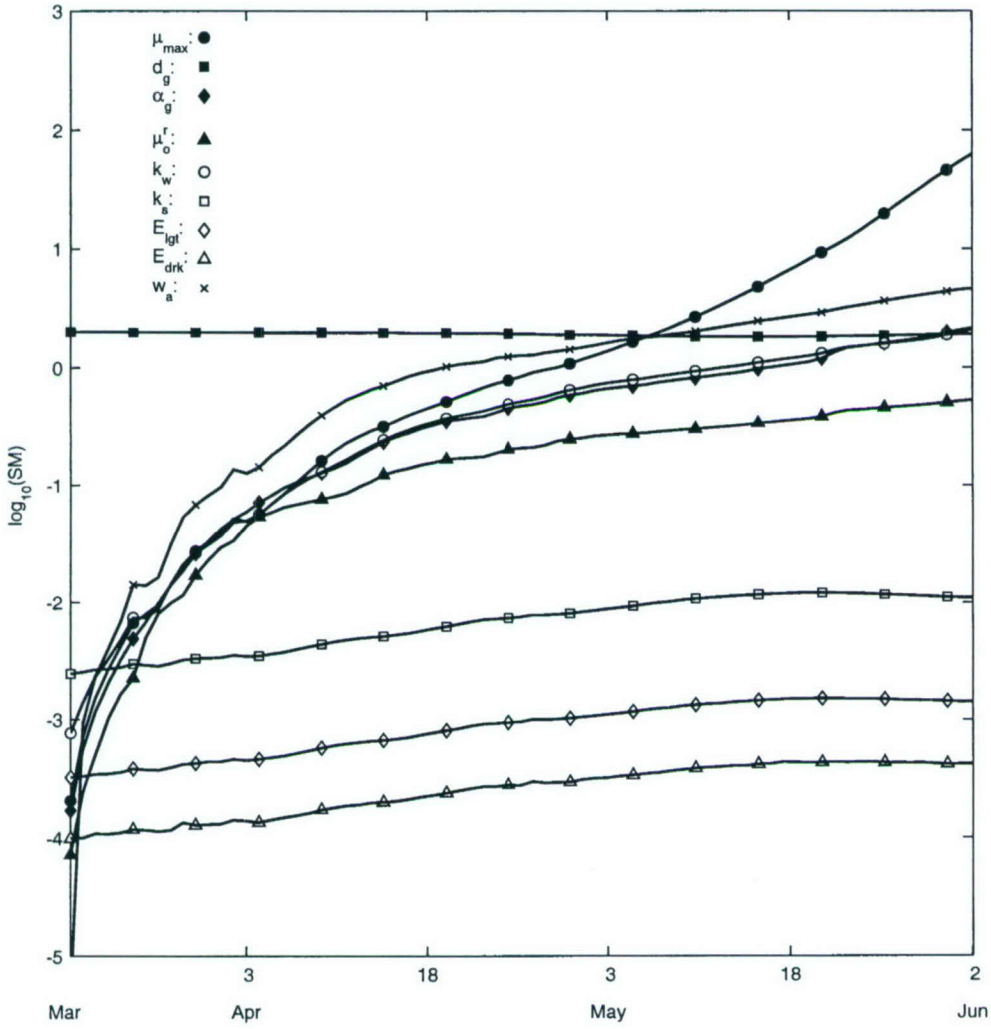


Figure 10: The baseline model sensitivity metric. The germination depth (d_g) dominates the baseline model sensitivity until early May, when it is eclipsed by the maximum growth rate.

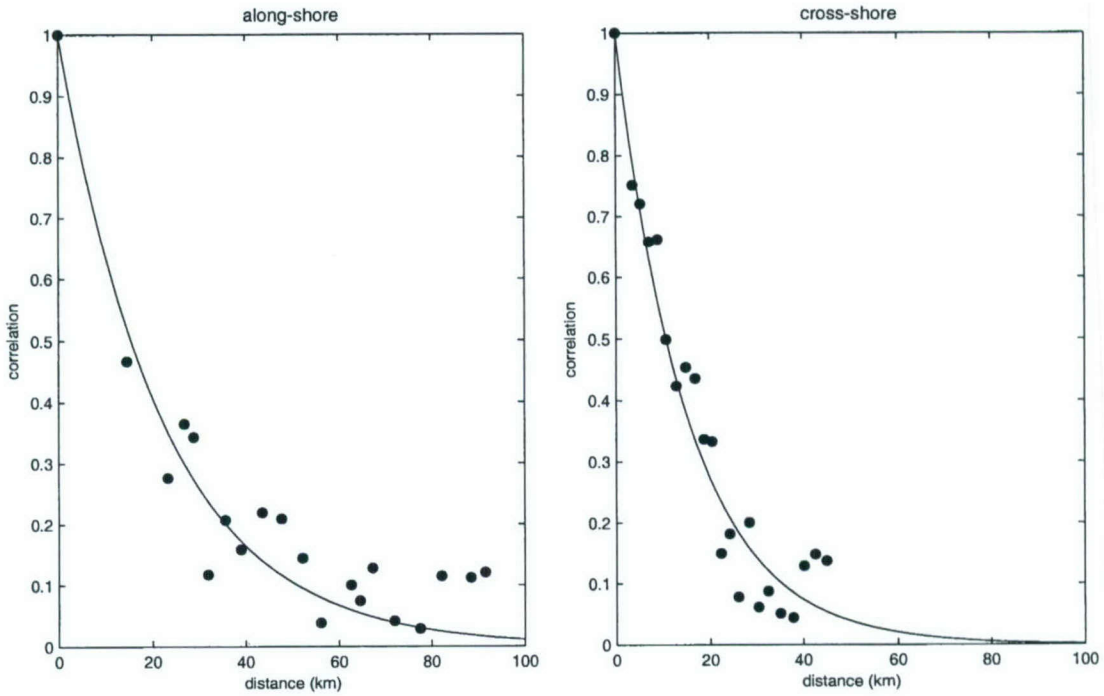


Figure 11: The along-shore (left panel) and cross-shore (right panel) autocorrelation functions for the $\log(y_i+1)$, where (y_i) is the observed concentration of *A. fundyense*. 500 pairs were used for for the along-shore bins, 250 for the cross-shore. Solid lines are an exponential fit to the autocorrelation data, with the along-shore decay -0.045 km^{-1} and the cross-shore -0.065 km^{-1}.

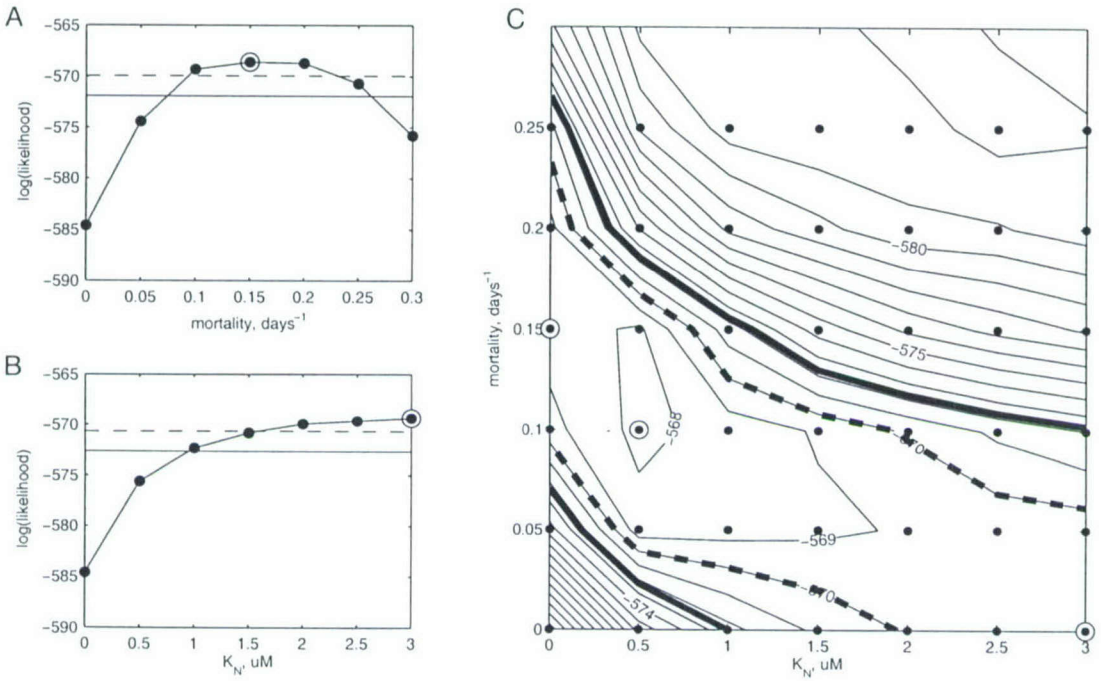


Figure 12: The MLRT results. **A.** Plot of log(L) for comparison of model structure II (mortality only) to structure I (the baseline model structure). Dots signify values of m where the likelihood was maximized. The maximum likelihood occurred at $m = 0.15$ day^{-1} (circled). The dashed horizontal line marks the 90% confidence limit, the solid horizontal line marks the 99% confidence limit. **B.** Plot of log(L) for comparison of nutrients only (structure III) to structure I. Markings are the same as in A. **C.** Contours (interval = 1) of log(L) as a function of K_N and m. The thick dashed line marks the border of the 90% confidence region. The thick solid line, marks the 99% confidence interval. The best simulation occurs at $K_N = 0.5$ μM, $m = 0.1$ day^{-1} (circled). The points along the ordinate are those from the mortality model structure. Those along the abscissa are from the nutrient model structure. Best simulations for each of these cases, as well as the baseline model (origin), are circled.

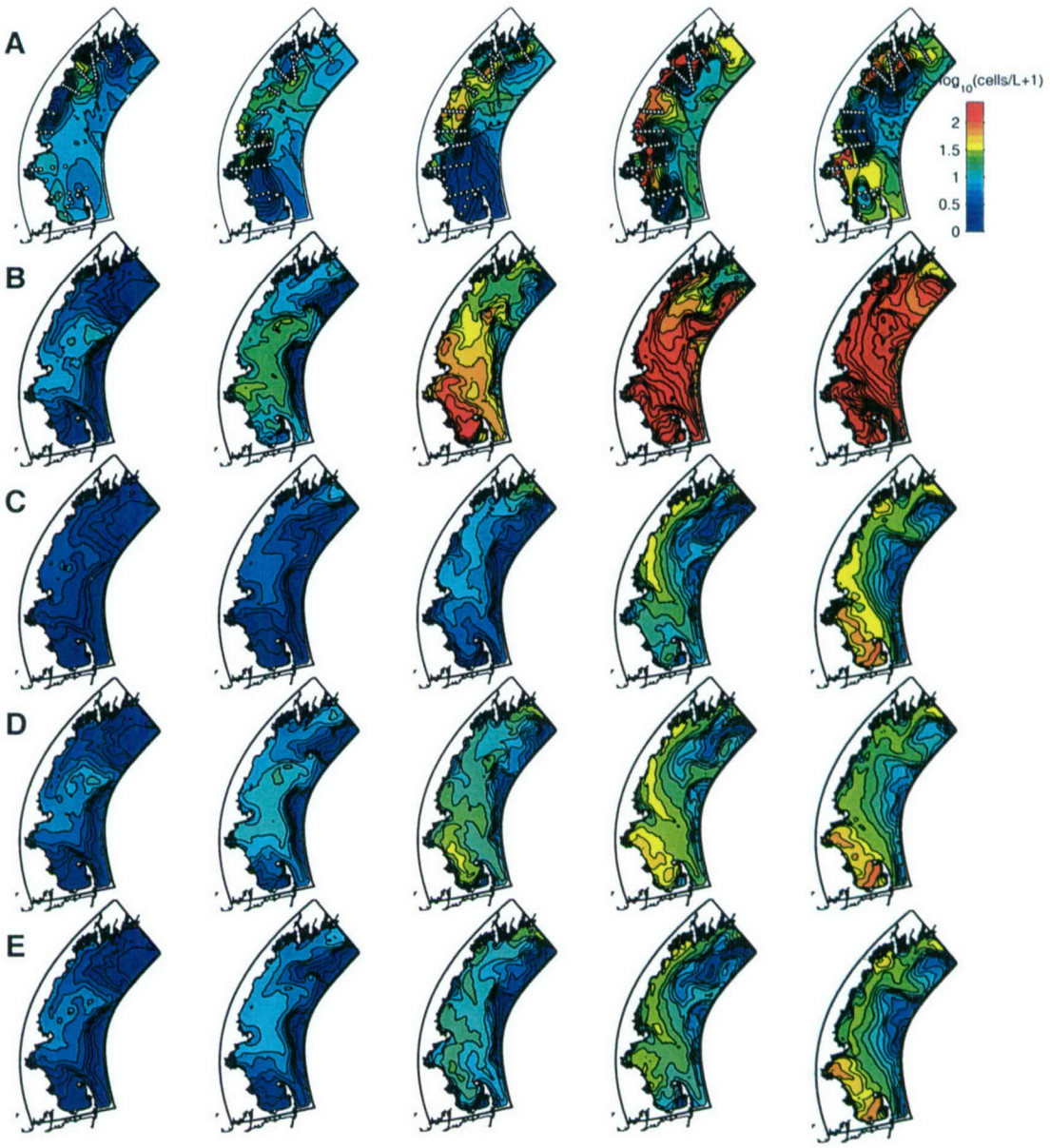


Figure 13: Surface *A. fundyense* observations and model output for each of the RMRP surveys. Cruises 1-5 go from left to right across the figure. All units are in $\log_{10}(cells/L+1)$. **Row A:** Mapping of the surface *A. fundyense* observations. **Row B:** The best results for the baseline model structure. **Row C:** The best results for the mortality only model structure. **Row D:** The best results for the nutrients only model structure. **Row E:** The best overall result using both nutrients and mortality.

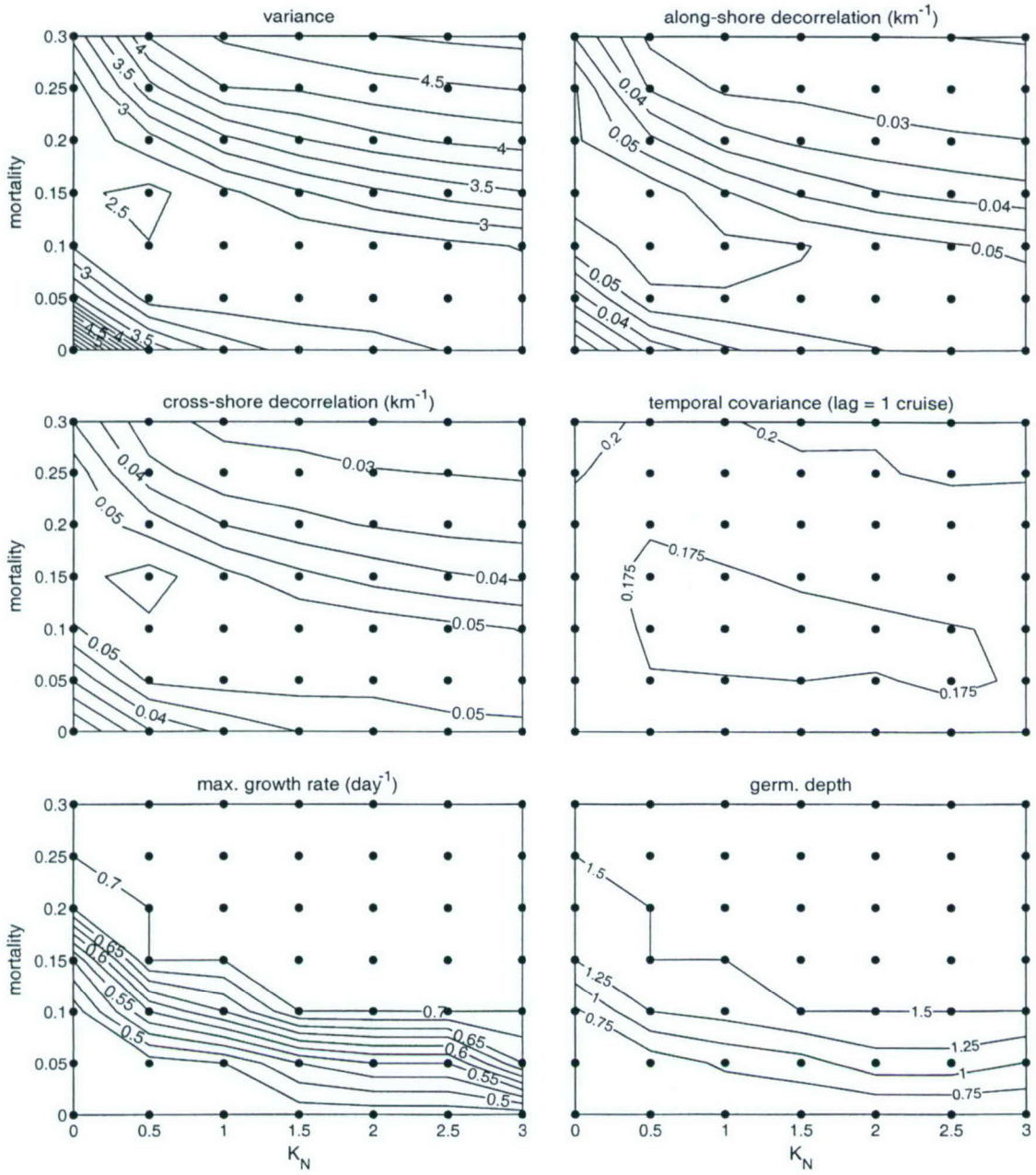


Figure 14: The properties of misfits for the 2D parameter space in Fig. 11c. Note that the maximum likelihood estimate ($\hat{m} = 0.10\,\text{day}^{-1}$, $\hat{K}_N = 0.5\,\mu\text{M}$) and the minimum variance estimate ($\hat{m} = 0.15\,\text{day}^{-1}$, $\hat{K}_N = 0.5\,\mu\text{M}$) do not coincide precisely due to the action of the spatial and temporal covariance.

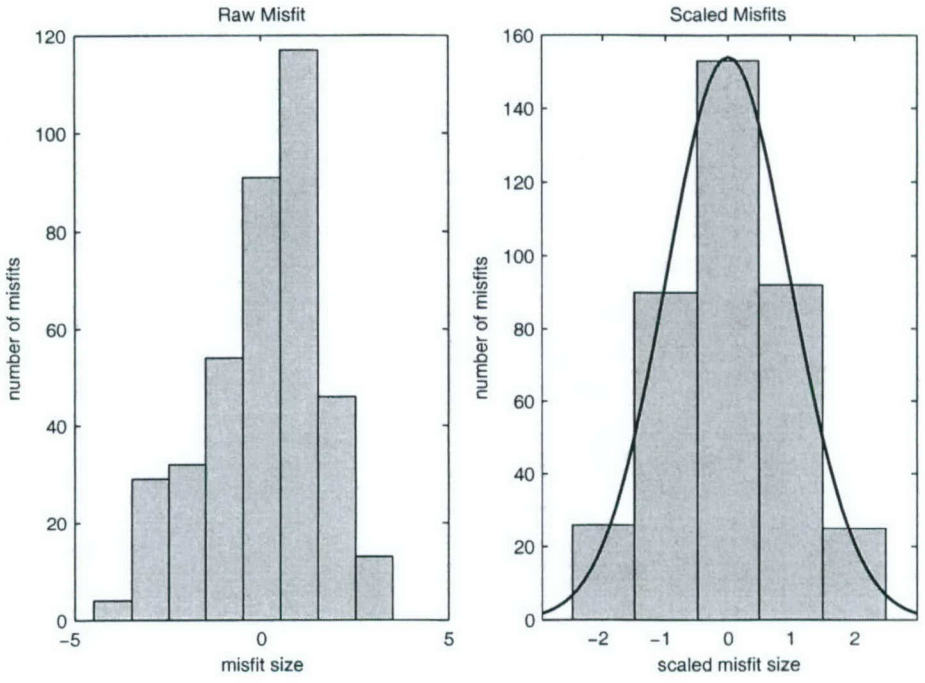


Figure 15: The left plot shows a histogram of the misfits associated with the optimal run. The right plot shows those same misfits after scaling by the covariance matrix. If the statistical representation has adequately described the primary features of the model/data misfits, the scaled misfits will be normally distributed with mean 0 and a variance of 1 (solid line in second panel).

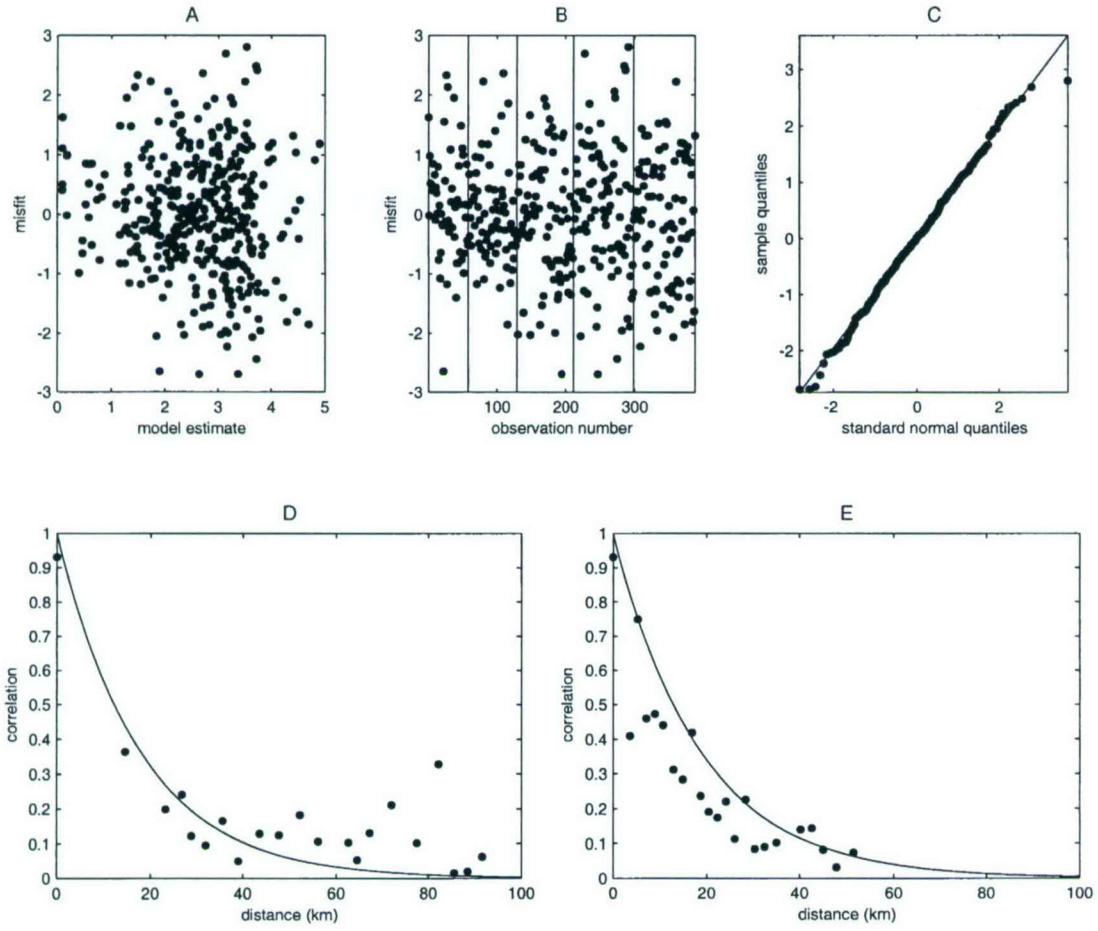


Figure 16: Misfit model diagnostics. **A:** plot of scaled misfit versus $\hat{y}$ to detect variation in the error model as a function of the modeled value. **B:** Plot of the misfit versus the order in which the observations were taken. Vertical lines delineate the boundaries between different cruises (cruise 1 = 1-58, cruise 2 = 59-128, cruise 3 = 129-211, cruise 4 = 212-298, cruise 5 = 299-386). **C:** Probability plot of the scaled residuals. **D:** Plot of the residual autocorrelation for points oriented in the along-shore direction (0-30°) based on local bathymetry followed by the model grid (•) and the along-shore decay estimated by the m.l.e. (black line r_y = -0.0566 km^{-1}). **E:** Plot of the residual autocorrelation for points oriented in the cross-shore direction (30-90°) based on the local bathymetry followed by the model grid (•) and the cross-shore decay estimated by the m.l.e. (black line, r_x = -0.0541 km^{-1}).

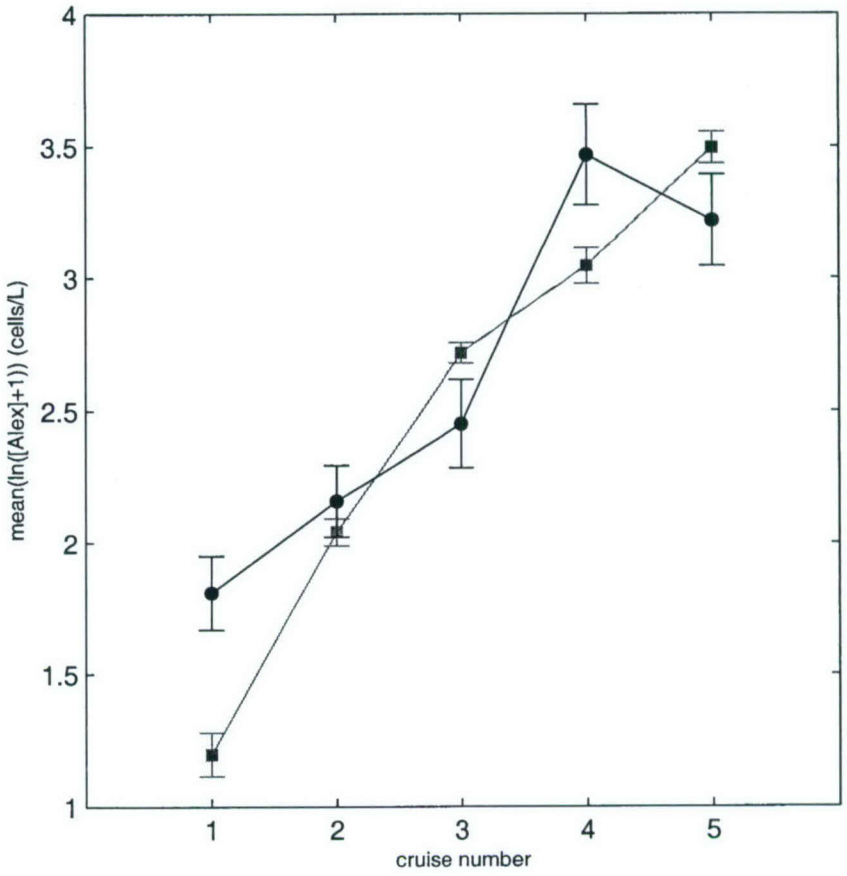


Figure 17: Plot of the observed mean cruise magnitude (•) versus the modeled mean cruise magnitude (■) for each of the 5 surveys. Bars delineate standard deviations in the sample mean.

Chapter 3

Evaluating Hypotheses for the Initiation and Development of *Alexandrium fundyense* Blooms in the Western Gulf of Maine using a Coupled Physical-Biological Model

Submitted to Deep Sea Research, Part II

Charles A. Stock, Dennis J. McGillicuddy, Andrew R. Solow, Donald M. Anderson

Abstract

A coupled physical/biological model and observations are used to investigate the factors governing the initiation and development of an *Alexandrium fundyense* bloom in the western Gulf of Maine (WGOM) during the spring of 1993. The physical circulation is simulated using a 3D primitive equation model forced by climatological sea surface elevation and observed winds, irradiance, and river outflow. This is coupled with a biological model constructed from laboratory and field data that estimates the germination and growth rates of *A. fundyense* as a function of environmental conditions. Four biological model structures of increasing complexity are considered, with each structure representing a hypothesis for factors controlling bloom initiation and development. The model/data fit is optimized over the uncertainty in the parameters to which the model is most sensitive. The significance of changes in the model/data fit between model structures is quantified using a maximum likelihood ratio test.

The baseline biological model, which parameterizes growth as only a function of temperature, salinity, and light, severely over-estimates observed *A. fundyense* abundance in the late spring. It is thus rejected with greater than 99% confidence in favor of biological models that include a mortality term or a dependence of growth on dissolved inorganic nitrogen (DIN). The overall best-fit simulation uses both nitrogen dependence and mortality. However, simulations using one or the other of these factors could not be differentiated from the best-fit case with greater than 90% confidence. The best-fit model captures the general timing and magnitude of the observed bloom and some of its secondary features. However, considerable misfits may exist in the point-to-point comparison, and some regional misfits remain. Diagnosis of the cell budget suggests that germination from a large cyst bed offshore of Casco Bay provides the majority of cells comprising spring *A. fundyense* populations within the WGOM. The size of the modeled bloom is largely set by the size of this cyst-driven source. Transport of cells from the eastern Gulf of Maine becomes increasingly important later in the spring, and this may be the dominant source of cells in the summer. Net growth of the modeled *A. fundyense* populations is first limited by low water temperatures and then by the combined influence of nitrogen and mortality. This results in low domain-averaged net growth rates (< 0.05 day^{-1}) throughout much of the simulation. However, rates were often elevated locally and therefore added notable spatial structure to the bloom. Primary uncertainties within the biological model include spatial and temporal variability in mortality, and the influence of sediment dynamics on the size and spatial character of the cyst driven source. The approach presented here can be extended to evaluate increasingly complex biological models as additional thresholds and rates are understood. At each step, the likelihood ratio test can determine the degree to which added biological complexity is supported by available data.

1. Introduction

Blooms of the toxic dinoflagellate *Alexandrium fundyense* are annually recurrent phenomena in the Gulf of Maine during the spring and summer months. Toxins produced by *A. fundyense* lead to paralytic shellfish poisoning (PSP), a potentially fatal illness caused by consumption of shellfish from exposed regions. This public health risk necessitates rigorous monitoring of potentially affected areas and has lead to repeated closures of shellfish beds along the coast and in the offshore waters of the Gulf of Maine (Shumway, et al., 1988). Within the marine food web, PSP has been linked to mortality of larval and juvenile stages of fish (White, et al., 1989), and even the death of marine mammals such as humpback whales (Geraci, et al., 1989). An understanding of the factors that determine the distribution and abundance of *A. fundyense* within the Gulf of Maine is therefore of considerable scientific, economic, and public health interest.

The Gulf of Maine (Fig. 1) is a continental shelf sea separated from the North Atlantic by a series of shoals. In the spring, density contrasts between high salinity slope-water within the Gulf's three deep basins and fresher coastal waters derived from the Scotian Shelf and local river input drive a mean counter-clockwise coastal surface current (Brooks, 1985). This feature, referred to as the Maine Coastal Current (MCC), is characterized by a series of segments and branch points (Lynch, et al., 1997). The direction of flow at the branch points is modulated by a diverse set of factors including wind, river input, bathymetric effects, and the strength of the geopotential low that generally forms over Jordan Basin in response to dense slope water in its interior (Brooks and Townsend, 1989, Brooks, 1994, Lynch, et al., 1997, Pettigrew, et al., 1998). *A. fundyense* blooms within the coastal region to the south and west of Penobscot Bay, herein referred to as the western Gulf of Maine (WGOM), are considered in this study.

The region to the northeast is referred to as the eastern Gulf of Maine (EGOM). The segment of the coastal current within the WGOM if referred to as the WMCC, while the segment to the east is referred to as the EMCC.

Blooms of *A. fundyense* occurring in spring within the WGOM exhibit patterns in distribution and abundance largely consistent with the "plume advection hypothesis" (Franks and Anderson, 1992a, Anderson, et al., 2004a). This hypothesis calls for the WMCC driven transport of established populations of *A. fundyense* from the northeast to the southwest in close association with the buoyant plume of the Kennebec/Androscoggin River. Downwelling favorable winds accelerate the along-shore transport and trap the plume and associated cells against the coast. Upwelling favorable winds move the plume and cells offshore. An *A. fundyense* source is invoked in the Casco Bay region or further northeast. Patterns in shellfish toxicity show a mean progression from the Casco Bay area to the south that is consistent with this dynamic (Franks and Anderson, 1992b).

Extensive *A. fundyense* surveys undertaken in the WGOM during the spring of 1993 (Anderson, et al., 2004a) provide an additional means of testing the plume advection hypothesis and to further explore the underlying dynamics. However, strong advective and mixing processes in the WGOM can produce a geographic separation between observed *A. fundyense* populations and their source regions. This makes the underlying bloom dynamics difficult to understand from survey data alone. In this study, a coupled physical/biological model is used to investigate the dual influence of biological rates and physical transport on the observed *A. fundyense* distribution. The physical component of the model provides an estimate of the currents and hydrography, while the

biological component provides an estimate of the germination and net growth rates of *A. fundyense* as a function of environmental conditions.

Considerable uncertainty exists within the biology, and five potential biological model structures are considered (Table 1). The first four structures are nested: the more complex model structures reduce to the more simple cases when specific parameter values are chosen. The first structure is the baseline case, which poses net growth as only a function of temperature, light, and salinity. The next two structures build upon the baseline model by adding the possibility of mortality and nutrient dependence respectively. The fourth considers nutrients and mortality in combination. The fifth case, that of zero net-growth imposes the condition that growth and mortality processes are in perfect balance, resulting in zero net-growth throughout the domain at all times. This is a limiting case that will be used to aid in understanding the role that growth and mortality processes play in determining the magnitude and spatial/temporal characteristics of the bloom. The fact that this is not within the nested set of models structures has statistical consequences that will be discussed.

Each of these biological model structures constitutes a different hypothesis for the factors controlling the initiation and development of *A. fundyense* blooms in the WGOM. Hypotheses are evaluated through a quantitative, statistical comparison of model results with 1993 survey data. The goal is to identify a set of dynamics capable of recreating the general timing and magnitude of bloom events, not the detailed structure of the bloom. The steps are summarized as follows:

1. The model/data fit is optimized for each hypothesized biological model structure over the uncertainty in the parameters to which the model is most sensitive.

2. A maximum likelihood ratio test is used to evaluate the significance of changes in the optimal model/data fit.
3. A simpler model structure is rejected in favor of that which is more complex if the improvement gained by adding an additional factor or factors is statistically significant.
4. Simulations are assessed and diagnosed to gain insight into bloom dynamics.

Model diagnosis focuses on identifying the primary source of *A. fundyense* cells contributing to spring toxicity in the WGOM and on elucidating the factors controlling bloom development. It is stressed that the methodology outlined above and described in detail below is iterative in nature. The model/data misfits encountered under the most basic hypothesis considered herein suggest possible alternatives that may better explain the observations. In a like manner, the model/data misfits remaining at the conclusion of this analysis will be discussed, as they suggest avenues for further model improvement.

2. Methods

2.1 The Field Data

A field program including 5 ship surveys and mooring deployments carried out in 1993 provides the observational basis for this study (Anderson, et al., 2004a, Geyer, et al., 2004). The duration of each survey was 2-3 days and they were spaced approximately 2 weeks apart (April 12-14, April 28-30, May 10-13, May 24-27, June 4-6). *A. fundyense* cell counts were taken at the surface (Fig. 2, top panel) and, for ~75% of the stations, at 10 meters. Hydrographic and nutrient data, including phosphate, silicate, nitrate, nitrite, and ammonium (Martorano and Loder, 1997), was also collected.

Nutrient ratios consistently suggest dissolved inorganic nitrogen (Fig. 2, bottom panel) to be limiting relative to phosphorous assuming Redfield stoichiometry. Currents were measured at a mooring near Cape Porpoise (Fig. 1) using a vector-measuring current meter (VMCM) at 5 meters, and vector-averaging current meters (VACM) at 27 and 50 meters. The near surface measurements required a 25° clockwise rotation to correct for compass error believed to be due to interference with battery packs in adjacent sensors (see Geyer at al., 2004 for details). The correction has a minor influence on the along-shore flow, but the offshore component should be treated with caution.

2.2 The Physical Model

The circulation is modeled using the Estuarine, Coastal and Ocean Model (ECOM) (Blumberg and Mellor, 1987). This model solves the primitive equations using finite differences on a curvilinear orthogonal grid. ECOM has been used extensively to model coastal and estuarine flows (Blumberg, et al., 1993) and has previously been applied in the Gulf of Maine region (Signell, et al., 1993, McGillicuddy, et al., 2003). The model configuration is essentially that used in McGillicuddy et al. (2003). The study domain (Fig. 1) is covered by a grid of 130 cells in the alongshore direction and 70 in the cross-shore. Grid cells range in size from 1.5-3 km. 12 sigma layers (i.e. each layer is a constant fraction of the water depth) are specified in the vertical with increased resolution near the surface in order to better resolve river plume dynamics. Vertical mixing is calculated with the Mellor-Yamada level 2.5 turbulence closure (Mellor and Yamada, 1982, Galperin, et al., 1988), and horizontal mixing is calculated using the method of Smagorinsky (1963).

Forcing (Table 2, Fig. 3) was chosen to capture the principle aspects of the large-scale circulation and hydrography in the WGOM, particularly the transport associated with the WMCC and the vernal warming of surface waters. The duration of the simulation is from March 19 - June 6. In addition to heat flux calculations described in Table 2, surface temperature fidelity is ensured by relaxing toward the observed sea surface temperature using an additive term proportional to the difference between modeled (T) and observed (T_{obs}) surface temperatures (Ezer and Mellor, 1992, He and Weisberg, 2002):

$$Q = Q_{calc} + \rho_w c_p C(T - T_{obs})$$

Where Q_{calc} is the heat flux (watts/m^2) calculated by the bulk formulae, ρ_w is the water density, c_p is the specific heat of sea water at constant pressure, and C is a constant, which is given a value of 2 m/day. The observed surface temperatures are provided by 11 maps covering the simulation period constructed from 8 day best AVHRR Oceans Pathfinder SST (PO.DAAC, (1985)) satellite data using the objective analysis algorithm of Bretherton et al. (1976) as implemented by Hendry and He (1996).

2.3 The Biological Model

Alexandrium species are characterized by a complex life cycle that includes both a resting cyst and a vegetative cell (Anderson, 1998). The transition between resting and vegetative stages occurs through the process of germination. The biological model used in this study and described in detail below is a single component model containing parameterizations of *A. fundyense*[3] germination, as well as subsequent growth and

[3] It is recognized that two forms of *Alexandrium* can be responsible for shellfish toxicity in the WGOM: *A. tamarense* and *A. .fundyense*. We consider these to be varieties of the same species(Anderson, et al., 1994,

swimming behavior (summarized in Table 3 and Fig. 4). Ecosystem effects on *A. fundyense* abundance are parameterized through approximations of their influence on the rates within the *A. fundyense* population dynamics model. The biological model is necessarily simplified, and it is not expected that all scales of variability within the *A. fundyense* bloom will be reproduced. This is consistent with the goals of the analysis (i.e. recreating the timing and magnitude of the bloom events). Neglected complexity should be considered intrinsic to the hypotheses: neglect is equivalent to the assumption that the importance of a given process is of second order relative to those included at the space and time scales of interest. Model data misfits may then be analyzed in light of this neglected complexity and new hypotheses formulated.

2.3.1 Germination

Rates of *A. fundyense* cyst germination are regulated by an endogenous circannual clock (Anderson and Keafer, 1987) and by a suite of environmental factors including temperature (Anderson, 1980), light, and oxygen, the absence of the latter preventing germination entirely (Anderson, et al., 1987). The construction of a germination function based on laboratory and field data is described in detail in Anderson et al. (submitted). Briefly, laboratory data was used to estimate cyst germination rates (G) as a function of bottom water temperature (T) and non-spectral irradiance (E) (Fig. 4A). The influence of the endogenous clock was accounted for by multiplying the germination rate by an endogenous clock factor (EC, Fig. 4B), which is the ratio of the germination potential at any time (t) relative to the maximum potential:

Scholin, et al., 1995). Neither antibody nor oligonucleotide probes can distinguish between them, only detailed analysis of the thecal plates on individual cells can provide this resolution. *A. fundyense* is therefore used to refer to both forms.

$$G(T,E,t) = EC(t) \times G(T,E)$$

The irradiance experienced by the cysts is the end result of exponential attenuation within the water column and within the sediment (decay coefficients k_w and k_s respectively). The rate is then averaged over the estimated depth of sediment (d_g) assumed oxygenated and over which newly germinated cells can reach the water column during the bloom season. This "germination depth" was estimated using the penetration of short-lived isotopes, cyst fluorescence measurements, and biochemical measurements within the sediment (see Anderson, et al., submitted), and a range from 0.5-1.5 cm is considered.

The resulting germination function is applied to a map of the cyst concentration within the top 1 cm of sediment from surveys taken between 1997 and 2003 (Fig. 4C). The vast majority of the cyst measurements were taken in 1997, and it is assumed that the primary features of the cyst map are robust over the 4 years separating the cyst and RMRP surveys (see supporting discussion in Anderson et al. (submitted) and McGillicuddy et al. (submitted)). The resulting flux (F_g) of cells from germination is:

$$\mathrm{F_g} = \int_o^{d_g} G(T,E(z),t) \times [Cysts/cm^3]_o \, dz$$

where $[Cysts/cm^3]_o$ is the initial concentration of cysts in the top centimeter. The flux was calculated relative to the initial number cysts to be consistent with the laboratory experiments upon which they were based. It is notable that the validity of the above expression requires the assumption that the cyst concentration is uniform over the top 1.5 cm. This is justified based on the high correlation (0.85) and the similar mean concentrations (87 cysts/cm^3, 106 cysts/cm^3) of cysts from the 0-1 cm and 1-3 cm sediment layers within the study domain.

2.3.2 Swimming

Newly germinated cells swim upward at w_a m/day (Table 3) until the mean depth of the 1% light level ($z_1 = 21$ meters) is reached. It is assumed that there is no cell mortality during this transit. Above this level, diminution of the vertical swimming speed to the natural boundary condition of $w_a = 0$ at $z = 0$ is specified in order to match the observed vertical distribution of *A. fundyense*. The ratio of the mean abundance at the surface to that at 10 meters for stations with abundance measurements at both depths (~75%) is 2:1 and there is a strong correlation between the measured abundances at the two depths for the same station (correlation coefficient of 0.71 after log transformation). It was found that attenuating the swimming speed with:

$$w_a(z < z_1) = w_a(z > z_1) \times \left(1 - \tanh\left(\frac{(z_1 - z)}{10}\right)\right)$$

produced ratios of mean surface to mean 10 meter abundance between 1.75:1 and 2.25:1 for a broad range of biological model parameter values. More complex migration strategies have been observed for *A. fundyense* (Anderson and Stolzenbach, 1985, MacIntyre, et al., 1997, Cullen, et al., submitted). However, in the WGOM, *A. fundyense* have not been observed to engage in strong coordinated migrations either in the laboratory or the field (Poulton, 2001, Cullen, et al., submitted) so such behavior is omitted here.

2.3.3 Growth

The *A. fundyense* growth function is dependent on temperature (T), salinity (S), non-spectral irradiance (E) and, for model structures containing nutrient dependence, the DIN concentration. The temperature dependence was formed by fitting a cubic

polynomial to *A. fundyense* growth data collected for different isolates in the region (R^2 = 0.79, see Table 3 for references). This function was then normalized to form a factor between 0-1 that expresses the degree of temperature limitation relative to the maximum growth observed:

$$f(T) = -0.000513T^3 + 0.0160T^2 - 0.0867T + 0.382 \qquad T > 5^o C$$
$$f(T) = 0.283 - 0.0343(5 - T) \qquad T < 5^o C$$

The linear extrapolation below 5° C was used to prevent irregular extrapolation in regions not well constrained by data. The salinity dependence was formed in a similar way (R^2 = 0.45):

$$f(S) = 0.0000882S^3 - 0.00808S^2 + 0.220S - 0.872$$

These two factors scale the light and nutrient saturated growth rate at optimal temperature and salinity, $\mu_{max}(T_{opt}, S_{opt})$, to determine the light saturated growth rate at any T, S (Fig. 4d):

$$\mu_{\max}(T,S) = \mu_{\max}(T_{opt}, S_{opt}) \times f(T) \times f(S)$$

The light dependence takes the form suggested by Platt and Jassby (1976) for photosynthesis- irradiance relationships and used by Langdon (1987, 1988) in studies of phytoplankton growth (see Table 3 for definitions and units):

$$\mu(E,T,S) = \left(\mu_{\max}(T,S) + \mu_o^r\right)\tanh\left(\frac{\alpha_g E}{(\mu_{\max}(T,S) + \mu_o^r)}\right) - \mu_o^r$$

Nutrient dependence is modeled by the Monod formulation with half-saturation K_N:

$$\mu(DIN,T,S) = \mu(T,S) \times \frac{[DIN]}{K_N + [DIN]}$$

The dependence of the growth rate on the ambient DIN concentration within this formulation can be problematic in unsteady conditions due to potential variability in

nitrogen uptake physiology and the internal nitrogen cell quota (e.g. Conway and Harrison, 1977, Droop, 1983). Such variability has been observed in *Alexandrium* species (Flynn, et al., 1996). However, while the Monod formulation is limited in its ability to represent detailed nitrogen metabolism, it is valid for assessing the average level of the dependence of growth on ambient DIN and should be interpreted in this way. The range of K_N considered herein was chosen to encompass the range of half-saturation constants for nitrogen dependent growth and uptake commonly encountered in the phytoplankton literature (Table 3). The limiting case of $K_N = 0$ μM asserts that *A. fundyense* is not significantly DIN limited during the simulation period.

The evolution of the DIN field is specified based on survey data (i.e. fig. 2b). This is justified on the basis that typical peak *A. fundyense* cell concentrations in the WGOM (~10^2-10^3 cells/L) are small relative to the total abundance of other phytoplankton species (~10^4-10^6 cells/L without inclusion of nano or picoplankton abundance (Marshall, 1984)) and therefore contributes little to the large scale nutrient evolution. A linear interpolation is used to specify nutrients at times between cruises. The most limiting factor of light or nutrients determines the ultimate growth rate as per Liebig's law of the minimum (Liebig, 1845):

$$\mu(E, DIN, T, S) = \min\left(\mu(E, T, S), \mu(DIN, T, S)\right)$$

2.3.4 Mortality

Mortality (m) is defined loosely here as a vegetative cell being removed from the water column. It is meant to represent the losses of *A. fundyense* by cell mortality, zooplankton grazing, and encystment. Grazing losses inflicted on *A. fundyense* are a complex function of both the heterotrophic and autotrophic communities (Teegarden and

Cembella, 1996, Turner and Tester, 1997). Encystment is generally thought to occur in response to adverse environmental conditions and has been triggered by nutrient limitation in the laboratory (Anderson, et al., 1984, Anderson and Lindquist, 1985). However, the precise thresholds and rates for nutrient driven encystment have been difficult to characterize, and it has been equally difficult to observe in the field (Anderson, 1998). Mortality is therefore applied as a constant average rate (day^{-1}). The intent of applying mortality in such a rudimentary way is to evaluate the necessity of a first order loss term to recreate the observed bloom magnitude, given knowledge of the source and growth characteristics. The range in Table 3 is chosen to allow the possibility of negligible mortality rates to rates that would overcome all but very swift growth. The hypotheses containing this term assume that space/time variability in mortality during bloom initiation and development is of secondary importance to this overall mean rate.

2.4 The Coupled Model

The final equation governing the evolution of *A. fundyense* within the domain is:

$$\frac{\partial C}{\partial t} + \nabla \cdot \left((v + w_a) C \right) = \nabla \cdot K \nabla C + \mu C - mC + F_g$$

Where C is the concentration of *A. fundyense*, v is the fluid velocity, K is the diffusivity. The initial concentration of *A. fundyense* is set to 0 everywhere, as the beginning of the run (March 19) is generally before the start of the bloom season. Observed cell concentrations along the northern-most transect are extrapolated onto the northern boundary to provide the EGOM inflow condition. Concentrations along the other boundaries are assumed 0. Interior concentrations are advected out during outflow, and boundary concentrations are relaxed back to the specified values during subsequent

inflows. Time scales for this relaxation were chosen to represent the relative duration of outflow events (0.5 along the northern boundary, 2 days along the eastern boundary, and 4 days to the South).

2.5 Model/Data comparison

2.5.1 The Statistical Description of the Model/Data Misfit

Evaluation of model simulations is done through a point-to-point comparison between the model results and the surface observations in a manner closely related to least squares. Given that *A. fundyense* concentrations vary over several orders of magnitude, it is expected that the model/data misfit (ε) will exhibit exponential properties:

$$\varepsilon_i = \ln(c_{obs,i} + 1) - \ln(c_{\mathrm{mod},i} + 1)$$

where $c_{obs,i}$ is the observed *A. fundyense* concentration at point i, and $c_{mod,i}$ is the model output (in cells/L). One was added to all values so that zero cell concentrations can be included in the analysis. Misfits between any two simulations using different combinations of parameters ($\theta_1 ... \theta_N$, Table 3) are compared based on their relative likelihood (L), which takes account of both the misfit magnitude and spatial and temporal properties:

$$L(\theta_1 .... \theta_n ; \varepsilon) = \frac{\exp(-\frac{1}{2} \times \varepsilon^T C_{\varepsilon\varepsilon}^{-1} \varepsilon)}{(2\pi)^{M/2} \sqrt{\det(C_{\varepsilon\varepsilon})}}$$

This is the joint normal probability for a set of model/data misfits (e.g. Wunsch, 1996). In this case, ε is a vector of $M = 386$ misfits, T is the transpose, "det" is the determinant, and $C_{\varepsilon\varepsilon}$ is the spatial/temporal covariance matrix. The central diagonal of the covariance

matrix contains the misfit variance (σ^2). Spatial covariance between any two misfits *i,j* is represented with exponential decay terms in the along-shore (r_x) and cross-shore (r_y) directions:

$$C_{ij} = \rho_{\Delta t} \times \sigma^2 \times \exp\left(-r_y \times \sqrt{\Delta y^2 + \left(\frac{r_x}{r_y} \Delta x \right)^2} \right)$$

The possibility of temporal correlation is introduced with the factor $\rho_{\Delta t}$. The roughly equal bi-weekly spacing of the cruises makes it possible to use the number of cruises separating any two observations as a proxy for temporal lag. Thus, $\rho_{\Delta t=1}$ corresponds to the correlation between points at the same spatial location, but separated by 1 cruise. For points taken during the same cruise, this factor ($\rho_{\Delta t=0}$) has a value of 1. Only correlations between points separated by 1 or 2 cruises are considered herein. The parameters describing the covariance matrix (σ^2, r_{as}, r_{cs}, $\rho_{\Delta t=1}$, and $\rho_{\Delta t=2}$) are chosen to maximize *L* for the set of misfits produced by each choice of the biological model parameters using a simplex parameter space search (Press, et al., 1985). Multiple starting points were used to test for the presence of local minima and no such occurrences were found. Increasing likelihood is marked by decreasing misfit variance and spatial/temporal misfit scales, revealing the close relationship between maximum likelihood and least squares minimization. This also highlights the objective determination of the misfit scales that the likelihood approach provides. Quantification of the misfit scales and their relationship to the explicitly resolved scales of motion in the physical model provides useful information when considering further biological model improvement relative to limitations of the physical simulation and observations.

The choice of a statistical description for the misfit can rarely be done on purely theoretical grounds. Other descriptions could be chosen, and some objective measure of the ability of the statistical description to represent the primary features of the model/data misfits is needed. One means of doing this is by inspection of the scaled misfits: $C_{\varepsilon\varepsilon}^{-1/2} \times \varepsilon$. If the statistical description is appropriate, the scaled misfits will be normally distributed with mean 0, variance 1. This condition is robustly met (e.g. Fig. 5). Additional discussion of the verification of the misfit model is given in Chapter 2.

2.5.2: Optimization over the Biological Model Parameters

To compare the performance of the different model structures in Table 1, the likelihood (L) of the misfits must be maximized over the uncertainty in the biological model parameters included within each structure. The search for optimal parameter values was carried out manually with a large set of numerical simulations. Due to the large number of parameters, it is not practical to systematically evaluate the entire range of parameter space. The optimization process was therefore restricted to parameters to which the model was most sensitive. These parameters were identified using the bulk sensitivity metric:

$$SM(t) = \frac{\left(\iiint_{domain} C(x,y,z,t)dxdydz \right)_{\theta=\theta_{high}}}{\left(\iiint_{domain} C(x,y,z,t)dxdydz \right)_{\theta=\theta_{low}}}$$

where C is the concentration of *A. fundyense*. Multiplied by 100, this factor is the percent change in the total number of cells in the domain induced by varying each parameter θ (Table 3) from the value producing the lowest *A. fundyense* abundance (θ_{low}) to the

value producing the highest (θ_{high}). Uncertainty in two parameters: μ_{max} and d_g, generally controls greater than 90% of the variability in this metric for the baseline model (Fig. 6). The likelihood was thus maximized only over the uncertainty in μ_{max} and d_g for the baseline model, m was added for the mortality only case, K_N for nutrients only, and K_N and m for mortality and nutrients. The remaining biological model parameters are given central values within their uncertainty range.

2.5.3 Testing Hypotheses: The Maximum Likelihood Ratio Test

The maximum likelihood ratio test (MLRT) is used to estimate the significance of differences in the optimal fit for the different model structures. The test compares the likelihood associated with a null hypothesis (L_o) that purports specific values of one or more of the biological model parameters, to the likelihood associated with an alternative (L_1) that allows one or more of the biological model parameters set by the null hypothesis to vary over their uncertainty. For example, in comparing model structures with and without mortality, the following ratio is formed:

$$\lambda = \frac{L(\mu_{\max}, d_g, m = 0; \varepsilon)}{L(\mu_{\max}, d_g, m; \varepsilon)} = \frac{L_o}{L_1}$$

Note that the parameter space in the denominator of the ratio has an additional degree of freedom – the alternative hypothesis is the more complex model structure. As such, the maximum likelihood in the denominator will be at least as large as that of the numerator. As this ratio becomes much less than 1, the null hypothesis becomes less likely than the alternative, and rejection of the null hypothesis is supported.

The degree of significance with which the null hypothesis can be rejected is estimated by invoking the properties of the MLRT for large sample sizes. It can be shown (Cox and Hinckley, 1974) that, if the null hypothesis is true the quantity:

$$-2\ln(\lambda) = -2(\ln(L_o) - \ln(L_1))$$

will asymptotically approach a χ^2 distribution with degrees of freedom equal to the additional number of free parameters in the alternative hypothesis. The ability to reject a null hypothesis can thus be estimated based on the size of $-2\ln(\lambda)$ relative to what is expected from a χ^2 statistic with the appropriate number of degrees of freedom.

As mentioned previously, the case of zero net growth is considered outside of the nested set formed by the first four model structures. This fifth structure is a very precise hypothesis: it calls for patterns in mortality and growth that precisely cancel to give zero net growth at all times and in all places. None of the first four model structures reduce to this case under the parameter ranges in Table 3, nor does this case reduce to any of the first four cases. It is therefore impossible to define a difference in degrees of freedom or associate a quantitative significance to changes in the misfits between the zero net growth case and the other structures. However, qualitative comparison still provides insight into the role of net growth in bloom development.

3. Results

3.1 The Physical Circulation

Comparison of modeled and observed currents at the Cape Porpoise mooring (see Fig. 1b for location) shows that the physical model recreates the magnitude and direction of the WMCC in the spring of 1993 (Fig. 7). The modeled 5 meter current has a slightly larger westward component than that observed, but this may be attributable in part to the

uncertainty in the surface observations referred to in the Methods, as no such discrepancy exists at 27 or 50 meters. Both the modeled and observed surface currents exhibit a similar response to the wind, veering further east (off-shore) during periods of upwelling (e.g. mid to late April). The direction of the mean surface circulation (Fig. 8) is generally consistent with the climatology of Lynch et al. (1997). The primary difference is the decreased flow magnitude in March/April for the 1993 simulation. This is supported by the mooring comparison, and is therefore attributed to the non-climatological elements of the physical simulations (Table 2).

The vernal warming of sea surface temperatures is well captured by the model (Fig. 9, top panel) although there is a slight tendency for the modeled warming to lag behind the observations. The majority of this signal was captured by the observed and modeled heat flux, with the augmentation term adding an average of 18% to the incident short-wave irradiance averaged over the day. Part of this augmentation may be the result of over-estimation of the transfer of heat below 10m, which results in a more gradual thermocline in the model relative to the observations (not shown). Both the modeled and observed surface salinity show a strong response to the wind (Fig. 9, bottom panel), with upwelling winds transporting freshwater off-shore (e.g. cruise 3) and downwelling winds pressing it against the coast (e.g. cruises 1 and 2). The modeled surface salinity is, on average, 0.7 ppt greater than that observed. This may be due to either elevated mixing in the model, or the failure to transport enough fresh water through the northern boundary. It is recognized that this may have some influence on the sharpness of frontal accumulations. However, it is likely to have little influence of *A. fundyense* growth (Fig. 4d) and has not compromised the transport within the coastal current (Fig. 7).

While not perfect, the level of hydrodynamic skill described above should be sufficient for the goals of the analysis: to evaluate the ability of the model to match the general timing and magnitude of bloom events. It is accepted that mesoscale circulation features that cannot be deterministically simulated by the present forcing, motions left unresolved by the present grid spacing, and imperfectly known forcing, initial conditions, and boundary conditions will contribute a certain level of noise to the model/data comparison. The limitations that this noise imposes on achievable fit will be discussed in more detail below.

3.2 Biological Model Results

3.2.1: The Baseline Model

The best baseline model simulation is achieved by setting both μ_{max} and d_g to the lower limits of their uncertainty (Table 4). The resulting simulation captures the progressive rise in mean cell concentrations during the first three cruises, as well as the minimal cell concentrations in Massachusetts and Cape Cod Bays during the first two cruises (Fig. 10A). While much of the observed small-scale patchiness has admittedly been smoothed over (e.g. the failure to recreate 4 observations of 30-100 cells/L observed just outside of Casco Bay during cruise 1), these misfits alone are not inconsistent with the goal of capturing the timing and magnitude of the observed bloom. However, the skill of the baseline model degrades from Cape Ann southward in the third cruise, and the model grossly over-estimates *A. fundyense* populations throughout the domain thereafter. This generates large misfits correlated over long spatial scales and a correspondingly low likelihood (Table 4). Thus, while the promising start of the baseline model simulation

supports the plausibility of the cyst-driven source, there appears to be a serious flaw in the baseline model dynamics later in the simulation.

3.2.2 Mortality Only

When mortality (m) is added as a degree of freedom, the maximum likelihood result occurs at $m = 0.15$ day^{-1} (Table 4). Modeled *A. fundyense* concentrations in this case decrease during the first two cruises relative to the baseline, but they remain largely consistent with the magnitude of those observed (Fig. 10B). However, unlike the baseline model, the modeled cell abundance no longer increases well beyond that observed during the last 3 cruises. This leads to a marked decrease in the misfit variance, its spatial and temporal scales, and a corresponding increase in the likelihood relative to the baseline model (Table 4). The significance of this improvement in fit is shown by comparison of values of the maximum likelihood for different choices of mortality (Fig. 11A). The overall maximum for the mortality only structure (m=0.15 day^{-1}) serves as the likelihood of the alternative, "baseline and mortality" hypothesis (i.e. $\log(L_1)$=-568.7). The dashed and solid horizontal lines define the 90% and 99% confidence intervals around this best case respectively. That is, they identify likelihood thresholds below which it is possible to reject null hypotheses stating specific values of m with 90% and 99% certainty. The hypothesized baseline model (m=0 day^{-1}) yields a maximum likelihood ($\log(L_o)$=-584.6) far below both thresholds, and it can thus be strongly rejected. This is also true at the 90% level for null hypotheses that claim specific values of $m <= 0.05$ day^{-1}, and those that claim specific values of $m >= 0.025$ day^{-1}. However, hypotheses claiming specific values of m within the clearly defined maximum between m = 0.1-0.2 day^{-1} are not distinguishable from the best simulation at the 90% level. The

maximum likelihood ratio test thus provides information necessary to reject the baseline model, and identifies a range of mortality values that produce statistically similar results.

3.2.3: Nutrients Only

When K_N is added as a degree of freedom, the maximum likelihood simulation occurs with $K_N = 3.0$ μM (Fig. 10C, Table 4), but values greater than 1.5 μM produce results that are statistically similar at the 90% level (Fig. 11B). As was the case with mortality, the baseline model structure can be strongly rejected based on its inability to control cell levels during the last 2 cruises of the field season (compare Fig. 10A and Fig. 10C). Clearly, some additional loss or limitation is needed to reproduce the timing and magnitude of the bloom although it is not yet clear if this is best provided by nitrogen limitation or mean mortality.

3.2.4: Mortality and Nutrients

When both nutrients and mortality are included, the best simulation occurs at $K_N = 0.5$ μM and $m = 0.1$ day^{-1} (Fig. 10D, Table 4). Consideration of this last model structure expands the 1-dimensional likelihood analyses of Figs. 11A-B into a 2-dimensional, K_N, m parameter space (Fig. 11C). The thick dashed and solid contours define the 90% and 99% confidence regions within the parameter space and are accordingly based on a χ^2 distribution with 2 degrees of freedom. The baseline model is located at the origin (circled). The points along the ordinate are those shown in Fig. 11A for the mortality only case, and those along the abscissa are those from the nutrients only case. The best simulations on each of these axes, along with the best overall, are circled. The confidence contours identify a broad band of parameter values that produce

statistically similar results. The baseline model lies far outside of both regions, and can thus be strongly rejected. However, points associated with the nutrients only case (abscissa) and with only mortality case (the ordinate) lie within the 90% confidence region and cannot be rejected.

To understand the differences between the mortality only, nutrients only, and mortality and nutrients structures, closer inspection of the misfits during the last three cruises is needed (Fig 10B-D). Two are particularly notable. First, the maximum likelihood run for all three simulations produce cell populations in much of Massachusetts Bay during cruise 3, before they are observed. This misfit increases as mortality decreases (e.g. Fig. 10B versus Fig. 10C). A second notable misfit occurs offshore and to the North of Cape Ann during cruise 5. *A. fundyense* concentration highs are observed in Casco Bay and Massachusetts Bay regions during cruise 4. These high patches are well connected by an intervening population during cruise 4, but this connection largely disappears in the observations by cruise 5. The maximum likelihood simulations for the remaining model structures all reproduce the highs near Casco Bay and within Massachusetts Bays (although they are damped relative to the observations). However, only simulations with nutrient dependence begin to capture the attenuation in the connecting population between cruise 4 and cruise 5. This is due to the nearly complete depletion of nutrients within the intervening region by cruise 4 (see Fig. 2b). The optimal run has the most success in minimizing the combined effect of these two misfits: The moderate mortality rate (0.1 day^{-1}) controls the cell abundance in Massachusetts Bay during cruise 3, while the combination of nitrogen dependence and mortality begins to recreate the attenuation of the *A. fundyense* population between Casco

Bay and Massachusetts Bay from cruise 4 to cruise 5. However, the increase in skill is not enough to strongly differentiate the maximum likelihood run using both mortality and nutrients from those using either mortality or nutrients.

3.2.5: Zero Net Growth

The best run imposing the condition of zero net growth is summarized in Table 4 and shown in Fig. 10E. Although it is impossible to attach a level of significance to the change in fit between the best overall run and the zero net growth case (see discussion in Methods), there is a notable decrease in the likelihood and corresponding increase in the misfit variance for the latter. Comparison of the modeled fields reveals that the largest difference between the two simulations is the inability of the zero net growth case to create regions of increased abundance near Casco Bay and within Massachusetts Bay during the last two cruises. The best simulation also produces a bloom that is generally more constrained to coastal areas, as is suggested by the observations. However, it is notable that the zero net growth simulation produces a bloom of approximately the right magnitude. Growth and mortality contribute to potentially important spatial features within the bloom, but they do not dramatically change the overall cell abundance.

3.3 Model Diagnosis

While the best run produces a smoothed version of the observations and considerable misfits exist at individual points, it does capture much of the seasonal progression of bloom magnitude from April to June. It has also begun to recreate several of the bloom's spatial aspects, such as the high *A. fundyense* concentrations within Massachusetts Bay and near Casco Bay. The relatively small decorrelation length scale

of the misfits (~18-20 km e-folding scale, Table 4) supports this assessment. The existence of some larger misfits is acknowledged (i.e. those discussed above) and these will be revisited in the Discussion. However, the achieved level of fit warrants diagnosis of the present simulations to gain insight into bloom dynamics, albeit only over broad scales. Diagnosis focuses primarily on inspection of *A. fundyense* fluxes and cell inventories within the domain (Fig. 12) and factors limiting net growth (Fig. 13). Diagnosis is not limited to the optimal simulation but includes the best simulations from the mortality only, nutrients only, and mortality and nutrients cases (Table 4). These simulations are representative of the range of results within the 90% confidence interval of Fig. 11C. The results from the zero net growth case are also included in Fig. 12, as they provide a useful comparison.

The germination of offshore cysts (those lying in waters of > 50 meters in depth) provides the largest flux of new *A. fundyense* cells to the domain throughout the first half of all the representative simulations (Fig. 12, panels A-D), and remains important throughout. The flux from inshore cysts is only 7% that of those offshore for all three simulations. The introduction of new cells due to net growth (growth - mortality, panel C) is notable yet not dominant, as it accounts for 10-46% of the total new cell flux during the simulation period. It becomes more prominent toward the end of the simulations, particularly for those models with weak or no nutrient dependence. The flux of cells through the northern boundary accounts for just 7-11% of new cells introduced to the domain during the simulation period. However, over the last month of the simulation this flux reaches 19-38% of that produced by cysts within the domain.

Panels E and F show that the increase in the transport of cells from the EGOM results from both an increase in cell concentration along the boundary and an increase in the tendency of the current to flow to the southwest. The mean current transporting *A. fundyense* into the domain through the northern boundary in March and April is 4.1 cm/sec, while it reaches 6.1 cm/sec in May and June. This occurs despite the increased prevalence of upwelling favorable winds in May/June, which periodically interrupts the southwest surface flow, pushing cells within the domain out the northern boundary (note the coincidence of outward velocities and sharp perturbation in the mean cell concentration with upwelling winds in Fig. 3, this is most apparent during the episode from June 2-3). This increased tendency for southwest flow in May and June relative to March and April is present in the climatology (Lynch, et al., 1997), where it is caused by the spreading of dense slope water from Jordan to Wilkinson Basin. The concurrent increase in cell abundances along the northern boundary (panel E) is consistent with a delayed peak in toxicity in the EGOM relative to the WGOM (Anderson, 1997). The peak cell concentrations observed in the EGOM in the summer months are generally much greater than those observed in the WGOM (Townsend, et al., 2001). Thus, although wind patterns influence the modeled import of cells from the EGOM over short time scales, patterns in *A. fundyense* abundance and the climatological circulation suggests that transport of cells from the EGOM becomes increasingly important to toxic outbreaks in the WGOM as spring progresses into summer.

The overall importance of *A. fundyense* cells originating from different potential sources is a function of both the flux of new cells, and subsequent net growth within the domain. Cells originating from offshore cystbeds, inshore cystbeds, and flow from the

EGOM were therefore tracked as separate populations (Fig. 12, panels G-I). Cells originating from offshore cysts are most prominent, accounting for 72 to 83% of the total number of cells in the domain at any time. Cells originating from inshore cystbeds and cells originating in the EGOM account for 7 to 10% and 8 to 18% respectively. These contributions increase to 10 to 11% and 17 to 32% by the last week of the simulation. Comparison of the best-fit and zero net growth cases reveal little change in the total cell number. In general, changes via net growth are limited to a factor of 2 difference for all parameter settings within the 90% confidence interval of Fig. 11C (not shown).

Comparison of the modeled domain-averaged net growth rate to what the rate would be with light at saturation intensity and one additional growth-influencing factor removed (Fig. 13) suggests prominent roles of temperature, nitrogen limitation, and mortality in limiting the net-growth of cells within the domain. Light only imposes a significant limitation during sporadic cloudy days, primarily at the beginning of the run (note the sharp downward spikes in net growth in late March and early April). Removal of this signal allows focus on longer time scale trends that evolve over the bloom season. Temperature is the predominant factor slowing the realized net growth until early May for all the simulations. In early May, the temperature rises rapidly (Fig. 9), DIN concentrations drop (Fig. 2b) and, in all cases except the mortality only run, nitrogen begins playing a more prominent role in limiting the realizable net growth. That is, if the influence of temperature were removed late in the simulation, nitrogen limitation would still prevent net growth rates from increasing sharply. In the case of mortality only run, the lack of a nutrient dependence causes temperature and mortality to remain prominent factors in the limitation of realizable net growth throughout the simulation. The resulting

domain-averaged realized net growth remains low (< 0.05 day^{-1}) throughout most of the run duration for all three simulations. This low net growth accounts for the considerable similarity between Figs. 11B-D and Fig. 11E (the zero net growth case), while spatial variability in the net growth rate accounts for the notable differences in the simulated fields near Casco Bay and within Massachusetts Bay.

4. Discussion

The model/data comparison above has provided further insight into the sources of cells contributing to spring *A. fundyense* blooms in the WGOM and the factors limiting their development. The analysis clearly identifies the need for the addition of mortality or nutrient limitation to the baseline biological model to match the observed bloom timing and magnitude. The best run includes both mortality and nutrient limitation, but simulations using only one or the other produce statistically similar results.

The importance of nitrogen to bloom development is supported by several other studies. Poulton et al. (2001) observed trends in *A. fundyense* toxin composition in the WGOM that were consistent with nitrogen stress late in the spring. In addition, McGillicuddy et al. (submitted), using a similar set of biological models within a Gulf-wide domain, found that excluding nutrient dependence led to unreasonably large summer *A. fundyense* abundance in the WGOM. It is therefore notable that the mortality case herein shows strong positive net growth (Fig. 13) and a notable increase in *A. fundyense* abundance (Fig. 12) at the end of the simulation. This suggests that the "mortality only" would fail if the simulation were extended into the summer months and observations were available.

There is also evidence that argues for the importance of mortality. Studies of zooplankton grazing carried out in the region (Teegarden, et al., 2001, Cambell, et al., (submitted), Turner and Borkman, (submitted)) suggest that common mesozooplankton species do not selectively avoid toxic *A. fundyense* when the dinoflagellate is present at the low concentrations commonly observed in the WGOM. Although mesozooplankton grazing loss rates in offshore waters were generally < 1%/day (18 of 22 experiments, see Turner and Borkman (submitted)), several cases exhibited very high rates (up to 117%/day) due to high grazer abundance, with a mean rate of 5.79%/day. Both the mean and the median (i.e. <1%/day) observed rates fall within the range of uncertainty in the rates inferred from the model (Fig. 11C). However, the observed variance in the grazing loss is not represented in the present model, and may thus contribute to the remaining misfit.

The potential linkage of encystment with nutrient stress (Anderson, et al., 1984) may also drive strong spatial/temporal variability in the mortality. Enhancement of loss rates in areas of low DIN may enable the model to better capture the observed decrease in abundance off-shore and to the north of Cape Ann between cruises 4 and 5. However, thresholds and rates for such a loss term must be determined to test this hypothesis.

Analysis of the development of the misfit in Cape Cod and Massachusetts Bays during cruise 3 (not shown) reveals that the increase in *A. fundyense* abundance between cruise 2 and cruise 3 (April 28-May 10) is due to positive net growth within the region, and not a transport event. The origin of this misfit is thus due to either an error in transport of cells into the region before cruise 2, or an error in the estimation of net growth between cruise 2 and cruise 3. It is notable that this latter period does cover a

sharp transition in the factors influencing net-growth: the temperature increases, a strong thermocline develops, and nutrient concentrations decrease rapidly. The simplifying assumptions of the biological model (e.g. constant mortality, invariant vertical swimming behavior, Monod nutrient dependence) are perhaps most questionable during this period and more resolution of these dynamics may be needed to match observations at that time. However, uncertainty in the germination source may also influence this misfit, as the source properties along with the circulation determine the transport of cells into Massachusetts Bay before cruise 2. The influence of sediment dynamics on the germination source has been identified as a prominent uncertainty in this regard (Fig. 6, d_g). The addition of a sediment dynamics model (e.g. Shull, 2001) may provide the means of investigating this uncertainty. However, the complexity of the processes involved (e.g. Wheatcroft and Martin, 1996), and connecting these processes to cyst germination makes this a formidable challenge.

Improvement to the biological model is made difficult not just due to the challenge of parameterizing increasingly complex biological processes, but also because of difficulties detecting changes in the model/data fit that result from improvements in the biological model. Detection can be confounded by limited spatial/temporal coverage and uncertainty in the observations, or by errors in the physical simulation that are reflected in the biological misfit. In view of this, it is notable that the spatial decorrelation scales of the remaining misfit in the optimal run are only ~20 km. Turbulent physical motions at this scale, while resolved by the model grid, are not simulated deterministically by the physical model and thus are likely contribute prominently to the remaining misfit. Thus, while the presence of some larger misfits (e.g.

Cape Cod Bay during cruise 3) suggest that some further detection of biological model improvement may be possible within the present model/data pairing, the predominance of smaller scale misfits suggests diminishing returns.

Errors and limitations in the physical simulation can arise from many sources, including grid scale resolution, approximations of hydrodynamic processes (e.g. turbulent mixing), and uncertainty in the initial fields, forcing and boundary conditions. Uncertainty in boundary conditions and forcing are often particularly prominent and this can be addressed either through increased direct observation or through data assimilation strategies. Such strategies have been implemented successfully to improve circulation model performance in coastal regions (Lynch and Naimie (2002) provide an overview of recent efforts). However, success is contingent upon the availability of relevant observations (current, pressure etc.) for assimilation. The data streams of the Gulf of Maine Ocean Observing System (Richert, et al., 2000) may be particularly useful to such efforts. Upon improvement of the physical simulation the appropriate metrics for measurement of the physical model skill must also be considered, as these are specific to the application (see discussion in Hetland and Signell (2004). While the measurements of physical model fidelity presented herein were appropriate for evaluating use of the physical simulation to attempt to match the general timing and magnitude of bloom events, different physical metrics and observations would be required if the goal were to match the small-scale structure of the bloom.

5. Conclusions

The findings of this study are largely consistent with the WGOM bloom dynamics outlined by Franks and Anderson (1992a) and in subsequent refinements (Anderson et al.,

2004). However, quantitative analysis of the 1993 RMRP data within the context of a coupled physical/biological model provides several additional insights. Simulations suggest that cysts germinated from beds offshore of Casco Bay are capable of providing the majority of cells needed to account for the observed timing and magnitude of *A. fundyense* spring blooms in the WGOM. Cells from inshore cysts play a relatively minor role, although contributions may be significant locally. As the spring progresses into summer, the EGOM source increases in importance due to the climatological tendency toward along-shore flow in May/June at the Penobscot Bay branch point and increasing cell levels in the EGOM. The average net *A. fundyense* growth rate is low, being first limited by low sea surface temperatures, and then by a combination of depleted nutrients and mortality. The model/data comparison was unable to determine the relative importance of these latter factors. Overall, augmentation of the modeled cell abundance via net growth was modest, strongly linking the bloom magnitude to the size of the sources to the north. This is consistent with the southward transport of established populations hypothesized by Franks and Anderson (1992a). However, despite the fact that the domain-averaged net growth was low, simulations suggest that growth processes do create important spatial/temporal features within the bloom, including elevated concentrations near Casco Bay and Massachusetts Bay later in the simulation. Such features may be an important source of variability in the predominantly along-shore progression of toxicity in the Western Gulf of Maine.

Anderson, D. M., 1980. Effects of temperature conditioning on development and germination of *Gonyaulax tamarensis* (Dinophyceae) hypnozygotes. Journal of Phycology 16, 166-172.

Anderson, D. M., 1997. Bloom dynamics of toxic *Alexandrium* species in coastal waters. Limnology and Oceanography 42, 1009-1022.

Anderson, D. M., 1998. Physiology and bloom dynamics of toxic *Alexandrium* species, with emphasis on life cycle transitions. In: Anderson, D. M., Cembella, A. D. ,Hallegraeff, G. M. (Eds.), Physiological Ecology of Harmful Algal Blooms. Springer-Verlag, Berlin, pp. 29-48.

Anderson, D. M., Keafer, B. A., 1987. The endogenous annual clock in the toxic dinoflagellate *Alexandrium tamarensis*. Nature 325, 616-617.

Anderson, D. M., Keafer, B. A., Geyer, W. R., Signell, R. P., Loder, T. C., 2004a. Toxic *Alexandrium* blooms in the Gulf of Maine: the "plume advection hypothesis" revisited. Limnology and Oceanography (submitted).

Anderson, D. M., Kulis, D. M., Binder, B. J., 1984. Sexuality and cyst formation in the dinoflagellate *Alexandrium tamarensis*: Cyst yield in batch cultures. Journal of Phycology 20, 418-425.

Anderson, D. M., Kulis, D. M., Doucette, G. J., Gallagher, J. C., Balech, E., 1994. Biogeography of toxic dinoflagellates in the genus *Alexandrium* from the northeastern United States and Canada. Marine Biology 120, 467-478.

Anderson, D. M., Lindquist, N. L., 1985. Time-course measurements of phosphorous depletion and cyst formation in the dinoflagellate *Gonyaulax tamarensis* Lebour. Journal of Experimental Marine Biology and Ecology 86, 1-13.

Anderson, D. M., Stock, C. A., Keafer, B. A., Bronzino, A. C., Matrai, P., Thompson, B., Keller, M., McGillicuddy, D. J., Hyatt, J., 2004b. Experimental and modeling observations of *Alexandrium fundyense* cyst dynamics in the Gulf of Maine. Deep-Sea Research, Part II (submitted).

Anderson, D. M., Stock, C. A., Keafer, B. A., Bronzino, A. C., Matrai, P., Thompson, B., Keller, M., McGillicuddy, D. J., Hyatt, J., submitted. Experimental and modeling observations of *Alexandrium fundyense* cyst dynamics in the Gulf of Maine. Deep-Sea Research, Part II

Anderson, D. M., Stolzenbach, K. D., 1985. Selective retention of two dinoflagellates in a well-mixed estuarine embayment: the importance of vertical migration and surface avoidance. Marine Ecology Progress Series 25, 39-50.

Anderson, D. M., Taylor, C. D., Armbrust, V. E., 1987. The effects of darkness and anaerobiosis on dinoflagellate cyst germination. Limnology and Oceanography 32, 340-351.

Bauerfeind, E., Elbrachter, M., Steiner, R., Throndsen, J., 1986. Application of Laser Doppler Spectroscopy (LDS) in determining swimming velocities in motile phytoplankton. Marine Biology 93, 323-327.

Blumberg, A. F., Mellor, G. L., 1987. A description of a three-dimensional coastal ocean circulation model. In: Heaps, N. (Ed.), Three-Dimensional Coastal Ocean Models. American Geophysical Union, pp. 1-16.

Blumberg, A. F., Signell, R. P., Jenter, H. L., 1993. Modelling transport processes in the coastal ocean. Journal of Marine Environmental Engineering 1, 31-52.

Bretherton, F. P., Davis, R. E., C.B., F., 1976. A technique for objective analysis and design of oceanographic experiments applied to MODE-73. Deep-Sea Research, Part II 23, 559-582.

Brooks, D. A., 1985. Vernal circulation in the Gulf of Maine. Journal of Geophysical Research 90, 4687-4705.

Brooks, D. A., 1994. A model study of the buoyancy-driven circulation in the Gulf of Maine. Journal of Physical Oceanography 24, 2387-2412.

Brooks, D. A., Townsend, D. W., 1989. Variability of the coastal current and nutrient pathways in the eastern Gulf of Maine. Journal of Marine Research 47, 303-321.

Cambell, R. G., Teegarden, G. J., Cembella, A. D., Durbin, E. G., 2004. Zooplankton grazing impacts on *Alexandrium* spp. in the near-shore environment of the Gulf of Maine. Deep Sea Research, Part II (submitted).

Carpenter, E. J., Guillard, R. R. L., 1971. Intraspecific differences in the nitrate half-saturation constants for three species of marine phytoplankton. Ecology 52, 183-185.

Conway, H. L., Harrison, P. J., 1977. Marine diatoms grown in chemostats under silicate or ammonium limitation. IV. Transient response of *Chaetoceros debilis, Skeletonema costatum,* and *Thalassiosira gravida* to a single addition of limiting nutrient. Marine Biology 43, 33-43.

Cox, D. R., Hinckley, D. V., 1974. Theoretical Statistics. Chapman Hall, London, 511 pages.

Cullen, J. J., Wood, Barnett, Normandeau, Ryan, 2004. Behavioral and physiological variability among strains of the toxic dinoflagellate *Alexandrium fundyense* from the Gulf of Maine. Deep-Sea Research, Part II (submitted).

Droop, M. R., 1983. 25 years of algal growth kinetic, a personal view. Botanica Marina 26, 99-112.

Eppley, R. W., Rogers, J. N., McCarthy, J. J., 1969. Half-saturation constants for uptake of nitrate and ammonium by marine phytoplankton. Limnology and Oceanography 14, 912-920.

Eppley, R. W., Thomas, W. H., 1969. Comparison of half-saturation "constants" for growth and nitrate uptake of marine phytoplankton. Journal of Phycology 5, 365-369.

Etheridge, S. M., Roesler, C. S., Doucette, G. J., 2004. *Alexandrium fundyense* isolate-specific responses to temperature, irradiance, and salinity: Potential growth rate and toxicity in the Gulf of Maine and Bay of Fundy. Deep-Sea Research, Part II (submitted).

Ezer, T., Mellor, G. L., 1992. A numerical study of the variability and the separation of the Gulf Stream, induced by surface atmospheric forcing and lateral boundary flows. Journal of Physical Oceanography 22, 660-682.

Flynn, K., Jones, K. J., Flynn, K. J., 1996. Comparisons among species of *Alexandrium* (Dinophyceae) grown in nitrogen- or phosphorous-limiting batch culture. Marine Biology 1996, 9-18.

Franks, P. J. S., Anderson, D. M., 1992a. Alongshore transport of a toxic phytoplankton bloom in a buoyancy current: *Alexandrium tamarense* in the Gulf of Maine. Marine Biology 112, 153-164.

Franks, P. J. S., Anderson, D. M., 1992b. Toxic phytoplankton blooms in the Gulf of Maine: testing hypotheses of physical control using historical data. Marine Biology 112, 165-174.

Fung, I. Y., Harrison, D. E., Lacis, A. A., 1984. On the variability of the net longwave radiation at the ocean surface. Reviews of Geophysics and Space Physics 22, 177-193.

Galperin, B., Kantha, L. H., Hassid, S., Rosati, A., 1988. A quasi-equilibrium turbulent energy model for geophysical flows. Journal of Atmospheric Science 45, 55-62.

Geraci, J. R., Anderson, D. M., Timperi, R. J., Staubin, D. J., Early, G. J., Prescott, J. H., Mayo, C. A., 1989. Humpback Whales (*Megaptera novaeangliae*) fatally poisoned by dinoflagellate toxin. Canadian Journal of Fisheries and Aquatic Science 46, 1895-1898.

Geyer, W. R., Signell, R. P., Fong, D. A., Wang, J., Anderson, D. M., Keafer, B. A., 2004. The freshwater transport and dynamics of the western Maine Coastal Current. Continental Shelf Research 24, 1339-1357.

He, R., Weisberg, R. H., 2002. West Florida shelf circulation and temperature budget for the 1999 spring transition. Continental Shelf Research 22, 719-748.

Hendry, R., He, I., 1996. Technical Report on Objective Analysis (OA) Project. Bedford Institute of Oceanography, Dartmouth, Nova Scotia, 105 pages.

Hetland, R. D., Signell, R. P., 2004. Modeling coastal current transport in the Gulf of Maine. Deep-Sea Research, Part II (submitted).

Kamykowski, D., Reed, R. E., Kirkpatrick, G. J., 1992. Comparison of the sinking velocity, swimming velocity, rotation and path characteristics among six marine dinoflagellate species. Marine Biology 113, 319-328.

Kuhl, M., Jorgensen, B. B., 1994. The light of microbenthic communities: Radiance distribution and microscale optics of sandy coastal sediments. Limnology and Oceanography 39, 1368-1398.

Langdon, C., 1987. On the causes of interspecific differences in the growth-irradiance relationships for phytoplankton. Part I. A comparitive study of the growth irradiance relationships of three marine phytoplankton species: *Skelotonema costatum, Olithodiscus luteus* and *Gonyaulax tamarensis*. Journal of Plankton Research 9, 459-482.

Langdon, C., 1988. On the causes of interspecific differences in the growth-irradiance relationship for phytoplankton. Part II: A general review. Journal of Plankton Research 10, 1291-1312.

Large, W. G., Pond, S., 1981. Open ocean momentum flux measurements in moderate to strong winds. Journal of Physical Oceanography 11, 329-336.

Large, W. G., Pond, S., 1982. Sensible and latent heat flux measurements over the ocean. Journal of Physical Oceanography 12, 464-482.

Liebig, J., 1845. On chemical processes in the nutrition of vegetables. In: Chemistry and its applications to agriculture and physiology. L. Playfair, Peterson, PA, pp.

Lomas, M. W., Glibert, P. M., 2000. Comparison of nitrate uptake, storage, and reduction in marine diatoms and flagellates. Journal of Phycology 36, 903-913.

Lynch, D. R., Holboke, M. J., Naimie, C. E., 1997. The Maine coastal current: spring climatological circulation. Continental Shelf Research 17, 605-634.

Lynch, D. R., Naimie, C. E., 1993. The M2 tide and its residual on the outer banks of the Gulf of Maine. Journal of Physical Oceanography 23, 2222-2253.

Lynch, D. R., Naimie, C. E., 2002. Hindcasting the Georges Bank circulation, Part II: wind-band inversion. Continental Shelf Research 22, 2191-2224.

MacIntyre, J. G., Cullen, J. J., Cembella, A. D., 1997. Vertical migration, nutrition and toxicity in the dinoflagellate *Alexandrium tamarense*. Marine Ecology Progress Series 148, 201-216.

MacIsaac, J. J., Grunseich, G. S., Glover, H. J., Yentsch, C. M., 1979. Light and nutrient limitation in *Gonyaulax excavata*: nitrogen and carbon trace results. In: Taylor, D. L. ,Seliger, H. H., (Eds.), Toxic Dinoflagellate Blooms: proceedings of the second conference on toxic dinoflagellate blooms, Key Biscayne, Florida. Elsevier/North-Holland, pp. 107-110.

Marshall, H. G., 1984. Phytoplankton distribution along the eastern coast of the USA. Part V. Seasonal density and cell volume patterns in the northeastern continental shelf. Journal of Plankton Research 6, 169-193.

Martorano, C. D., Loder, T. C., 1997. Nutrient dynamics during blooms of *Alexandrium* spp. in the southwestern Gulf of Maine. Masters Thesis, University of New Hampshire, Biogeochemical Systems Center, Durham, NH, USA, unpublished.

McGillicuddy, D. J., Anderson, D. M., Lynch, D. R., Townsend, D. W., 2004. Mechanisms regulating the large-scale seasonal development of *Alexandrium fundyense* blooms in the Gulf of Maine. Deep-Sea Research, Part II

McGillicuddy, D. J., Signell, R. P., Stock, C. A., Keafer, B. A., Keller, M. D., Hetland, R. D., Anderson, D. M., 2003. A mechanism for offshore initiation of harmful algal blooms in the coastal Gulf of Maine. Journal of Plankton Research 25, 1131-1139.

Mellor, G. L., Yamada, T., 1982. Development of a turbulence closure model for Geophysical Fluid Problems. Reviews of Geophysical and Space Physics 20, 851-875.

Naimie, C. E., Loder, J. W., Lynch, D. R., 1994. Seasonal variation in the three-dimensional residual circulation on Georges Bank. Journal of Geophysical Research 99, 15,967-15,989.

Pettigrew, N., Townsend, D., Xue, H., Wallinga, J., Brickley, P., Hetland, R., 1998. Observations of the eastern Maine Coastal Current and its offshore extensions in 1994. Journal of Geophysical Research Vol. 103, 30,623-30,639.

Physical-Oceanography-DAAC, 1985. AVHRR Oceans Pathfinder global equal-angle best SST NOAA, NASA. http://www.podaac.jpl.nasa.gov.

Platt, T., Jassby, A. D., 1976. The relationship between photosynthesis and light for natural assemblages of coastal marine phytoplankton. Journal of Phycology 12, 421-430.

Poulton, N. J., 2001. Physiological and behavioral diagnostics for nitrogen limitation for the toxic dinoflagellate *Alexandrium fundyense*. Ph.D., Woods Hole/MIT Joint Program, Biological Oceanography, Woods Hole, MA, unpublished.

Prakash, A., 1967. Growth and toxcity of a marine dinoflagellate, *Gonyaulax tamarensis*. Journal of the Fisheries Research Board of Canada 24,

Press, W. H., Flannery, B. P., Teukolsky, S. A., Vetterling, W. T., 1985. Numerical Recipes, The Art of Scientific Computing. Cambridge University Press, Cambridge, 818 pages.

Richert, E., Pettigrew, N., Beard, M., Incze, L., Irish, J., Panchang, V., Roesler, C., Thomas, A., Townsend, D. W., Xue, H., 2000. A proposal to implement the Gulf of Maine Ocean Observing System. Proposal to: Office of Naval Research, 43 pages.

Scholin, C. A., Hallegraeff, G. M., Anderson, D. M., 1995. Molecular evolution of the *Alexandrium tamarense* "species complex" (Dinophyceae): Dispersal in the North American and West Pacific regions. Phycologia 34, 472-485.

Shull, D. H., 2001. Transition-matrix model of bioturbation and radionuclide diagenisis. Limnology and Oceanography 46, 905-916.

Shumway, S. E., Sherman-Caswell, S., Hurst, J. W., 1988. Paralytic shellfish poisoning in Maine: Monitoring a monster. Journal of Shellfish Research 7, 643-652.

Signell, R. P., Jenter, H. L., Blumberg, A. F., 1993. Modeling the seasonal circulation in Massachusetts Bay. In: Estuarine and Coastal Modeling III, Oak Brook, Illinois. pp. 578-590.

Smagorinsky, J., 1963. General circulation experiments with the primitive equations, I. The basic experiment. Monthly Weather Review 99-164.

Sommer, U., 1991. A comparison of the Droop and Monod models of nutrient limited growth applied to natural populations of phytoplankton. Functional Ecology 5, 535-544.

Teegarden, G. J., Cambell, R. G., Durbin, E. G., 2001. Zooplankton feeding behavior and particle selection in natural phytoplankton assemblages containing toxic *Alexandrium spp.* Marine Ecology Progress Series 218, 213-226.

Teegarden, G. J., Cembella, A. D., 1996. Grazing of toxic dinoflagellates, *Alexandrium* spp., by adult copepods of coastal Maine: implications for the fate of paralytic shellfish toxins in marine food webs. Journal of Experimental Marine Biology and Ecology 196, 145-176.

Townsend, D. W., Pettigrew, N. R., Thomas, A. C., 2001. Offshore blooms of the red tide dinoflagellate *Alexandrium* sp., in the Gulf of Maine. Continental Shelf Research 21, 347-369.

Turner, J. T., Borkman, D. G., 2004. Impact of zooplankton grazing on *Alexandrium* spp. blooms in the offshore Gulf of Maine. Deep Sea Research, Part II (submitted).

Turner, J. T., Tester, P. A., 1997. Toxic marine phytoplankton, zooplankton grazers, and pelagic food webs. Limnology and Oceanography 5, 1203-1214.

Watras, C. J., Chisholm, S. W., Anderson, D. M., 1982. Regulation of growth in an estuarine clone of *Gonyaulax tamarensis* Lebour: salinity-dependent temperature responses. Journal of Experimental Marine Biology and Ecology 62, 25-37.

Wheatcroft, R. A., Martin, W. H., 1996. Spatial variation in short-term (^{234}Th) sediment bioturbation intensity along an organic carbon gradient. Journal of Marine Research 54, 763-792.

White, A. W., Fukuhara, O., Anraku, M., 1989. Mortality of fish larvae from eating toxic dinoflagellates or zooplankton containing dinoflagellate toxins. In: Okaichi, T., Anderson, D. M. ,Nemoto, T. (Eds.), Red Tides: Biology, Environmental Science, and Toxicology. Elsevier, New York, pp. 395-398.

Wunsch, C., 1996. The Ocean Circulation Inverse Problem. Cambridge University Press, New York, 442 pages.

Table 1: Summary of the growth rate dependence for the 5 biological model structures. T = temperature, S = salinity, E = irradiance, N = nutrients (i.e. dissolved inorganic nitrogen), NA = not applicable (see text)

Structure	Growth Rate Dependence	Mortality
baseline	T, S, E	no
mortality	T, S, E	yes
nutrients	T, S, E, N	no
mortality and nutrients	T, S, E, N	yes
zero net growth	NA	NA

Table 2: Physical Model Forcing

Forcing	Source/Description
Sea Surface Elevation	M_2 tide from Gulf of Maine tidal model (Lynch and Naimie, 1993) Mean elevation from bi-monthly climatology (Naimie, et al., 1994)
Wind	Portland off-shore buoy (NDBC #44007), applied throughout domain and translated to shear via Large and Pond (1981)
River discharge	USGS stream gauges at 4 major rivers: Charles, Saco, Merrimack, and the Kennebec/Androscoggin
Boundary T,S	Interpolated and extrapolated from mooring and survey data
Initial T,S	spatially averaged climatology (Naimie, et al., 1994)
Heat Flux	Shortwave radiative heat flux from land-based sensor at Woods Hole Sensible and latent heat fluxes estimated using Portland off-shore buoy data and the bulk formulae of Large and Pond (1982). Longwave flux estimated using Portland off-shore buoy data and relationships of Berliand and Berliand as described in Fung et al. (1984)

Table 3: Parameters in the Biological Model

Symbol	Definition	Units	Range	Sources
K_N	Half-saturation constant for nutrient limited growth	μM	0-3	Eppley et al. (1969), Eppley and Thomas (1969), Lomas and Glibert (2000), Carpenter and Guillard (1971), MacIsaac et al. (1979), Sommer (1991)
m	Spatially and temporally averaged mortality	day^{-1}	0-0.3	see text
$\mu_{max}(T_{opt},S_{opt})$	The maximum growth rate under optimal temperature and salinity conditions.	day^{-1}	0.46-0.70	Cullen et al. (this volume), Langdon (1987), Etheridge et al. (this volume), Watras et al. (1982), Keafer and Kulis (unpub. data)[1]
μ_o^r	The maintenance respiration rate	day^{-1}	0.15-0.25	Cullen et al. (submitted)
α_g	The growth efficiency	day^{-1} W^{-1} m^2	0.017-0.056	Cullen et al. (submitted)
d_g	The mean depth of sediment over which cysts are able to germinate and contribute to the bloom	cm	0.5-1.5	Anderson et al. (2004b)
E_{lgt}	Light level for germination under "light" conditions.	watts/m^2	1.2-3.6	Anderson et al. (submitted)
E_{drk}	Light level for germination under dark conditions.	watts/m^2	0.1% of I_{lgt} to 10% of I_{lgt}.	Anderson et al. (submitted)
k_w	Mean diffuse attenuation in water column.	m^{-1}	0.15-0.25	Townsend et al. (2001)
k_s	Mean diffuse attenuation in the sediment	mm^{-1}	2-5	Kuhl and Jorgensen (1994)
w_a	Vertical swimming speed	m/day	5-15	Bauerfiend et al.(1986), Kamykowski et al. (1992)

[1] Sources used for formulation of the growth versus temperature dependence polynomial are: Etheridge et al. (2004), Langdon (1987), Watras et al. (1982), and Keafer and Kulis (unpublished data). Sources used for the salinity dependence polynomial are: Etheridge et al. (2004) and Prakash (1967).

Table 4: Parameters of statistical model for the best run for each model structure. Note that two variance values are reported. The first is that associated with the 386 observed misfits. The second is that fit by in the likelihood process. While the two are close in size, differences reflect the influence of space/time correlation and incomplete sampling.

	baseline	mortality	nutrients	mortality + nutrients	zero net growth
$\mu_{max}(day^{-1})$	0.460	0.525	0.460	0.575	NA
$d_g(cm)$	0.5	1.25	0.50	1.25	1.25
$m(day^{-1})$	0	0.15	0	0.1	NA
$K_N(\mu M)$	0	0	3.0	0.5	NA
$log(L)$	-584.6	-568.7	-569.3	-567.7	-572.9
σ^2(observed misfits)	7.10	2.46	2.55	2.34	2.63
σ^2(fit by likelihood)	6.35	2.56	2.71	2.51	2.81
$r_{cs}(km^{-1})$	0.0194	0.0534	0.0492	0.0541	0.0487
$r_{as}(km^{-1})$	0.0196	0.0566	0.0520	0.0566	0.0503
$\rho_{\Delta t=1}$	0.189	0.196	0.182	0.170	0.203
$\rho_{\Delta t=2}$	0.113	0.106	0.083	0.084	0.084

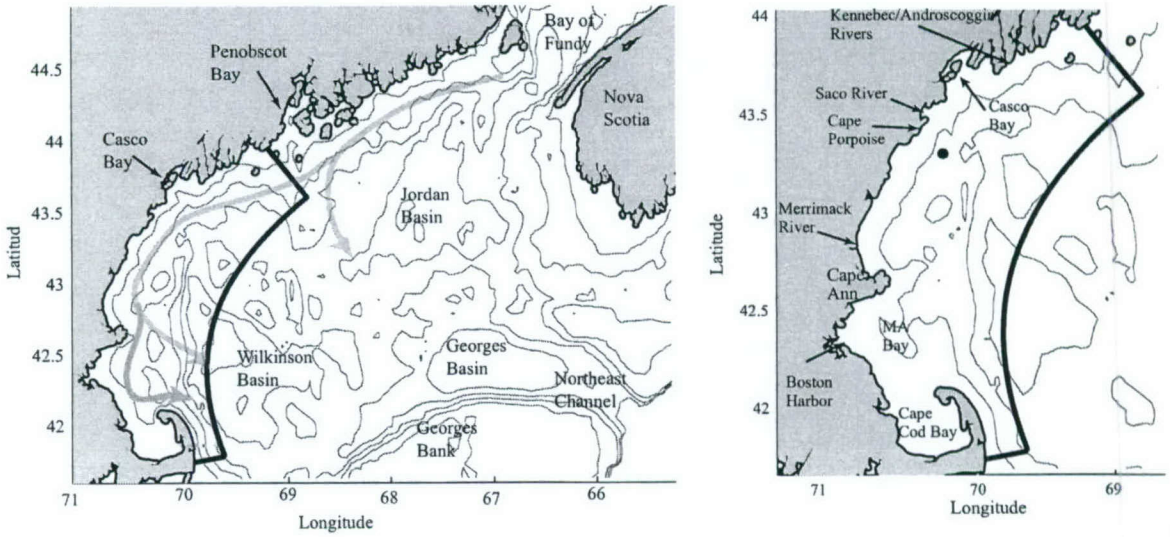


Figure 1: **Left Panel:** The Gulf of Maine and study region. The study domain is outlined in black. Depth contours are at 50, 100, 150 and 200 meters. The direction of the flow of the Maine Coastal Current (adapted from Lynch et al., 1997) is shown as a thick gray line. Branch points off-shore of Penobscot Bay and Cape Ann are notable. **Right Panel**: Close-up of the study region. River outflow locations are highlighted (the Charles River outflow is within Boston Harbor). The closed circle marks the location of the Cape Porpoise Mooring, while the open circle marks the location of the Portland Meteorological Buoy (NDBC station #44007).

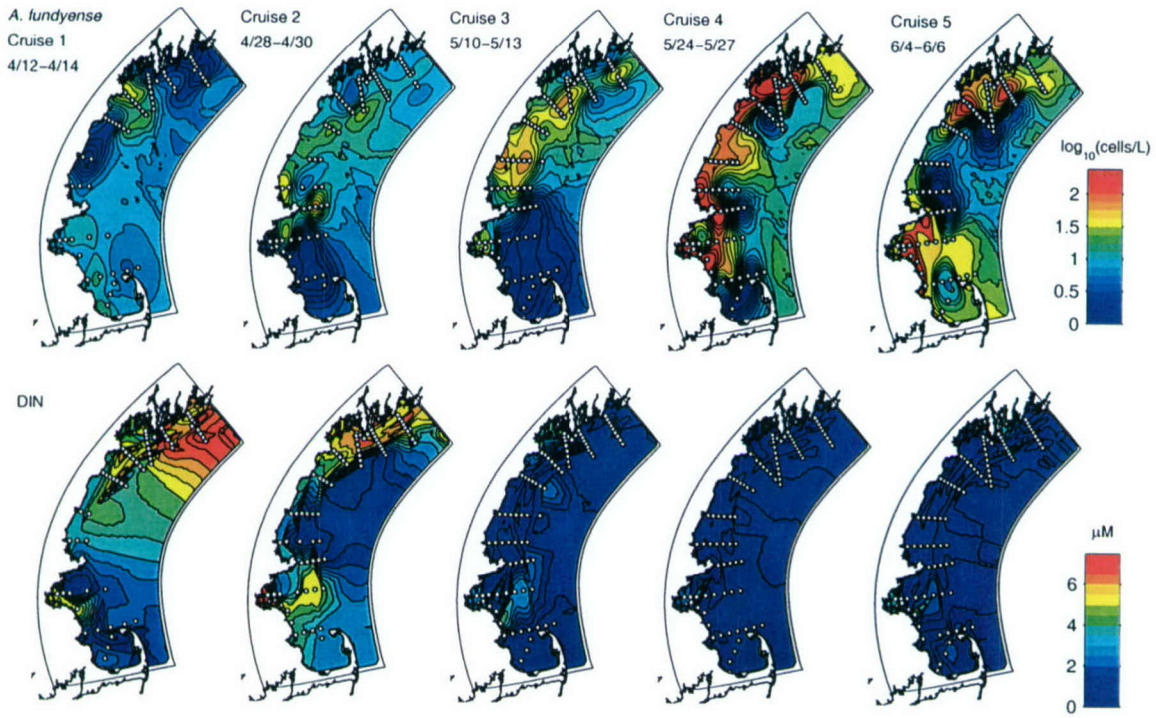


Figure 2: The RMRP field data. White circles are observation points. Columns correspond to cruises 1-5. **Top Panel:** The observed surface distribution of *A. fundyense* (cells/L on a $\log_{10}$ scale) during the spring 1993 RMRP surveys (Anderson et al., 2004a). The contour interval is 0.125. **Bottom Panel:** Surface dissolved inorganic nitrogen (DIN, µM) measured during the 1993 RMRP surveys (Martorano and Loder, 1997). The contour interval is 0.5 µM.

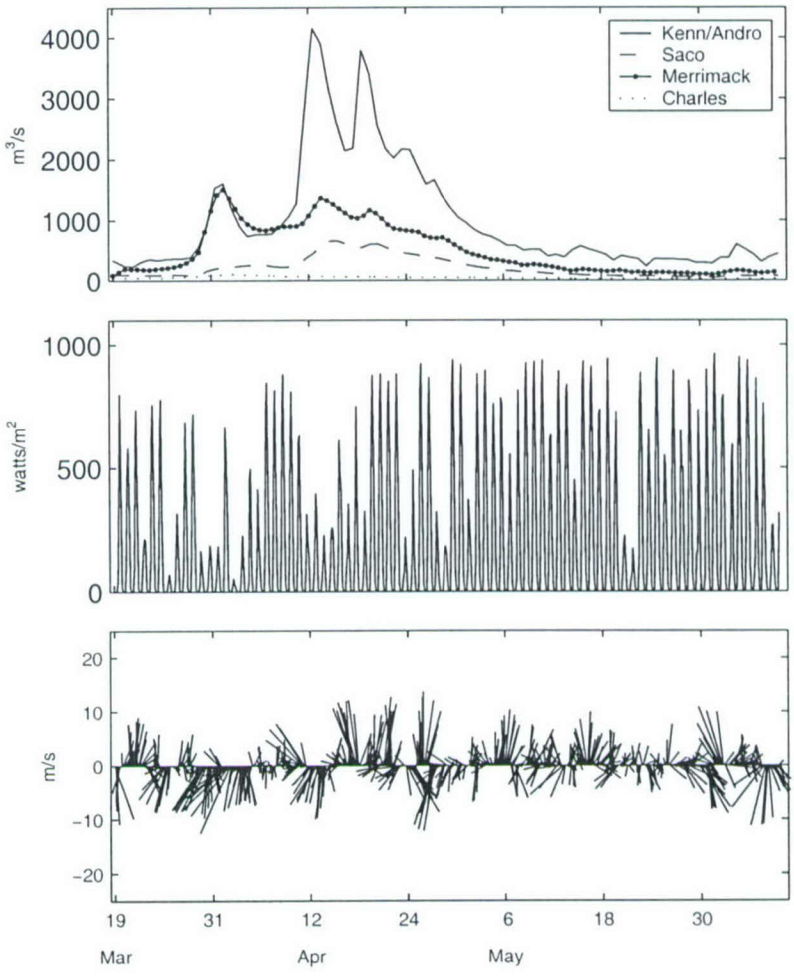


Figure 3: The physical model forcing. **Top panel**: river outflow in m^3/sec for each of the 4 modeled river inputs within the domain. **Middle panel**: short wave radiation flux (watts/m^2). **Bottom panel**: wind speed and direction (m/sec).

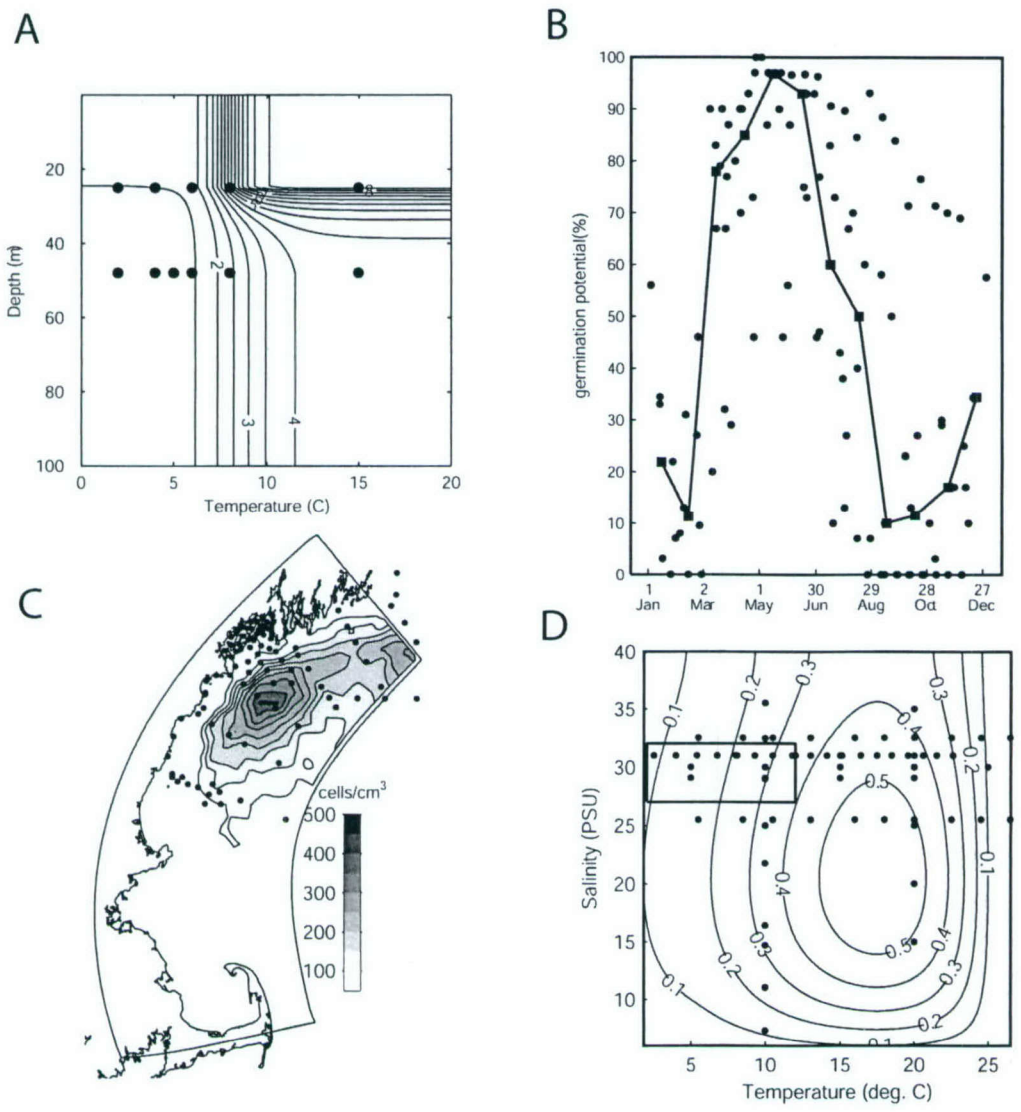


Figure 4(A-D): The biological model summary. All plots show observations as black dots. **A:** The germination rate (%/day) at the sediment surface as a function of temperature and light. Light has been converted to depth using a diffuse attenuation coefficient (k_w) of 0.2 m^{-1} and a representative day-averaged surface irradiance of 350 watts/m^2. **B:** The endogenous clock function. The squares give the estimated germination potential for each month based on a median filter of data from 7 different cyst isolates within the Gulf of Maine. This curve is normalized to produce a factor between 0 and 1 that scales the germination rate. **C:** The cyst map (cysts/cm^3) in the top cm. **D:** The growth rate (day^{-1}) as a function of temperature and salinity. This plot uses $\mu_{max}(T_{opt},S_{opt})=0.58$ day^{-1}. The boxed area contains the conditions encountered over the vast majority of the domain for the duration of the simulations.

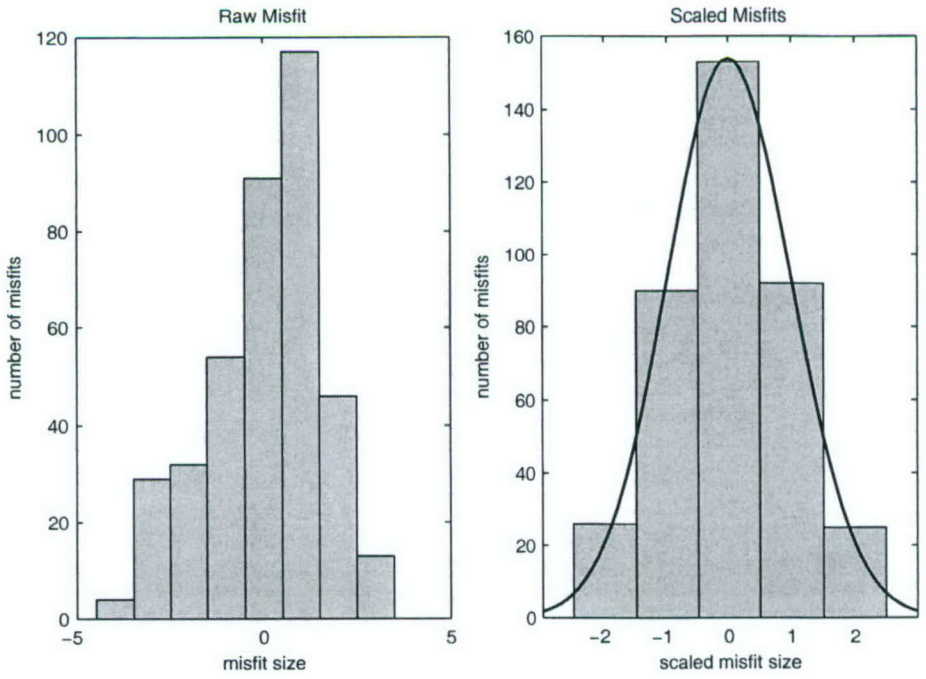


Figure 5: Error model verification. The left plot shows a histogram of the misfits associated with the optimal run. The right plot shows those same misfits after scaling by the covariance matrix. If the statistical representation has adequately described the primary features of the model/data misfits, the scaled misfits will be normally distributed with mean 0 and a variance of 1 (solid line in second panel).

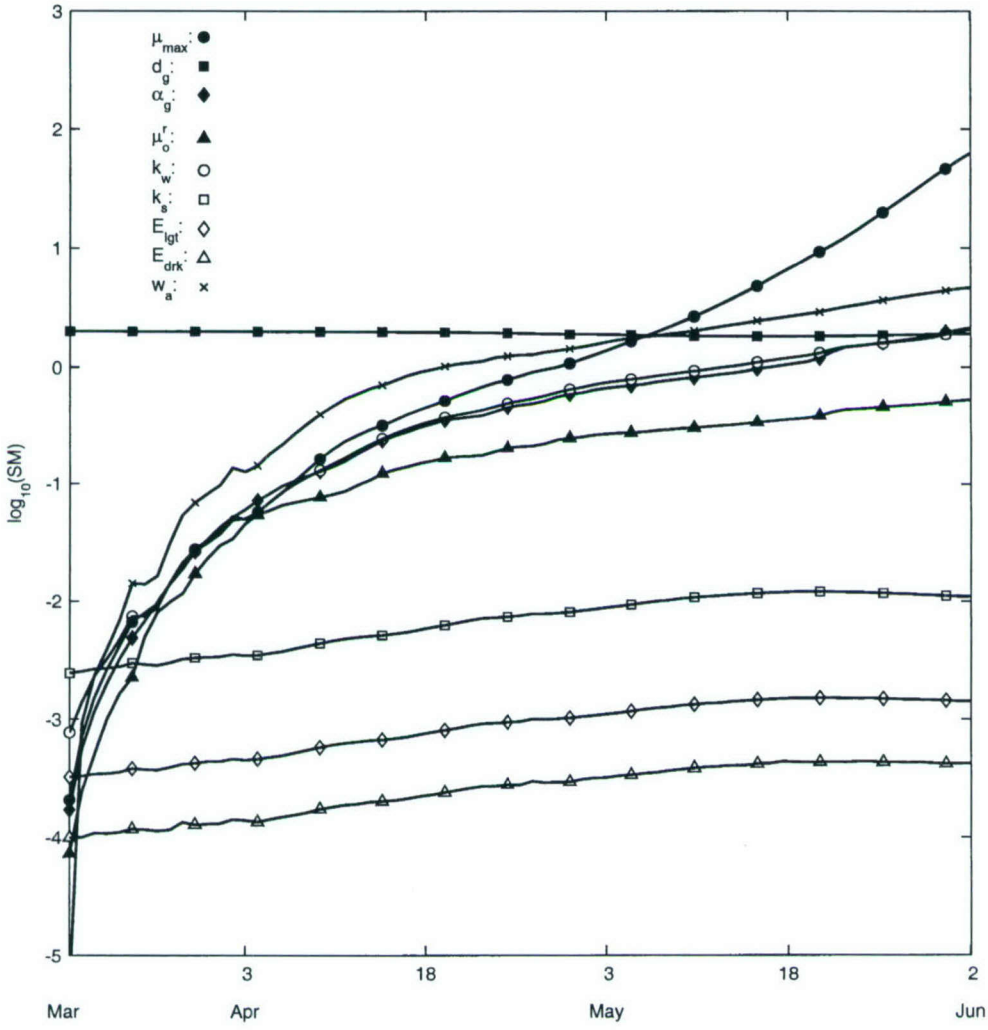


Figure 6: The baseline model sensitivity metric. The germination depth (d_g) dominates the baseline model sensitivity until early May, when it is eclipsed by the maximum growth rate.

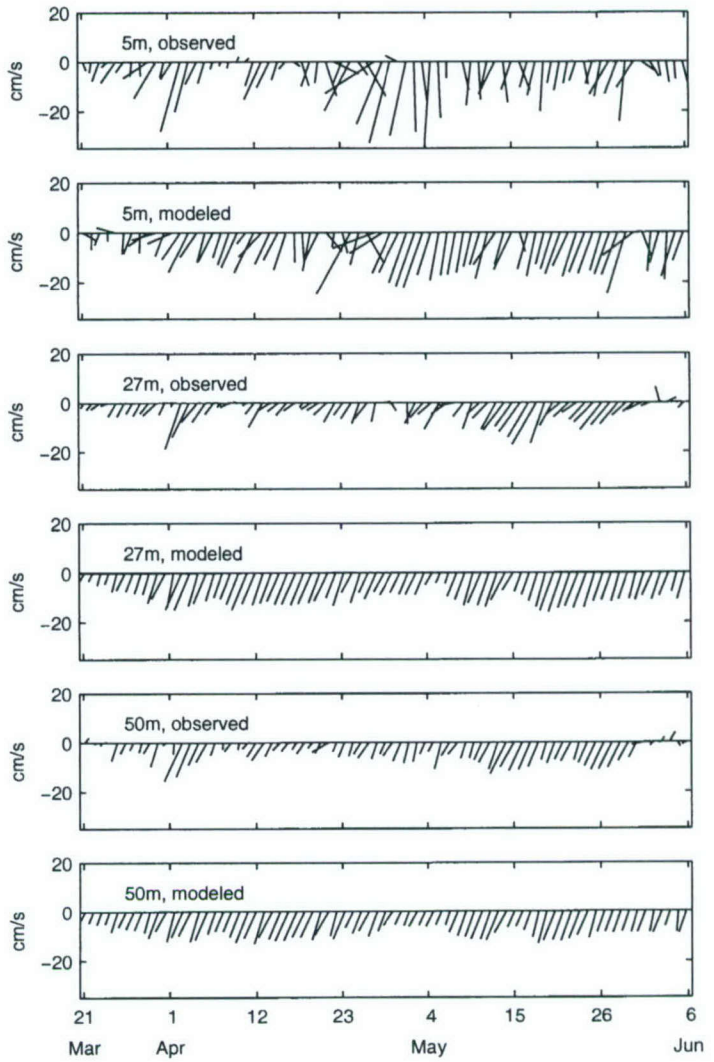


Figure 7: Comparison of modeled and observed current speed and direction at the Cape Porpoise mooring.

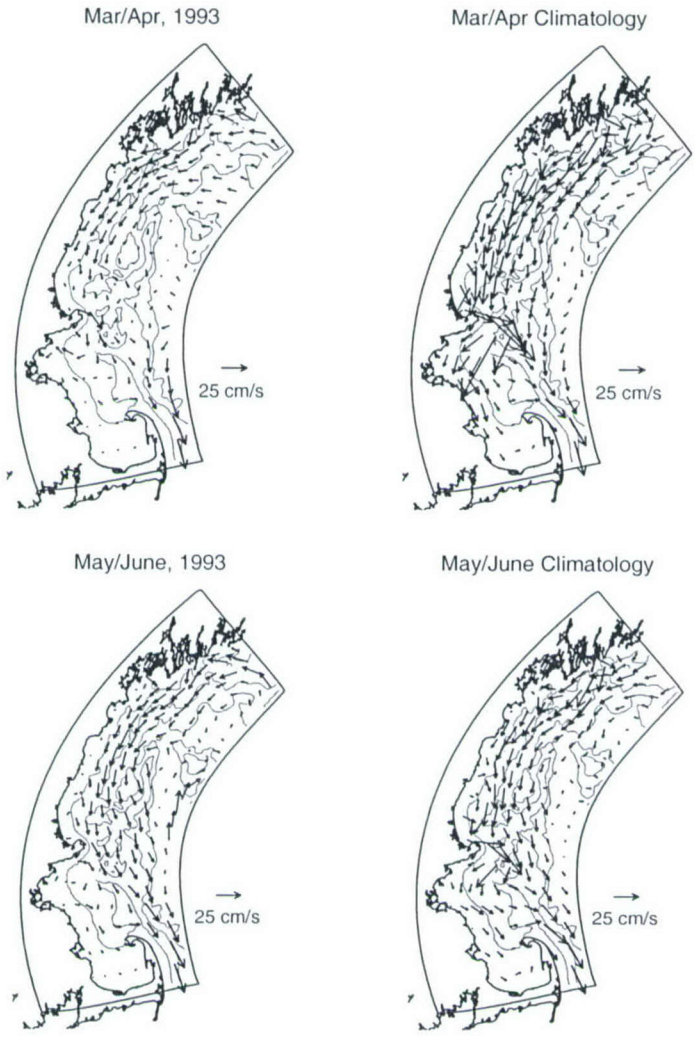


Figure 8: Comparison of modeled mean surface currents from March 19-April 30 and May 1 - June 6 (left panel) to the mean surface currents of the March/April and May/June climatology of Lynch et al. (1997).

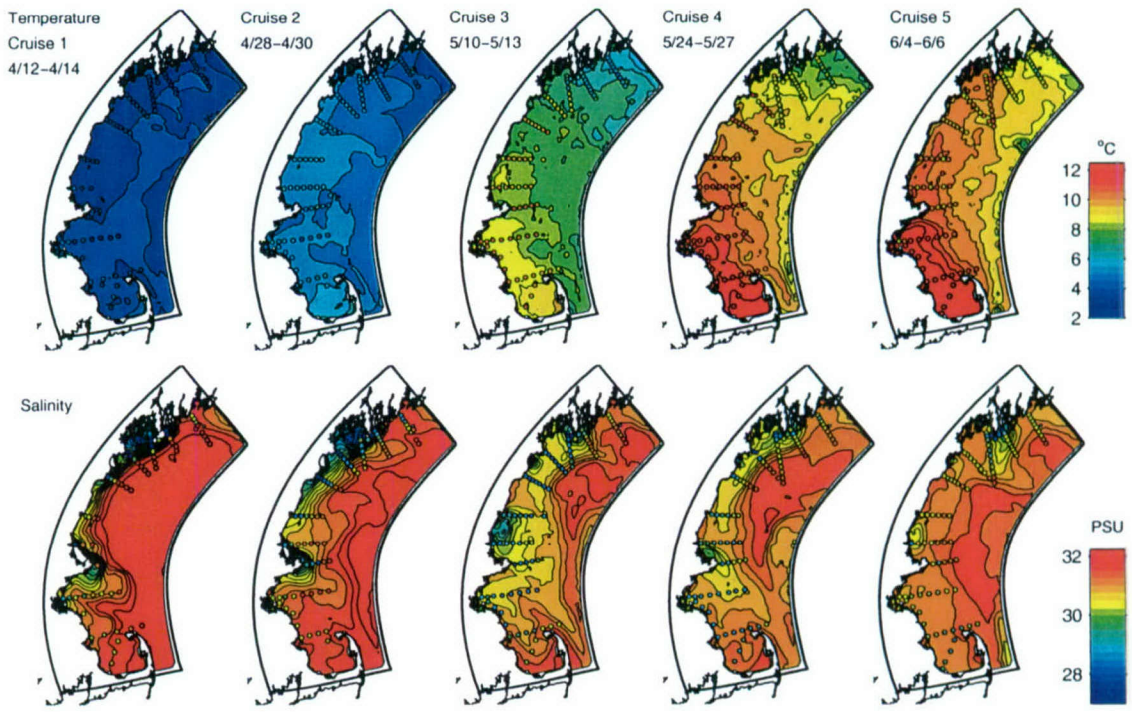


Figure 9: Surface (2m) temperature and salinity comparison. **Top panel:** Modeled surface temperature (colored contours) versus observations (colored dots). The dots and contours are on the same color scale. Closely matching colors corresponds to a close model/data match. **Bottom Panel:** Modeled surface salinity (colored contours) versus observations (colored dots).

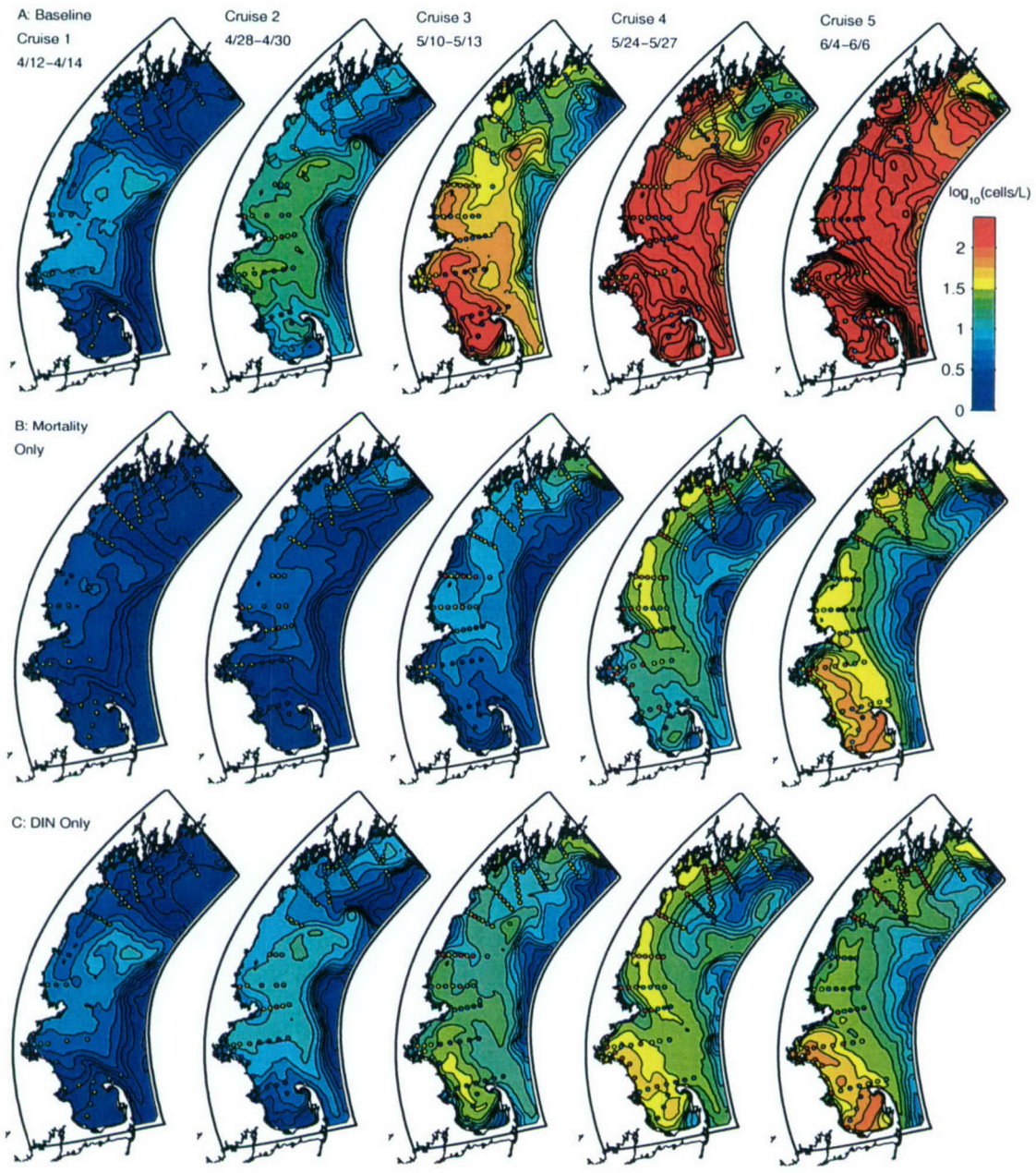


Figure 10 (A-C)

(Caption on the following page)

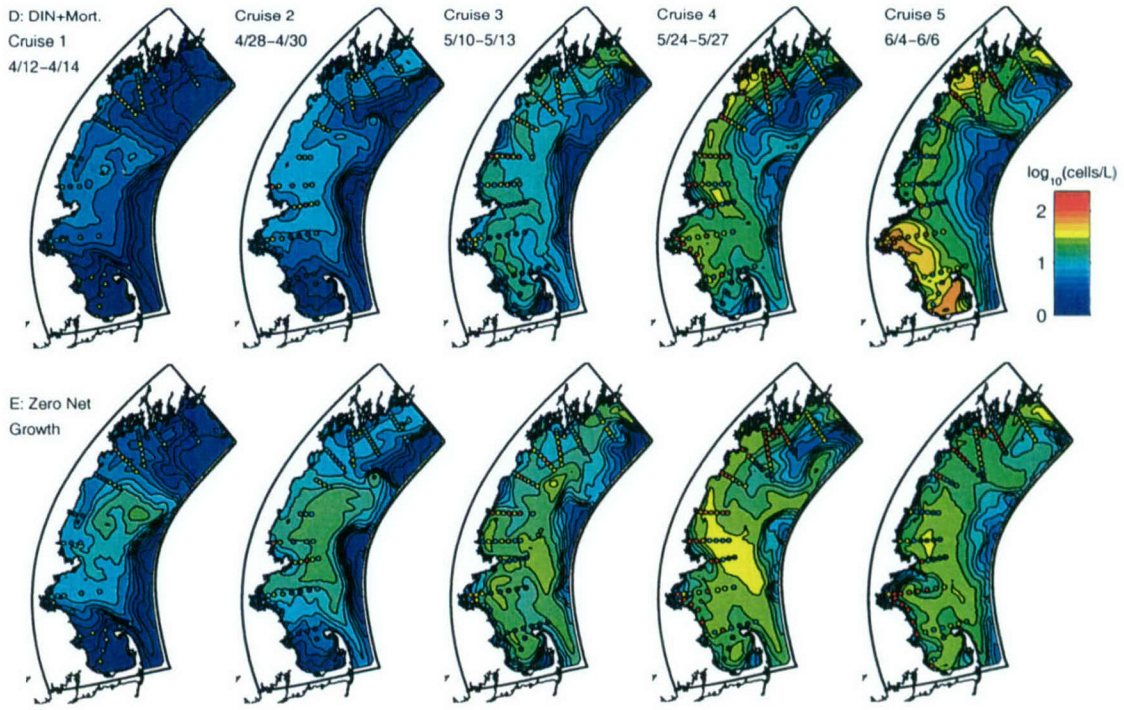


Figure 10: Model/Data comparisons: Model output for all panels is color contoured, while observations are overlaid as colored dots. Units are $\log_{10}$(cells/L). Both the model output and the observations are plotted on the same color-scale, meaning that closely matching colors corresponds to a closely matching model/data fit. Each horizontal panel corresponds to output in table 4, with each column corresponding to a cruise. Panels are as follows: **A:** best baseline model, **B:** best model with mortality only, **C:** best model with nutrient dependence only, **D:** best run with mortality and nutrient dependence, **E:** The best simulation with net growth set to 0.

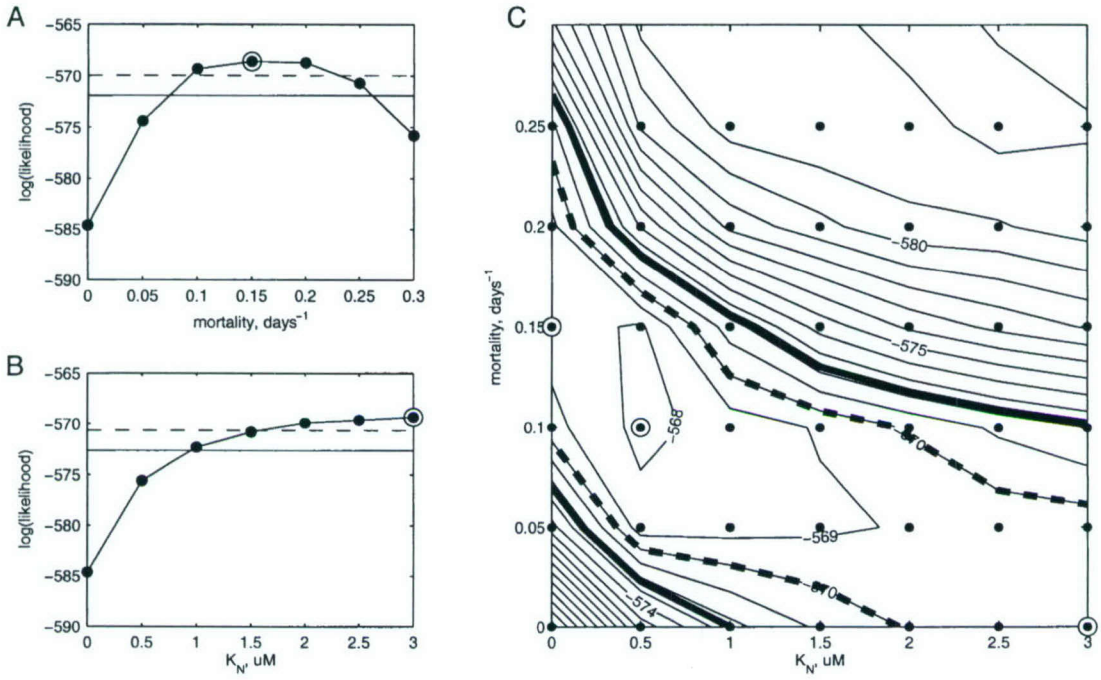


Figure 11: The MLRT results. **A.** Plot of log(L) for comparison of model structure II (mortality only) to structure I (the baseline model structure). Dots signify values of m where the likelihood was maximized. The maximum likelihood occurred at $m = 0.15$ day^{-1} (circled). The dashed horizontal line marks the 90% confidence limit, the solid horizontal line marks the 99% confidence limit. **B.** Plot of log(L) for comparison of nutrients only (structure III) to structure I. Markings are the same as in A. **C.** Contours (interval = 1) of log(L) as a function of K_N and m. The thick dashed line marks the border of the 90% confidence region. The thick solid line, marks the 99% confidence interval. The best simulation occurs at $K_N = 0.5$ μM, $m = 0.1$ day^{-1} (circled). The points along the ordinate are those from the mortality model structure. Those along the abscissa are from the nutrient model structure. Best simulations for each of these cases, as well as the baseline model (origin), are circled.

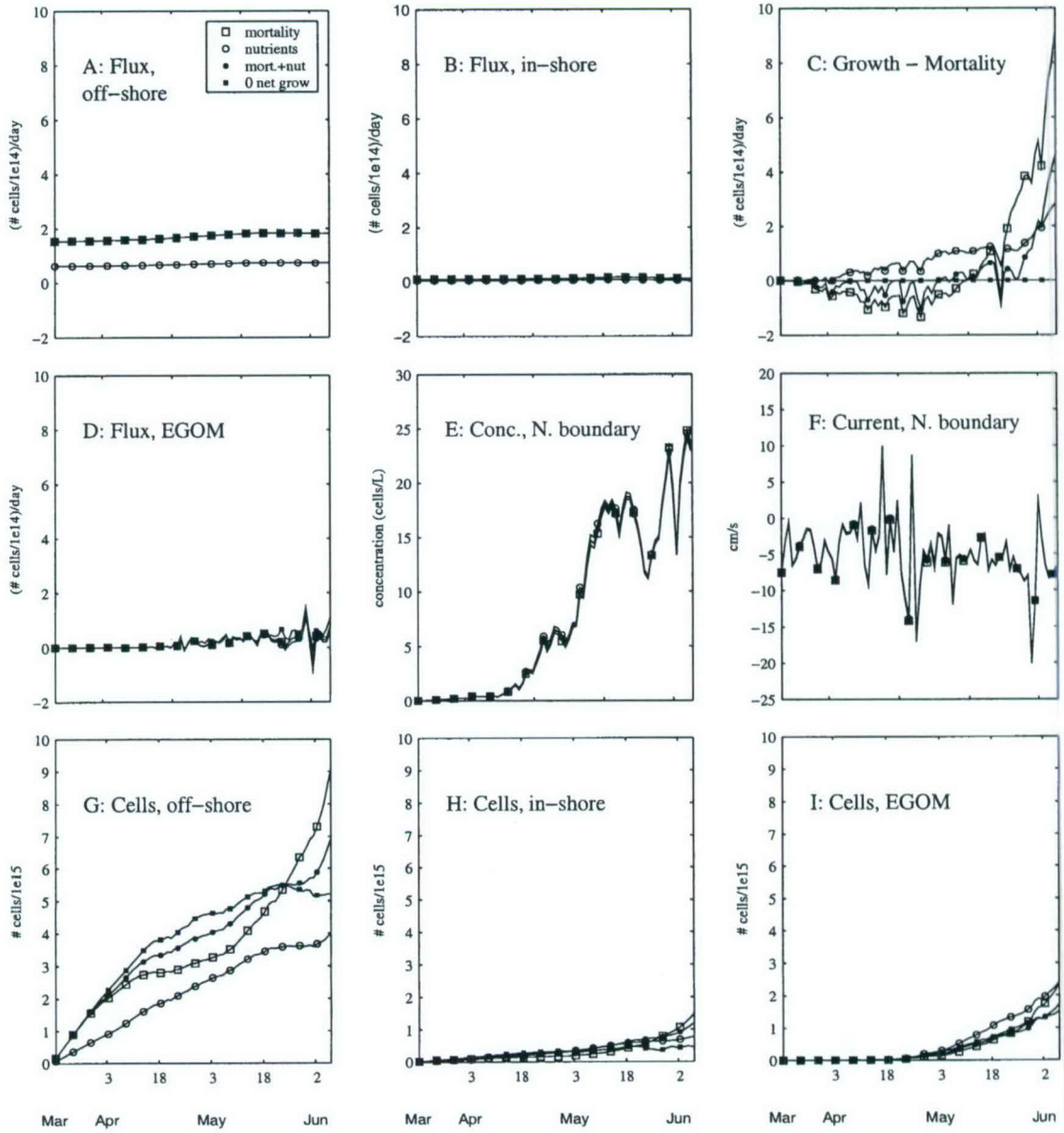


Figure 12: The cell budget. Cell fluxes and inventories are tracked from various sources for each of the last 4 runs in table 4. Panels are as follows, **A:** Flux of newly germinated cells from off-shore (> 50m deep) cyst beds. **B:** Flux of newly germinated cells from in-shore (< 50m) cyst beds. **C:** New cells produced via net growth. **D:** Flux of cells through the northern boundary, presumably from the EGOM. **E:** Mean concentration along the northern boundary (over the top 10m) **F:** The current velocity across the northern boundary. Negative values are into the domain. **G:** The total number of cells within the domain that originated from offshore cysts. **H:** The total number of cells in the domain that originated from inshore cysts. **I:** The total number of cells that originated from the EGOM (north boundary).

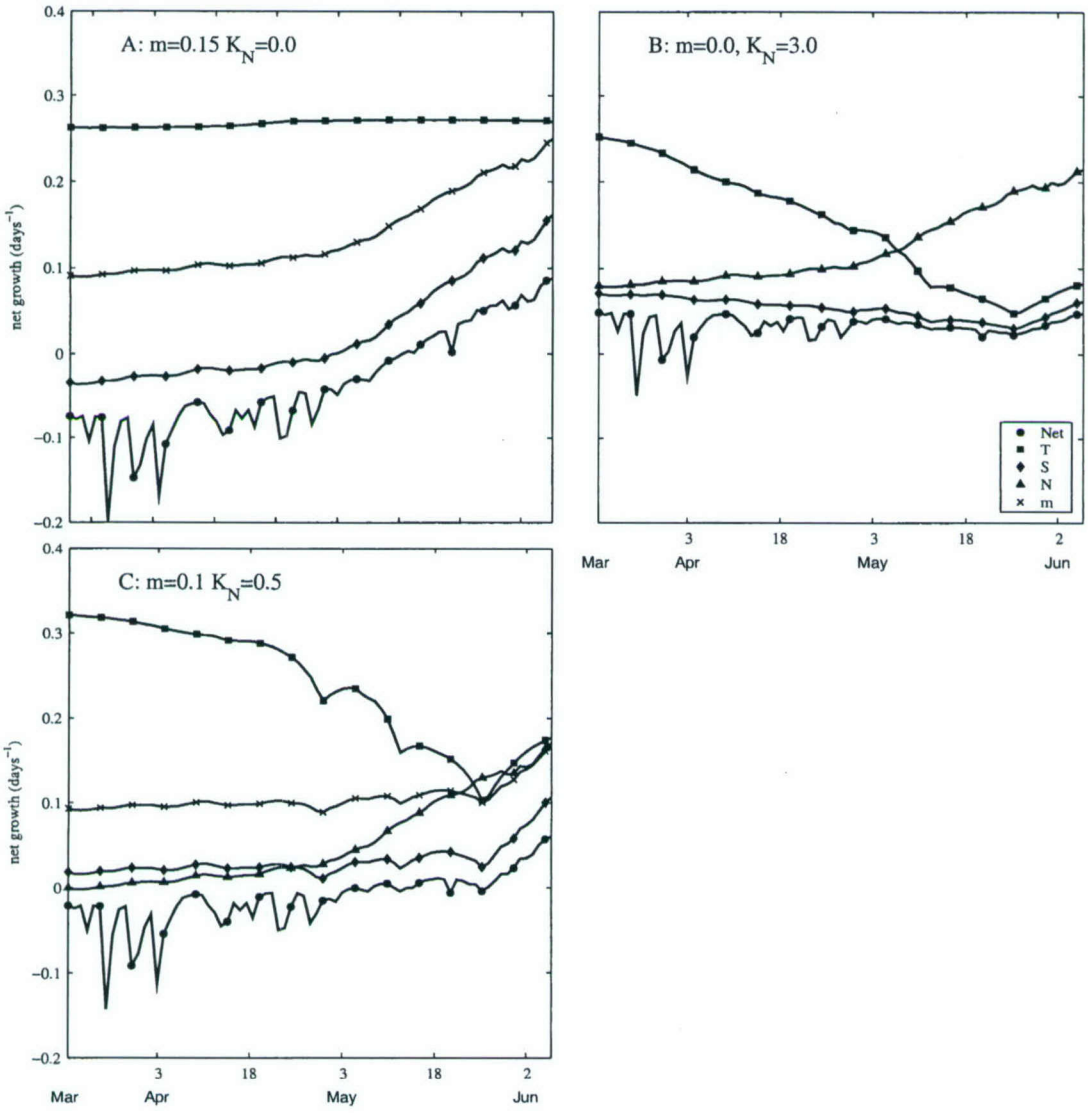


Figure 13: Net growth analysis. Panels correspond to simulations in columns 2-4 of table 4 (marked in upper left corner of each plot). The line marked with closed circles is the actual domain averaged net growth. Other lines correspond to what the domain averaged net growth would be with light at saturation and one other growth-influencing factor removed. Factors are T = temperature, S = salinity, N = nutrients (DIN), and m = mortality.

Chapter 4

A Comparative Modeling Study of Blooms of the Toxic Dinoflagellate *Alexandrium fundyense* in the Western Gulf of Maine in 1993 and 1994

Abstract

A coupled physical/biological model is used to study the dynamics underlying observed blooms of the toxic dinoflagellate *Alexandrium fundyense* in the western Gulf of Maine (WGOM) in 1993 and 1994. Shellfish toxicity was prevalent along the entire coast in the spring of 1993, but was less severe in 1994 and restricted to areas north of Cape Ann. A range of biological model parameters invoking different levels of nitrogen dependence and mortality found capable of recreating the timing and magnitude of the 1993 bloom (Chapter 3) is first tested against the 1994 data. The model performs similarly with parameter choices invoking moderate or strong nitrogen dependence, but the fit deteriorates otherwise. Diagnosis of simulations capable of matching prominent observed bloom features suggests that the sources of cells, realized growth rates, and total cell abundance are similar for the two analyzed years despite notable differences in the warming of surface waters and spring nutrient drawdown. This supports the hypothesis that variability in physical transport is primarily responsible for differences in shellfish toxicity between the two years.

Diagnosis of *A. fundyense* transport during the two years suggests that the main source of variability is the wind, with differences in local river inputs playing a minor role. While individual wind events last only a few days, differences in sequences of wind events drive changes in the cross and along-shore transport apparent in monthly averages. Predominant upwelling winds pushed *A. fundyense* cells away from coastal areas in April of 1994 and decreased along-shore transport relative to more downwelling favorable 1993 conditions. However, while upwelling winds retarded along-shore transport, the persistent influence of the Gulf-wide circulation ensured the eventual delivery of cells to Cape Ann during both years. The direction of flow at Cape Ann is also highly sensitive to wind, with upwelling favorable winds pushing cells offshore and around Cape Cod, and relaxed or downwelling winds favoring entry into Massachusetts and Cape Cod Bays (MB/CCB). Cells entered the bays during both years and, although influxes started nearly 1 month later in 1994, similarly sized populations were present in the region by late May. However, strong repeated upwelling in early June of 1994 flushed cells out of Massachusetts Bay and kept cells away from the coast, while continued relaxed and downwelling winds allowed cells to penetrate more deeply in 1993 and induce toxicity along the coast.

The circulation within MB/CCB (particularly that of Cape Cod Bay) is highly retentive. Cells within this region in June encounter rapidly warming surface waters that increase growth rates to an extent that cannot be countered by the simple losses and limitations within the biological model. The combination positive growth and retention leads to rapidly increasing cell abundance in the region at the end simulations during both years. This feature is most severe in simulations without nitrogen dependence, but occurs in all cases. It is suggested that increased resolution of loss/limitation processes is necessary for the model to properly capture bloom termination in this region. Casco Bay, in contrast, is less retentive and populations within that region are strongly influenced by inflows of cells from the EGOM. Increased model skill in this region requires better constraint of these inflows.

1. Introduction

Blooms of the toxic dinoflagellate *Alexandrium fundyense* are annually recurrent phenomena in the Gulf of Maine during the spring and summer months. Toxins produced by *A. fundyense* lead to paralytic shellfish poisoning (PSP), a potentially fatal illness caused by consumption of shellfish from exposed regions. This public health risk necessitates rigorous monitoring of potentially affected areas and has lead to repeated closures of shellfish beds along the coast and in the offshore waters of the Gulf of Maine (Shumway, et al., 1988). Within the marine food web, PSP has been linked to mortality of larval and juvenile stages of fish (White, et al., 1989), and even the death of marine mammals such as humpback whales (Geraci, et al., 1989). An understanding of t he factors that determine the distribution and abundance of *A. fundyense* within the Gulf of Maine is therefore of considerable scientific, economic, and public health interest.

The Gulf of Maine (Fig. 1) is a continental shelf sea separated from the North Atlantic by a series of shoals. In the spring, density contrasts between high salinity slope-water within the Gulf's three deep basins and fresher coastal waters derived from the Scotian Shelf and local river input drive a mean counter-clockwise coastal surface current (Brooks, 1985). This feature, referred to as the Maine Coastal Current (MCC), is characterized by a series of segments and branch points (Lynch, et al., 1997). The direction of flow at the branch points is modulated by a diverse set of factors including wind, river input, bathymetric effects, and the strength of the geopotential low that generally forms over Jordan Basin in response to dense slope water in its interior (Brooks and Townsend, 1989, Brooks, 1994, Lynch, et al., 1997, Pettigrew, et al., 1998). *A. fundyense* blooms within the coastal region to the south and west of Penobscot Bay, herein referred to as the western Gulf of Maine (WGOM), are considered in this study.

The region to the northeast is referred to as the eastern Gulf of Maine (EGOM). The segment of the coastal current within the WGOM if referred to as the WMCC, while the segment to the east is referred to as the EMCC.

Alexandrium species[4] are characterized by a life cycle that includes both a resting benthic cyst and a vegetative cell (Anderson, 1998), and transitions between these stages have long been thought critical to understanding bloom dynamics in coastal waters (Anderson and Wall, 1978, Anderson, et al., 1983). The transition between resting and vegetative stages occurs through the process of germination. Rates of germination are controlled by diverse factors including light, temperature, oxygen in the sediments, and an internal endogenous clock (Anderson, 1980, Anderson and Keafer, 1987, Anderson, et al., 1987, Anderson, et al., submitted, Matrai, et al., submitted). Upon germination, vegetative *A. fundyense* cells swim upward to the euphotic zone, where they undergo a stage of vegetative growth. Some strains enlist coordinated vertical migrations in response to nutrients and light during this stage (Cullen, et al., 2004). However, this does not appear to be the case for strains encountered in the WGOM (Poulton, 2001). The vegetative growth stage terminates with the formation of gametes that fuse to form a new cyst. The onset of encystment has been difficult to observe in the field, but it is thought to be a reaction to environmental stress and has been induced by nutrient depletion in the laboratory (Anderson, et al., 1984, Anderson and Lindquist, 1985).

[4] It is recognized that two forms of *Alexandrium* can be responsible for shellfish toxicity in the WGOM: *A. tamarense* and *A. .fundyense*. We consider these to be varieties of the same species(Anderson, et al., 1994, Scholin, et al., 1995). Neither antibody nor oligonucleotide probes can distinguish between them, only detailed analysis of the thecal plates on individual cells can provide this resolution. *A. fundyense* is therefore used to refer to both forms.

Populations of *A. fundyense* in the WGOM (Fig. 2) are thought to derive from a combination of germination of benthic cysts in the region near Casco Bay and transport of cells from the EGOM (Anderson, et al., 2004a, Chapter 3). Patterns in cell abundance and toxicity in the region are largely consistent with the "plume advection hypothesis" (Franks and Anderson, 1992a, Anderson, et al., 2004a). This hypothesis calls for the WMCC driven transport of established populations of *A. fundyense* from the northeast to the southwest in close association with the buoyant plume of the Kennebec/Androscoggin River. Detailed interactions between *A. fundyense* and the river plume can be complex (Hetland, et al., 2002, McGillicuddy, et al., 2003, Anderson, et al., 2004a). However, one robust and prominent dynamic is that downwelling favorable winds (those blowing toward the south/southwest) accelerate the along-shore transport and trap the plume and associated cells against the coast. Upwelling favorable winds slow along-coast transport and move the plume and cells offshore, potentially leading to dispersal. Such wind forcing dominates the transport of *A. fundyense* over short (1-3 day) time scales. However, the persistent flow of the MCC (e.g. Fig. 1) is of primary importance over seasonal time scales, with baroclinic currents generated by local river input also contributing significantly to the alongshore transport (Geyer, et al., 2004).

The interweaving of the complex life history of *A. fundyense* and the dynamic physical environment of the WGOM suggests the use of a coupled physical-biological model to diagnose bloom dynamics in the region. A previous study (Chapter 3) compared the results of such a model to *A. fundyense* observations collected in the WGOM during the spring of 1993 (Anderson, et al., 2004a, Geyer, et al., 2004). These simulations started with a simple "baseline" biological model describing the germination

of *A. fundyense* from resting cysts within the sediments and subsequent growth. It was found that uncertainty in the maximum growth rate and the depth of sediment over which cyst could germinate and reach the water column dominated the uncertainty in the baseline model results. The model/data fit of the baseline model was optimized over the uncertainty in these two parameters using the method of maximum likelihood. Results showed that the baseline biological model embedded in a simulation of the WGOM circulation could match the magnitude and spatial character of the bloom early in the spring, but severely overestimated observations in May and June. Two additional parameters were thus considered: a spatially and temporally mean mortality (m), and a dependence of growth on dissolved inorganic nitrogen (DIN) modeled via Monod kinetics with half-saturation constant K_N. Optimal model results then captured the timing and magnitude of the *A. fundyense* bloom during the period of observation (April 10-June 6), albeit not the detailed patchiness. However, while the baseline model was rejected, statistical analysis was unable to strongly differentiate between the model/data fit attained by simulations using moderate mortality, a high nutrient dependence, or a combination of both (Fig. 3).

The level of uncertainty evident in Fig. 3 prevented analysis of detailed aspects of bloom development, but several features of the broad-scale dynamics were robust over the parameter range. Cysts lying in the waters offshore of Casco Bay accounted for the majority of the spring *A. fundyense* population in the WGOM during the period bounded by the surveys. Inputs of cells from the EGOM became more important later in the spring and this may serve as the dominant source of new cells to the region in the summer. Domain-averaged net growth rates remained low (< 0.05 day^{-1}) for the duration

of the simulation, as rates were first limited by low water temperatures and then by a combination of nutrient dependence and mortality. However, rates could be elevated locally and often added notable spatial structure to the bloom.

While these results contribute additional insight into the factors controlling the initiation and development of the 1993 *A. fundyense* bloom, the dynamics have yet to be tested against a second independent set of observations to determine the robustness of the inferred dynamics. Fortunately, such a set of was collected during the spring of 1994 (Fig. 4, Anderson, et al., 2004a). Interestingly, patterns in shellfish toxicity and cell abundance were notably different between the two years, suggesting a challenging test of the robustness of the modeled dynamics. In 1993, toxicity was prevalent along the Maine coast, and extended into Cape Cod and Massachusetts Bays. In 1994, toxicity was low along the Maine Coast and was not observed in Massachusetts and Cape Cod Bays. These differences were primarily attributed to the increased prevalence of upwelling winds in 1994, which push *A. fundyense* populations offshore, slow their propagation along the coast, and lead to greater dispersal (Anderson, et al., 2004a).

The objectives of this study are twofold. The first is to evaluate the optimal parameter values suggested by the 1993 analysis against the 1994 data. This provides a first assessment of the inter-annual robustness of the biological model within the WGOM and may also narrow the parameter uncertainty space in Fig. 3. The second objective is to provide additional insight into the physical and biological dynamics underlying the differences in the 1993 and 1994 blooms and subsequent patterns in shellfish toxicity. Of particular interest are the bloom dynamics near Casco Bay and those within Massachusetts Bay and Cape Cod Bay (MB/CCB) and subsequent toxicity within the

region. The first objective is attained by enlisting a modified version of the 1994 physical simulation used by Anderson et al. (2004a), combining it with the biological model used in Chapter 3, and comparing the properties of the model/data misfit to those of the 1993 simulations. This is done over a range of parameter values within the confidence region of Fig. 3 (circled). The second objective is approached through diagnosis any validated simulations resulting from the first step.

2. Methods

2.1 The Field Data

The observations used in this study were collected as part of the Regional Marine Research Program and will herein be referred to as the "RMRP surveys". Detailed descriptions of the field efforts can be found in Anderson et al. (2004a), Geyer et al. (2004), and Martorano and Loder (1997). The survey coverage and observed surface *A. fundyense* distributions are summarized by Fig. 4 (1993 cruises), and Fig. 5 (1994 cruises). *A. fundyense* cell counts were taken at the surface and, for a subset of the stations, at 10 meters. Hydrographic and nutrient data, including phosphate, silicate, nitrate, nitrite, and ammonium was also collected. Nitrogen was predominantly limiting assuming Redfield Stoichiometry (Martorano and Loder, 1997). The Maine Department of Marine Resources and the Massachusetts Division of Marine Resources conduct routine monitoring of shellfish toxicity in the region via the standard mouse bioassay for PSP (AOAC 1980). Data from the blue mussel *Mytilus edulis* at key stations in 1993 and 1994 are summarized in Fig. 6 (Anderson, et al., 2004a).

Survey coverage and timing during the two years is notably different, and reflects a change in the sampling strategy. The 1993 surveys were a series of 5 cruises of roughly

equal temporal spacing (~ 2 weeks) and coverage of the majority of the domain. The 1994 surveys sought to examine short-term changes in the cell distribution by conducting repeated large-scale surveys with a separation of only several days. These large-scale surveys were then augmented by several ancillary cruises with partial study area coverage. The 1994 surveys also started later in the season (April 28 rather than April 12), but continued through June. This change required several adjustments to the methodology in Chapter 3, most notably a change in the manner by which levels of dissolved inorganic nitrogen (DIN) is specified. This and other adjustments will be highlighted in the sections that follow, and robustness of previous results to these adjustments will be shown.

Moorings were also deployed as part of the field effort (Geyer, et al., 2004), and the Cape Porpoise P2 location (Fig. 1) common to both years is used herein. Currents were measured using a vector-measuring current meter (VMCM) at 5 meters, and a vector averaging current meters (VACM) at 27 and 50 meters. The near surface measurements required a 25° clockwise rotation to correct for compass error believed to be due to interference between battery packs and adjacent sensors (see Geyer at al., 2004 for details). The correction has a minor influence on the along-shore flow, but the observed cross-shore component should be treated with caution.

2.2 The Biological Model

The baseline biological model contains parameterizations of the germination and growth of *A. fundyense* and is summarized in Fig. 7 and Table 1. Detailed descriptions of the functions and their construction can be found in Anderson et al. (submitted), within Chapter 3, and within the appendices. It is particularly notable that the model has only

one biological state variable: the concentration of *A. fundyense*. Ecosystem effects on *A. fundyense* abundance are therefore parameterized through approximations of their influence on the rates within the *A. fundyense* population dynamics model.

Two additions to the baseline model are considered: mortality and nitrogen dependent growth. Mortality (m) is defined loosely as a vegetative cell being removed from the water column. It is meant to represent the mean loss rate of *A. fundyense* via cell mortality, zooplankton grazing, and encystment over the course of bloom initiation and development and is therefore applied as a constant average rate (day^{-1}). The intent of applying mortality in such a rudimentary way is to evaluate the necessity of a first order loss term to recreate the observed bloom magnitude, given knowledge of the source and growth characteristics. Dependence on dissolved inorganic nitrogen is modeled by the Monod formulation with half-saturation K_N. It is recognized that this formulation is problematic in unsteady conditions due to potential variability in nitrogen uptake physiology and the internal nitrogen cell quota (e.g. Conway and Harrison, 1977, Droop, 1983). However, while the Monod formulation is limited in its ability to represent detailed nitrogen metabolism, it is valid for assessing the average level of the dependence of growth on ambient DIN and should be interpreted in this way. The DIN concentration is provided by relationships linking it to hydrographic properties (see section 2.4).

The final equation governing the evolution of *A. fundyense* within the domain is:

$$\frac{\partial C}{\partial t} + \nabla \cdot \left((v + w_a) C \right) = \nabla \cdot K \nabla C + \mu C - mC + F_g + F_B$$

Where C is the concentration of *A. fundyense*, v is the fluid velocity, w_a the vertical swimming rate of *A. fundyense*, K is the diffusivity, μ is the growth rate, m the mortality rate, and F_g is the change in concentration due to the flux of new cells from the sediment

via germination, and F_B is the change in cell concentration due to the flux of cells through the horizontal boundaries of the domain. w_a is attenuated in the euphotic zone so that general consistency with the surface to 10 meter *A. fundyense* concentrations is maintained (see Chapter 3). The initial concentration of *A. fundyense* is set to 0 everywhere, as the beginning of the run (March 19) is generally before the start of the bloom season. Observed cell concentrations along the northern-most transect are extrapolated onto the northern boundary to provide the EGOM inflow condition. Concentrations along the other boundaries are assumed 0. Interior concentrations are advected out during outflow, and boundary concentrations are relaxed back to the specified values during subsequent inflows. Time scales for this relaxation were chosen to represent the typical duration of outflow events along each boundary (0.5 days along the northern boundary, 2 days along the eastern boundary, and 4 days to the South).

The relative simplicity of this biological model is recognized, and it is only intended that it capture the timing and magnitude of the observed bloom, not the fine scales of variability. Neglected complexity should be considered intrinsic to the hypotheses represented by each model formulation: neglect is equivalent to the assumption that the importance of a given process is of second order relative to those included at the space and time scales of interest. Model data misfits may then be analyzed in light of this neglected complexity and new hypotheses formulated.

2.3 The Physical Model

The physical component of the dynamics model is provided by the 3D, non-linear Estuarine, Coastal and Ocean Model (ECOM) (Blumberg and Mellor, 1987). Its formulation is that initially presented in McGillicuddy et al. (2003) and Anderson et al.

(2004a) with modifications described in Chapter 3. The study domain (Figs. 1, 2) is covered by a grid of 130 cells in the along-shore direction and 70 in the cross-shore. Grid cells dimensions range from 1.5-3 km. 12 sigma layers (i.e. each layer is a constant fraction of the water depth) are specified in the vertical with increased resolution near the surface to better resolve river plume dynamics. Vertical mixing is calculated using the Mellor-Yamada level 2.5 turbulence closure (Mellor and Yamada, 1982, Galperin, et al., 1988).

Forcing (Table 2, Fig. 8) was chosen to capture the principle aspects of the large-scale circulation and hydrography in the WGOM, particularly the transport associated with the WMCC and the vernal warming of surface waters. Primary differences between the two years include increased local river inputs during April of 1993, but a more sustained May input in 1994. In addition, March and April of 1993 were marked by several pronounced downwelling favorable wind events, while the same period in 1994 exhibited more consistent upwelling. This shifted in May, with 1994 having more downwelling favorable events, and then back to 1993 in June. Lastly, 1994 surface waters were saltier, and this is reflected in both the initial and boundary conditions (Table 2). The period covered by the physical simulation was expanded from March 19-June 6 to March 19-July 1 to cover all of the 1994 data. This also encompasses the majority of the period of maximum germination potential.

The primary adjustment from previous efforts is that the application of climatological barotropic forcing is now via a Flather condition (Flather, 1976) rather than a clamp on the sea surface elevation. This specification relies on both the climatological depth averaged velocity normal to the boundary ($\overline{U}_{n,c}$) and the

climatological sea surface elevation at the boundary (η_c) to calculate a depth averaged normal velocity to force the model ($\overline{U}_n$) at each time step:

$$\overline{U}_n = \overline{U}_{n,c} \pm \frac{c}{h}(\eta - \eta_c)$$

Where $c = \sqrt{gh}$ is the external gravity wave speed, and η is the sea-surface elevation at the first interior node. The sign of the above relation is set to radiate perturbations from the expected climatological forcing outward at the gravity wave speed. The above condition thus maintains stability by allowing a temporary response to local dynamics, but relaxes back to specified forcing to maintain the characteristics of the mean, climatological flow. This switch was made for stability purposes only, and the condition is not claimed to be any more or less realistic than the previous clamped condition.

2.4 Nutrients

Previous work (Chapter 3) relied on a linear interpolation between biweekly surveys to specify DIN concentrations. However, the less regular spacing of the 1994 cruises and their later start (after the spring nutrient drawdown) prevents application of this approach herein. Fortunately, notable relationships between DIN and hydrography exist (Fig. 9). While an inverse relationship with DIN is present both for temperature and salinity, the decline in DIN in saline waters near 5° C is particularly striking. This latter trend is consistent with spring bloom initiation (and subsequent nutrient drawdown) being driven by increases in irradiance and limitations to the mixing depth in a manner similar to the dynamics described by Sverdrup (1953). Such a balance has been invoked to explain spring blooms in the WGOM in numerous studies dating back to the work of Gran and Braarud (1935) (Townsend and Spinrad (1986) provide additional discussion

and an overview of this early work). It is recognized that thermal stratification is not the only factor limiting the mixing depth. However, the strong linkage between sea surface temperature, increasing irradiance, and increasing water column stability in temperate seas suggests SST as a good correlate for the spring nutrient drawdown. The following functional fit was thus used to isolate the prominent patterns between DIN and hydrography (Fig. 9):

$$N = N_{\max} - \delta_{NT} f(T) + \delta_{NS} f(T) f(S)$$

Where $f(T)$ and $f(S)$ are scaling factors between 0 and 1:

$$f(T) = \frac{1}{2}\left(\tanh(\alpha_T T - \beta_T) + 1\right)$$

$$f(S) = \frac{1}{2}\left(\tanh(\alpha_S S - \beta_S) + 1\right)$$

Constants and their interpretations are listed in Table 3. The functional fits were derived using least-squares on the data after it had been power transformed ($p = 0.25$) to create symmetry in the residuals (e.g. Hoaglin, et al., 1983). This reduces the influence of sporadic high patches and creates an effect similar to fitting the median of the data rather than the mean.

There is considerable small-scale patchiness in the nutrient field that is not captured by the functional fit, and the R^2 value is modest (0.34). However, this is partly due to the scarcity of high DIN observations. Binning the data clearly reveals that the primary seasonal patterns are captured within the combined data (Fig. 10, top row). However, breaking down the data by year reveals a general lack of pre-drawdown points in 1994. It is thus recognized that the validity of this function in 1994 rests on the assumption that the relationship between the DIN drawdown and hydrography is similar

during the two years. This general consistency is supported by the work of Petrie and Yeats (2000), although exceptions have been noted (Keller, et al., 2001).

The one consistent outlier to the trends of Figs. 9-10 was the station immediately adjacent to Boston Harbor, which tended to show elevated nitrogen regardless of the hydrography. This pattern is attributed to nutrient inputs from Boston and the robust nature of this result is supported by more detailed, concurrent studies of the region (Kelly and Doering, 1997). The DIN concentration at Boston Harbor was thus specified as the mean of the observations taken during the 1993/1994 surveys (5.95 μM).

2.5 The Model/Data Comparison

Model performance in 1994 is measured relative to that in 1993 according to the size and spatial/temporal scales of the misfits. These properties are estimated via the method of maximum likelihood (e.g. Cox and Hinckley, 1974) applied in the manner described in Chapter 2. Essentially, the covariance properties of the misfits associated with a given choice of biological model parameters are estimated in such a way that the resulting covariance matrix best explains the misfits in a probabilistic sense. While the spatial/temporal scales over which misfits are coherent provide valuable information and will be discussed, the misfit variance serves as the primary validation metric.

The primary assumptions made in applying the methodology are that the differences of the log transformed observations and model output have an approximate normal distribution, and that the covariance decay is adequately described by:

$$C_{ij} = \rho_{\Delta t} \times \sigma^2 \times \exp\left(- r_y \times \sqrt{\Delta y^2 + \left(\frac{r_x}{r_y} \Delta x \right)^2} \right)$$

Where C_{ij} is the covariance between any two points i and j, σ^2 is the estimated misfit variance and lies along the diagonal of the covariance matrix, Δx and Δy are the approximate cross-shore and along-shore distances between i and j (km), r_x and r_y are the cross-shore and along-shore covariance decay coefficients (km^{-1}), and $\rho_{\Delta t}$ is a temporal covariance term. The rationale behind this model choice is that it is a relatively simple combination of parameters that is able to represent the primary observed characteristics of the misfit. Chapter 2 offers a more extensive discussion and justification.

The change in sampling strategy in 1994 does require a small adjustment to the covariance function. In chapter 1, the roughly equal bi-weekly spacing of the cruises made it possible to use the number of cruises separating any two observations as a proxy for temporal lag. Thus, $\rho_{\Delta t=1}$ corresponded to the correlation between points at the same spatial location, but separated by 1 cruise and so forth. The less regular spacing of the cruises in 1994 makes it necessary to enlist a second parametric relationship:

$$\rho_{\Delta t} = \exp(e^{-r_t t})$$

Where t is the time (days) between the midpoints of the cruises, and r_t is a temporal decay coefficient ($days^{-1}$).

3. Results

3.1 The Physical and Nutrient Model

The vernal warming of the sea surface is well captured by the model during both years (Figs. 11 and 12, top panels). The modeled and observed salinity (middle panels) both show the influence of strong wind forcing, with downwelling favorable winds

restricting the plume to the coast and sharpening salinity gradients (e.g. cruises 1 and 2 of 1993), and upwelling favorable winds spreading the plume offshore (e.g. cruise 3 of 1993, cruises 1a, 1b, 5a and 6 of 1994). While the spatial relationship between the model salinity and observations is consistent, there is a small systematic bias in the model (+0.7 and +0.5 PSU in 1993 and 1994). This has been attributed, at least in part, to elevated vertical mixing due to sharp variations in the depths of the models sigma layers over regions of steep topography (Anderson, et al., 1998). However, contributions may also derive from the initial and boundary conditions.

The modeled DIN concentrations (bottom panels of Figs. 11-12) are predominantly linked to temperature and consistent with the bulk of the observations. DIN is largely depleted throughout most of the period covered by the surveys, with the exception of cruises 1 and 2 of 1993. The hydrographic relationships have captured the observed depletion of DIN by May in 1994 (Fig. 12, cruise 1a, 1b), relative to the elevated levels during the same time period in 1993 (Fig. 11, cruise 2). The highly localized nitrogen signatures at the mouths of the major river outflows are apparent in the modeled fields, although they are damped relative to the observations.

Modeled and observed currents at the Cape Porpoise mooring are generally consistent in both 1993 and 1994 at all depths (Fig. 13a-b). In 1993, strong alongshore surface currents were associated with an early spring freshet and several pronounced downwelling events in April. The strength of this current is maintained throughout May in both the model and the observations. There is some disagreement in the cross-shore component at the surface, with the observations suggesting a more offshore flow. However, it is unclear how much of this is due to the aforementioned compass error. In

June, the modeled and observed velocities weaken considerably presumably in response to reduced local baroclinicity after the abatement of the spring freshet as well as prevalent upwelling favorable winds.

In 1994, surface currents are weaker in April relative to 1993 and have a larger offshore component. This decrease is associated with small local river inputs during the first 2 weeks of the month and persistent upwelling winds. The surface along-shore velocity increases in May following the spring freshet. There are several notable downwelling favorable events (e.g. May 18) and river output is relatively high throughout the month. Surface current strength decreases dramatically in June and turns offshore in both the model and observations. This is associated with sustained upwelling and a rapid decrease in local freshwater input.

Overall, the model shows considerable skill in recreating the primary features of the spring hydrography, nutrients and circulation in 1993 and 1994. It is recognized that the modeled fields are generally damped relative to the observations (particularly with respect to DIN). However, the level of skill demonstrated above suggests that the physics is adequate for the evaluation of the coupled model's ability to recreate the timing and magnitude of bloom events. Possible consequences of missed physical and nutrient dynamics will be discussed in more detail below.

3.2 Modeled Bloom Assessment

Comparison of the results of simulations using a range of parameter values from the confidence interval in Fig. 3 (circled) suggest that the 1993 misfit statistics from Chapter 3 are stable to the methodology adjustments required for this study (Table 4,

columns 5 and 6). There has been a slight downward shift in the misfit variance, but it is well within the uncertainty derived from the maximum likelihood estimation.

The application of the 1993 derived parameter values to the 1994 data set (Table 4, column 7) reveals that biological models invoking a moderate to strong nitrogen dependence maintain similar performance during both years. The variance and spatial scales of the misfits have increased slightly relative to those in 1993, but changes are well within the estimated standard deviations about the variance parameter. Simulations relying exclusively on mean mortality, in contrast, show a sharp jump in the variance of the misfits and their spatial scale from 1993 to 1994. Deterioration is also evident in biological models invoking a low dependence on nitrogen and moderate mortality (K_N = 0.5 μM, m = 0.10 day^{-1}), which were narrowly favored in the 1993 analysis.

With the exception of these latter two cases, the spatial decay scale of the misfit variance (~20 km e-folding) roughly corresponds to the observed *A. fundyense* patch scale (Chapter 2). The fact that larger spatial scales do not dominate the misfit statistics suggests that the low-frequency, large-scale aspects of the observations are reasonably captured by the model. The temporal decay is much faster in 1994, but this is primarily due to the presence of more closely spaced cruises, as both results minimize temporal covariance between adjacent surveys and rely instead on spatial correlation within the cruises to explain the misfit properties.

Comparisons for three of the simulations in Table 4 with increasing levels of nitrogen dependence are shown in Fig. 14 (1993) and Fig. 15 (1994). The magnitude of the early season *A. fundyense* population and its intensification through June are apparent in the model, although features are not as sharp as suggested in the observations. Several

characteristics of the along-coast progression are also reasonably captured, although there is also some disagreement. In 1993, both modeled and observed *A. fundyense* populations in MB/CCB are limited through the second cruise (4/28-4/30), before substantial influx and subsequent increases in concentration thereafter. This is consistent with the shellfish toxicity data (Fig. 6), which show an initial spike in toxicity at the Annisquam station on May 3, and toxicity at Cohasset on May 17. After May 17, both the model and the data show increases in cell abundance and toxicity in Massachusetts Bay, and penetration into Cape Cod Bay.

In 1994, the modeled population is offshore and south of that observed during cruises 1a and 1b. This may be related to the limited constraint of the physical and biological quantities along the northern boundary and will be discussed in more detail below. The near complete absence of *A. fundyense* from MB/CCB during the first two cruises is well reproduced by all biological model settings. Low shellfish toxicity in 1994 was observed at Annisquam on May 9, and again between May 26 and June 13. These features are consistent with patterns suggested by the model output, which show low cell concentrations in the area just north of Cape Ann by the end of April, and more substantial abundances by late May. Both the model and observations suggest that *A. fundyense* was within Massachusetts Bay by late May, early June. However, the model predicts the propagation of cells into Cape Cod Bay, where no toxicity and few cells were observed. After *A. fundyense* enters the bays, strong and persistent upwelling winds during the late May/early June period in 1994 drive them offshore, as suggested by a persistent area of relatively low *A. fundyense* concentration adjacent to the Scituate and Cohasset stations from cruise 5a through cruise 7. This flushes many of the cells out of

Massachusetts Bay, but the (potentially erroneous) cells within Cape Cod Bay are maintained.

Despite some agreement between the model and data initial statistical and qualitative comparison, there are several common model/data misfits. These start with the failure of all of the parameter combinations to represent the substantial small-scale variability present in the observations. This was accepted *a-priori*, as the goal is to capture the timing and magnitude of the bloom. However, larger scale misfits also exist. It was noted in Chapters 2 and 3 that the 1993 simulations tend to exhibit moderate but systematic over-estimations of the observed cell abundance in MB/CCB during cruise 3. A second persistent region of misfit in both years develops near Casco Bay, where the model has difficulty matching the magnitude of the observed concentrations (e.g. cruise 4 in 1993 and particularly cruise 1a, 1b in 1994). The most striking difference between the model and observations however, is the degree of bloom proliferation in MB/CCB in mid-June of 1994. This is particularly notable in $K_N = 0$ μM case, and it is this misfit that drives the deterioration in the statistics evident in Table 4. All of these misfits will be diagnosed more closely below.

3.3: Diagnosis of the Modeled Bloom Dynamics

The focus of the diagnosis starts with a comparison of the domain-wide patterns in 1993 and 1994, and then shifts to MB/CCB and Casco Bay regions along the transport between them. Three simulations from Table 4 showing similar misfit properties are analyzed: $K_N = 0.5$ μM, $m = 0.1$ day^{-1}; $K_N = 1.5$ μM, m=0.05 day^{-1}; and K_N=3.0 μM, m = 0 day^{-1}. The $K_N = 0.5$ μM, $m = 0.1$ day^{-1} case is included as a low K_N bounding case, as the estimated standard deviations around the misfit variance nearly intersect and it was

found optimal in Chapter 3. These three simulations differ not only in the relative importance placed on mortality and nutrient dependence, but also in source and growth dynamics. Simulations with a high dependence on mortality generally call for larger germination sources and high growth (d_g and μ_{max} in Table 4), while those relying solely on nutrients for limitation invoke a smaller source and a lower growth rate. The simulations thus span a range of proposed source and development dynamics capable of explaining the primary observed features of spring *A. fundyense* blooms in the WGOM.

3.3.1: Domain-wide Bloom Patterns

Diagnosis of the domain-averaged dynamics (Figs. 16-18) suggests that the contributions from different sources of *A. fundyense* cells in the WGOM and the overall biological dynamics were similar in 1993 and 1994 and consistent with the results of Chapter 3. The germination of cysts lying in deep sediments provides the bulk of the flux of new cells into the domain for both years through May (Fig. 16). These cysts lie in dark, cold conditions and germinate at slow rates (~1%/day), forming a persistent source that depletes by mid-June. Cysts in shallow waters germinate at only slightly faster rates due to rapid light attenuation in the water column and sediments and deplete over a similar 3-month time scale. However, the shallow cyst abundance is much less and germination in shallow waters thus contributes little. The flow of cells from the EGOM gradually increases in importance throughout the simulation. Net growth (i.e. growth - mortality) makes a notable yet non-dominant contribution until late May. After this point, additions via net growth rapidly increase, becoming dominant in June. This is

most pronounced in simulations with only weak dependence on nitrogen, but actually occurs in all cases.

The impact of growth between the two years is similar despite the fact that the spring nutrient drawdown is several weeks earlier in 1994 (Fig. 17). The modest influence of this effect within the model is due to the complimentary limitation of growth by temperatures and nutrients (Chapter 3, McGillicuddy, et al., submitted). In cold waters, DIN concentrations are high, but the attainable net growth rate is low (i.e. Fig. 7). In warm waters, the attainable growth rate increases, but nutrients decrease (i.e. Fig. 10). The result is relatively low net growth through early June for all biological model parameters in both years (Fig. 17, middle panel). By mid-June, net growth has increased in all cases, leading to the large cell budget contributions apparent in Fig. 16. The percent enhancement in *A. fundyense* abundance relative to simulations with net-growth set to zero reflect these pattern in growth rate (Fig. 17, bottom panel).

The resulting number of *A. fundyense* cells in the domain is similar for the two years both in total and when divided by source (Fig. 18). This result, combined with those of Figs. 16-17 supports the hypothesis (Franks and Anderson, 1992a, Anderson, et al., 2004a) that changes in the severity of toxic outbreaks between years are primarily the result of changes in transport, not changes in bloom magnitude driven by variability in the factors governing germination and growth. It also reaffirms that, in a domain-averaged sense, the germination of cysts lying in large cyst beds offshore of Casco Bay are a plausible source of cells for spring blooms in WGOM. These results rest on several assumptions, most notably that the initial cyst distribution was stable between 1993 and 1994. This assumption will be addressed in greater detail during the discussion.

The tendency of the modeled bloom to grow rapidly under all biological model settings in late June rather than terminate (as supported by the shellfish toxicity data) suggests that an aspect of the termination dynamics may be missing or incompletely represented in the present model. Within the model simulations, this proliferation is driven by three factors: 1) the tendency for hydrodynamic retention of cell within areas of complex coastal geometry (Figs. 14-15, particularly under the arm of Cape Cod), 2) high maximum growth rates at high temperatures (Fig. 7), and 3) the simplicity of the DIN dependence and mortality. The fact that all simulations have sharply increasing growth rates and cell numbers by mid-June suggests that the "mortality only" case is simply the least effective at capturing bloom termination. This aspect of the simulations and its implications will be addressed in greater detail during the discussion. For now, it is noted that analysis focuses on dynamics through early June in recognition that the model likely departs from observed dynamics after that point.

3.3.2: Along-shore Transport and Bloom Patterns in Massachusetts and Cape Cod Bays

One of the most striking differences between the two years was the high shellfish toxicity observed in MB/CCB from late May through June in 1993, compared to its complete absence in 1994. Model output shows a clear correspondence between the net flux of *A. fundyense* into MB/CCB from the north and downwelling favorable winds (Fig. 19, top two panels). All of the major net inflow events in the model correspond with downwelling or relaxed wind conditions, but the reverse is not always true. If the downwelling occurs too early in the season, *A. fundyense* has yet to reach the Cape Ann branch point from its remote sources. Such events occur in 1993 in late March, and in

1994 in mid-March and early April. Note that while the April 10-12 downwelling event leads to a prominent pulse of cells in 1993, the 1994 simulation shows very little response to downwelling winds during the same period.

The difference in this latter aspect of the inflow response between the two years is due to variability in early season alongshore transport velocity of *A. fundyense* from the sources to the north and the Cape Ann Branch point. The monthly mean modeled along-shore transport velocity of *A. fundyense* along a transect stretching to the 125m isobath at Cape Porpoise (see Fig. 2 for location) is southwest during both years, but faster in April of 1993 than in 1994 (Fig. 19, second row, text). Sensitivity tests interchanging the river and wind forcing reveal that wind patterns were primarily responsible for this difference. The mean along-shore transport velocity associated with the downwelling favorable 1993 wind patterns are nearly a factor of 2 greater than that produced in otherwise identical simulations but forced with 1994 wind (Fig. 19, third row). Alternation of the local river input (Fig. 19, bottom row) had a much less profound influence on the transport.

In May, all simulations again exhibit persistent southwesterly transport velocities. Increases in May velocities are evident in 1993 simulations with 1994 wind and/or river forcing. However, closer inspection of model output (not shown) suggests that this is due to differences in the deep (~100m) salinity field between Jeffreys Ledge and the coast that accrue during the simulation. 1993 simulations combined with 1994 wind and/or river forcing show less freshening of this water during May relative to those featuring just 1993 forcing. This saltiness leads to a deepening of a pressure low offshore of Cape Porpoise in mid to late May that persists through June. Focus herein is on differences in the early season transport and this feature of the sensitivity simulations is not diagnosed

herein. It is noted, however, that the evolution of the salinity field within the complex bathymetry of the WGOM can influence the transport notably.

To further quantify the contributions of local river input and wind to net transport, simulations were run with each removed (Fig. 20). Results of the removal of wind forcing show a steady transport velocity of similar magnitude but less variability than those in Fig. 19. There is first a net inflow of cells into MB/CCB during April, and then a steady outflow. This transition occurs after the development of a high pressure in the bays in response to the accumulation of freshwater, as well as the outflow of previously introduced *A. fundyense* populations growing within the region. It is notable that, in the absence of a significant pressure gradient, the "no wind" tendency at the Cape Ann branch point is to direct flow into the bay. The simulation eliminating inputs from local rivers (bottom panel) suggests that these rivers are not critical to the along-coast flow or delivery of cells into the bays. The transport velocity driven by the Gulf-wide circulation and the flow of freshwater through the northern boundary from remote freshwater sources (e.g. the Penobcot river) is of similar magnitude to simulations that include local river inputs.

Inspection of the cell budget within MB/CCB (Fig. 21) reveals patterns reflecting the transport in Fig. 19 and that parallel the domain-averaged growth in Fig. 17. Cells are introduced to the region much earlier in 1993, and the total abundance is markedly greater in April and early May of 1993 than in 1994 for all three analyzed biological models. However, the two years converge by late May and early June due to the persistent southwesterly flow of the Gulf-wide circulation and sustained downwelling on May 16-20 (refer to Fig. 19). During the first two weeks of June, winds in 1993 are light

or downwelling favorable while 1994 exhibits a series of strong upwelling wind events punctuated by brief relaxations. The former patterns allow cells to penetrate more deeply in Cape Cod Bay, while the latter moves cells away from the coast and "pumps" them out of Massachusetts bay (i.e. note the series of strong net outflows associated with upwelling events in 1994).

Patterns of growth within MB/CCB mirror those over the rest of the domain, although they are slightly elevated due to the presence a limited area of high DIN in Boston Harbor. The increases in growth rates that lead to the proliferation of cells throughout the domain occur earlier in the season due to more rapid warming (Fig. 21, middle panel). This leads to very sharp June increases in cell abundance beyond that which can be accounted for by inflow, particularly for the low K_N case (Fig. 21, top panel). This result suggests that dynamics within the MB/CCB contribute strongly to the rapid increases in total cell abundance and growth rates noted in the domain wide averages (Figs. 16-18) at the end of the simulation. Lastly, it is notable that the *A. fundyense* populations within the region are primarily of WGOM origin (Fig. 21, bottom panel).

3.3.3: Bloom Patterns near Casco Bay

The region near Casco Bay has been identified as a persistent region of moderate misfit in the model. Growth patterns are similar to those throughout the domain (Fig. 22, middle panel), but notable June increases in *A. fundyense* cell abundance are only apparent in the low K_N case (Fig. 22, top panel). This suggests that cell losses via advection largely offset the influence of positive net-growth, contrasting sharply with the

MB/CCB region. Analysis also shows that the modeled population in this region is strongly influenced by cells from the EGOM (Fig. 22, bottom panel).

4. Discussion

4.1: Explaining Patterns in the observed A. fundyense *Blooms in 1993 and 1994*

This study suggests the plausibility of the following dynamics to explain patterns in observed *A. fundyense* abundance and shellfish toxicity in the WGOM during 1993 and 1994: Persistent sources of new *A. fundyense* cells were provided via germination from cyst beds near Casco Bay and the inflow of vegetative cells from the EGOM during both years. Germination of cysts off-shore of Casco Bay (> 50m) provided the majority of cells, but inflow from the EGOM became more important later in the spring and within the Casco Bay region. Net growth rates were similarly low in both years despite differences in vernal warming and DIN. This was due to the inhibitory effects of both low temperature and low nutrients on growth and the fact that favorable conditions for one of these factors correlates strongly with unfavorable conditions for the other.

A. fundyense cells were transported to the south and west through the action of Gulf-wide circulation with some enhancement via local river inputs. Wind patterns provided the most significant source of variability between years. Upwelling winds (i.e. April 1994) slowed the along-shore transit and moved cells away from the coast, while downwelling winds accelerated transport and delivered cells to inshore areas (i.e. April 1993). Though individual wind events lasted only a few days, differences in monthly wind patterns were responsible for significant changes in the along-shore *A. fundyense* transport velocity evident over longer time scales. The persistent influence of the Gulf-wide circulation ensured that *A. fundyense* cells eventually reached the Cape Ann branch

point in both years. This influence, and a series of downwelling events in May of 1994 largely removed early season differences in the along-shore extent of bloom during the two years. This resulted in similar cell abundances in Massachusetts Bay in late May of both years, and consequently a similar potential for wide-spread June toxicity.

Strong confirmation of the dynamics underlying the toxicity differences during the two years in June is limited by the proliferation of modeled *A. fundyense* populations and the suspicion that these populations may have penetrated too deeply into Cape Cod bay in 1994. However, evidence suggests that repeated upwelling during the first weeks of June 1994 was critical to the absence of toxicity within the region in 1994. These winds created a persistent buffer between *A. fundyense* cells and the Scituate and Cohasset stations and "pumped" cells out of the region. Downwelling and relaxed winds during this same period in 1993, in contrast, were critical to the shoreward movement of cells in 1993 and their penetration into Cape Cod Bay.

This set of dynamics is largely consistent with previous explanations for the differences between the two years (Anderson, et al., 2004a) and the dynamics outlined in the original plume advection hypothesis (Franks and Anderson, 1992a). At the most fundamental level, the assertion that differences in physical transport not the biological dynamics are primarily responsible for inter-annual differences in toxicity has withstood scrutiny within a coupled physical-biological model. It is noted however, that this result is highly dependent on the presumed inter-annual stability of the cyst map. While mechanisms for the replenishment of these cyst beds have been suggested (Anderson, et al., submitted, McGillicuddy, et al., submitted) these are still not well constrained and it

is recognized that the dynamics described herein may be influenced by longer term trends in the cyst distribution.

The above analysis also provides a quantitative look at the contributions made by various physical and biological elements of the bloom dynamics, and has identified several areas where the modeled dynamics may be flawed. These dynamics were discussed in a domain-wide sense in Chapter 1, and the consistency between 1993 and 1994 was demonstrated above. This section will therefore focuses on dynamics in two key regions and the transport between them: Casco Bay and the MB/CCB.

4.2: Casco Bay Bloom Dynamics

The region near Casco Bay was often associated with moderate misfits, and dynamics in the region were diagnosed more closely in part to better understand their probable origin. It was noted that the proliferation of cells in June was less dramatic than that in MB/CCB despite similarities in the growth patterns (Fig. 22). The co-occurrence of significant positive growth in the region but stable cell abundance suggests limited retention of cells, and strongly links the abundance of cells at any time to recent transport and upstream concentration. The considerable fraction of modeled *A. fundyense* in the region of EGOM origin suggests dynamics associated with this inflow to be one potential source of misfit. This is also supported by the study of Luerssen et al. (submitted), that suggests a strong linkage between outbreaks of toxicity in the region near Casco Bay and transport of cells from the EGOM.

In the model herein, *A. fundyense* concentrations at this inflow are specified using observed *A. fundyense* concentration from the northern-most transect. While the spatial

extrapolation required is modest, the temporal coverage of the cruises is limited and nothing is known of concentration below 10 meters. In addition, the strong wind-driven response observed over the rest of the WGOM domain cannot be completely captured along the boundary, as dynamics are pinned to a mean climatological condition. Inadequate resolution of these dynamics likely contributes to the Casco Bay misfits, and improvement would require either more resolved observations of the physical and biological conditions along the boundary, or an expanded model domain.

4.3: *Along-shore Bloom Transport at Cape Porpoise*

The results of the analysis of the contributions from various aspects of the physical forcing to the net transport of *A. fundyense* are generally consistent with conclusions derived by Geyer et al. (2004). Baroclinic gradients resulting from local river inputs were not the dominant source of along-shore transport velocity, with the Gulf-wide circulation able to maintain a persistent southwesterly flow in their absence. The wind stress was found to produce motions consistent with Ekman dynamics and be a strong source of variability over short time scales (see also Fong, et al., 1997). However, the present study further suggests that variability in monthly wind patterns can lead to variation in the along-shore transport velocity over longer time scales. This is notable relative to previous discussion of Franks and Anderson (1992b), that linked variability in southwestward bloom propagation to the strength of the second rainfall induced spring freshet in late April/early May. Results herein shift the emphasis for this variability to the wind patterns. A possible explanation for the strong relationship between river flow and the transport inferred by Franks and Anderson is provided by the correspondence

between downwelling favorable winds and cloudy days (i.e. winds with a strong southerly component are associated with low irradiance in Fig. 8).

It is recognized that conclusions regarding the transport are only strictly valid for 1993 and 1994, and each term in the balance is subject to significant fluctuations. The ranges of the bloom's response to fluctuations in wind and river input have not been explored over a full range of inter-annual variability. There are also fluctuations in strength of the Gulf-wide circulation linked to variability in the character and volume of water flowing across the Scotian Shelf or the Northeast Channel (e.g. Brown and Irish, 1992). Lastly, it is noted that variations in the forcing constituents do not add linearly, but interact in complex ways dictated by the equations of motion.

4.4: Bloom Patterns in Massachusetts and Cape Cod Bays

As initially suggested by Franks and Anderson (1992) and again noted by Anderson et al. (2004a), wind patterns are particularly critical to the transport of cells past Cape Ann and subsequent toxicity within MB/CCB. This study places particular emphasis on variations in wind during the first two weeks of June and their subsequent influence on the transport of cells within the bays to explain differences in June toxicity within the region in 1993 and 1994. Inspection of the toxicity records presented by Franks and Anderson (1992b) shows that significant periods of weak or downwelling winds preceded the induction of toxicity in nearly every case, suggesting that relaxed or downwelling conditions are a necessary (although not always sufficient) condition for the initiation of toxicity in the region.

The persistent alongshore influence of the Gulf-wide flow and suggests a high probability of cells reaching the Cape Ann branch point. This creates a temporal window of risk where a series of wind relaxations and/or downwelling could initiate toxicity along the Massachusetts coast. The model suggests that the front end of this window is set by the initiation of the germination source and the travel time between the sources and the branch point. It has also highlighted some aspects of the physical environment may lead to variability in the time to arrival. Controls on the end of the risk, however, are less clear. The modeled germination source within the WGOM is persistent, and is further prolonged by inflows from the EGOM. Physically, the transition from spring to summer is marked by a weakening of the Gulf-wide circulation (Lynch, et al., 1997), a shift towards upwelling favorable winds (Manning and Strout, 2001), and decreases in the local river inputs. All of these would decrease the effectiveness of the transport mechanisms from source regions to the north and decrease the probability of cells entering MB/CCB. However, these seasonal patterns in the physics were represented in both the 1993 and 1994 simulations, and transport into MB/CCB of *A. fundyense* in both years.

One aspect of these simulations that may lead to an over-estimation of this window of risk for introduction of cells into MB/CCB is the steady nature of the modeled germination source. The influence of sediment dynamics on the size and spatial/temporal character of this source has been identified as a large uncertainty in the model (Chapter 3). It is assumed that the pool of cysts available to germinate during a given year is set by those within the depth of oxygenated sediment and over which newly germinated cells can reach the water column. This depth was estimated based on the penetration of short-

lived isotopes, cyst fluorescence measurements, and biochemical measurements within the sediments (see Anderson, et al., submitted). However, if the pool of cysts fluctuates strongly with, for example, sediment mixing events, a more erratic series of inputs from cyst germination would result. The window over which cells can be introduced into MB/CCB would than not be a prolonged period in the spring, but consist of disjoint times determined by germination events and the transport time to Cape Ann. Such dynamics would make inputs less probable, as relaxations in the upwelling wind would need to coincide precisely with the arrival of these patches at Cape Ann.

If cells do enter MB/CCB, residence times within the region have been estimated to be between 20-50 days (Geyer, et al., 1992). Such strong retentive properties suggest that the WGOM is not simply a "flow-through" system. Parts of the region exhibit retention properties more similar to restricted embayments. In these regions, the onset of encystment and other biotic controls such as grazing are assumed to play primary roles in the termination of the bloom (Anderson, et al., 1983). It is likely the incomplete representation of these processes that leads to the June proliferation of cells within the simulations herein. Potential mechanisms were discussed in Chapter 3 and include encystment as well as spatial/temporal variability in grazing. This discussion will not be reproduced here apart from noting that increased understanding of the factors controlling these processes is necessary if bloom termination is to be properly modeled.

One final notable aspect of the dynamics in MB/CCB is that the population is primarily comprised of cells originating within the WGOM. It has been suggested (Anderson, et al., submitted) that decreases in toxicity in the MB/CCB region in recent years may be linked to the gradual attenuation of cyst beds off-shore of Casco Bay after

large blooms in the region from 1972-1974. The results herein suggest that such attenuation would effectively reduce cell abundance within the region.

5. Conclusions

The performance of a coupled physical/biological model of *A. fundyense* blooms was largely maintained when model settings tuned to 1993 observations were applied to 1994 surveys. While previous analyses showed a slight (but statistically insignificant) preference for low DIN dependence and high mortality, the results herein suggest that parameter choices with moderate to high DIN dependence are more robust and maintain skill later in the bloom season. Diagnosis of the underlying bloom dynamics suggests similarity in the biological dynamics between years, thus supporting existing hypotheses that factors driving differences in toxicity between years are primarily physical in nature. Differences in the wind forcing are suggested as the primary source of bloom transport variability in 1993 and 1994 over both daily and monthly time scales, with the direct influence of local river inputs of secondary importance. Regardless of the wind forcing, the persistent influence of the Gulf-wide circulation transports cells to the south. The model captures several aspects of bloom magnitude and along-shore transport, but two particularly notable misfits exist. First, the late season proliferation of cells in the domain for all model settings, particularly in retentive areas, suggests the need for increased knowledge of the losses and limitations on the vegetative *A. fundyense* stage. Second, model/data misfits near Casco Bay are likely related to errors in transport through the EGOM. It is suggested that a combination of more resolved observations and a physical model better able to capture the circulation dynamics along this boundary is needed to understand the origin of these misfits.

Anderson, D. M., 1980. Effects of temperature conditioning on development and germination of *Gonyaulax tamarensis* (Dinophyceae) hypnozygotes. Journal of Phycology 16, 166-172.

Anderson, D. M., 1998. Physiology and bloom dynamics of toxic *Alexandrium* species, with emphasis on life cycle transitions. In: Anderson, D. M., Cembella, A. D. ,Hallegraeff, G. M. (Eds.), Physiological Ecology of Harmful Algal Blooms. Springer-Verlag, Berlin, pp. 29-48.

Anderson, D. M., Chisholm, S. W., Watras, C. J., 1983. The importance of life cycle events in the population dynamics of *Gonyaulax tamarensis*. Marine Biology 76, 179-190.

Anderson, D. M., Geyer, W. R., Butman, B., Signell, R. P., Franks, P. J. S., Loder, T. C., 1998. RMRP Final Technical Progress Report, Project GMR-20. Woods Hole Oceanographic Institution, Woods Hole, 15 pages.

Anderson, D. M., Keafer, B. A., 1987. The endogenous annual clock in the toxic dinoflagellate *Alexandrium tamarensis*. Nature 325, 616-617.

Anderson, D. M., Keafer, B. A., Geyer, W. R., Signell, R. P., Loder, T. C., 2004a. Toxic *Alexandrium* blooms in the Gulf of Maine: the "plume advection hypothesis" revisited. Limnology and Oceanography (submitted).

Anderson, D. M., Kulis, D. M., Binder, B. J., 1984. Sexuality and cyst formation in the dinoflagellate *Alexandrium tamarensis*: Cyst yield in batch cultures. Journal of Phycology 20, 418-425.

Anderson, D. M., Kulis, D. M., Doucette, G. J., Gallagher, J. C., Balech, E., 1994. Biogeography of toxic dinoflagellates in the genus *Alexandrium* from the northeastern United States and Canada. Marine Biology 120, 467-478.

Anderson, D. M., Lindquist, N. L., 1985. Time-course measurements of phosphorous depletion and cyst formation in the dinoflagellate *Gonyaulax tamarensis* Lebour. Journal of Experimental Marine Biology and Ecology 86, 1-13.

Anderson, D. M., Stock, C. A., Keafer, B. A., Bronzino, A. C., Matrai, P., Thompson, B., Keller, M., McGillicuddy, D. J., Hyatt, J., 2004b. Experimental and modeling observations of *Alexandrium fundyense* cyst dynamics in the Gulf of Maine. Deep-Sea Research, Part II (submitted).

Anderson, D. M., Stock, C. A., Keafer, B. A., Bronzino, A. C., Matrai, P., Thompson, B., Keller, M., McGillicuddy, D. J., Hyatt, J., submitted. Experimental and modeling observations of *Alexandrium fundyense* cyst dynamics in the Gulf of Maine. Deep-Sea Research, Part II

Anderson, D. M., Taylor, C. D., Armbrust, V. E., 1987. The effects of darkness and anaerobiosis on dinoflagellate cyst germination. Limnology and Oceanography 32, 340-351.

Anderson, D. M., Wall, D., 1978. Potential importance of benthic cysts of *Gonyaulax tamarensis* and *G. excavata* in initiating toxic dinoflagellate blooms. Journal of Phycology 14, 224-234.

Bauerfeind, E., Elbrachter, M., Steiner, R., Throndsen, J., 1986. Application of Laser Doppler Spectroscopy (LDS) in determining swimming velocities in motile phytoplankton. Marine Biology 93, 323-327.

Blumberg, A. F., Mellor, G. L., 1987. A description of a three-dimensional coastal ocean circulation model. In: Heaps, N. (Ed.), Three-Dimensional Coastal Ocean Models. American Geophysical Union, pp. 1-16.

Brooks, D. A., 1985. Vernal circulation in the Gulf of Maine. Journal of Geophysical Research 90, 4687-4705.

Brooks, D. A., 1994. A model study of the buoyancy-driven circulation in the Gulf of Maine. Journal of Physical Oceanography 24, 2387-2412.

Brooks, D. A., Townsend, D. W., 1989. Variability of the coastal current and nutrient pathways in the eastern Gulf of Maine. Journal of Marine Research 47, 303-321.

Brown, W., Irish, J., 1992. The annual evolution of geostrophic flow in the Gulf of Maine: 1986-1987. Journal of Physical Oceanography 22, 445-473.

Carpenter, E. J., Guillard, R. R. L., 1971. Intraspecific differences in the nitrate half-saturation constants for three species of marine phytoplankton. Ecology 52, 183-185.

Conway, H. L., Harrison, P. J., 1977. Marine diatoms grown in chemostats under silicate or ammonium limitation. IV. Transient response of *Chaetoceros debilis, Skeletonema costatum,* and *Thalassiosira gravida* to a single addition of limiting nutrient. Marine Biology 43, 33-43.

Cox, D. R., Hinckley, D. V., 1974. Theoretical Statistics. Chapman Hall, London, 511 pages.

Cullen, J. J., Wood, Barnett, Normandeau, Ryan, 2004. Behavioral and physiological variability among strains of the toxic dinoflagellate *Alexandrium fundyense* from the Gulf of Maine. Deep-Sea Research, Part II (submitted).

Droop, M. R., 1983. 25 years of algal growth kinetic, a personal view. Botanica Marina 26, 99-112.

Eppley, R. W., Rogers, J. N., McCarthy, J. J., 1969. Half-saturation constants for uptake of nitrate and ammonium by marine phytoplankton. Limnology and Oceanography 14, 912-920.

Eppley, R. W., Thomas, W. H., 1969. Comparison of half-saturation "constants" for growth and nitrate uptake of marine phytoplankton. Journal of Phycology 5, 365-369.

Etheridge, S. M., Roesler, C. S., Doucette, G. J., submitted. *Alexandrium fundyense* isolate-specific responses to temperature, irradiance, and salinity: Potential growth rate and toxicity in the Gulf of Maine and Bay of Fundy. Deep-Sea Research, Part II (submitted).

Ezer, T., Mellor, G. L., 1992. A numerical study of the variability and the separation of the Gulf Stream, induced by surface atmospheric forcing and lateral boundary flows. Journal of Physical Oceanography 22, 660-682.

Flather, R. A., 1976. A tidal model of the north-west european continental shelf. Memoires Societe Royale des Sciences de Liege 6, 141-164.

Fong, D. A., Geyer, W. R., Signell, R. P., 1997. The wind-forced response of a buoyant coastal current: Observations of the western Gulf of Maine plume. Journal of Marine Systems 12, 69-81.

Franks, P. J. S., Anderson, D. M., 1992a. Alongshore transport of a toxic phytoplankton bloom in a buoyancy current: *Alexandrium tamarense* in the Gulf of Maine. Marine Biology 112, 153-164.

Franks, P. J. S., Anderson, D. M., 1992b. Toxic phytoplankton blooms in the Gulf of Maine: testing hypotheses of physical control using historical data. Marine Biology 112, 165-174.

Fung, I. Y., Harrison, D. E., Lacis, A. A., 1984. On the variability of the net longwave radiation at the ocean surface. Reviews of Geophysics and Space Physics 22, 177-193.

Galperin, B., Kantha, L. H., Hassid, S., Rosati, A., 1988. A quasi-equilibrium turbulent energy model for geophysical flows. Journal of Atmospheric Science 45, 55-62.

Geraci, J. R., Anderson, D. M., Timperi, R. J., Staubin, D. J., Early, G. J., Prescott, J. H., Mayo, C. A., 1989. Humpback Whales (*Megaptera novaeangliae*) fatally poisoned by dinoflagellate toxin. Canadian Journal of Fisheries and Aquatic Science 46, 1895-1898.

Geyer, W. R., Gardner, G. B., Brown, W. S., Irish, J., Butman, B., Loder, T. C., Signell, R. P., 1992. Physical Oceanographic Investigations of Massachusetts and Cape Cod Bays. Woods Hole Oceanographic Institution, Woods Hole, 497 pages.

Geyer, W. R., Signell, R. P., Fong, D. A., Wang, J., Anderson, D. M., Keafer, B. A., 2004. The freshwater transport and dynamics of the western Maine Coastal Current. Continental Shelf Research 24, 1339-1357.

Gran, H. H., Braarud, T., 1935. A quantitative study of the phytoplankton in the Bay of Fundy and the Gulf of Maine (including observations on hydrography, chemistry, and turbidity). Journal of the Biological Board of Canada 1, 279-467.

Hetland, R. D., McGillicuddy, D. J., Signell, R. P., 2002. Cross-frontal entrainment of plankton into a buoyant plume: the frog tongue mechanism. Journal of Marine Research 6, 763-777.

Hoaglin, D. C., Mosteller, F., Tukey, J. W., 1983. Understanding Robust and Exploratory Data Analysis. In: Hoaglin, D. C., Mosteller, F., Tukey, J. W., (Eds.), Understanding Robust and Exploratory Data Analysis. Wiley, New York, pp.

Kamykowski, D., Reed, R. E., Kirkpatrick, G. J., 1992. Comparison of the sinking velocity, swimming velocity, rotation and path characteristics among six marine dinoflagellate species. Marine Biology 113, 319-328.

Keller, A. A., Taylor, C., Oviatt, C., Dorrington, T., Holcombe, G., Reed, L., 2001. Phytoplankton production patterns in Massachusetts Bay and the absence of the 1998 winter-spring bloom. Marine Biology 138, 1051-1062.

Kelly, J. R., Doering, P. H., 1997. Monitoring and modeling primary production in coastal waters: studies in Massachusetts Bay 1992-1994. Marine Ecology Progress Series 148, 155-168.

Kuhl, M., Jorgensen, B. B., 1994. The light of microbenthic communities: Radiance distribution and microscale optics of sandy coastal sediments. Limnology and Oceanography 39, 1368-1398.

Langdon, C., 1987. On the causes of interspecific differences in the growth-irradiance relationships for phytoplankton. Part I. A comparitive study of the growth irradiance relationships of three marine phytoplankton species: *Skelotonema costatum, Olithodiscus luteus* and *Gonyaulax tamarensis*. Journal of Plankton Research 9, 459-482.

Lomas, M. W., Glibert, P. M., 2000. Comparison of nitrate uptake, storage, and reduction in marine diatoms and flagellates. Journal of Phycology 36, 903-913.

Luerssen, R. M., Thomas, A. C., Hurst, J. W., submitted. Relationships between satellite-measured thermal features and *Alexandrium*-imposed toxicity in the Gulf of Maine. Deep Sea Research, Part II

Lynch, D. R., Holboke, M. J., Naimie, C. E., 1997. The Maine coastal current: spring climatological circulation. Continental Shelf Research 17, 605-634.

Lynch, D. R., Naimie, C. E., 1993. The M2 tide and its residual on the outer banks of the Gulf of Maine. Journal of Physical Oceanography 23, 2222-2253.

MacIsaac, J. J., Grunseich, G. S., Glover, H. J., Yentsch, C. M., 1979. Light and nutrient limitation in *Gonyaulax excavata*: nitrogen and carbon trace results. In: Taylor, D. L. ,Seliger, H. H., (Eds.), Toxic Dinoflagellate Blooms: proceedings of the second conference on toxic dinoflagellate blooms, Key Biscayne, Florida. Elsevier/North-Holland, pp. 107-110.

Manning, J., Strout, G., 2001. Georges Bank winds: 1975-1997. Deep Sea Research, Part II 48, 115-135.

Martin, J. L., Wildish, D. J., 1994. Temporal and spatial dynamics of *Alexandrium* cysts during 1981-1984 and 1992 in the Bay of Fundy. In: Forbes, R., (Ed.), Fourth Canadian Workshop on Harmful Marine Algae, Can Tech, Rept. Fish Aquat Sci., pp. 2016.

Martorano, C. D., Loder, T. C., 1997. Nutrient dynamics during blooms of *Alexandrium* spp. in the southwestern Gulf of Maine. Masters Thesis, University of New Hampshire, Biogeochemical Systems Center, Durham, NH, USA, unpublished.

Matrai, P., Thompson, B., Keller, M. D., submitted. *Alexandrium* spp. from eastern Gulf of Maine: Circannual excystment of resting cysts. Deep Sea Research II

McGillicuddy, D. J., Anderson, D. M., Lynch, D. R., Townsend, D. W., submitted. Mechanisms regulating the large-scale seasonal development of *Alexandrium fundyense* blooms in the Gulf of Maine. Deep-Sea Research, Part II

McGillicuddy, D. J., Signell, R. P., Stock, C. A., Keafer, B. A., Keller, M. D., Hetland, R. D., Anderson, D. M., 2003. A mechanism for offshore initiation of harmful algal blooms in the coastal Gulf of Maine. Journal of Plankton Research 25, 1131-1139.

Mellor, G. L., Yamada, T., 1982. Development of a turbulence closure model for Geophysical Fluid Problems. Reviews of Geophysical and Space Physics 20, 851-875.

Naimie, C. E., Loder, J. W., Lynch, D. R., 1994. Seasonal variation in the three-dimensional residual circulation on Georges Bank. Journal of Geophysical Research 99, 15,967-15,989.

Petrie, B., Yeats, P., 2000. Annual and interannual variability of nutrients and their estimated fluxes in the Scotian Shelf - Gulf of Maine region. Canadian Journal of Fisheries and Aquatic Science 57, 2536-2546.

Pettigrew, N., Townsend, D., Xue, H., Wallinga, J., Brickley, P., Hetland, R., 1998. Observations of the eastern Maine Coastal Current and its offshore extensions in 1994. Journal of Geophysical Research Vol. 103, 30,623-30,639.

Physical-Oceanography-DAAC, 1985. AVHRR Oceans Pathfinder global equal-angle best SST NOAA, NASA. http://www.podaac.jpl.nasa.gov.

Platt, T., Jassby, A. D., 1976. The relationship between photosynthesis and light for natural assemblages of coastal marine phytoplankton. Journal of Phycology 12, 421-430.

Poulton, N. J., 2001. Physiological and behavioral diagnostics for nitrogen limitation for the toxic dinoflagellate *Alexandrium fundyense*. Ph.D., Woods Hole/MIT Joint Program, Biological Oceanography, Woods Hole, MA, unpublished.

Prakash, A., 1967. Growth and toxcity of a marine dinoflagellate, *Gonyaulax tamarensis*. Journal of the Fisheries Research Board of Canada 24,

Scholin, C. A., Hallegraeff, G. M., Anderson, D. M., 1995. Molecular evolution of the *Alexandrium tamarense* "species complex" (Dinophyceae): Dispersal in the North American and West Pacific regions. Phycologia 34, 472-485.

Shumway, S. E., Sherman-Caswell, S., Hurst, J. W., 1988. Paralytic shellfish poisoning in Maine: Monitoring a monster. Journal of Shellfish Research 7, 643-652.

Sommer, U., 1991. A comparison of the Droop and Monod models of nutrient limited growth applied to natural populations of phytoplankton. Functional Ecology 5, 535-544.

Stock, C. A., McGillicuddy, D. J., Solow, A. R., Anderson, D. M., submitted. Evaluating hypotheses for the initiation and development of *Alexandrium fundyense* blooms in the western Gulf of Maine using a coupled physical-biological model. Deep Sea Research II

Sverdrup, H. U., 1953. On Conditions for the Vernal Blooming of Phytoplankton. Journal du Conseil Pour l'Exploration de la Mer 18, 287-295.

Townsend, D. W., Pettigrew, N. R., Thomas, A. C., 2001. Offshore blooms of the red tide dinoflagellate *Alexandrium* sp., in the Gulf of Maine. Continental Shelf Research 21, 347-369.

Townsend, D. W., Spinrad, R. W., 1986. Early spring phytoplankton blooms in the Gulf of Maine. Continental Shelf Research 6, 515-529.

Watras, C. J., Chisholm, S. W., Anderson, D. M., 1982. Regulation of growth in an estuarine clone of *Gonyaulax tamarensis* Lebour: salinity-dependent temperature responses. Journal of Experimental Marine Biology and Ecology 62, 25-37.

White, A. W., Fukuhara, O., Anraku, M., 1989. Mortality of fish larvae from eating toxic dinoflagellates or zooplankton containing dinoflagellate toxins. In: Okaichi, T., Anderson, D. M. ,Nemoto, T. (Eds.), Red Tides: Biology, Environmental Science, and Toxicology. Elsevier, New York, pp. 395-398.

White, A. W., Lewis, C. M., 1982. Resting cysts of the toxic, red tide dinoflagellate *Gonyaulax excavata* in Bay of Fundy sediments. Canadian Journal of Fisheries and Aquatic Science 39, 1185-1194.

Table 1: Biological model parameters

Symbol	Definition	Units	Range	Sources
K_N	Half-saturation constant for nutrient limited growth	μM	0-3	Eppley et al. (1969), Eppley and Thomas (1969), Lomas and Glibert (2000), Carpenter and Guillard (1971), MacIsaac et al. (1979), Sommer (1991)
m	Spatially and temporally averaged mortality	day^{-1}	0-0.3	see text
$\mu_{max}(T_{opt},S_{opt})$	The maximum growth rate under optimal temperature and salinity conditions.	day^{-1}	0.46-0.70	Cullen et al. (submitted), Langdon (1987), Etheridge et al. (submitted), Watras et al. (1982), Keafer and Kulis (unpub. data)[1]
μ_o^r	The maintenance respiration rate	day^{-1}	0.15-0.25	Cullen et al. (submitted)
α_g	The growth efficiency	day^{-1} W^{-1} m^2	0.017-0.056	Cullen et al. (submitted)
d_g	The mean depth of sediment over which cysts are able to germinate and contribute to the bloom	cm	0.5-1.5	Anderson et al. (2004b)
E_{lgt}	Light level for germination under "light" conditions.	watts/m^2	1.2-3.6	Anderson et al. (submitted)
E_{drk}	Light level for germination under dark conditions.	watts/m^2	0.1% of I_{lgt} to 10% of I_{lgt}.	Anderson et al. (submitted)
k_w	Mean diffuse attenuation in water column.	m^{-1}	0.15-0.25	Townsend et al. (2001)
k_s	Mean diffuse attenuation in the sediment	mm^{-1}	2-5	Kuhl and Jorgensen (1994)
w_a	Vertical swimming speed	m/day	5-15	Bauerfiend et al.(1986), Kamykowski et al. (1992)

[1] Sources used for formulation of the growth versus temperature dependence polynomial are: Etheridge et al. (submitted), Langdon (1987), Watras et al. (1982), and Keafer and Kulis (unpublished data). Sources used for the salinity dependence polynomial are: Etheridge et al. (submitted) and Prakash (1967).

Table 2: Physical Model Forcing

Forcing	Source/Description
Sea Surface Elevation	M_2 tide from Gulf of Maine tidal model (Lynch and Naimie, 1993) Mean elevation from bi-monthly climatology (Naimie, et al., 1994)
Wind	Portland off-shore buoy (NDBC #44007), applied throughout domain and translated to shear via Large and Pond (1994)
River discharge	USGS stream gauges at 4 major rivers: Charles, Saco, Merrimack, and the Kennebec/Androscoggin
Boundary T,S	Interpolated and extrapolated from mooring and survey data
Initial T,S	1993: spatially averaged climatology (Naimie, et al., 1994) 1994: spatially averaged climatology with surface salinities adjusted for anomalously high salinity (Signell, personal communication)
Heat Flux	Shortwave radiative heat flux from land-based sensor at Woods Hole Sensible and latent heat fluxes estimated using Portland off-shore buoy data and the bulk formulae of Large and Pond (1982). Longwave flux estimated using Portland off-shore buoy data and relationships of Berliand and Berliand as described in Fung et al. (1984). Heat Fluxes are adjusted via the method of Ezer and Mellor (1992) to drive the model toward surface temperature estimates derived from a combination of AVHRR pathfinder data (PO.DAAC, (1985))*.

Table 3: Nutrient model parameters

Parameter	Value	Description
N_{max}	4.67	The maximum (pre spring draw-down) concentration of DIN without riverine influence (μM)
δ_{NT}	3.97	The change in DIN associated with the development of the thermocline without riverine influence (μM)
δ_{NS}	3.11	The change in DIN concentration associated with riverine influence (μM)
α_T	1.76	Coefficient proportional to the change in DIN for each unit of warming in surface waters (~μM/°C).
α_S	0.87	Coefficient proportional to the change in DIN for each unit of freshening in surface waters (~μM/PSU)
β_T	7.71	β_T / α_T is the temperature at which the DIN draw-down is occurring at its maximal rate. (°C)
β_S	24.10	β_S / α_S at which augmentation of DIN via freshening occurs at its maximal rate. (PSU)

Table 4: Summary of the statistical properties of the model/data misfit. Rows correspond to different parameter combinations over a range of nitrogen/mortality dependence (columns 1-4). Statistical properties are given in columns 4-7. The top entry is the estimated misfit variance along with the standard deviation around this estimate. The middle entries are the cross-shore and along-shore decay scales (km^{-1}) associated with the best variance estimate. The bottom entry is the temporal correlation. This is reported for separations of one and two biweekly cruises for the Chapter 1 results (column 5), and as a decay rate ($days^{-1}$) with calculated values at 2 and 4 weeks for results in this study (columns 6 and 7).

K_N (μM)	m ($days^{-1}$)	μ_{max} ($days^{-1}$)	d_g (cm)	1993 bloom from Chapter 1	1993 bloom with adjustments	1994 bloom with adjustments
0	0.15	0.525	1.25	2.56 (2.37-2.80) -0.053, -0.057 0.20, 0.11	2.55 (2.26-2.93) -0.054, -0.053 -0.13 (0.16, 0.03)	4.04 (3.49-4.80) -0.034, -0.029 -0.94 (0, 0)
0.5	0.1	0.575	1.25	2.51 (2.28-2.79) -0.054,-0.057 0.17,0.08	2.50 (2.21-2.86) -0.056, -0.055 -0.13 (0.16, 0.03)	3.45 (3.01-4.02) -0.041, -0.035 -0.86 (0, 0)
1.5	0.1	0.700	1.40	2.52 (2.32-2.76) -0.055 -0.055 0.16, 0.06	2.48 (2.20-2.84) -0.057, -0.056 -0.13 (0.16, 0.03)	2.74 (2.44-3.13) -0.055, -0.044 -0.77 (0, 0)
1.5	0.05	0.525	0.90	2.59 (2.36-2.87) -0.052, -0.054 0.17, 0.07	2.52 (2.23-2.89) -0.056, -0.55 -0.13 (0.16, 0.03)	2.87 (2.55-3.30) -0.051, -0.042 -0.78 (0, 0)
3.0	0.05	0.650	1.00	2.61 (2.38-2.86) -0.052, -0.054 0.17, 0.07	2.54 (2.24-2.91) -0.056, -0.054 -0.13 (0.16, 0.03)	2.71 (2.41-3.09) -0.055, -0.044 -0.78 (0, 0)
3.0	0	0.460	0.50	2.71 (2.45-3.02) -0.049, -0.052 0.18, 0.08	2.61 (2.31-3.00) -0.053, -0.052 -0.13 (0.16,0.03)	2.93 (2.60-3.37) -0.050, -0.041 -0.86 (0, 0)

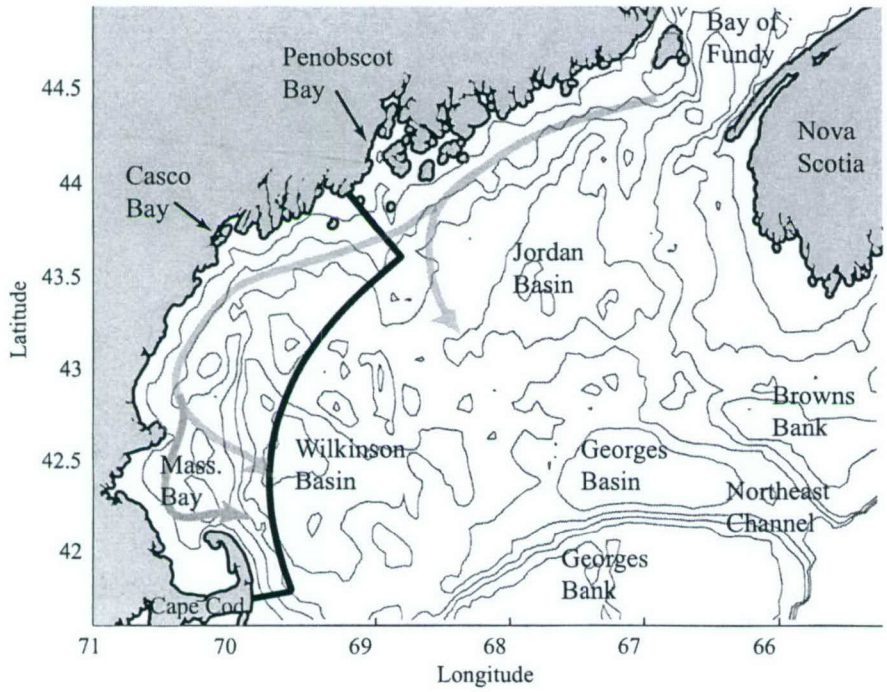


Figure 1: The Gulf of Maine and study region. The study domain is outlined in black. Depth contours are at 50, 100, 150 and 200 meters. The direction of flow of the Maine Coastal Current (adapted from Lynch et al., 1997) is shown as a thick gray line. Branch points off-shore of Penobscot Bay and Cape Ann are notable.

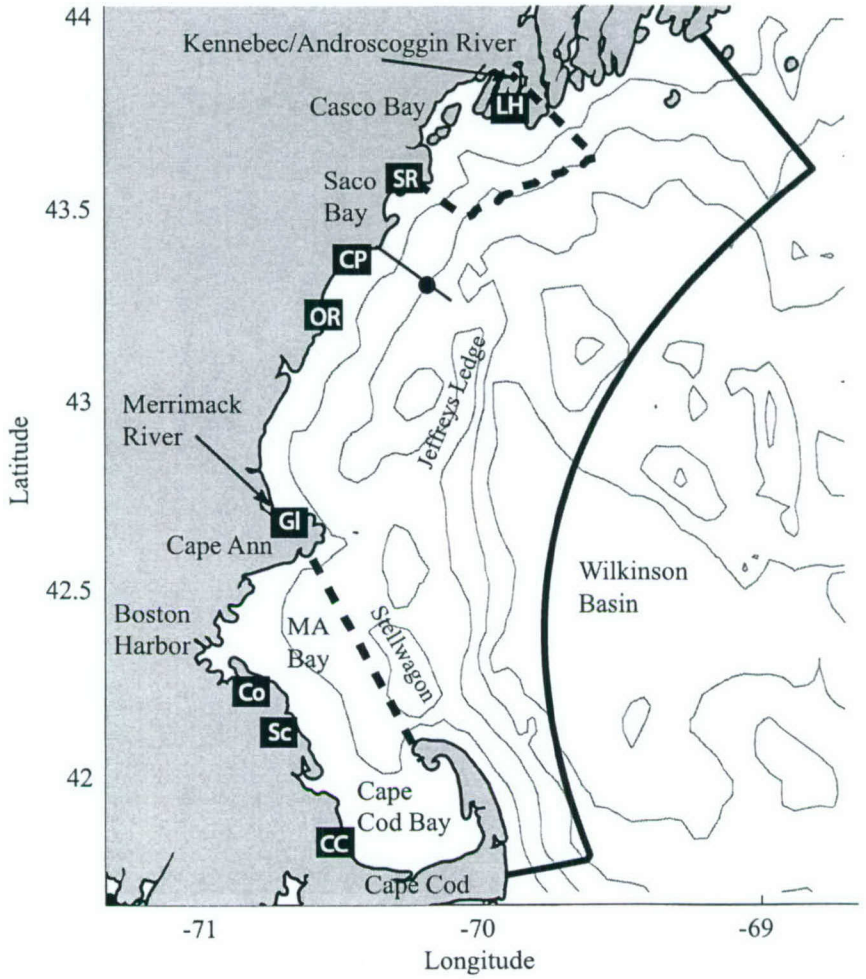


Figure 2: The WGOM. The thick, solid line outlines the model domain. The closed circle shows the location of the Cape Porpoise Mooring. The along-shore and cross-shore transport of *A. fundyense* is calculated across the line intersecting the mooring. Thick dashed lines mark the edges of the Massachusetts Bay/Cape Cod Bay region and the Casco Bay region analyzed during model diagnosis. Locations of the shellfish monitoring stations are noted with closed circles and 2 letter codes. Codes are as follows: LH, Lumbo's Hole; SR, Spurwink River; CP, Cape Porpoise; OR, Ogunquit River; Gl, Gloucester-Annissquam; Co, Cohasset; Sc, Scituate; CC, Cape Cod Canal. Stellwagon refers to Stellwagon Bank.

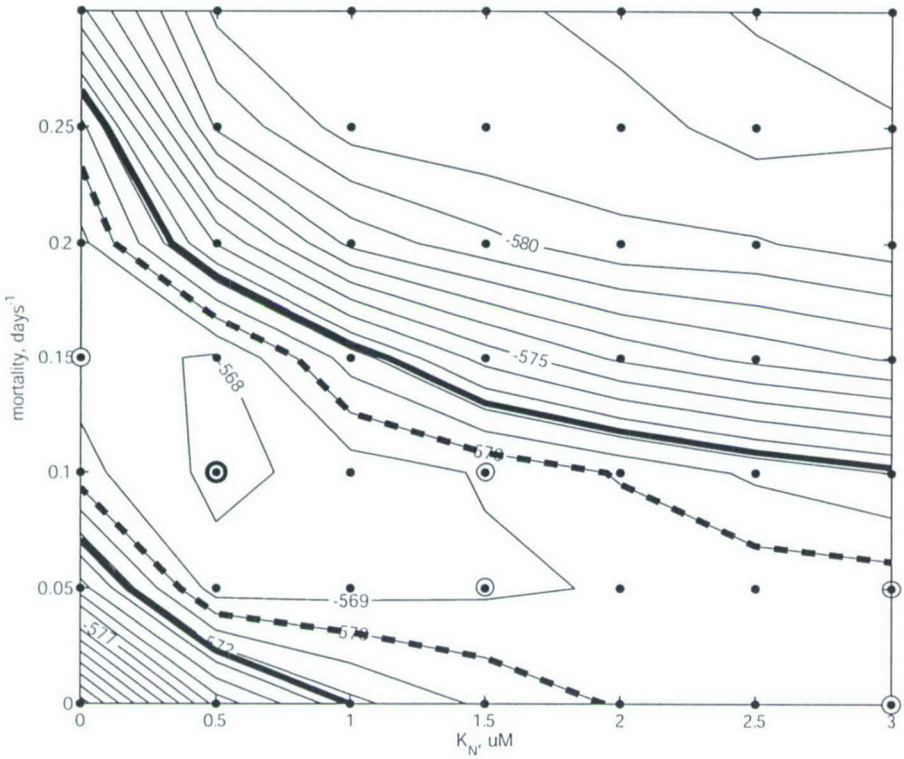


Figure 3: Optimization of the model data fit over mortality and nutrient dependence from Stock et al. (submitted). Contours are of the maximum likelihood associated with each choice of K_N and m in the biological model (increasing likelihood signals improvement in the model/data fit). The overall maximum likelihood occurs at $K_N = 0.05$ μM and $m = 0.1$ day^{-1} (bold circle). However, only parameter combinations falling outside of the solid dashed contour can be rejected can be rejected in favor of this best run with 90% confidence, and only those falling outside the thick solid contour can be rejected with 99% confidence. Thus, a wide range of parameter values produce results that are essentially statistically indistinguishable from the best case. This study tests a range of parameter settings within this interval (all circled dots) against the 1994 data. These span a range of relative dependencies on nitrogen and mortality for limiting bloom development.

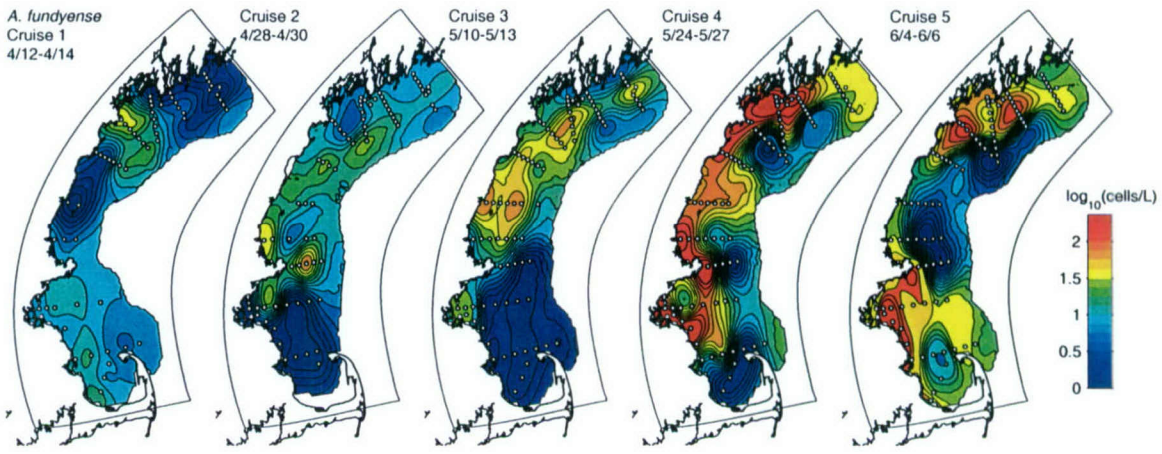


Figure 4: Surveys of *A. fundyense* taken during the spring of 1993 as part of the RMRP program. Cruise coverage extends to early June and cruises have roughly bi-weekly spacing.

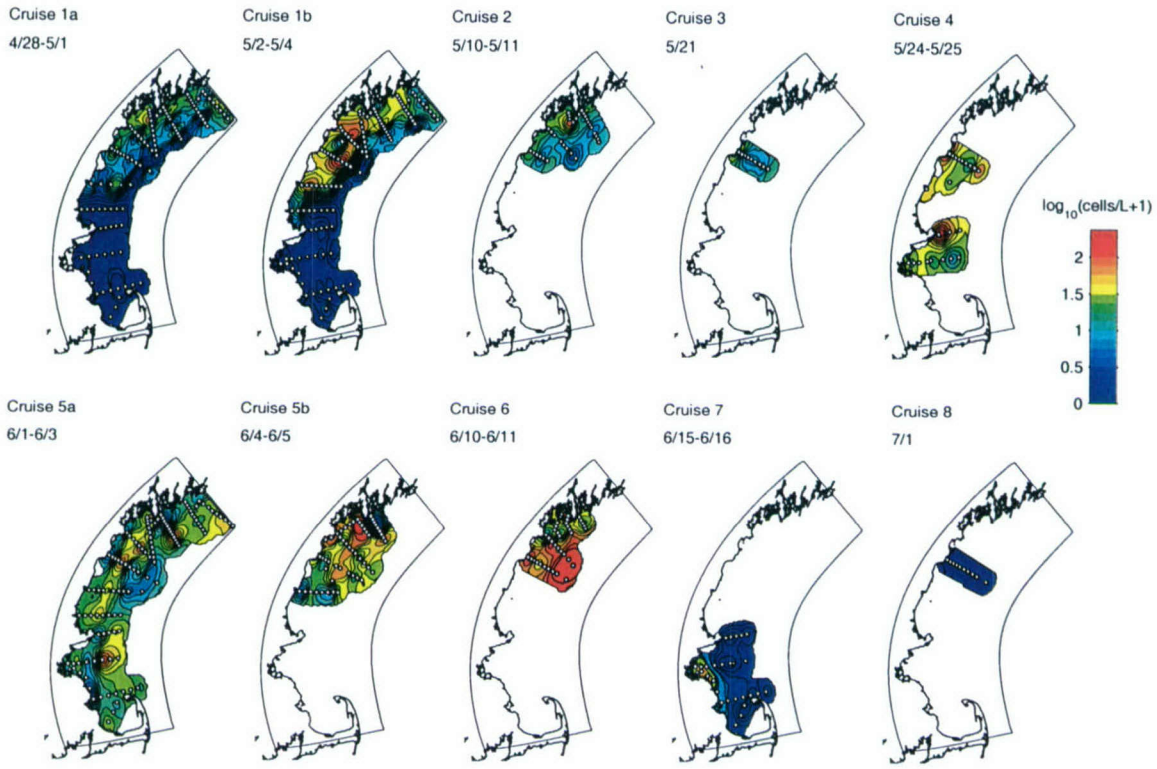


Figure 5: Surveys of *A. fundyense* taken during the spring of 1994 as part of the RMRP program. Two sets of cruises with near domain-wide coverage (1a,b, 5a,b) are spaced in close succession.

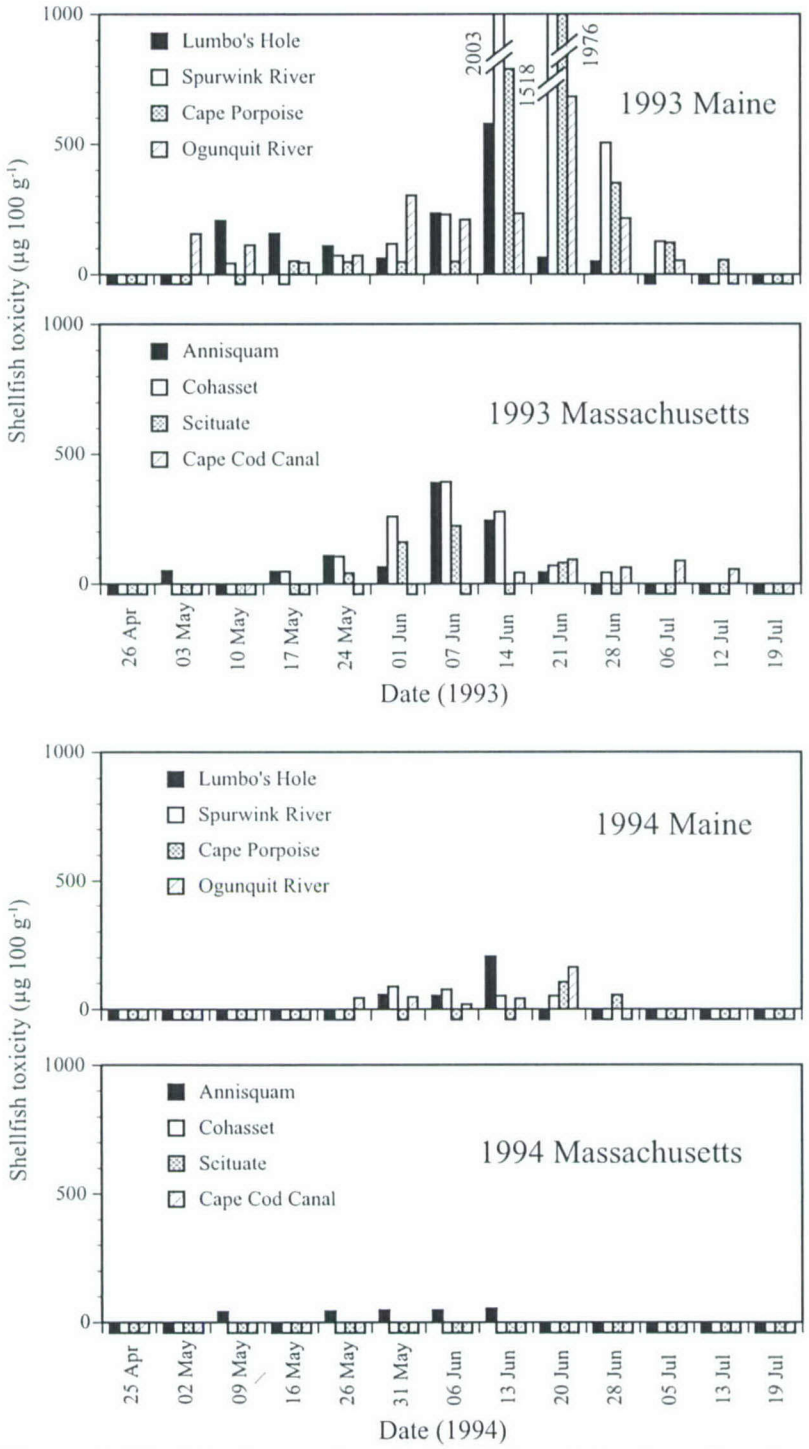


Figure 6: Weekly time series of shellfish toxicity (µg of saxitoxin equivalents per 100 g of shellfish meat) in the blue mussel *Mytilus edulis* reported for key stations in Maine and Massachusetts during the 1993 and 1994 *A. fundyense* bloom seasons (Anderson, et al., 2004a).

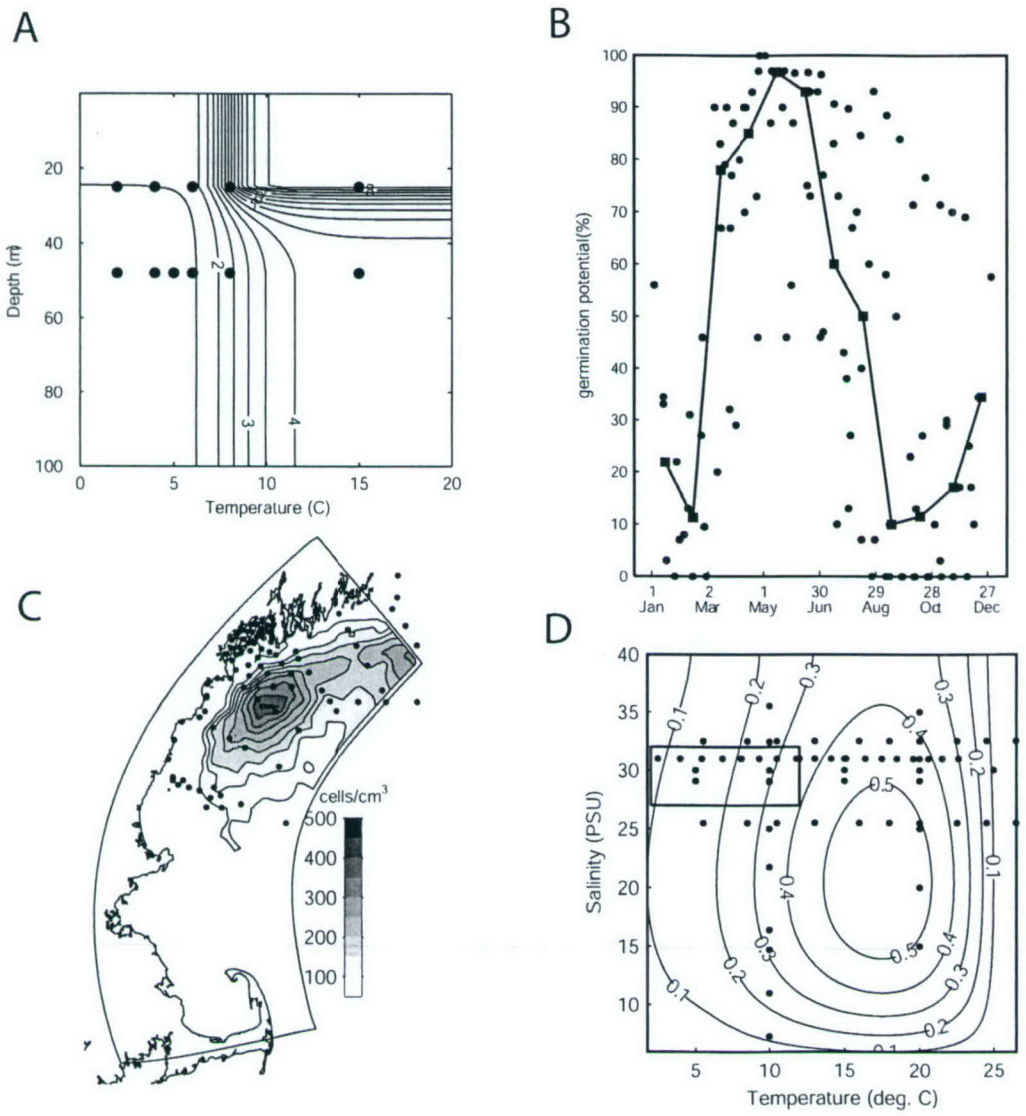


Figure 7(A-D): The biological model summary. All plots show shown as black dots. The germination rate is estimated as a function of temperature and light experienced by the resting cyst according to the laboratory derived relationship **A** (note that light has been translated to depth in the water column using a diffuse irradiance attenuation typical for Gulf of Maine waters). This rate is modified according to the germination potential **B**, which is controlled by an internal endogenous clock. The resulting rate is applied to a mapping of benthic cysts **C** to provide an estimate of the germination source. Once germinated, the cells swim up in the water column and grow according to the rates in panel **D** and a hyperbolic light/growth curve of the form suggested by Platt and Jassby (1976) for photosynthesis (not shown).

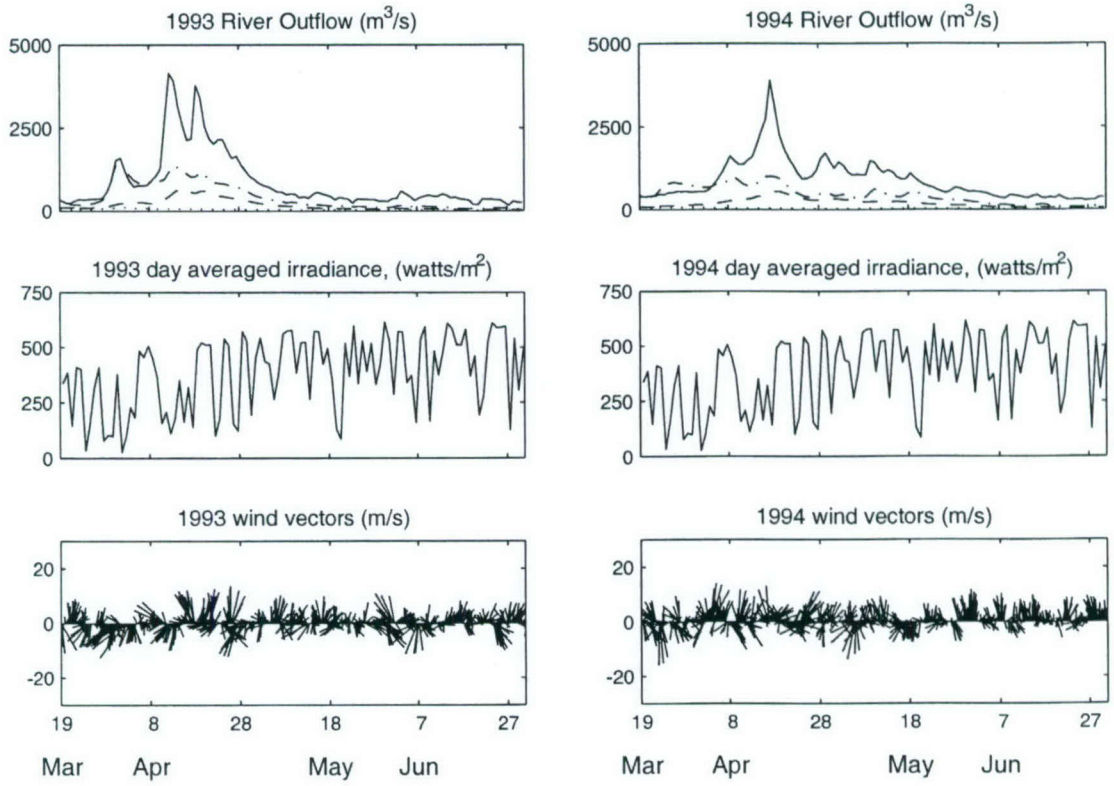


Figure 8: Physical model forcing for 1993 (left column) and 1994 (right column). Top panel: river inflow (m^3/s). Middle Panel: Average radiation (watts/m^2) from 6 AM-8 PM from land-based sensor at Woods Hole. Lower Panel: Wind speed and direction (m/s) in 3 hour intervals from the Portland Meteorological Buoy. Winds directed to the southwest are downwelling favorable, while those directed to the northeast are upwelling favorable.

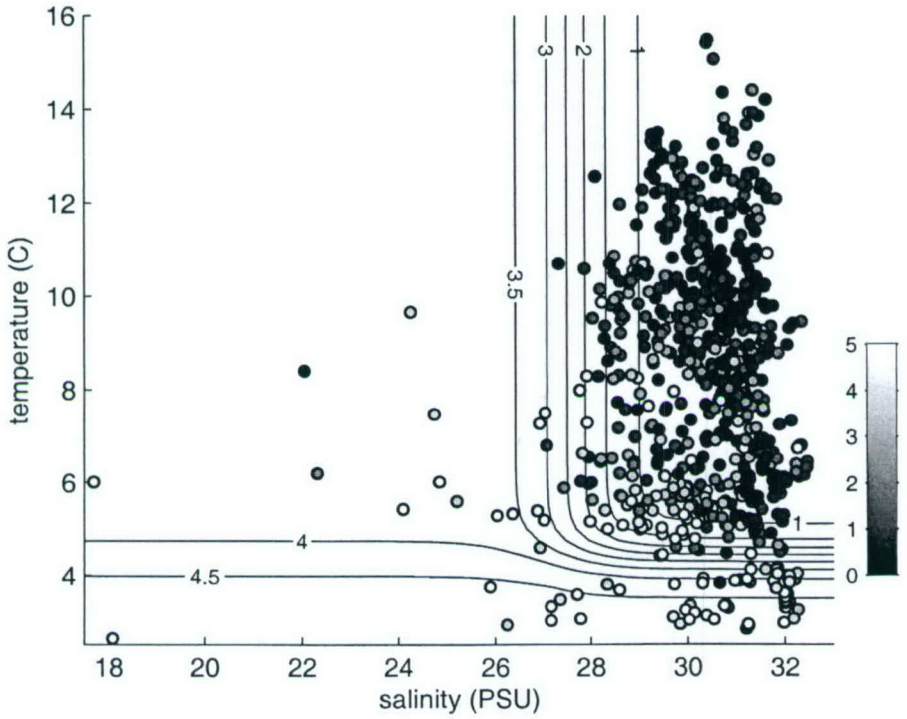


Figure 9: The functional relationship between hydrography and DIN based on the 1993 and 1994 data sets. Contour interval = 0.5 μM.

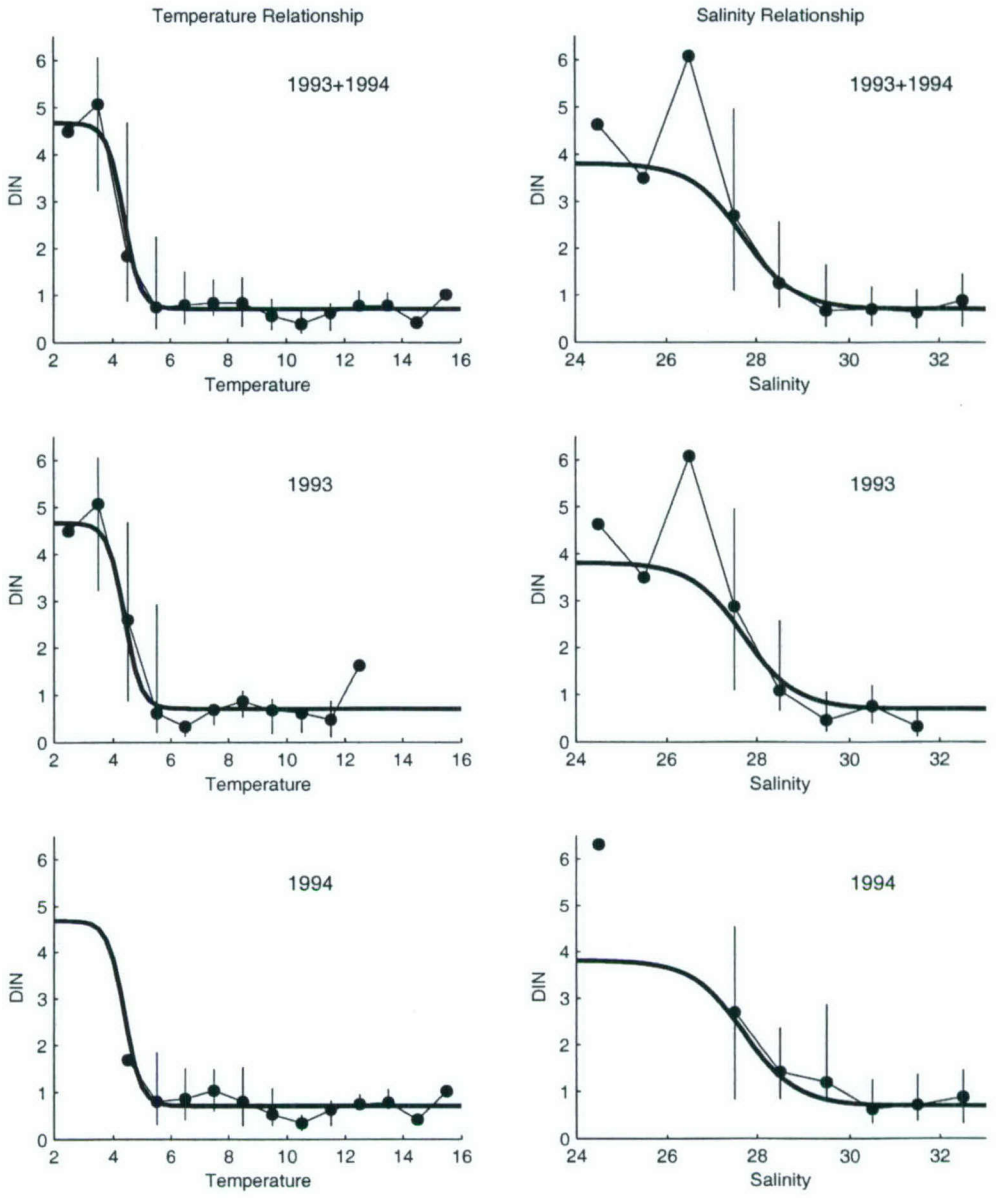


Figure 10: Primary features of the DIN relationships. **Left column:** The modeled spring nutrient DIN depletion at 31.25 PSU (-) associated with the warming of surface water and development of stratification versus the observed median DIN concentration in 1°C bins for all data between 30-32.5 PSU (•). The vertical lines show the range of the middle two quartiles of the ordered set of observations about the median. Ranges are only shown for bins with > 4 observations. **Right Column:** The modeled enhancement of DIN concentration in less saline water (-) versus the median of all observations from 5-13°C binned into 1 PSU intervals. Ranges are as in the left column.

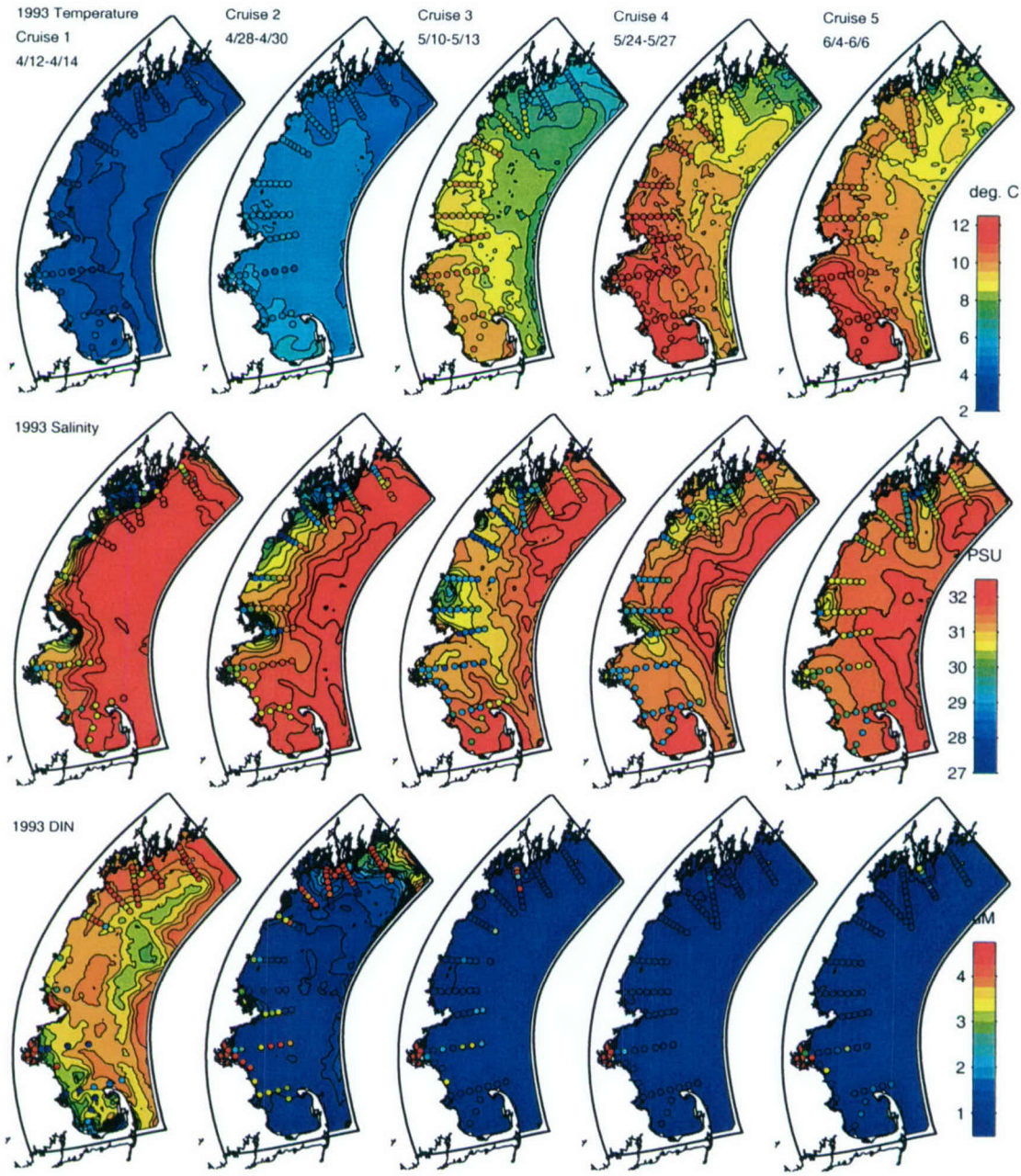


Figure 11: Comparison of the modeled and observed temperature **(top panel)**, salinity **(middle panel)**, and DIN **(bottom panel)** for 5 different cruises in 1993. Cruise dates are noted on the top of the figure and differ with Figure 12 according to the sampling plan. Observations are colored dots, model out is color contoured. Similar colors indicate a good model/data match.

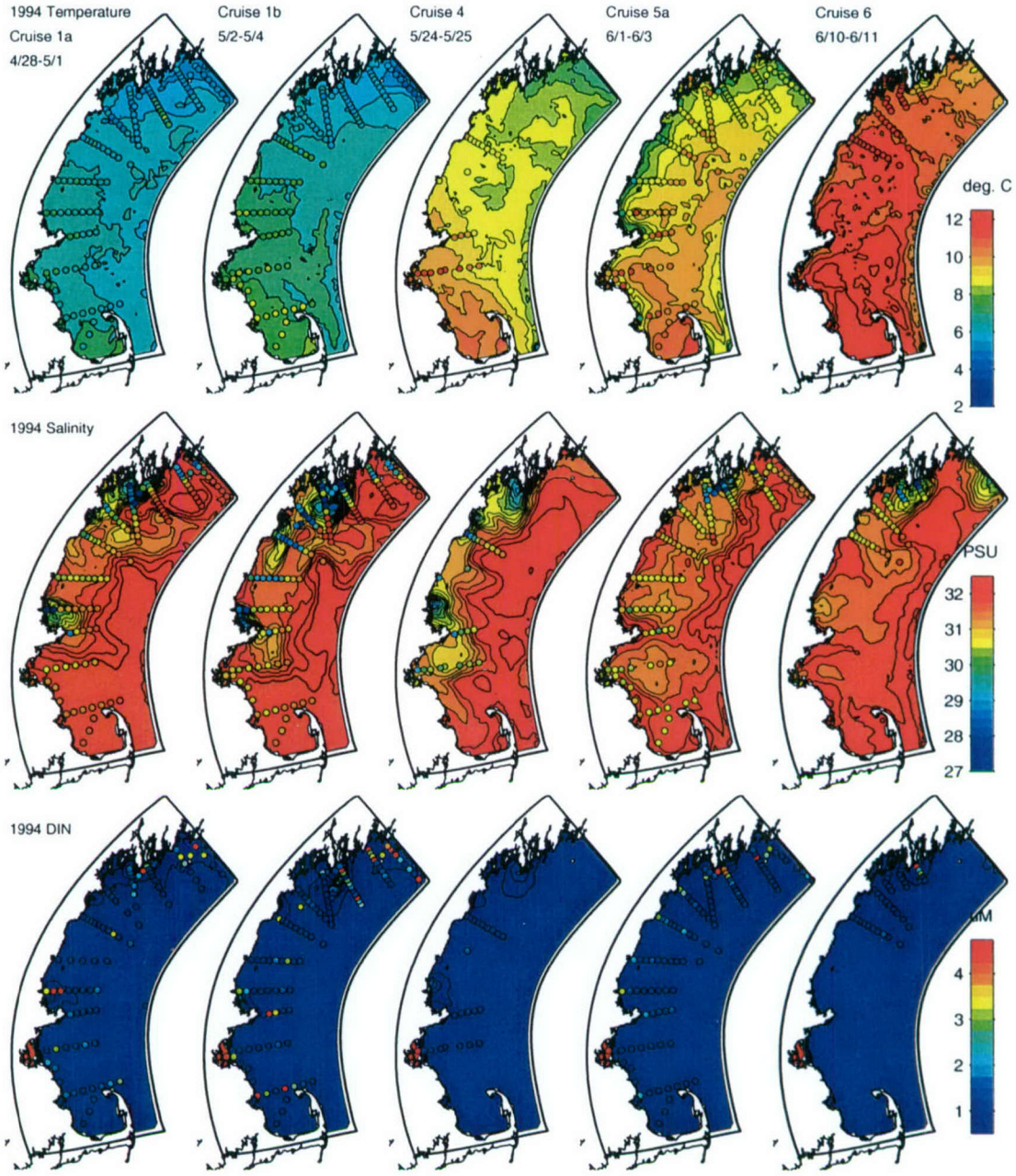


Figure 12: Comparison of the model and data temperature **(top panel)**, salinity **(middle panel)**, and nutrients **(bottom panel)** for 5 different cruises in 1994. Cruise dates are noted on the top of the figure and differ with Figure 11 according to the sampling plan. Observations are colored dots, model out is color contoured. Similar colors indicate a good model/data match.

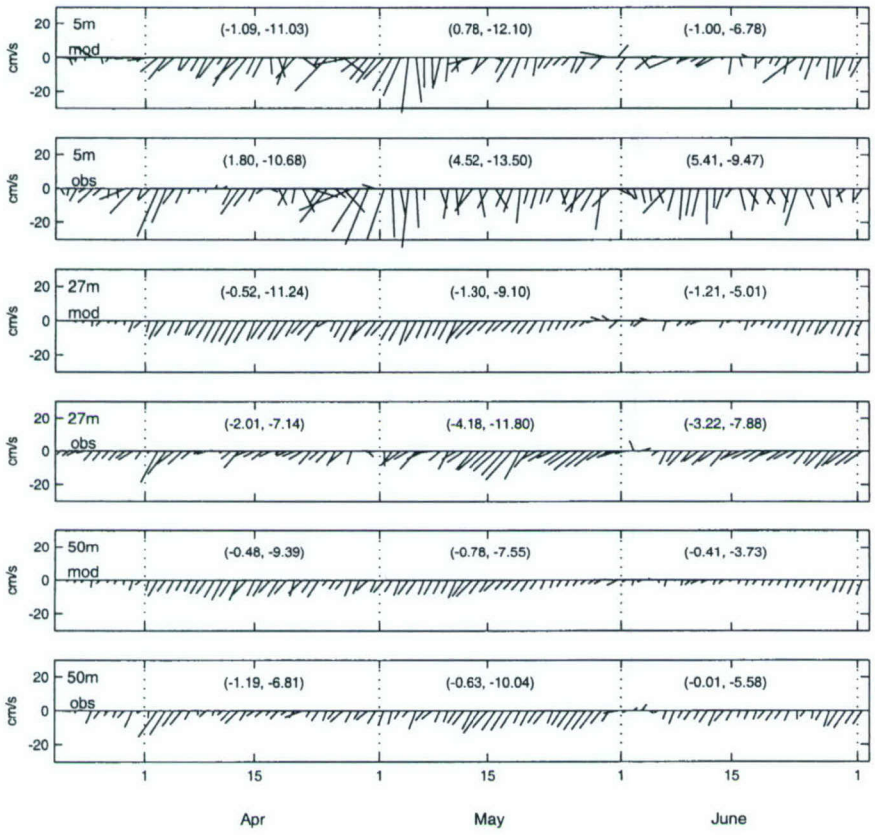


Figure 13a: 1993 Comparison of the modeled and observed current velocities at the Cape Porpoise offshore mooring site (Fig. 1, site P2 of Geyer et al. (2004)). Values listed in parentheses are the mean along-shore and cross-shore velocities for April, May and June. The along-shore is defined as 30° east of true north.

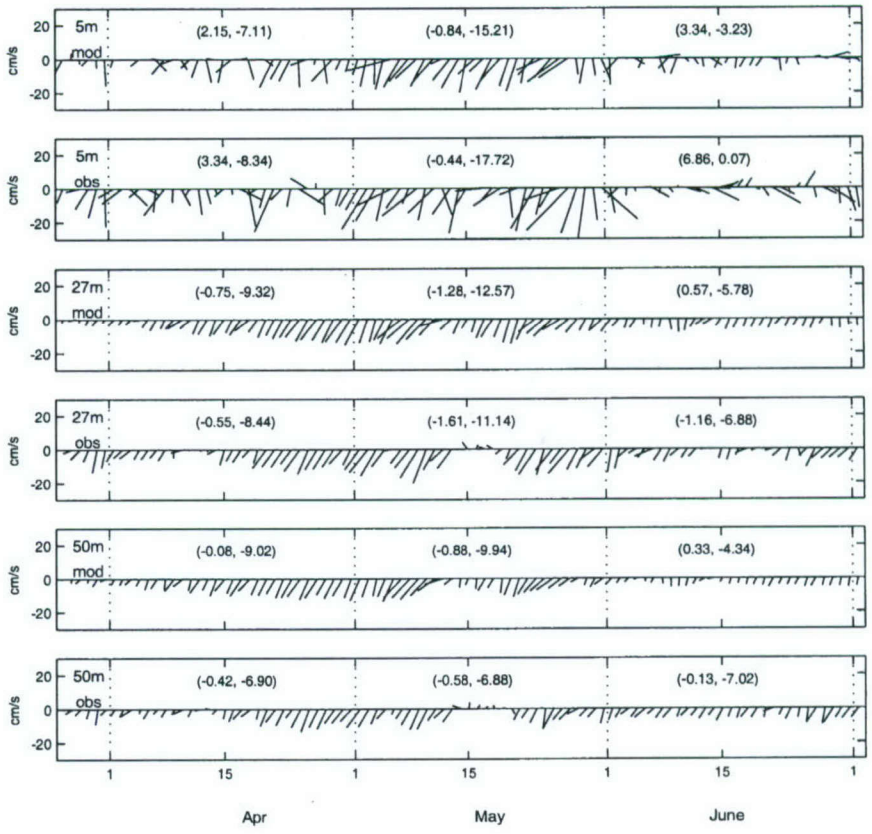


Figure 13b: 1994 comparison of observed and modeled velocities at the Cape Porpoise mooring site.

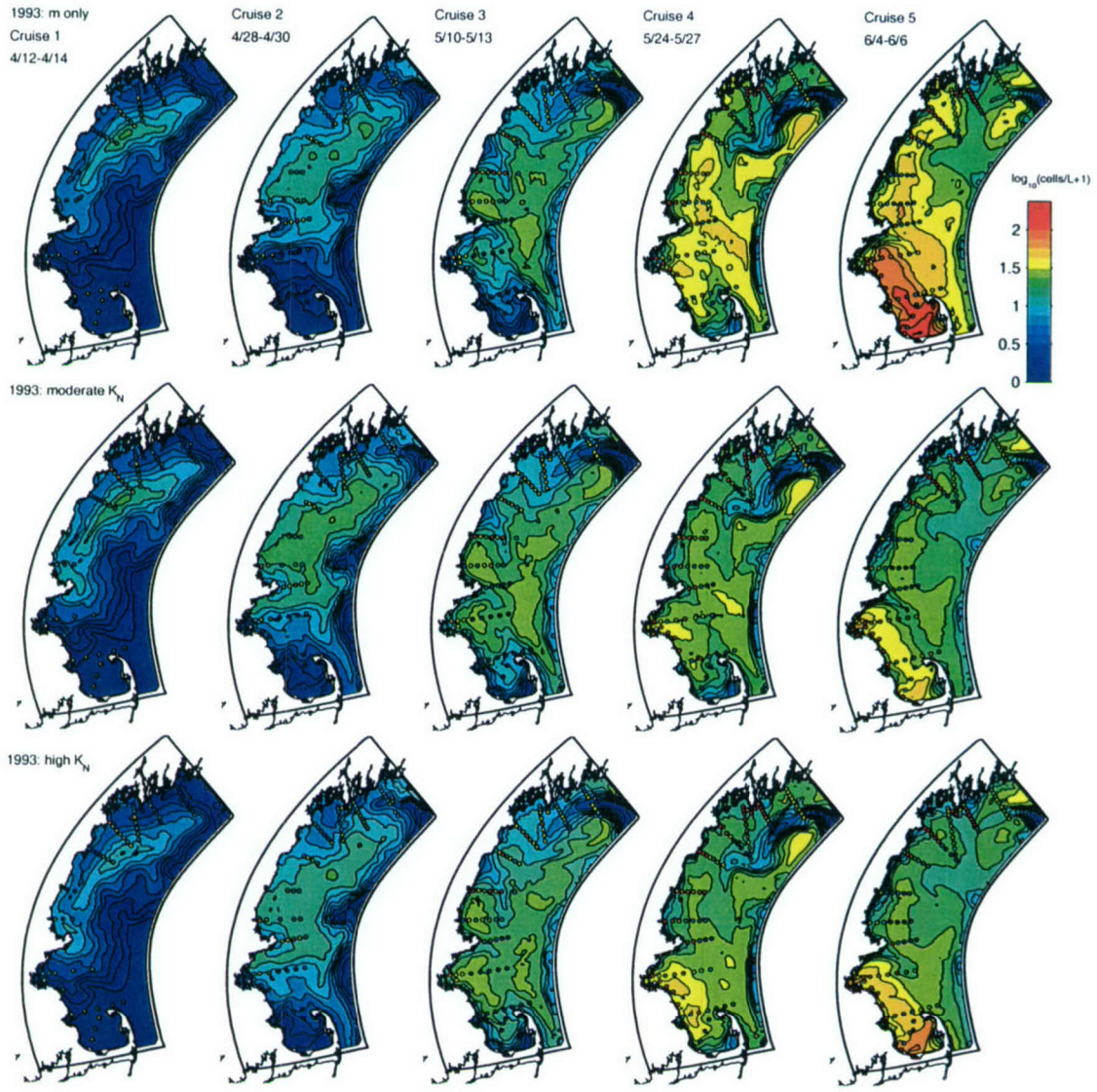


Figure 14: Model/Data comparison for 1993 simulations with mortality only: $K_N = 0.0$ μM, m = 0.15 day^{-1} (top panel), moderate nitrogen dependence: $K_N = 1.5$ μM, m = 0.05 day^{-1} (middle panel), and nutrients only: $K_N = 3.0$ μM, m = 0.0 day^{-1} (bottom panel). Color contours are model output and colored dots are observations plotted on the same log_{10} scale. Identically colored dots and contours indicate good model/data fit.

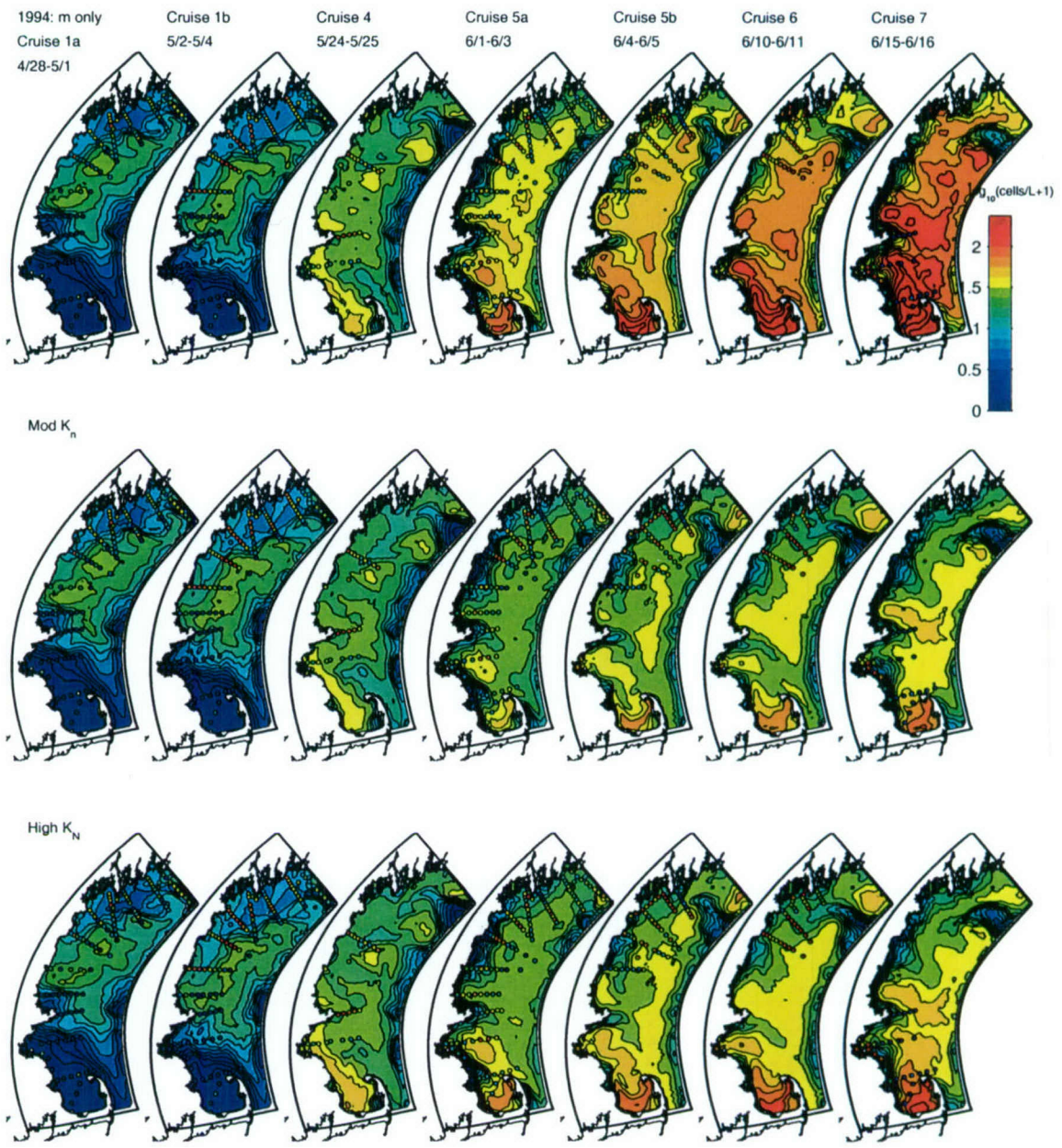


Figure 15: Model/Data comparison for 1994 for 7 cruises with mortality only: $K_N = 0.0$ μM, m = 0.15 day^{-1} (top panel), moderate nitrogen dependence: $K_N = 1.5$ μM, m = 0.05 day^{-1} (middle panel), and nitrogen dependence only: $K_N = 3.0$ μM, m = 0.0 day^{-1} (bottom panel). Color contours are model output and colored dots are observations plotted on the same log_{10} scale. Identically colored dots and contours indicate good model/data fit.

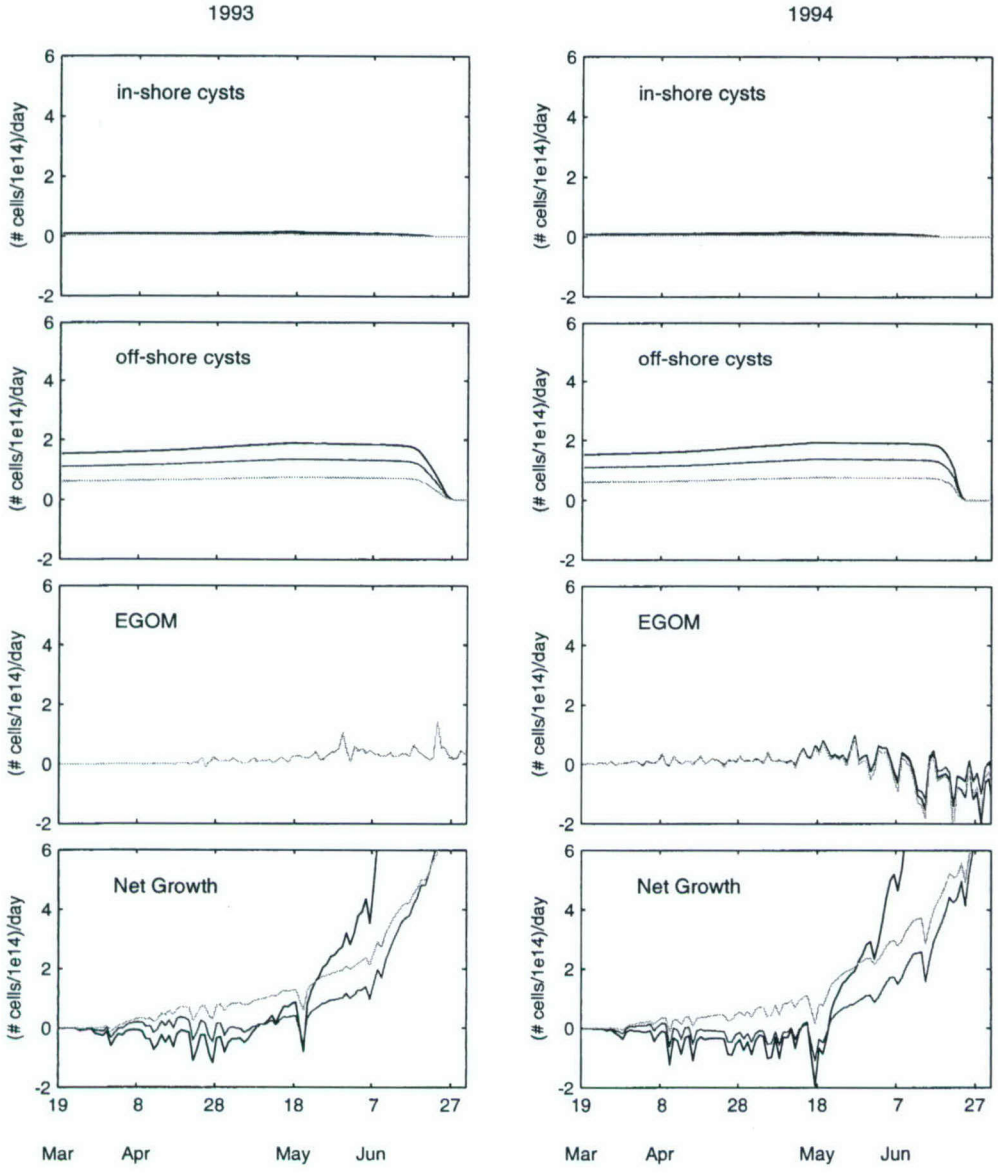


Figure 16: Summary of the flux of *A. fundyense* cells from various sources summed over the entire domain. Different curves refer to different parameter combinations in the biological model: black: K_N=0.5 μM, m = 0.1; medium gray: K_N=1.5 μM, m = 0.05; light gray: K_N=3.0 μM, m = 0.0. **Top panel:** Flux of cells from in-shore cyst beds (< 50m deep). **Second panel:** Flux of cells from off-shore cyst beds (> 50m deep). **Third panel:** Flux of cells through the northern boundary of the domain (presumably from the EGOM). **Fourth Panel:** Change in the number of cells resulting from net growth (growth - mortality).

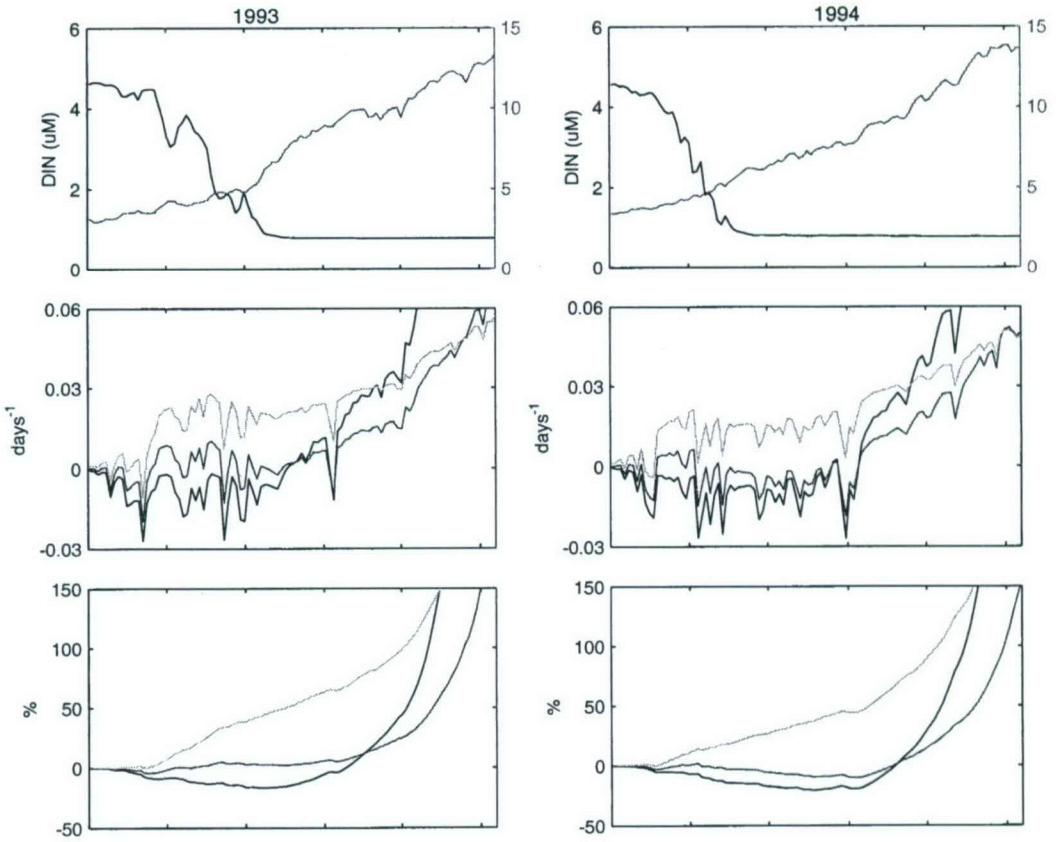


Figure 17: Summary of the domain averaged growth dynamics for the same three biological model settings as in Fig. 17. **Top Panel:** Trends in domain averaged DIN (dark line, left axis) and domain averaged temperature (gray line, right axis). **Middle Panel:** The domain averaged net growth rate for each of the three biological model settings (shading as in Fig. 17). **Bottom Panel:** The % change in the total number of cells relative to a simulation with net growth = 0 but with the other parameters the same.

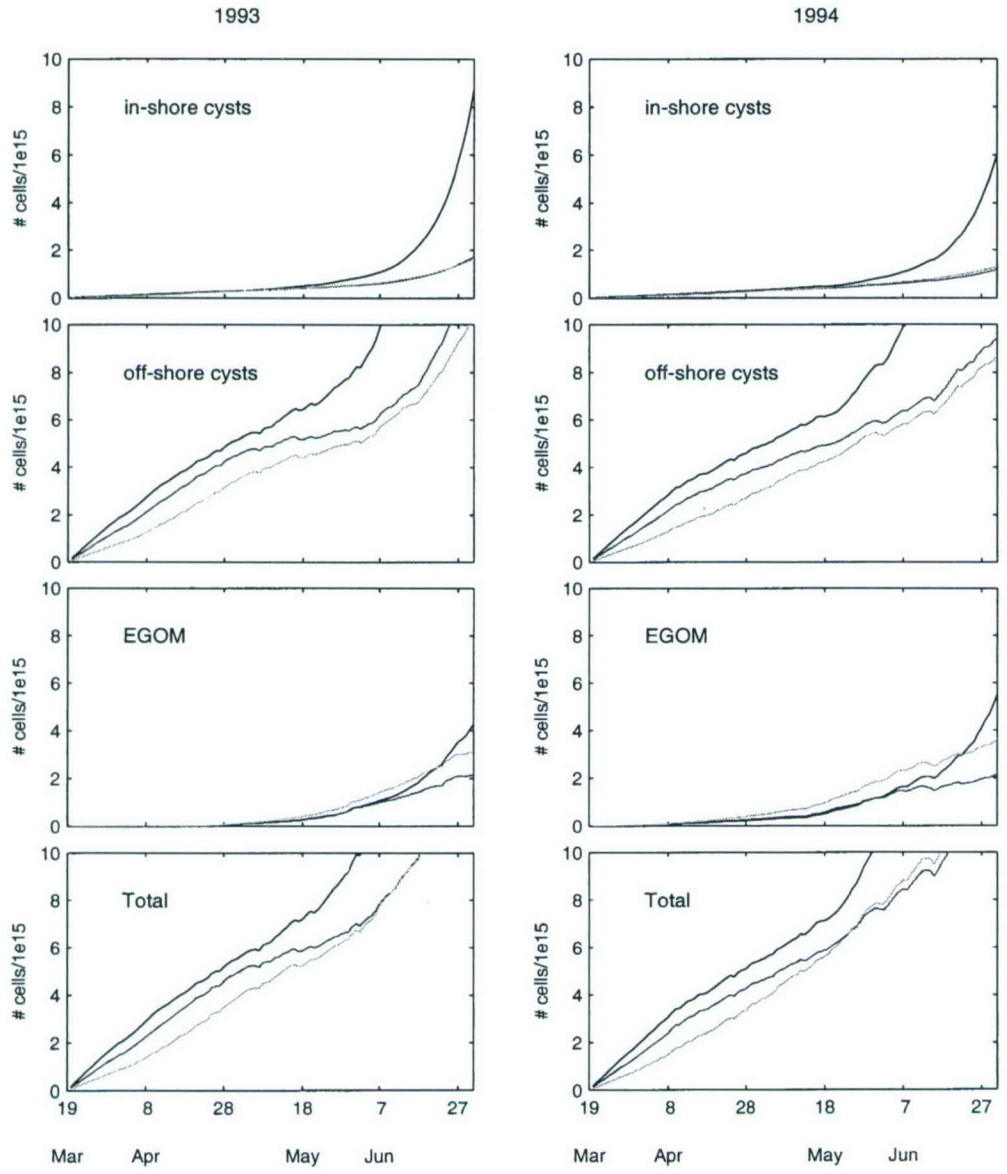


Figure 18: The total number of cells in the domain from each of three origins (top three panels), and the total number of cells (bottom panel) for both 1993 (left column) and 1994 (right column). Note that this total results from a combination of flux from each source (i.e. Fig. 17) and subsequent growth (i.e. Figs. 17-18).

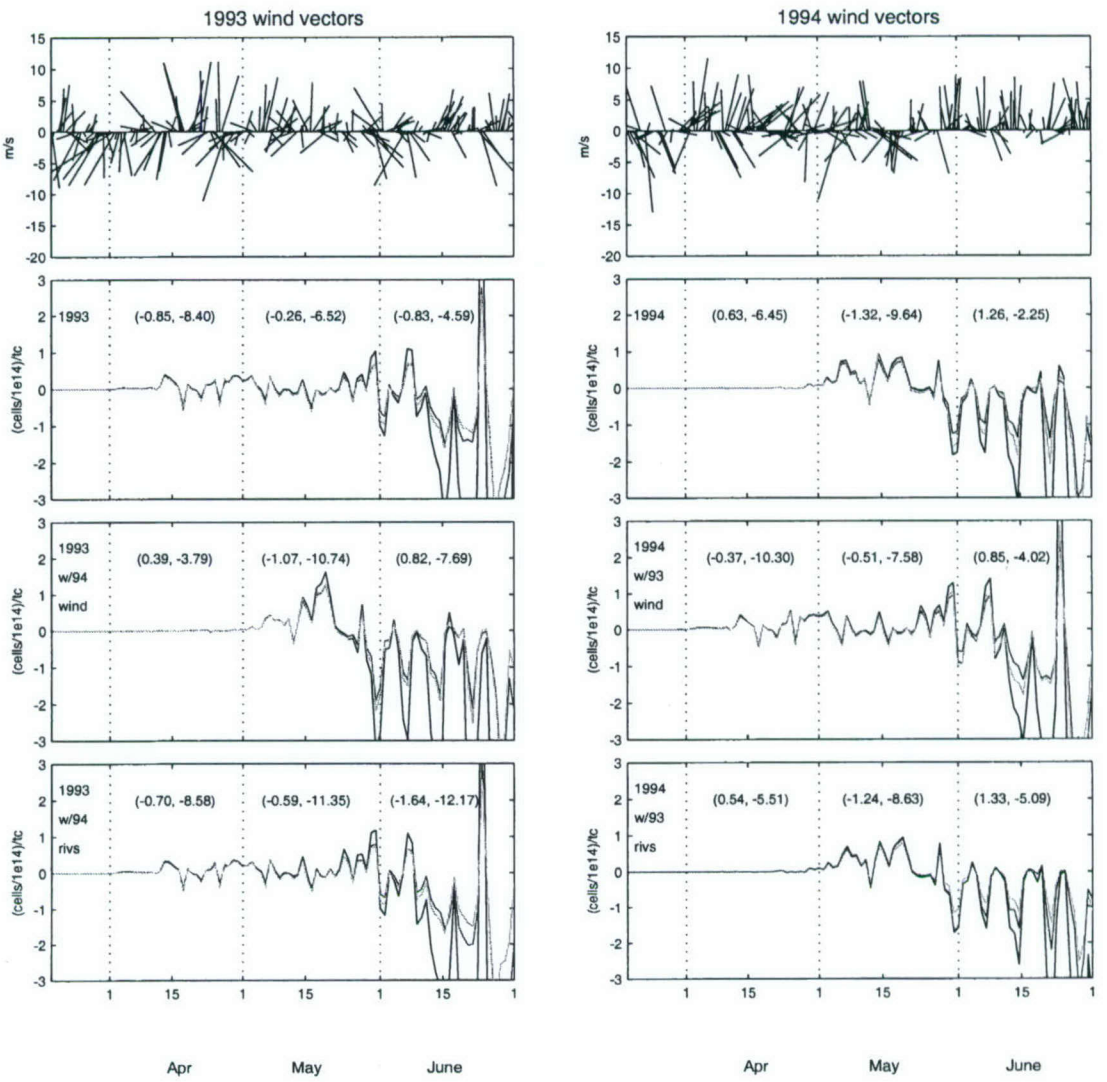


Figure 19: Wind patterns and the delivery of new cells into the Massachusetts Bay/Cape Cod Bay region for 1993 (left column) and 1994 (right column). Winds with a significant south/southeast component are downwelling favorable. **Top Panel:** Wind vectors for each year. **Second Panel:** Flux of cells (#/1e14 per M2 tidal cycle) advected into the MB/CCB control volume (+ in). Numbers are the average modeled cross-shore and along-shore *A. fundyense* transport velocity (cm/s) along a transect running from the coast to 125m across the Cape Porpoise mooring (Fig. 2). Colors of curves are as in Figs. 16-18. **Third Panel:** Same as second panel, but exchanging the wind forcing. **Fourth Panel:** Same as second panel, but exchanging the river forcing.

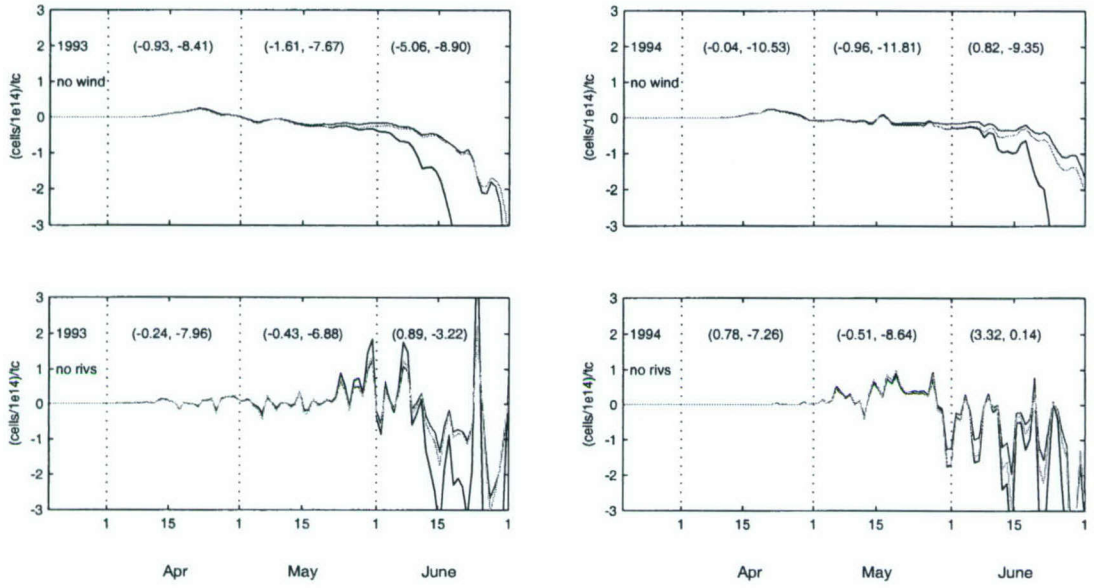


Figure 20: The delivery of new cells to Cape Cod and Massachusetts Bays for simulations with no wind (top panel) or no local river input (bottom panel) in 1993 and 1994. Markings and quantities plotted are as in Fig. 19.

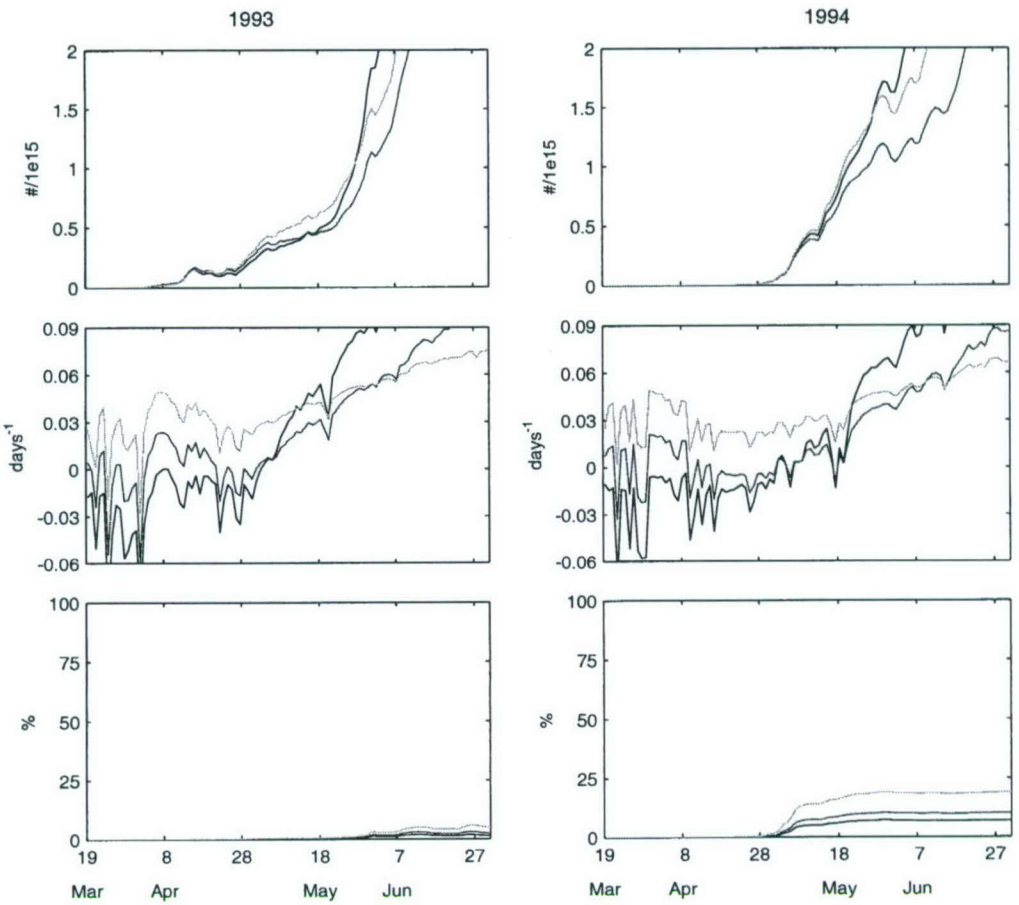


Figure 21: Characteristics of the *A. fundyense* populations within the Massachusetts Bay/Cape Cod Bay control volume in 1993 (left column) and 1994 (right column). **Top panel:** The total number of cells in the region for each of the three biological model settings. **Middle Panel:** The average growth rate of cells within the region. **Bottom Panel:** The % of cells within the region originating from the EGOM.

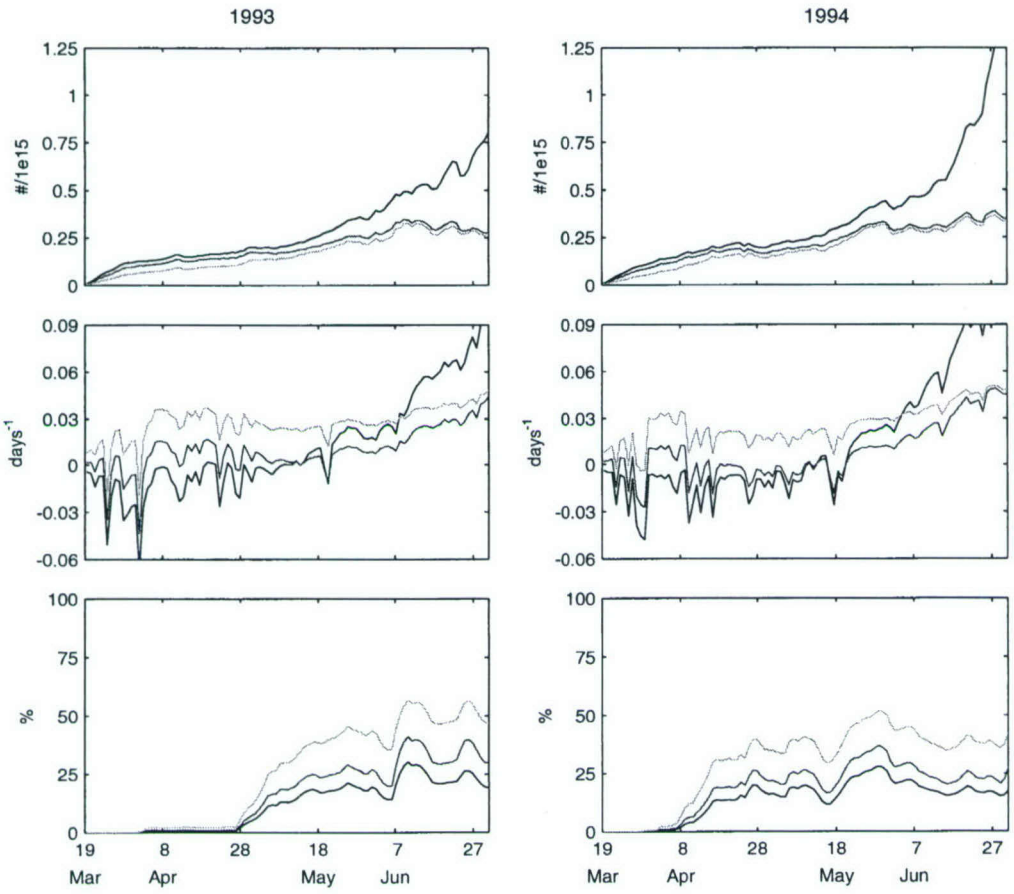


Figure 22: Characteristics of the *A. fundyense* populations within the Casco Bay control volume in 1993 (left column) and 1994 (right column). **Top panel:** The total number of cells in the region for each of the three biological model settings. **Middle Panel:** The average growth rate of cells within the region. **Bottom Panel:** The % of cells within the region originating from the EGOM.

Chapter 5

Summary

This thesis presents a series of studies using a physical-biological model and observations to investigate the dynamics underlying blooms of the toxic dinoflagellate *Alexandrium fundyense* in the western Gulf of Maine (WGOM). The model provided a synthesis of the processes thought to be influencing the distribution and abundance of *A. fundyense*. Formulations within the model were adjusted to represent different hypothesized dynamics. Observations were used to test the ability of each hypothesis to match bloom timing and magnitude. Models that captured several prominent features of the observed blooms were then diagnosed to gain insight into the processes influencing the bloom. This has proven to be very productive approach, particularly when robust statistical methods for comparison were incorporated. Contributions generally fall into two categories 1) methodological elements of general interest to marine ecosystem modelers, and 2) conclusions based on analyses herein that yield further insight into *A. fundyense* bloom dynamics in the WGOM.

5.1 Methodological Contributions

The most notable methodological contribution of this work is the application of maximum likelihood theory to constrain model parameters and test competing biological model hypotheses within a coupled physical-biological model. Such models are often characterized by many uncertain parameters. Estimates of these parameters are generally derived by choosing values that minimize a metric proportional to the difference between the model output and observations. However, diverse forms are encountered in the literature and the metric choice can have a profound influence on the model results and subsequent interpretation (Evans, 2003).

Maximum likelihood theory offers one sensible approach to this issue for several reasons. First, the estimates have a clear interpretation: they are those parameter values that minimize the amount of unexplained variability between the model and the data. Second, estimates derived using the principle of maximum likelihood have well defined statistical properties that are exploited by the maximum likelihood ratio to test hypotheses and build confidence intervals. Third, these properties are generally maintained for non-normal misfits and in the presence of nuisance parameters as long as the sample size is sufficiently large. Lastly, diagnostics exist to ascertain if the choice of the statistical description for the misfit is appropriate. Application of this methodology herein revealed substantial uncertainty around the best-fit parameter values. This suggests that false conclusions may have been reached had only the best-fit value been reported. It is hoped that this example, and the detailed discussion in Chapter 2 will spur wider use of such rigorous statistical methodologies during the model testing in the future, as they are largely absent from physical-biological modeling studies at present.

5.2 Contributions to *A. fundyense* bloom dynamics in the GOM

The primary goals of this thesis in relation to understanding *A. fundyense* blooms in the WGOM were 1) to quantitatively resolve the sources of cells responsible for the initiation of blooms in the WGOM, 2) to further resolve the factors controlling bloom transport, 3) to identify the factors that likely control net growth and estimate the impact of net growth on bloom magnitude, and 4) to identify major sources of uncertainty. The findings concerning these processes also serve as a test of plausibility for the various elements of the plume advection hypothesis.

Analyses in Chapters 3 and 4 provide the first quantitative estimates of the fluxes of vegetative cells from the various potential sources that may initiate blooms in the WGOM. Results suggest that the slow, steady germination of cysts in offshore cyst beds (> 50m water depth) over the course of ~3 months provide the majority of the seed population for WGOM *A. fundyense* blooms in a domain-averaged sense. Inshore cysts play a relatively minor role, contributing < 10% of the flux from those offshore. The flux of the cells from the EGOM becomes increasingly important as the spring progresses into summer, particularly in the region near Casco Bay. Primary uncertainties are the influence of sediment dynamics on the germination source, limited constraint of the EGOM and offshore boundary, and potential inter-annual variability in the cyst distribution.

A second contribution of these studies is that they provide the first quantitative treatment of the impact of net growth on WGOM *A. fundyense* cell distributions and the factors that limit it. There were several key results in this area. First, models capable of recreating the mean magnitude of the observed bloom from April to early June exhibit low (< $|0.05\ day^{-1}|$) domain-averaged net growth rates. The integrated effect of this is a notable, but non-dominant contribution to the bloom magnitude. Some additional spatial patterns are apparent relative to those simulations with net growth set to 0, but differences were not stark. The overall impact of net growth on bloom magnitude is similar in both 1993 and 1994, suggesting that it was not responsible for the large differences in toxicity during the two years.

Simulations identify low water temperatures as primarily responsible for modest net growth in April and May. A combination of mortality and nitrogen limitation is

invoked to slow net growth in May and June. Constraint of the relative importance of these two factors was poor in the 1993 analysis (Chapter 3). However, comparison of the best-fit 1993 values with 1994 data favored moderate or strong nitrogen dependence. This was primarily due to the ability of these simulations to better match the low mid-June abundance of *A. fundyense* in Massachusetts and Cape Cod Bay during 1994. The primary uncertainty in these net growth calculations is the precise nature and space/time variability of the mortality term. It is suggested that the inability to resolve this might be responsible for rapidly increasing cell abundance in areas of hydrodynamic retention (i.e. Cape Cod Bay) at the end of all simulations.

A third contribution is the investigation of the influence of various aspects of the physical model forcing on the transport of *A. fundyense*. The ability to turn aspects of the forcing on and off, as well as exchanges of forcing between years was particularly useful in this regard. Analyses (Chapter 4) suggest that *A. fundyense* transport velocities between Casco Bay and Cape Ann in 1993 and 1994 are maintained primarily by the steady along-coast flow associated with Gulf-wide circulation patterns. The magnitude of this velocity and its direction is modulated significantly by local wind patterns over both daily and monthly time scales in a manner consistent with Ekman dynamics. WGOM river inputs played a relatively minor role. Transport at the Cape Ann branch point and within Massachusetts and Cape Cod Bays (MB/CCB) is also strongly influenced by the wind. Periods of *A. fundyense* transport past Cape Ann and into MB/CCB were strongly correlated with downwelling or relaxed wind conditions. Upwelling conditions directed populations near Cape Ann around the arm of Cape Cod. Within MB/CCB, upwelling creates a separation between cells and coastal areas and

prevents penetration of the bloom deeper into Cape Cod Bay. Downwelling or relaxed conditions caused cells to impinge upon the coast and penetrate more deeply into Cape Cod Bay. Prevalent upwelling in 1994 is suggested as the primary reason for the lack of toxicity in MB/CCB and greatly decreased toxicity along the Maine coast. The primary uncertainty their generality subject to inter-annual fluctuations in the elements of the forcing.

There are several general implications of the dynamics summarized above. First, the magnitude of the *A. fundyense* bloom in the WGOM is closely linked to the initiating sources. Second, barring dramatic shifts in these source terms, inter-annual differences in shellfish toxicity are strongly linked to physical forcing, particularly the wind. Lastly, *A. fundyense* accumulates in areas of strong hydrodynamic retention such as Cape Cod Bay, and loss terms may be pivotal to capturing bloom termination in such regions. The first two implications are consistent with the basic ideas within the plume advection hypothesis: populations established by the source terms to the north are advected to the south subject to strong wind forcing which profoundly influence shellfish toxicity. It is suggested herein that the local river plumes may not be as critical to the along-shore transport as initially thought, and the finding regarding inshore cysts suggests that Casco Bay may also not be the critical source region, but the essential elements of the Franks and Anderson (1992a, 1992b) appear plausible over the majority of the WGOM.

5.3: Future Steps

5.3.1: Methodological Development

Despite the demonstrated utility application of maximum likelihood theory described herein, there are several areas where it could be improved. The first is the replacement of the manual parameter space search applied for the likelihood estimation herein with a more advanced parameter search algorithm such as the adjoint method (e.g. Lawson, et al., 1995). This should enable more efficient analyses in the future. The likelihood function naturally enters the adjoint methodology as a cost function. In addition, the estimates of the likelihood gradients provided by the adjoint are useful sensitivity metrics.

A second area where improvement could be made is through an increased understanding of the different components of the misfit. For example, knowledge of the typical misfits resulting from comparison of a "correct" biological model to observations in the presence of only physical uncertainty would be a useful interpretive benchmark. This information could also be used to construct a filter designed to identify misfits not explained by such physics. Alternatively, such a filter could be applied before comparison in the hope that filtering "noise" *a-priori* will tighten parameter constraints. Characterization of this physically generated noise could be approached using Monte-Carlo simulations that perturb various aspects of the physical model forcing and track the variability generated at the observation points.

5.3.2: Further Study of A. fundyense *Bloom Dynamics*

Direction for future research of *A. fundyense* bloom dynamics can be gained through consideration of the salient aspects of the dynamics summarized in Section 5.2 along with prominent uncertainties. The close link between the abundance of *A. fundyense* in the WGOM and the size of the initiating sources suggests the importance continued work toward understanding variability in these sources. The uncertainties identified herein are the influence of sediment dynamics on cyst germination, inter-annual cyst variability, and inflows from the EGOM. The dominant role of the physics in explaining shellfish toxicity patterns in the region suggests the importance of understanding how inter-annual variability in the different constituents of the forcing influences the conclusions drawn above. Lastly, the inability of the present model to capture bloom termination due to the presence of rapidly increasing populations in areas of hydrodynamic retention at the end of the simulations suggests further study of processes governing the space and time variability of sources and sinks.

Diverse approaches should be used to resolve these problems. Several issues involve further resolution of dynamics that are simplified in these studies. Among these are the influence of sediment dynamics on the ability of cysts to germinate and further resolution of loss terms and limitations. Laboratory and field studies that constrain these processes will likely provide improved quantitative estimates if incorporated into the existing model. As more advanced physiological processes are resolved, explicit resolution of cell nutrition or other components of the ecosystem such as zooplankton may be required. The first of these refinements would favor the use of an individual

based model, as time histories of nutrient uptake would likely be necessary. The second refinement would require insertion of the *A. fundyense* dynamics model into an ecosystem model.

The incorporation of more complex models will undoubtedly lead to more free parameters, making the methodology herein (and further improvement to it) even more critical. Indeed, the degree and nature of the noise in the model/data comparison suggests that it may have difficulty detecting the influence of improvements in the biology within the model/data fit. However, the inability of the model/data comparison to provide additional constraint does not prevent incorporation of more advanced dynamics as a means to measure the probable influence of a process using parameters constrained in the laboratory or field. It only implies that the observations cannot differentiate the more complex model from a simpler option that may be equally plausible.

Some of the issues described above are not rooted in uncertainties in the governing equations, but to the generality of the result. For example, the findings herein regarding *A. fundyense* transport are very robust, and their more general applicability is likely. However, a modeling study focused on the influence of the range of observed variability in the constituents of the forcing (i.e. local rivers, wind, gulf-wide circulation) to the transport processes critical to *A. fundyense* would add additional context to these results. The behaviors observed and thresholds identified in such a study would also be of great use as a guide for the construction of empirical models trying to relate observations of several key factors to toxicity within a region.

Many of the results stress linkages between WGOM *A. fundyense* blooms and those within other regions of the Gulf. Conclusions regarding the source provide two

examples. The first is the suggestion that shellfish toxicity in Casco Bay is closely linked to influxes of vegetative cells from the EGOM. The second is that the germination of deep cysts offshore of Casco Bay is particularly important to blooms in the WGOM. Current hypotheses concerning the maintenance of this cyst bed suggests replenishment, at least in part, by the encystment of cells associated with blooms to the east (Anderson, et al., submitted, McGillicuddy, et al., submitted). These both suggest the value of a more Gulf-wide approach, or at least the importance of properly constraining boundaries if local approaches are taken.

Much of the discussion has focused on future steps aimed at increasing understanding of the factors controlling the initiation and development of blooms in the Gulf of Maine - particularly in relation to the model/data framework developed in this thesis. However, the economic and public health implications of this research topic warrant ending discussion of future steps with how this work might translate into operational tools of use to regulators. Models such as that which is presented here will never eliminate the need for shellfish monitoring. Even if toxicity sub-models are implemented and considerable skill is shown, the extent of the risk demands *in-situ* testing. However, increased knowledge of the factors governing cell abundance and subsequent toxicity gained through these efforts can aid immensely in refining efforts to effectively monitor an extensive coastline with limited resources.

Areas just downstream of branch points of the coastal current provide good examples. Several results herein have contributed to linking toxicity in regions downstream of the Cape Ann and Penobscot Bay branch points to the forcing at these points and the presence of *A. fundyense* in their vicinity. If continued efforts allow the

behavior at such points to be distilled reliably into the values of several routinely sensed parameters (e.g. satellite SST, wind, and a bottom pressure measurement in Jordan Basin) critical times for sampling can be identified and the risk for missing a toxic event. In addition, ongoing research (McGillicuddy, et al., 2002, He, et al., submitted) suggests considerable skill in predicting drifter tracks in the Penobscot region on daily and weekly time scale using data assimilative models. These modeling efforts could compliment any empirically derived risk assessment. Lastly, incorporation of newly developed technologies for automated *in-situ* observing of *A. fundyense* (Scholin, et al., submitted) would further enhance such predictions. There thus appear to be rich prospects for the translation of the contributions of this work into direct operational use.

Anderson, D. M., Stock, C. A., Keafer, B. A., Bronzino, A. C., Matrai, P., Thompson, B., Keller, M., McGillicuddy, D. J., Hyatt, J., submitted. Experimental and modeling observations of *Alexandrium fundyense* cyst dynamics in the Gulf of Maine. Deep-Sea Research, Part II

Evans, G. T., 2003. defining misfit between biogeochemical models and data sets. Journal of Marine Systems 40-41, 59-54.

Franks, P. J. S., Anderson, D. M., 1992a. Alongshore transport of a toxic phytoplankton bloom in a buoyancy current: *Alexandrium tamarense* in the Gulf of Maine. Marine Biology 112, 153-164.

Franks, P. J. S., Anderson, D. M., 1992b. Toxic phytoplankton blooms in the Gulf of Maine: testing hypotheses of physical control using historical data. Marine Biology 112, 165-174.

He, R., McGillicuddy, D. J., Lynch, D. R., Smith, K. W., Stock, C. A., Manning, J. P., submitted. Data Assimilative Hindcast of the Gulf of Maine Coastal Circulation. Journal of Geophysical Research, Oceans 47 pages.

Lawson, L. M., Spitz, Y. H., Hofmann, E. E., Long, R. B., 1995. A data assimilation technique applied to a predator-prey model. Bulletin of Mathematical Biology 57, 593-617.

McGillicuddy, D. J., Anderson, D. M., Keafer, B. A., 2002. MERHAB: Forecasting *Alexandrium* Bloom Transport in the Gulf of Maine. Research Proposal, Woods Hole Oceanographic Institution, Woods Hole, 31 pages.

McGillicuddy, D. J., Anderson, D. M., Lynch, D. R., Townsend, D. W., submitted. Mechanisms regulating the large-scale seasonal development of *Alexandrium fundyense* blooms in the Gulf of Maine. Deep-Sea Research, Part II

Scholin, C. A., Doucette, G. J., Cembella, A. D., submitted. Prospects for developing automated systems for in situ detection of harmful algae and their toxins. In: Babin, M., Roesler, C. S. ,Cullen, J. J. (Eds.), Monographs on oceanographic methodology. UNESCO, pp. (submitted).

Appendix A

The Germination Model

Introduction

This document gives a detailed description of the *Alexandrium fundyense* germination model that was developed as part of the ECOHAB-Gulf of Maine program. A reference is provided by Anderson et al. (submitted), and the model has been used in several other studies (McGillicuddy, et al., 2003, McGillicuddy, et al., submitted-b, Stock, et al., submitted). The modeled rate of germination (G, % of initial cysts/day) is a function of bottom water temperature (T, °C), the day-light averaged irradiance (E, watts/m^2, 8 AM-6 PM), and an endogenous clock ($EC(t)$, where t is the year-day):

$$G(T,E,t) = EC(t) \times G(T,E)$$

The flux of *A. fundyense* from the cyst bed to the water column (F_g) is then estimated by applying the germination rate to an observed cyst distribution:

$$F_g = \int_0^{d_g} \left(G(T,E(z),t) \times [Cysts/cm^3]_o \right) dz$$

where d_g, the "germination depth" in centimeters, is an estimate of the depth of sediment over which cysts are exposed to oxygen and can gain access to the water column through the sediment grain matrix. It is notable that the germination rate multiplies the initial cyst concentration: $[Cysts/cm^3]_o$, rather then the present level of cysts. This is done for consistency with the germination time series data (see below). Three primary parts of the germination model are detailed herein:

- The temperature and light dependence
- The endogenous clock
- The germination depth estimation

Each section begins by describing the data and/or studies from which the function is formed. The function construction is then presented in detail, followed by a brief discussion of assumptions and limitations.

1 The Temperature and Light Dependence

1.1 Background and Data

Laboratory data from two cyst isolates was used to construct the dependence of *A. fundyense* germination on temperature and light. The first isolate was collected offshore of Casco Bay Maine (station 38, Latitude 43.50°N; Longitude 69.88°W) in approximately 125 meters of water. The second isolate was taken near the mouth of the Bay of Fundy (station 4, Latitude 44.89°N, Longitude 66.81°W) in 135-140 meters of water (figure 1). Time series of germination were tracked with cysts exposed to water temperatures of 2, 4, 6, 8, and 15 °C in "light" and "dark" conditions. The "light" condition was classified as an irradiance of 5-15 $\mu E/(m^2 s)$ applied on a 14:10 LD cycle. The "dark" condition excluded all light.

The experimental methods are described in detail in Anderson et al. (submitted). Briefly, cysts were collected from the top 2-6 cm of sediment and stored under anoxic conditions until 90-93% germination potential was shown (i.e. it was ensured that the germination rate would reflect the rate obtainable when the endogenous clock was not limiting). The sediment sample was then combined with F/2 media, made into uniform slurry, and divided into separate flasks for incubation under the various experimental conditions. The flasks were then harvested over time to produce germination and fluorescence time series for each condition (figure 2).

1.2 Function Construction

The slope of a linear fit was used to estimate a germination rate for each experimental time series. The fitting procedure was complicated by the asymptotic behavior of the data points as the germination potential was approached. To capture the slope of the germination curve over the time during which the majority of cysts germinate, only points of ≤ 90% germination and those taken ≤ 75 days after the beginning of the time series are included in the fit. The fitted lines were not forced through the origin to minimize the influence of any necessary acclimation to experimental conditions after transfer from cold, dark storage. The resulting slopes fit are shown in figures 3-6 and summarized in Table 1.

The discrete germination rates in table 1 were interpolated and extrapolated to other temperatures by fitting to the function:

$$G(T, E_{lgt}) = G_{\min}(E_{lgt}) + \frac{(G_{\max}(E_{lgt}) - G_{\min}(E_{lgt}))}{2} \times \{\tanh(\alpha(E_{lgt})T - \beta(E_{lgt})) + 1\}$$

$$G(T, E_{drk}) = G_{\min}(E_{drk}) + \frac{(G_{\max}(E_{drk}) - G_{\min}(E_{drk}))}{2} \times \{\tanh(\alpha(E_{drk})T - \beta(E_{drk})) + 1\}$$

Where E_{lgt} and E_{drk} refer to the irradiance under the "light" and "dark" experimental conditions. The hyperbolic tangent function allows for a linear relationship over moderate temperatures (slope = α) that is consistent with many previous investigations of seed germination behavior (Bewley and Black, 1978). It also allows for maximum germination rates ($G_{\max}$) and minimum germination rates ($G_{\min}$) to occur over broad ranges, which is suggested by previous observations of *A. fundyense* germination

behavior (Anderson, 1998). Fitted parameters are given in table 2 and the resulting function is shown in figure 7.

The light response is interpolated and extrapolated to other values using:

$$G(T,E) = G(T,E_{lgt}) \qquad E \geq E_{lgt}$$

$$G(T,E) = G(T,E_{drk}) \qquad E \leq E_{drk}$$

$$G(T,E) = G(T,E_{drk}) + \left(G(T,E_{lgt}) - G(T,E_{drk})\right) \times \frac{E - E_{drk}}{E_{lgt} - E_{drk}} \qquad E_{lgt} > E > E_{drk}$$

For the purpose of this calculation, E_{drk} is taken to be 1% of E_{lgt}. The irradiance used is the average value over 14 daylight hours (e.g. 6 AM - 8 PM), as experimental light conditions were on a 14:10 cycle. To approximate the light reaching the cysts within the sediment, observed surface shortwave irradiance is exponentially attenuated in the water column (k_w) and within the sediment (k_s). The resulting function is shown in figure 8. It is notable that the germination rate multiplies the initial cyst concentration, and not the concentration at any given time. This is done to be consistent with the germination time series data.

1.3 Discussion

The curve fitting thresholds and methods were chosen because 1) they are generally effective at minimizing contamination of the slope estimates by the asymptotic behavior of the germination time series as the germination potential is approached, 2) they did not lead to the elimination of large numbers of data points from consideration. Other thresholds were evaluated and performed fairly well, but those chosen exhibited the most robust performance over the range of experimental conditions. There are some

cases (e.g. 6° in the light) where subjective fitting may shift the result slightly. However, given the level of noise in the data and the uncertainty in the resulting slopes, it would tenuous to make any substantial inference based on the small changes that such subjective adjustments would create.

Consideration was also given to the usage of more complex functional forms for the fitting. However, such efforts are restricted by the necessity of associating one representative rate with each experimental condition. In addition, the increasing portions of the curves generally show a high degree of linearity and increasing complexity in the functional form is likely to make little difference to the overall character of the germination rate function.

The functions require a large amount of extrapolation and interpolation. Sensitivity tests within the Gulf of Maine (e.g. Stock et al., submitted) suggest that the uncertainty produced by the details of this interpolation and extrapolation is small relative to the uncertainty contributed by other aspects of the germination and growth model. However, this sensitivity is dependent upon the setting in which the model is used and should be revisited if the model is being applied in a markedly different environment (e.g. a shallow enclosed salt pond).

The strongest suggestion that differences may exist between the two isolates comes from the 8°C time series in the dark condition. In the other 7 cases where comparison between the WGOM isolate and the EGOM isolate is possible, estimated rates are very similar. Thus, despite the discrepancy at 8°C in the dark, differences are minimal and no attempt was made to construct separate functions for each strain.

2. The Endogenous Clock

2.1 Background and Data

The germination potential of *A. fundyense* is modulated by an internal endogenous clock (Anderson and Keafer, 1987, Matrai, et al., submitted). This clock is capable of preventing germination even when environmental conditions are favorable. Experimental data for construction of the endogenous clock were drawn from experiments by Anderson and Keafer (figure 9), Matrai et al. (figure 10) and from data presented by Bronzino (1998), (figure 11). The isolations used for the three data sets are summarized in Table 3.

The experimental protocol was similar in all cases. Detailed descriptions appear in Matrai et al. (submitted) and Bronzino et al. (1998). Briefly, once sediment samples were collected they, along with the cysts within them, were stored in dark, cold (2° C), anoxic conditions. Periodically (every 2 weeks in the Bronzino et al. and Matrai et al. experiments, and slightly less often in the earlier data) 30 cysts were isolated from the stored sediment and transferred to a culture well with f/2 medium. These wells were placed in an incubator at 15° C and subject to a 14:10 light/dark cycle with greater than 150 $\mu E/(m^2 s)$ of light. The germination of cysts in the 30 well plates was tracked periodically. Matrai et al. report the percentage of cysts germinated after 6 weeks, Bronzino and Anderson and Keafer report values after 4 weeks. There were other small differences in experimental technique between the different data sets. During the isolations in the 1980's, sediment was stored as a bulk sample, which required that storage conditions be compromised for short periods during the isolation process. Thereafter, the sediment for each isolation was stored in separate vials. Also, Matrai et al. (submitted) took slightly more exhaustive measures to ensure anoxic conditions during storage. However, in all cases, cysts taken out of storage showed a lack of fluorescence

suggesting that contamination with oxygen during storage was minimal and probably did not influence results (Keafer, personal communication).

Despite the similarities in experimental conditions, the different isolates show considerable variability in both the timing and the duration of peaks in germination potential. In the station 29 data, the three isolates show an initial peak in germination potential at three different times. Cysts from the 1984 sample reach maximum germination potential in early March, while the 1985 sample and 1987 samples reach germination peaks in the late spring and early summer. The 1985 sample also shows a more gradual climb to peak conditions than many of the other cyst samples. The results of Matrai et al. show an initial peak in germination potential for experiments initiated in February and March, and in this way are consistent with the initial peak of the 1984 station 29 cysts. Station 94 shows a more elongated decline from the peak than the station 61 and station 4 cysts. Lastly, the station 38 data show a late March/early April initial peak, and a slow decline in germination potential that is even more pronounced then station 94.

Potential reasons for the different patterns exhibited in figures 9-11 are discussed in Anderson (1998) and by Matrai et al. One possibility mentioned is that cysts within a particular sediment sample contain a mixture of strains with different genotypes, each with somewhat different endogenous clock strategies. If this were the case, one would expect variability based on the relative proportion of the different genotypes during any given year or at a particular location. A second possibility is that the different patterns result from interaction with environmental cues that "entrain" the endogenous clock in an external rhythm. This process is well described in Sweeney (1969):

> Just as in physical oscillations, the frequency of rhythms may be forced to match exactly that of some external oscillation, the alternation of light and darkness for example. When this occurs, the rhythm is said to be entrained by the external oscillation. The signal responsible for the entrainment has been called the 'zeitgeber' or 'time-giver'. Entrainment, of course, can only take place while the external oscillation is actually present. When a rhythm is not entrained, it is said to be free running and now shows its natural period.

Matrai et al. (submitted) estimated a natural period of 11 months (+/- 2 months). However, the predictable seasonal timing of *A. fundyense* blooms suggests that they have become entrained by a 12-month environmental rhythm. This entrainment phenomenon links the properties of clock to external cues: Although the clock operates in the absence of any environmental cues, environmental cues can influence the properties of the clock. This makes the task of constructing a function based on the data in figures 9-11 (i.e. constant environmental conditions) for use in the model (variable environmental conditions) more difficult. The validity of any representative endogenous clock constructed from the laboratory data described above requires assumptions about the relationship between the free-running and entrained rhythms that will be discussed below.

2.2 Function Construction

Data used to construct a representative endogenous clock cycle were restricted to those that 1) were taken during the first year after the cyst isolation date, and 2) were taken before the second observed rise in the germination potential (filled dots in figures 9-11). These points were binned into months according to the mid-point of the 4 or 6

week experiment. The median value of the experimental points in each bin was then used to assign a representative germination potential for each bin. The resulting function is shown in figure 12 and the values for each month are reported in table 4. The germination potential for each month is normalized with the maximum germination potential to form the normalized germination potential (NGP, table 4). The multiplier *EC*(t) within the germination model cycles between values of the NGP for each month using a linear interpolation.

Only data from the first 12 months after isolation were used because this minimizes shifts in the phase at a given yearday resulting from transition back to the natural period of the clock (~11 months) once constant environmental conditions are established. Peaks in the laboratory measured germination potential will be observed approximately 1 month earlier for each year that the cells have been isolated from environmental cues. If these additional years were included, there would be a bias toward earlier germination peaks in the representative model clock relative to the entrained clock (which the model hopes to approximate). The additional condition eliminating points associated with the second observed rise in the germination potential was added as an additional safeguard to this kind of contamination.

Experimental points are shifted to the mid-point of the experimental period because the reported germination potential represents an integration of the germination potential over the 4 (or 6) week experimental period. This is likely to have variable effects depending on the rate of change of the germination potential over the time of the experiment, the direction of that change, and the rate of germination. For example, if the rate of germination was fast relative to the experimental period and the germination

potential was increasing, the potential recorded would reflect the potential at the end of the experimental period. If the germination potential was decreasing and the rate of germination was still fast, the opposite would be true. That is, cysts would quickly germinate at the beginning of the experimental period (when the germination potential was high), and the decreasing potential later during the period would have little effect. Given that germination rates under the conditions used for the endogenous clock experiment (~5-10 %/day) act on time scales similar to the experimental period, the simplest way to minimize uncertainty associated with the temporal placement of the measured germination potential is to center it within the time period covered by the experiment.

The use of the median is designed to prevent the creation of a representative cycle that, because of averaging in variable areas, has properties that are dissimilar from any of the data sets contributing to it. Most notably, use of the mean would lead to a greatly damped oscillation. The peak germination potential would only be ~ 85%, while the minimum would be ~30%. The median focuses the fit on characteristics common to the majority of the cycles: A sharp late fall/winter low in the germination potential followed by an abrupt spring rise to just under 100%, then maintenance of the high potential throughout the spring and majority of the summer until a more gradual late summer, early fall decline.

2.3 Discussion

The ability to construct a representative endogenous clock function for *A. fundyense* in the Gulf of Maine based on the laboratory data described above rests on two primary assumptions:

1. The phase of the clock does not change when cysts are removed from the sediment and stored.
2. The first-order characteristics of the free-running clock (i.e. the duration and size of the peaks and troughs) are similar to those of the entrained clock.

Some support for these assertions is provided by measurement of cyst fluorescence in sediments from the field (Anderson and Keafer, 1985, Anderson, et al., submitted). Additional support is sparse. However, the assumption that the free-running clock is not drastically different than the characteristics favored by the environmental patterns that the clock has evolved to function within seems a reasonable starting point.

The influence imposed upon the endogenous clock by environmental cues means that care should be taken when applying this function to regions where the seasonal cycle is shifted significantly relative to that of the Gulf of Maine. Even when environmental conditions are similar, the variability between isolates suggest considerable uncertainty in the details of the function and care should be taken to avoid overly fine inferences regarding the temporal properties of the source as they relate to the endogenous clock.

3. Influence of Sediment Mixing

3.1 Background and Data

A. fundyense cysts reside in a dynamic sediment environment whose physical, chemical, and biological properties can have a profound influence on germination. Cysts can remain viable within the sediment for years and cyst distributions within the sediment show considerable vertical structure related to past history of deposition, germination,

and sediment mixing dynamics (Anderson, et al., 1982, Keafer, et al., 1992). Sediment dynamics can influence the cyst source in ways not within the basic model described above. Additional light attenuation within the sediment can slow rates below those shown in figure 8, oxygen depletion near the surface of the sediment can severely limit the depth over which cysts can germinate (Anderson, et al., 1987), and the impairment of upward vegetative cell movement within the sediment grain matrix can prevent newly germinated cells from ever reaching the water column. Each of these factors will be discussed briefly below after which the current modeling approach will be described and discussed.

Light attenuation within the sediment can be substantial. Kuhl and Jorgensen (1994) report a range of wavelength dependent diffuse light attenuation rates in sandy coastal sediments (63-250 μM grain size with diatom detritus) from 2-5 mm^{-1}, roughly ten thousand times the attenuation rate in the water column in typical coastal areas. It is thus necessary to consider light attenuation within the sediment for cysts lying even 1 mm below the sediment surface, as this is equivalent to as much as 25m of water column in typical coastal waters (~0.2 m^{-1}).

Anaerobic conditions completely suppress the germination of *A. fundyense* as well as the fluorescence that preceeds it (Anderson et al. 1987). Depletion of oxygen in the surface sediments is dependent upon multiple physical and biological factors including the amount of oxygen in bottom waters, mixing within the sediment, and the flux of organic matter to the sediment. In the Gulf of Maine, Anderson and Keafer (1985) noted that fluorescence of cysts was very low (7% on average) within the 1-2 cm sediment depth interval at station 29. Cysts taken above 1 cm showed a considerable

increase (39% on average, with a peak of 83% during the late spring). Results from a second nearby station (61 meters depth) are similar, although fluorescence at both depths was lower than those at the respective depths for station 29 (10% and 1% respectively, with a high value in the 0-1 cm interval of 23%). In addition, Hines (1991) noted anaerobic metabolisms were prevalent 1 cm into the water column for 2 of 3 cores in the western Gulf of Maine. The third core showed slowed rates of anaerobic activity at 1 cm and much increased rates at 3 cm.

The role of the sediment as a potential barrier between recently germinated cells and the water column can be stated in geometrical terms. The resting cyst and the vegetative cells produced upon germination are approximately 50 μM in diameter. Thus, a cyst germinating at 1 cm is likely to be nearly 200 body lengths away from the sediment surface. Presumably, this distance is blocked by a matrix of gravel, sand, silt and clay that is periodically shifting due to physical and biological processes. The vegetative cell must reach the surface via its own physical motion or be "mixed" upward. There is thus likely to be a critical depth below the sediment surface at which germinated cells are simply trapped in the sediment (over seasonal time scales) and never reach the water column. The depth of sediment that is mixed over monthly time scales offers a suitable first estimate for the depth scale. This depth can be approximated using short-lived natural radio-isotopes such as ^{234}Th or ^{7}Be, or artificially labeled sediment. Keafer et al. (1992) found ^{234}Th (half-life 24.1 days) was strongly depleted in the top 0.5-1 cm of sediment at station 29, which has sediment conditions typical of the large cyst-beds in the Gulf of Maine.

3.2 Function Construction

The approach to modeling the net effect of the complex processes above is to define a germination depth (d_g) chosen to represent the mean depth of sediment over which cysts are exposed to enough oxygen for germination and can reach the water column. The most direct estimates of this depth within the silt/clay sediments of the deeper regions of the Gulf of Maine comes from the combined results Anderson and Keafer (1985), Keafer et al. (1992), and Hines (1991), which suggest $d_g \sim 1$ cm. Results in Massachusetts Bay and in Long Island sound are not grossly inconsistent with this estimate (Aller and Cochran, 1976, Benninger, et al., 1979, Krishnaswami, et al., 1980, Wheatcroft, et al., 1994), although the reporting mixing depth is slightly larger. However, these results come from shallower water and, in the case of Massachusetts Bay, more sandy sediment than the conditions within the larger cyst beds.

It is assumed that mixing processes over the upper d_g centimeters maintains a relatively uniform cyst concentration, which allows approximation of the cyst flux without a z-dependence in the cyst concentration term.

The daylight-averaged irradiance is exponentially attenuated within the sediment:

$$E(z) = E_{bottom} \times e^{-k_s z}$$

Using k_s as estimated by Kuhl and Jorgensen. A central value of 3.5 mm^{-1} is chosen, and a range between 2 and 5 mm^{-1} is considered. E_{bottom} in the above expression is the irradiance at the bottom of the water column (i.e. the sediment surface).

3.3 Discussion

The primary assumptions of this approach are:

1. The cyst distribution over the top d_g centimeters is approximately uniform throughout the bloom season.
2. Spatial and temporal variation of d_g is secondary to the overall mean value.
3. The instantaneous germination rate of cysts is not heavily influenced by the time history of germination conditions over the time scales imposed by sediment mixing.
4. Re-supply of cysts from below d_g is negligible over the course of a bloom season (although not necessarily on inter-annual time scales).

Each of these assumptions are discussed below within the context of the Gulf of Maine. They should be revisited if applying this model to a different region.

Regarding assumption 1, observations of cyst variability within the top centimeter for the Gulf of Maine are very rare. One observation from station 29 (Anderson et al. unpublished data) shows 570 cysts/cm^3 from 0-0.5 cm, and 651 cysts/cm^3 from 0.5-1 cm which, given the observed variability in cyst concentration over several orders of magnitude within the Gulf of Maine, supports the assumption of uniformity. In addition, the fact that d_g was chosen to represent the depth of the rapidly mixed zone is consistent with this assumption.

Mixing rates below this upper layer quickly fall to 1-3% the mixing rate within it (Krishnaswami et al., 1980), suggesting that the upward flux of cysts from below the rapidly mixed layer is minimal during the bloom season. However, it is notable that this could be circumvented by persistent transport from deeper areas resulting from complex feeding behavior of benthic fauna.

Spatial variability in d_g is likely to result from gradients in benthic fauna and flora, changes in sediment type, changes in the energy of the overlying flows, and gradients in the amount of organic matter arriving at the sediment. The majority of cysts observed in the Gulf of Maine lie in similar sediments in relatively deep water (i.e. > 75 meters). This would tend to minimize spatial variability in d_g and support a spatially uniform d_g as a good starting point.

Temporal variability in sediment mixing rates has been noted in the aforementioned studies by Aller et al. (1976) and Wheatcroft et al. (1994). In both cases, the trends were attributed to seasonal shifts abundance and activity of benthic fauna. Mixing rates showed a distinct Fall maximum. Present simulations focus on the spring and summer time period, over which little and the value of d_g is chosen to reflect mixing during this time. Thus, although temporal variability in d_g may be significant for inter-annual simulations, it can probably be neglected in the present simulations, which primarily cover only the spring and summer.

Within the Gulf of Maine, simulations were highly influenced by uncertainty in d_g (Stock et al., submitted). A range of d_g from 0.5-1.5 cm was considered, essentially amounting to a factor of three uncertainty in the overall size of the source. Increased knowledge of sediment dynamics and their effect on the germination source would cut down this uncertainty, and provide for a more useful modeling tool.

Aller, R. C., Cochran, J. K., 1976. $^{234}T/^{238}U$ disequilibrium in nearshore sediment: particle reworking and diagenetic time scales. Earth and Planetary Science Letters 29, 37-50.

Anderson, D. M., 1998. Physiology and bloom dynamics of toxic *Alexandrium* species, with emphasis on life cycle transitions. In: Anderson, D. M., Cembella, A. D. ,Hallegraeff, G. M. (Eds.), Physiological Ecology of Harmful Algal Blooms. Springer-Verlag, Berlin, pp. 29-48.

Anderson, D. M., Aubrey, D. G., Tyler, M. A., Coats, W. D., 1982. Vertical and horizontal distributions of dinoflagellate cysts in sediments. Limnology and Oceanography 27, 757-765.

Anderson, D. M., Keafer, B. A., 1985. Dinoflagellate cyst dynamics in coastal and estuarine waters. In: Anderson, D. M., Baden, D. G. ,White, A. W. (Eds.), Toxic Dinoflagellates: Proceedings from the third International Conference. Elsevier, Amsterdam, pp. 219-224.

Anderson, D. M., Keafer, B. A., 1987. The endogenous annual clock in the toxic dinoflagellate *Alexandrium tamarensis*. Nature 325, 616-617.

Anderson, D. M., Stock, C. A., Keafer, B. A., Bronzino, A. C., Matrai, P., Thompson, B., Keller, M., McGillicuddy, D. J., Hyatt, J., submitted. Experimental and modeling observations of *Alexandrium fundyense* cyst dynamics in the Gulf of Maine. Deep-Sea Research, Part II

Anderson, D. M., Taylor, C. D., Armbrust, V. E., 1987. The effects of darkness and anaerobiosis on dinoflagellate cyst germination. Limnology and Oceanography 32, 340-351.

Benninger, L. K., Aller, R. C., Cochran, J. K., Turkekian, K. K., 1979. Effects of biological sediment mixing on the ^{210}Pb chronology and trace metal distribution in a Long Island Sound sediment core. Earth and Planetary Science Letters 43, 241-259.

Bewley, J. D., Black, M., 1978. Physiology and biochemistry of seeds in relation to germination. Springer-Verlag, New York, pages.

Bronzino, A. C., 1998. *Alexandrium* spp. cyst dynamics and their significance in bloom initiation in the Gulf of Maine. Woods Hole Oceanographic Institution, Woods Hole, MA, pages.

Keafer, B. A., Buesseler, K. O., Anderson, D. M., 1992. Burial of living dinoflagellate cysts in estuarine and nearshore sediments. Marine Micropaleontology 20, 147-161.

Krishnaswami, S., Benninger, L. K., Aller, R. C., Von Damm, K. L., 1980. Atmospherically-derived radio-nuclides as tracers of sediment mixing and accumulation in nearshore marine and lake sediments: evidence from ^{7}Be, ^{210}Pb, and $^{239,240}Pu$. Earth and Planetary Science Letters 47, 307-318.

Kuhl, M., Jorgensen, B. B., 1994. The light of microbenthic communities: Radiance distribution and microscale optics of sandy coastal sediments. Limnology and Oceanography 39, 1368-1398.

Matrai, P., Thompson, B., Keller, M. D., submitted. *Alexandrium* spp. from eastern Gulf of Maine: Circannual excystment of resting cysts. Deep Sea Research II

McGillicuddy, D. J., Anderson, D. M., Lynch, D. R., Townsend, D. W., submitted. Mechanisms regulating the large-scale seasonal development of *Alexandrium fundyense* blooms in the Gulf of Maine. Deep Sea Research II

McGillicuddy, D. J., Signell, R. P., Stock, C. A., Keafer, B. A., Keller, M. D., Hetland, R. D., Anderson, D. M., 2003. A mechanism for offshore initiation of harmful algal blooms in the coastal Gulf of Maine. Journal of Plankton Research 25, 1131-1139.

Stock, C. A., McGillicuddy, D. J., Solow, A. R., Anderson, D. M., submitted. Evaluating hypotheses for the initiation and development of *Alexandrium fundyense* blooms in the western Gulf of Maine using a coupled physical-biological model. Deep Sea Research II

Sweeney, B. M., 1969. Rhythmic phenomena in plants. Academic Press, New York, pages.

Wheatcroft, R. A., Olmez, I., Pink, F. X., 1994. Particle bioturbation in Massachusetts Bay: Preliminary results using a new deliberate tracer technique. Journal of Marine Research 52, 1129-1150.

Table 1: Fitted slopes and 90% confidence intervals for each germination time series.

Temperature (°C)	Dark Rate (WGOM)	Dark Rate (EGOM)	Light Rate (WGOM)	Light Rate (EGOM)
2	0.91 (0.25)	1.21 (0.34)	0.89 (0.27)	1.74 (0.62)
4	0.82 (0.24)	1.43 (0.30)	1.69 (0.15)	1.74 (0.77)
6	1.19 (0.17)	1.70 (0.37)	2.03 (0.52)	1.58 (0.34)
8	1.40 (0.32)	3.32 (0.60)	6.55 (1.76)	4.03 (0.60)
15	NA	4.24 (0.48)	NA	8.72 (3.51)

Table 2: Parameters fit to the germination function

parameter	units	$E = E_{lgt}$	$E = E_{drk}$
α	$(^{o}C)^{-1}$	0.790	0.394
β	dimensionless	6.27	3.33
G_{max}	%/day	8.72	4.26
G_{min}	%/day	1.50	1.04

Table 3: Data sets used for the construction of the endogenous clock.

Station # (see fig. 1)	Reference	Latitude (N)	Longitude (W)	Depth	Date of Isolation
29 (1)	Anderson and Keafer (1987)*	43	70.19'	146	Aug. 1984
29 (2)	Anderson and Keafer (1987)*	43	70.19'	146	July 1985
29 (3)	Anderson and Keafer (1987)*	43	70.19'	146	June 1986
38	Bronzino (1998)	43 30.29	69 52.72'	125	late Jan. early Feb. 1999
61	Matrai et al. (submitted)	43 33.75'	69 26.93	150	Dec. 9 1999
94	Matrai et al. (submitted)	43 40.29'	68 37.93	150	Dec. 10 1999
4	Matrai et al. (submitted)	44 53.47'	66 48.86	138	Jan. 27 2000

* Only a portion of the data from the August 1984 station was presented in the reference. Time series were continued after publication and on multiple isolates to verify the clock.

Table 4: Monthly values of the germination potential (GP, %), and the normalized germination potential (NGP)

	Jan	Feb	Mar	Apr	May	June	July	Aug	Sep	Oct	Nov	Dec
GP	21.9	11.25	78.0	85.0	96.8	93.0	60.0	50.0	10.0	11.5	17.0	34.5
NGP	0.23	0.12	0.81	0.88	1.00	0.96	0.62	0.52	0.10	0.12	0.18	0.36

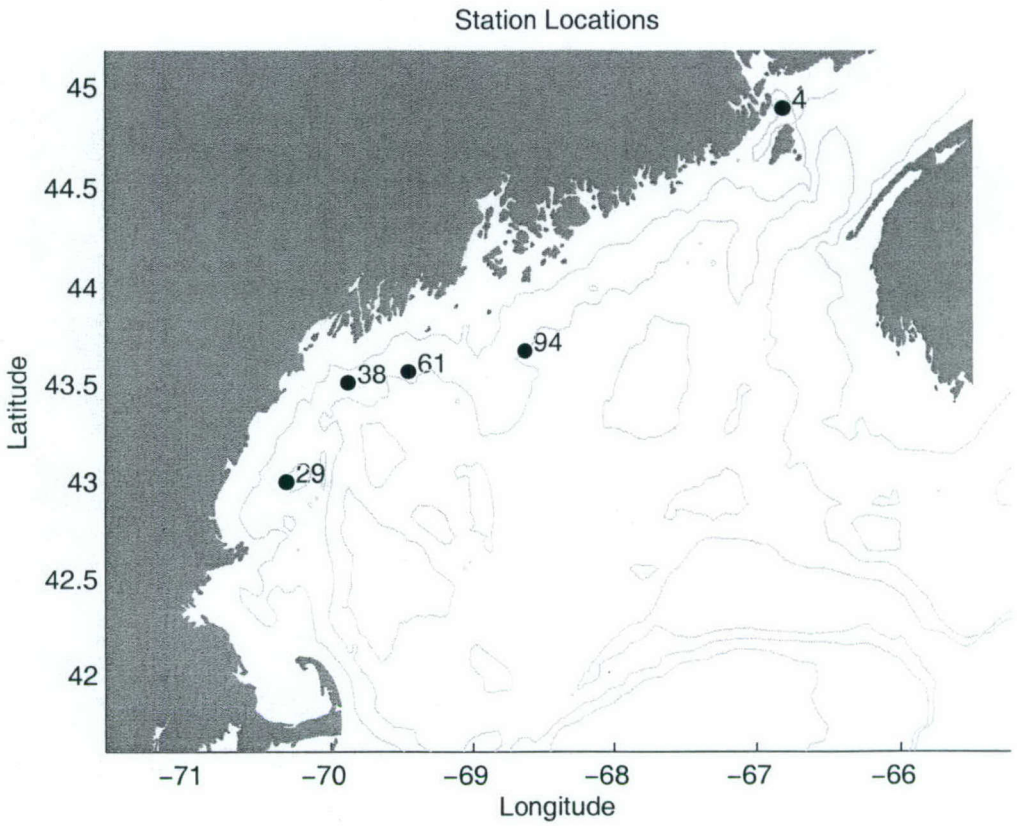


Figure 1: Stations where cysts were isolated for germination and endogenous clock experiments.

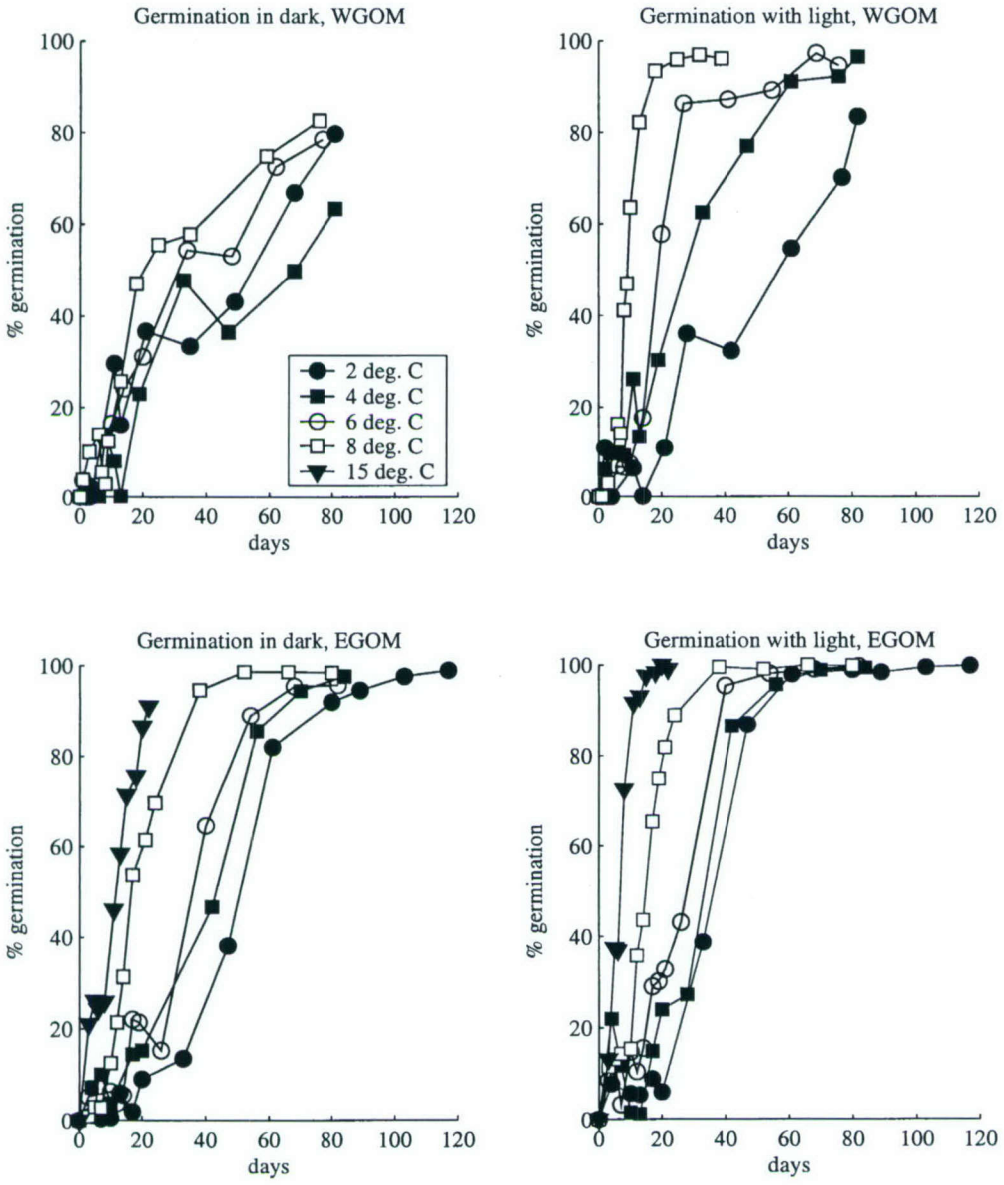


Figure 2: Germination time series data from station 38 (top panel, WGOM = Western Gulf of Maine), and data from station 4 (bottom panel, EGOM = Eastern Gulf of Maine). Note that a germination time series at 15° C was not taken for the WGOM case.

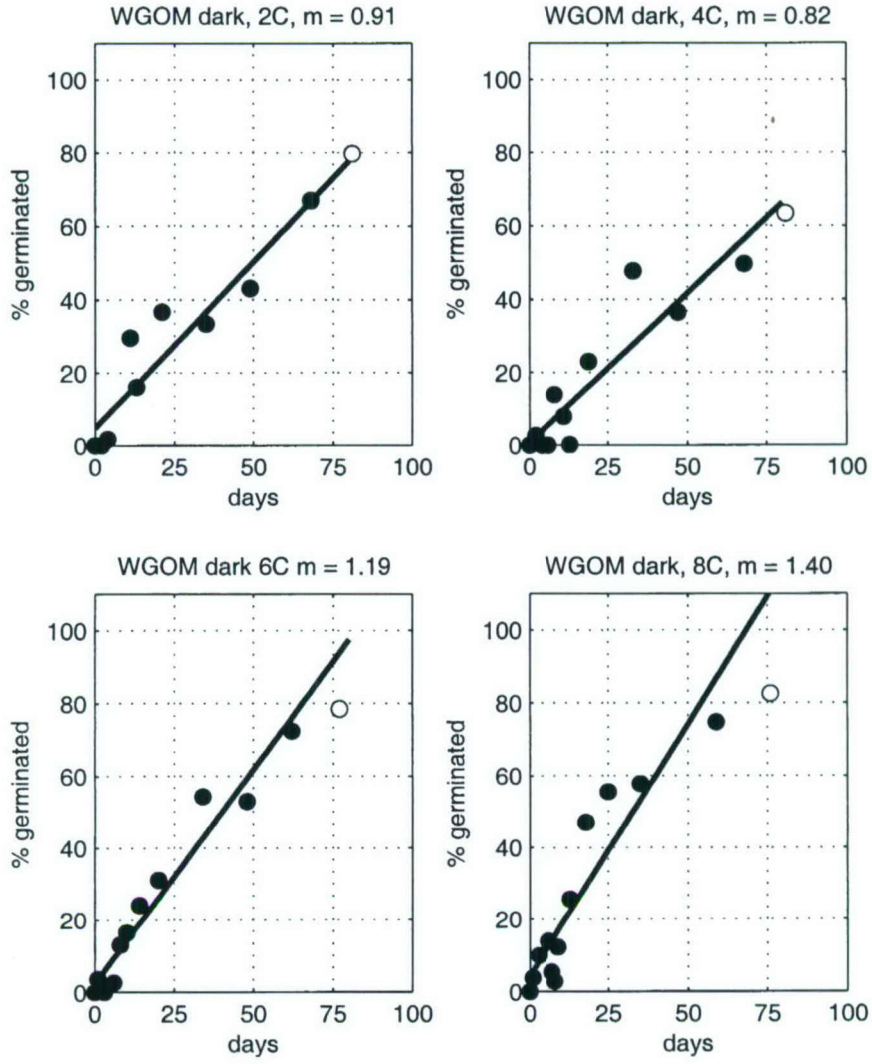


Figure 3: Fits to the WGOM (station 38) data in dark conditions. Solid circles are used in the fit, open circles are not.

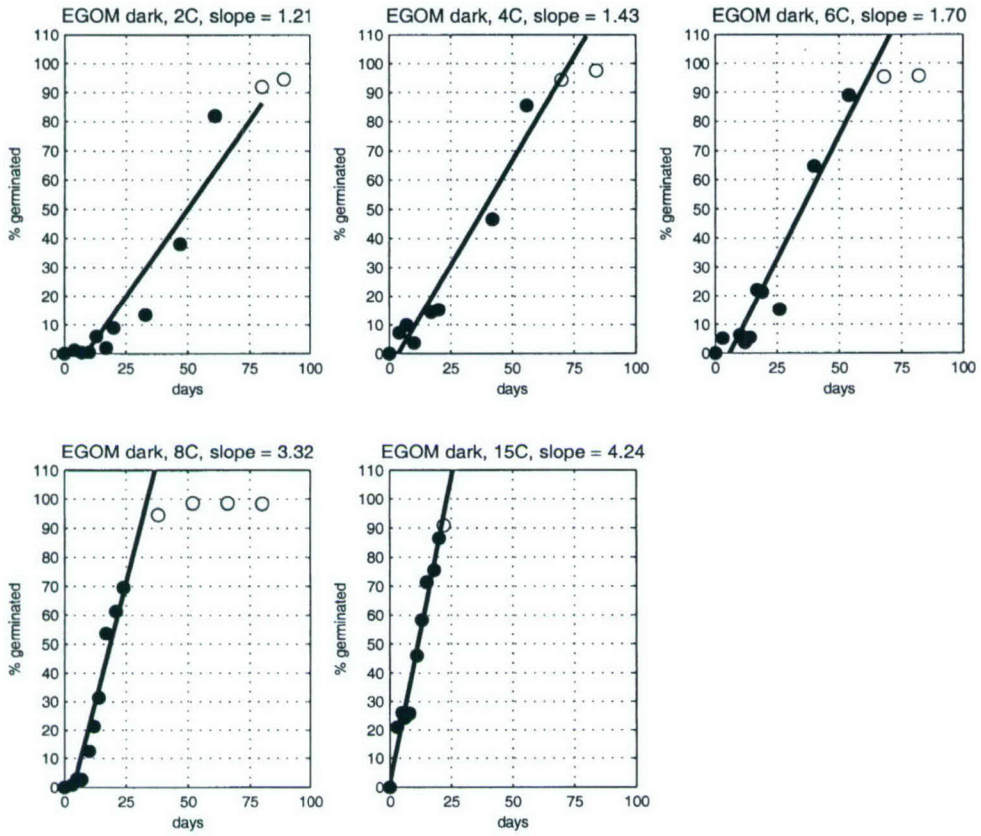


Figure 4: Fits to the EGOM (station 4) data with dark conditions. Solid circles are used in the fit, open circles are not.

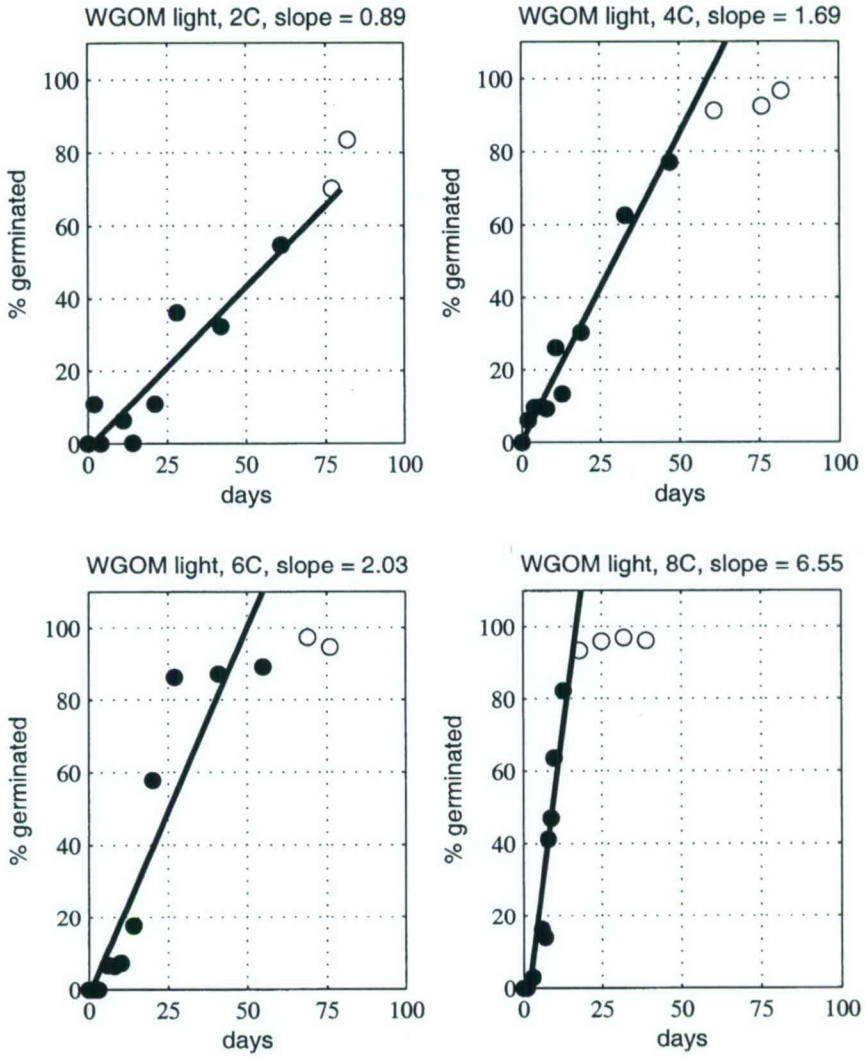


Figure 5: Fits to the WGOM (station 38) data with light conditions. Solid circles are used in the fit, open circles are not.

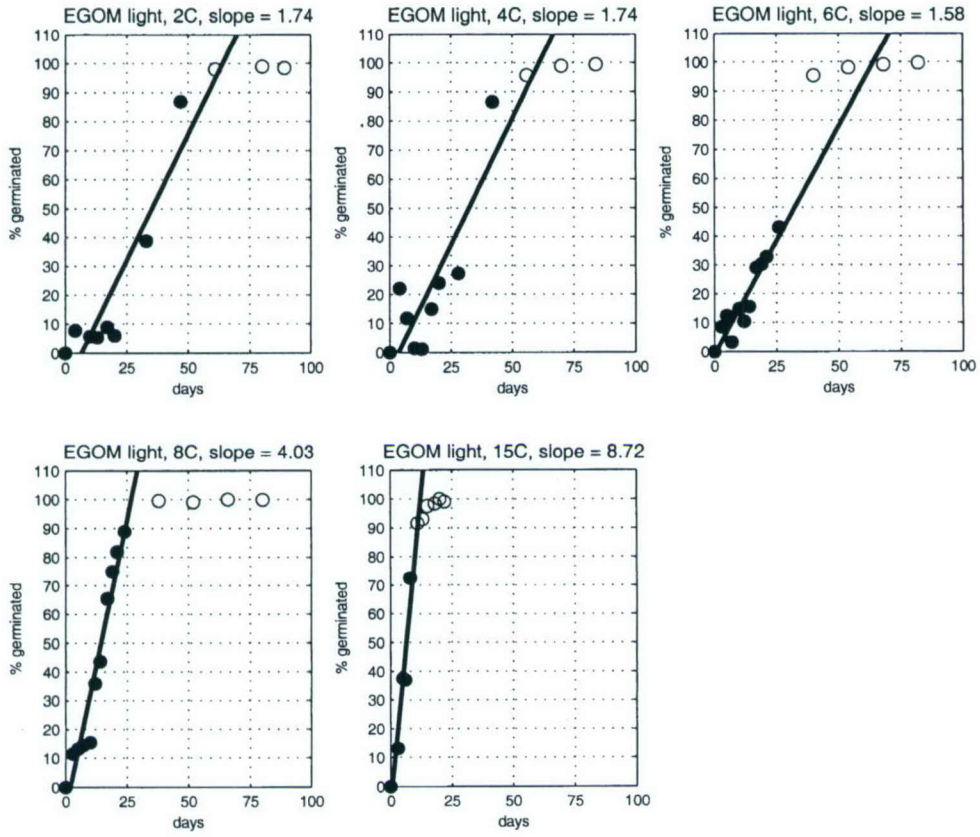


Figure 6: Fits to the EGOM (station 4) data with light conditions using the criteria described in section II above. Solid circles are used in the fit, open circles are not.

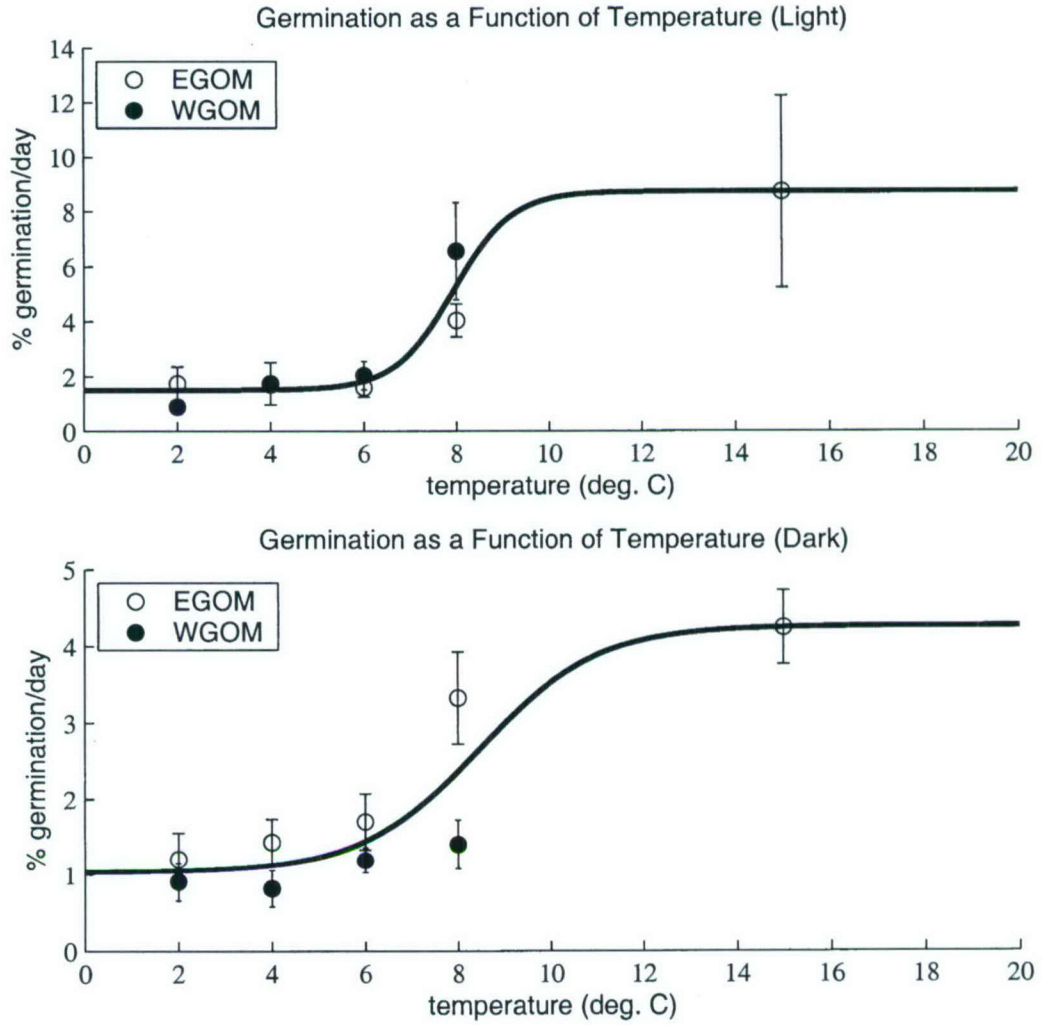


Figure 7. Germination as a function of temperature at $E=E_{lgt}$ (top panel) and $E=E_{drk}$ (bottom panel). The markers are experimental time series rate estimates with 90% uncertainty bounds (table 1). The dark line is the functional fit which drives the germination model. Parameters describing the fit are given in table 2.

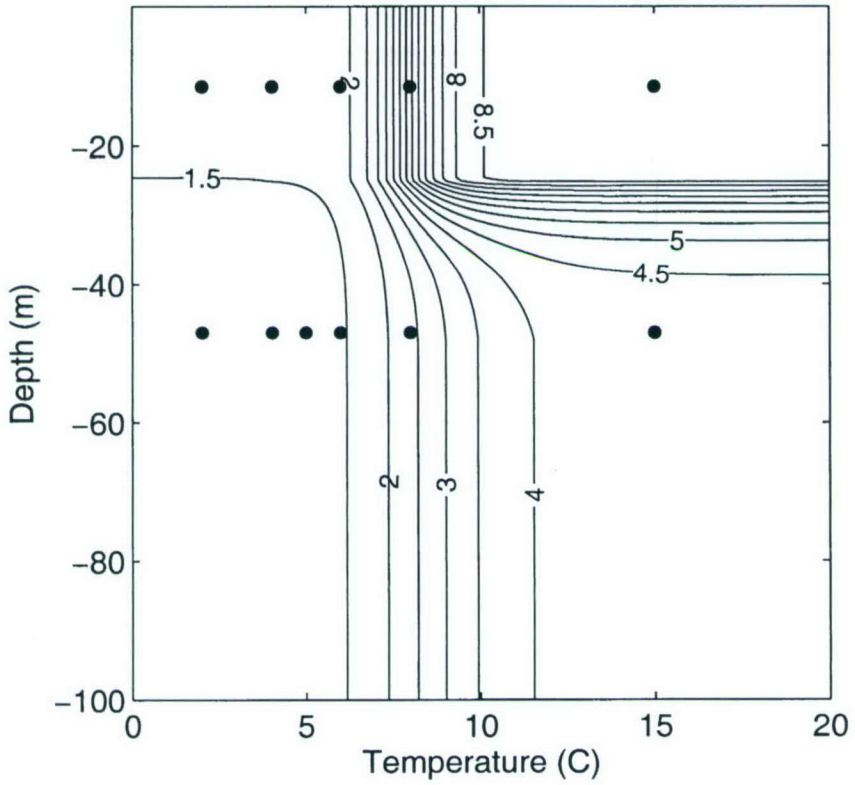


Figure 8: Contours (interval = 0.5 %/day)) of the model estimated germination rate (%/day) at the sediment surface as a function of light and temperature ($G(T,E)$). Light has been transformed to an equivalent depth using an exponential attenuation coefficient $k_w = 0.2$ m^{-1} and a typical day-averaged (8 AM-6 PM) irradiance of 345 watts/m^2. Markers show temperatures where experiments were carried out for light conditions (upper row) and dark conditions (bottom row). Note that these estimates are at the sediment surface, and there is additional light attenuation over the top cm of the sediment ($k_s = 3.5$ mm^{-1}) which is not shown.

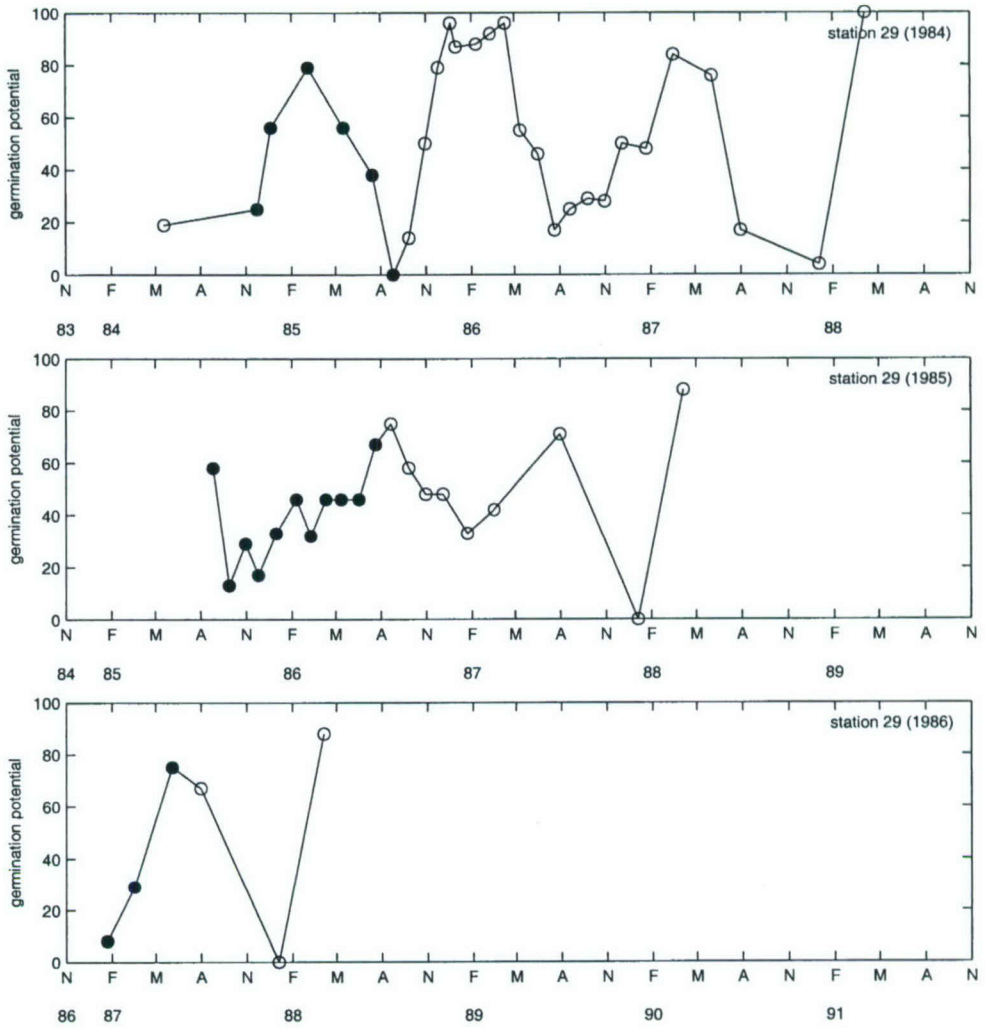


Figure 9: Endogenous clock experiment data for the three sediment isolations taken from station 29 near Cape Ann. Note that the axes are each 5 years in duration and all begin on November 1 to facilitate comparison of the shapes and phases of the germination potential data. "M" is May, "A" is August. Dates where experiments to measure the germination potential were *started* are shown as circles. Closed circles indicate points used in the formulation of the endogenous clock applied to the model, open circles are not. Note the early initial peak for the 1984 isolate (top panel) contrasted with the later peaks observed in 1985 and 1986. Also, note gradual climb to peak germination exhibited by the 1985 isolation. *Note that the first point in the 1984 time series is from an earlier sediment isolation at the same location, and it is thus not used in the model.*

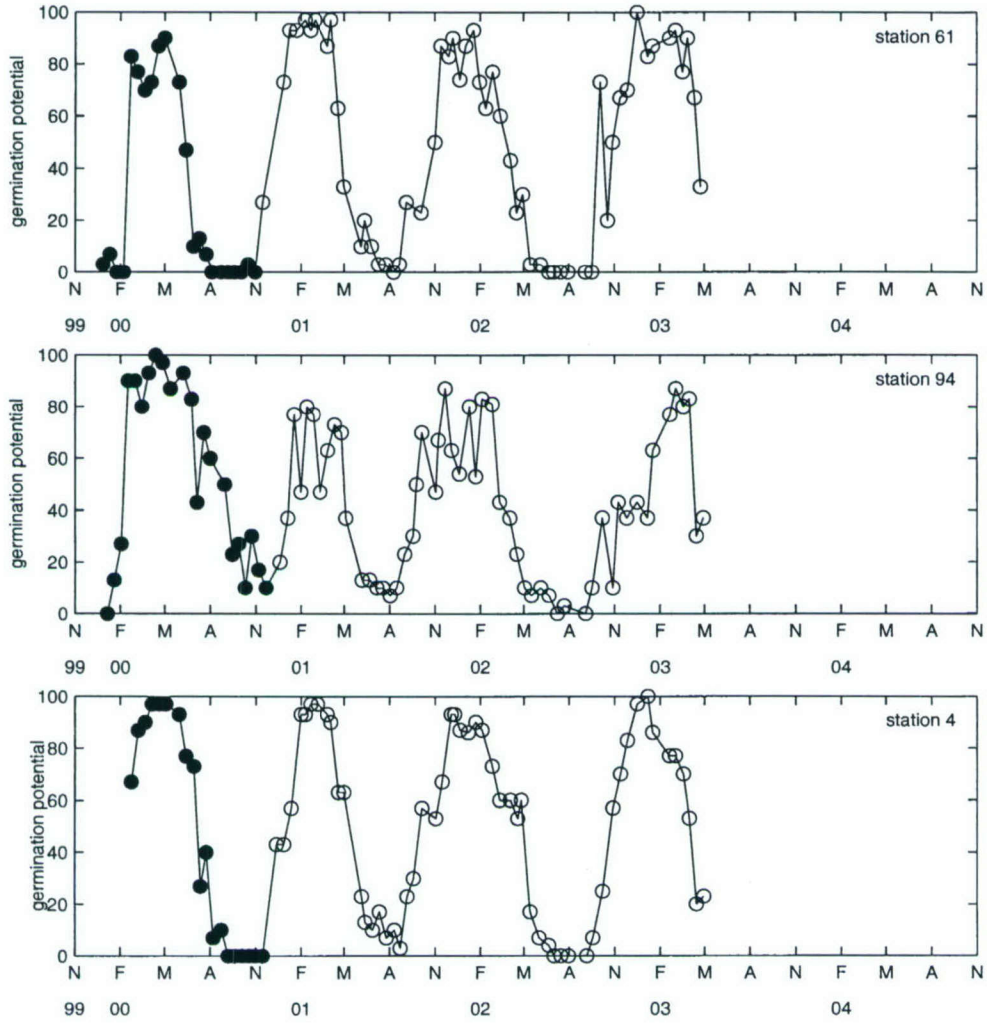


Figure 10: Endogenous clock experiment data for the three isolates presented in Matrai et al. (in prep.). Notation is as in figure 11. Note the fairly consistent late winter, early spring initial peak that is generally maintained into the early summer, also note the gradual decline in germination potential exhibited by station 94.

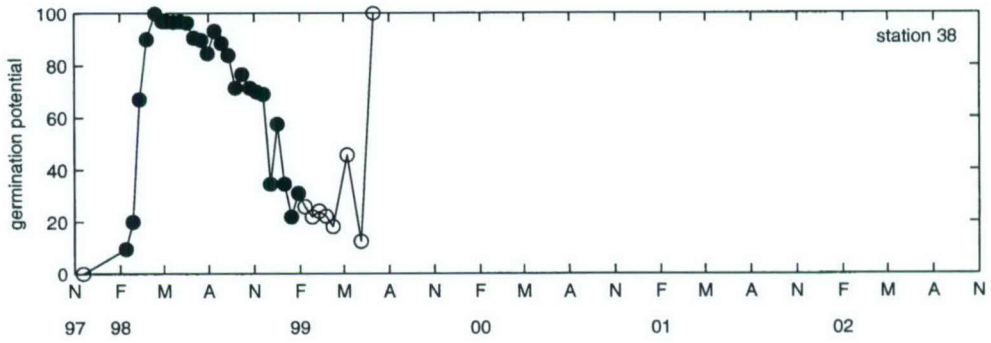


Figure 11: Endogenous clock data presented in Bronzino (1998). Notation is as in figures 9 and 10. The initial peak is in late March/early May, and the decline in germination potential after the peak is very slow. *Note that the first point in the data set is the result of an earlier isolation of cysts at the same location and it is thus not included in the model.*

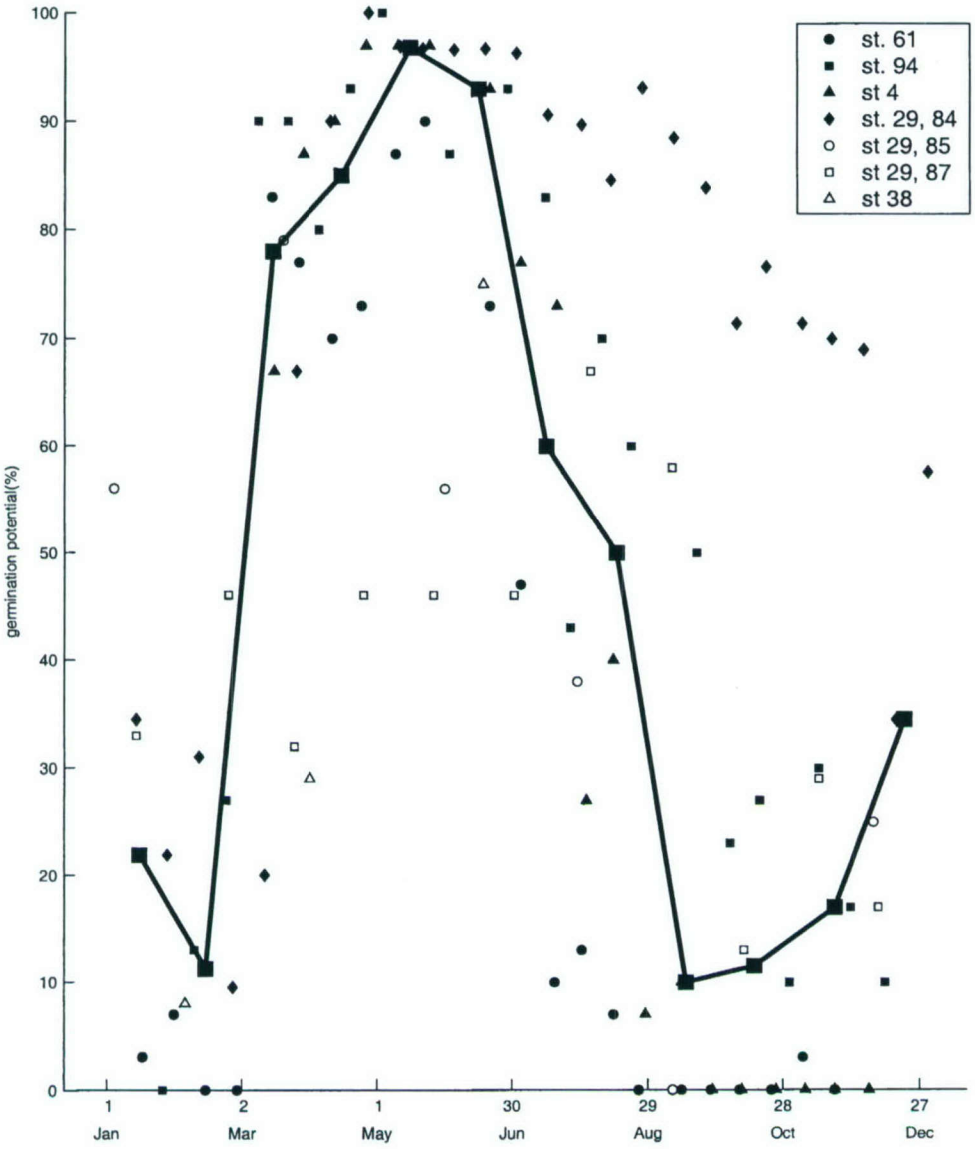


Figure 12: Data used for the specification of the endogenous clock (see legend) and resulting germination potential function (dark line). Large filled squares mark the mid-points of the months where the germination potential was estimated.

Appendix B

The Growth Model

This document gives a detailed description of the *Alexandrium fundyense* growth model that was developed as part of the ECOHAB-Gulf of Maine program. A reference is provided by Stock et al. (submitted), and model is also used in McGillicuddy et al. (McGillicuddy, et al., submitted).

The growth parameterization takes the form suggested by Platt and Jassby (1976) for photosynthesis, irradiance relationships and used by Langdon (1987, 1988) in studies of phytoplankton growth:

$$\mu(E,T,S) = \left(\mu_{\max}(T,S) + \mu_o^r\right)\tanh\left(\frac{\alpha_g E}{(\mu_{\max}(T,S) + \mu_o^r)}\right) - \mu_o^r$$

where μ_{max} is the maximum growth rate (days^{-1}) for a given temperature (T) and salinity (S), μ_o^r is the maintenance respiration rate (days^{-1}), E is the daylight-averaged irradiance (6 AM – 8 PM, watts/m^2), and α_g is the growth efficiency (m^2 watt^{-1} day^{-1}). Ranges, references and previous ranges considered are given in table 1. Table 2 summarizes the origins of the different *A. fundyense* isolates used in the studies that contributed to function construction.

The dependence of μ_{max} on temperature and salinity is formulated as follows:

$$\mu_{\max}(T,S) = \mu(T_{opt}, S_{opt}) \times f(T) \times f(S)$$

Where T_{opt} and S_{opt} are the optimal temperature and salinity for growth. $f(T)$ and $f(S)$ are scaling factors between 0 and 1. The temperature relationship was formulated using data from isolates GTCA29, GTCA28, GT6, GTMP, BOF, and MI that measured growth as a

function of temperature. The data from each isolate was normalized to the maximum growth value measured for the isolate. A cubic polynomial was fit to the normalized data greater than 5°C. Growth rates below 5°C were approximated with a linear extrapolation (i.e. the first term in the Taylor expansion of the polynomial about T = 5°C) to prevent anomalous extrapolation. The resulting relationship achieves an R^2 of 0.79. Lastly, the fit polynomial is normalized to ensure that a value of 1 is reached at peak germination (figure 1). This yields:

$$f(T > 5) = -0.000513T^3 + 0.0160T^2 - 0.0867T + 0.382$$
$$f(T \leq 5) = f(T = 5) - 0.0343(5 - T)$$

The salinity dependence $f(S)$ was constructed in similar fashion using data from Prakash (1967) and Etheridge and Roesler (isolates MI and BOF, figure 2). The resulting polynomial is:

$$f(S) = 0.0000882S^3 - 0.00808S^2 + 0.220S - 0.872$$

The salinity dependence is secondary to temperature over the normal range of salinities encountered in the western Gulf of Maine (25-33 PSU), and the relationship is rather noisy (R^2 = 0.45 before normalization). However, retaining the relationship despite this uncertainty allows assessment of the hypothesis that elevated cell concentrations in river plume waters can be explained by increased growth rates in waters of depressed salinity. The final relationship with both the T and S functionality is shown in figure 3.

The range of μ_{max} at optimal temperature and salinity is estimated based on adjustment of measured rates using the polynomial relationships described above. Most

experiments used in this study measured the light saturated growth rate at only a limited number of T, S values (often only one). For example, in the case that the growth rate for an isolate was measured only at 15C and ~30 ppt salinity, the relationships above suggest that measured rates here are about 94% optimal with respect to temperature, and 83% optimal with respect to salinity. The adjustment was thus done as follows:

$$\mu_{\max}(T_{opt}, S_{opt}) = \frac{\mu_{\max}(T,S)}{f(T)\times f(S)} = \frac{\mu_{\max}(T,S)}{0.94\times 0.83}$$

Note that there is an assumption here that the two factors act independently, and no attempt to account for variable uncertainty in growth estimates from the various studies.

The estimates of the growth efficiency (α) and the maintenance respiration (μ_o^r) relied solely on the Cullen data, which was exceptionally well resolved at low light conditions. This added resolution greatly improved confidence in the estimates of these two parameters relative to previous iterations of this model.

When nutrient dependence is added, it is assumed that only one factor apart from T and S can limit growth. For example, a dependence on dissolved inorganic nitrogen (DIN) is added as follows:

$$\mu(T,S,DIN) = \mu_{\max}(T,S)\times f(DIN)$$

f(DIN), like *f(T)* and *f(S)*, is another factor between 0 – 1. A Monod relationship is used to model the first order response of growth to DIN levels:

$$f(DIN) = \frac{[DIN]}{[DIN] + K_{DIN}}$$

[DIN] is the concentration of dissolved inorganic nitrogen in μM and K_{DIN} is an approximate half saturation constant for DIN (also in μM). $\mu(T,S,DIN)$ is then compared to $\mu(T,S,E)$ and the minimum of the two is taken:

$$\mu(T,S,E,DIN) = \min(\mu(T,S,E),\mu(T,S,DIN))$$

Interpretive limitations are imposed by the assumptions used in the model formulation. The model can only be used to test hypotheses concerning systems where temperature, salinity, light, and nutrients are thought to be the primary factors controlling growth. Several other potentially important factors, such as the role of turbulence (Thomas and Gibson, 1990, Sullivan, et al., 2003) and bacterial abundance (Yentsch, et al., 1975) have been neglected. The neglect of these factors must be considered an implicit part of each hypothesis tested with the above model.

Table 1: Growth function Parameters. Central value followed by standard deviation (in parentheses).

Symbol	Description	New Value	Sources
$\mu_{max}(T_{opt}, S_{opt})$	The maximum growth rate (day^{-1}) at optimal temperature and salinity.	0.58 (0.46-0.70)	Cullen et al. (in preparation); Langdon (1988); Watras et al. (1982); Keafer (unpublished data); Kulis (unpublished data); Etheridge and Roesler (2003)
α_g	The growth efficiency (m^2 $watts^{-1}$ day^{-1})	0.036 (0.017-0.056)	Cullen et al. (in preparation)
μ_o^r	The maintenance growth rate (day^{-1})	0.20 (0.15-0.25)	Cullen et al. (in preparation)

Table 2: Summary of different isolates used in growth function construction

Designation	**Origin**	**Source**
ccmp1978	Bay of Fundy	Cullen et al. (in preparation)
ccmp1979	Bay of Fundy	Cullen et al. (in preparation)
ccmp1980	Bay of Fundy	Cullen et al. (in preparation)
cb301	Casco Bay	Cullen et al. (in preparation)
cb307	Casco Bay	Cullen et al. (in preparation)
cb501	Casco Bay	Cullen et al. (in preparation)
GTMP	Mill Pond (Cape Cod)	Watras et al. (1982)
GTCA29	Near Cape Ann	Keafer (unpublished)
GTCA28	Near Cape Ann	Kulis (unpublished)
BOF	Bay of Fundy	Etheridge and Roesler (2003)
MI	Monhegan Island	Etheridge and Roesler (2003)
gt6	Near Cape Ann	Langdon (1987, 1988)
none	Head Harbour, Bay of Fundy	Prakash (1967)

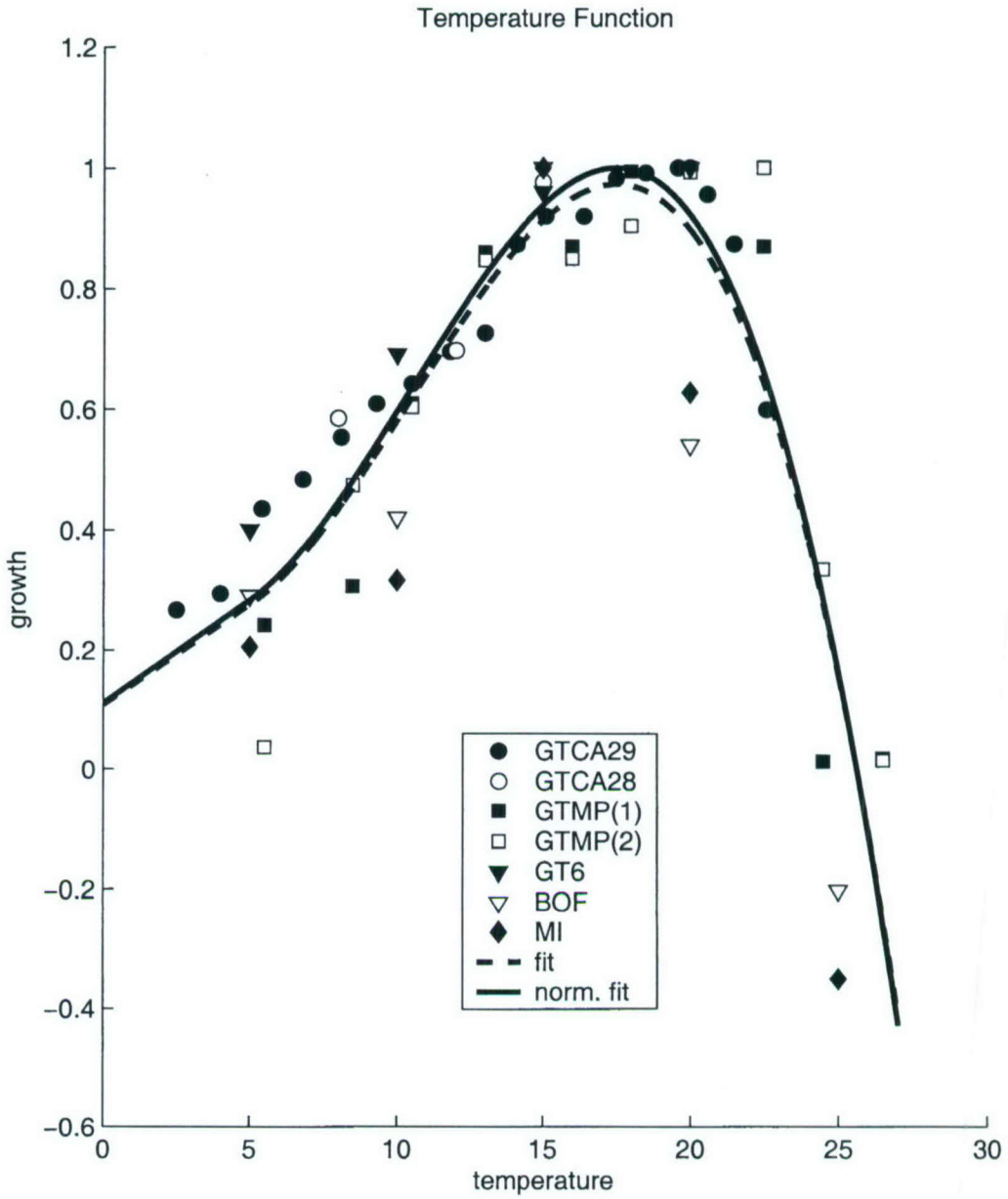


Figure 1: Temperature Scaling factor for application to the growth function. The dashed line is the relationship before final normalization to ensure a maximum value of 1 (solid line).

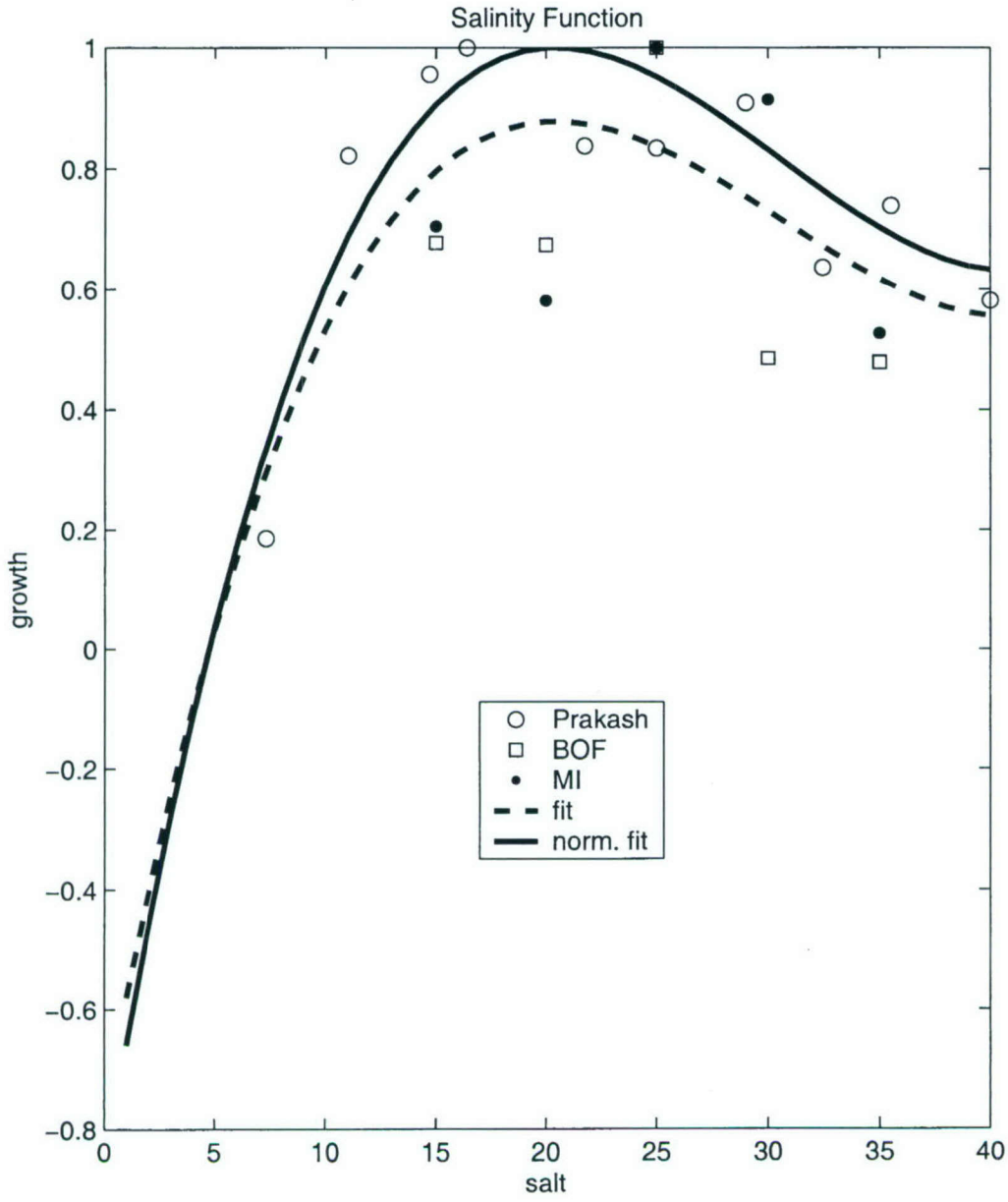


Figure 2: Salinity scaling factor for application to the growth function. The dashed line is the relationship before final normalization to ensure a maximum value of 1 (thick solid line).

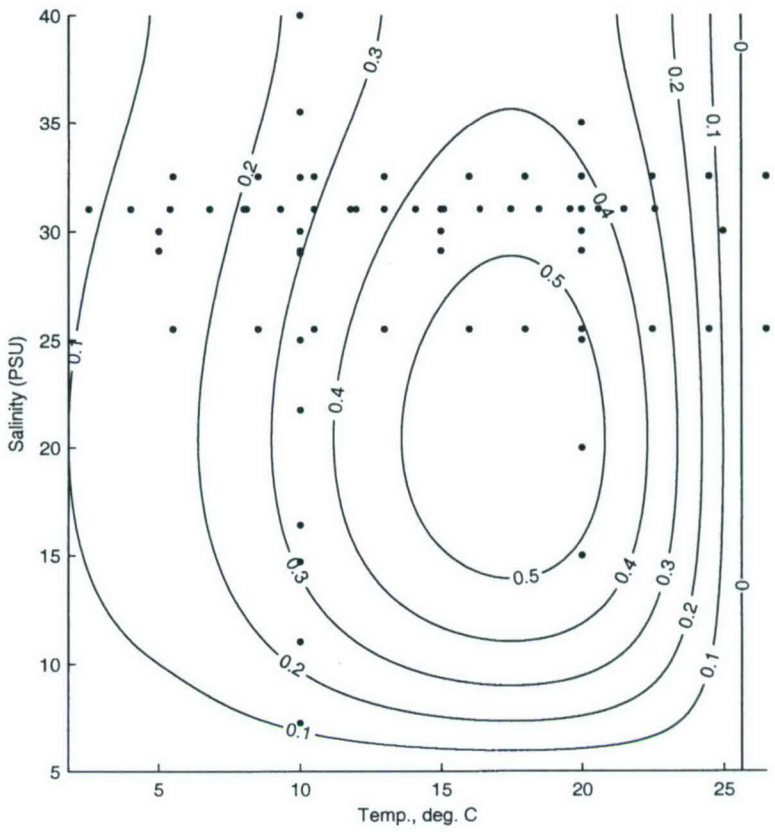


Figure 3: Maximum Growth Rate as a Function of T, S. Points indicate data coverage.

Cullen, J. J., Wood, Barnett, Normandeau, Ryan, in preparation. Behavioral and physiological variability among strains of the toxic dinoflagellate *Alexandrium fundyense* from the Gulf of Maine. Deep Sea Research II this volume,

Etheridge, S. M., Roesler, C. S., 2003. Geographic trends in *Alexandrium* spp. growth and toxicity as a function of environmental conditions. In: The Tenth International Conference on Harmful Algal Blooms, St. Petersburg FLA. in press, pp.

Langdon, C., 1987. On the causes of interspecific differences in the growth-irradiance relationships for phytoplankton. Part I. A comparitive study of the growth irradiance relationships of three marine phytoplankton species: *Skelotonema costatum, Olithodiscus luteus* and *Gonyaulax tamarensis*. Journal of Plankton Research 9, 459-482.

Langdon, C., 1988. On the causes of interspecific differences in the growth-irradiance relationship for phytoplankton. Part II: A general review. Journal of Plankton Research 10, 1291-1312.

McGillicuddy, D. J., Anderson, D. M., Lynch, D. R., Townsend, D. W., submitted. Mechanisms regulating the large-scale seasonal development of *Alexandrium fundyense* blooms in the Gulf of Maine. Deep-Sea Research, Part II

Prakash, A., 1967. Growth and toxcity of a marine dinoflagellate, *Gonyaulax tamarensis*. Journal of the Fisheries Research Board of Canada 24,

Stock, C. A., McGillicuddy, D. J., Solow, A. R., Anderson, D. M., submitted. Evaluating hypotheses for the initiation and development of *Alexandrium fundyense* blooms in the western Gulf of Maine using a coupled physical-biological model. Deep Sea Research II

Sullivan, J., Swift, E., Donaghay, P., Rines, J., 2003. Small-scale turbulence affects the division rate and morphology of two red-tide dinoflagellates. Harmful Algae 2, 183-199.

Thomas, W. H., Gibson, C. H., 1990. Quantified small-scale turbulence inhibits a red tide dinofaggellate, *Gonyaulax polyedra* Stein. Deep Sea Research 37, 1583-1593.

Watras, C. J., Chisholm, S. W., Anderson, D. M., 1982. Regulation of growth in an estuarine clone of *Gonyaulax tamarensis* Lebour: salinity-dependent temperature responses. Journal of Experimental Marine Biology and Ecology 62, 25-37.

Yentsch, C. M., Cole, E. J., Salvaggio, M. G., 1975. Some of the growth characteristics of *Gonyaulax tamarensis* isolated from the Gulf of Maine. In: LoCicero, V. R., (Ed.), Proceedings of the first international conference on toxic dinoflagellate blooms, Boston. Massachusetts Science and Technology Foundation, pp. 163-180.

50272-101

REPORT DOCUMENTATION PAGE	1. REPORT NO. MIT/WHOI 2005-02	2.	3. Recipient's Accession No.

4. Title and Subtitle

Blooms of the Toxic Dinoflagellate *Alexandrium fundyense* in the Gulf of Maine: Investigations Using a Physical-Biological Model

5. Report Date February 2005

6.

7. Author(s) Charles A. Stock

8. Performing Organization Rept. No.

9. Performing Organization Name and Address

MIT/WHOI Joint Program in Oceanography/Applied Ocean Science & Engineering

10. Project/Task/Work Unit No. MIT/WHOI 2005-02

11. Contract(C) or Grant(G) No.

(C) OCE-9808173

(G)

12. Sponsoring Organization Name and Address

National Science Foundation
EPA STAR Fellowship
WHOI Academic Programs Office

13. Type of Report & Period Covered Ph.D. Thesis

14.

15. Supplementary Notes

This thesis should be cited as: Charles A. Stock, 2004. Blooms of the Toxic Dinoflagellate *Alexandrium fundyense* in the Gulf of Maine: Investigations Using a Physical-Biological Model. Ph.D. Thesis. MIT/WHOI, 2005-02.

16. Abstract (Limit: 200 words)

Blooms of the toxic dinoflagellate *Alexandrium fundyense* are annually recurrent in the western Gulf of Maine (WGOM) and pose a serious economic and public health threat. In this thesis, a biological model of the *A. fundyense* life cycle developed from laboratory and field data is combined with a circulation model to test hypotheses concerning the factors governing *A. fundyense* blooms in the springs of 1993 and 1994. Several biological model structures are tested against the 1993 observations using the method of maximum likelihood. Analysis suggests that either nitrogen limitation or mortality is needed to match observed patterns. Application of 1993 optimized values to 1994 shows similar fit is maintained only for those runs with nitrogen limitation. Model diagnosis suggests that cysts germinating offshore of Casco Bay provide a plausible source of cells for the blooms, although inputs from the eastern Gulf of Maine become significant as the season progresses. Net growth rates are generally low and have a limited influence on bloom magnitude. The model suggests that differences in shellfish toxicity during the two years result primarily from differences in the wind and its influence on along and cross-shore transport of cells.

17. Document Analysis **a. Descriptors**

Gulf of Maine
Harmful Algal Blooms
modeling

b. Identifiers/Open-Ended Terms

c. COSATI Field/Group

18. Availability Statement

Approved for publication; distribution unlimited.

19. Security Class (This Report) UNCLASSIFIED

21. No. of Pages 269

20. Security Class (This Page)

22. Price

(See ANSI-Z39.18) *See Instructions on Reverse*

OPTIONAL FORM 272 (4-77)
(Formerly NTIS-35)
Department of Commerce